Multi-scale evaluation of bone combining indentation, in situ XCT mechanics and digital volume correlation

Aikaterina Karali

This thesis is submitted in fulfilment of the requirements for the award of the degree of

Doctor of Philosophy of the

University of Portsmouth

To my siblings,

“*γνῶθι σαύτόν*” –Χείλωνας Δαμαγήτου

Contents

Declaration

Whilst registered as a candidate for the above degree, I have not been registered for any other research award. The results and conclusions embodied in this thesis are the work of the named candidate and have not been submitted for any other academic award.

Aikaterina Karali

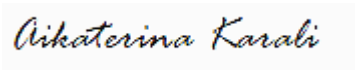

Word count ~45000

Acknowledgments

This PhD has been the biggest part of my life for the last 3 years and there are many people whose help has been vital for its completion.

Firstly, I would like to thank my supervisor Dr Gianluca Tozzi, for his support and full-of-ideas mind, which he shared with me way before this project even started, when we first met in 2013. Since then he inspired me and showed me the way to achieve all this and many more. My biggest gratitude goes to my second supervisor Dr Jurgita Zekonyete who supported and believed in me. Thanks are also due to my third supervisor Dr Gordon Blunn who gave guidance when needed and motivated me with his knowledge. At last, I want to thank, for his advice and contributions, Dr Enrico Dall'Ara from the University of Sheffield, who has not formally been in my supervision team but has actively supported me with his suggestions and knowledge on biomechanics.

I would like to express my gratitude to the University of Portsmouth for giving me the means to complete all this work and the people in the faculties of Technology and Science for their help and contributions Mr Geoff Britton, Dr Chulin Jiang, Robber Elliott , Dr Robin Rumney, Dr Marta Roldo, Lowrie Varyo. Special thanks also goes Dr Alex P. Kao for his friendship, kindness, willingness to assist and listen to me.

A big thank you goes to our group in room A2.09 that has been a support system, most of you are now Doctors, I want to thank all of you together and separately because each one of you gave me something different and all of you together gave me hope in a daily basis. Dr Hayder Murad for believing in me like no one, who is not related to me, has ever done. Dr Ahmed Ahmed for proofreading the work, his inspirational talks, positivity and open mind, Dr Marco Curto for his coffees and uncomfortable hugs, Dr Marta Peña Fernández for our long conversations and always being honest and the last addition to our little team Roxane Bonithon for her help in all of my projects both scientifically and mentally.

In all these years there have been many people in my life helping me to cope with all the challenges rising. I would like to thank Yordana Shopova and Katya Dimitrova for taking care of me and putting things into perspective when I lost focus. Fotios Germenis and Sotiris Ilkos for lifting my spirits. Vicky Protopsalti and Eleni Kritza for being there for me all these years even from the other side of Europe and our adventures together. I would also like to acknowledge the support of my little Greek family here in Portsmouth who made sure I also had some fun while constantly talking about bones.

Για το τέλος θα ήθελα να ευχαριστήσω την οικογένειά μου και τους φίλους μου που είναι στην Ελλάδα και παρ' όλ' αυτά ήταν δίπλα μου κάθε μέρα. Τη Μαρία Δημητρίου για τις συζητήσεις που κάναμε κάθε βράδυ με μπύρες στην παραλία, τη Μαρία Αλατζίδου που με έκανε να γελάω και με άκουγε με τις ώρες στο τηλέφωνο να μιλάω για κόκαλα. Την ξαδέρφη μου Σοφία Πετρίδου που όταν τη χρειαζόμουν ήταν πάντα εκεί βοηθώντας με να βάλω προτεραιότητες στη ζωή μου. Το Γιάννη Χρυσοστομάκη που μου έμαθε να σκέφτομαι και να αγαπάω τη φυσική. Το μεγαλύτερο ευχαριστώ πάει στους ανθρώπους που με μεγάλωσαν και που μεγάλωσα μαζί τους. Πρώτα θα ήθελα να ευχαριστήσω τις τρεις γιαγιάδες μου, Κατερίνα Καραλή, Ολυμπία Ταΐγανίδου και Ελένη Μαρίνου, η κάθε μία με στήριξε με διαφορετικό τρόπο σε όλη τη διάρκεια του διδακτορικού. Τη Μαρία Ταΐγανίδου και Ηλία Ανδρίτσο που είναι οι δεύτεροι γονείς μου, τα ξαδέρφια μου Ολυμπία και Κωνσταντίνο (ανδριτσάκια) που είναι αδέρφια μου και δεν μπορώ να θυμηθώ τη ζωή μου χωρίς την υποστηριξή τους. Θα ήθελα επισης να ευχαριστήσω τα αδέρφια μου Γιώργο και Αριστείδη Καραλή για την αμέριστη αγάπη τους και ενθαρρυνσή τους, ότι και να πω γι'αυτους τους δύο ανθρώπους είναι λίγο. Τέλος θα ήθελα να ευχαριστήσω τους γονείς μου, Σοφία Ταΐγανίδου και Ευαγγελο Καραλή. Τη μητέρα μου που δεν αμφέβαλε στιγμή για μένα και με δέχεται κάθε μέρα χωρίς προϋποθέσεις , τον πατέρα μου που μου έμαθε να αγαπάω, να προσπαθώ χωρίς να εγκαταλείπω, και να αφοσιώνομαι σε ό,τι κάνω.

Abstract

Bone is an anisotropic and heterogeneous material with hierarchical structure, hence its mechanical behaviour in the sub-microstructure (1-10 μm) affects its performance in the macrostructure. In recent years, the combination of high-resolution X-ray Computed Tomography (XCT) with in situ mechanical testing has been used to analyse bone morphology and mechanics at different resolution and specimen sizes.

The primary aim of this PhD work is to combine high-resolution X-ray computed tomography (XCT) imaging, in situ/ex situ mechanics and digital volume correlation (DVC) on native and regenerated bone tissue, to provide a better understanding of their mechanical behaviour and its relationship to their morphological properties. At first, the effect of laboratory-based XCT imaging irradiation on the bone tissue, at the sub-microstructure, was examined to ensure the reliability of the results in the in situ XCT experiments carried out in this work. Then, cortical bone microstructural morphology was analysed in relation to its performance during plastic deformation and crack initiation, as well as morphological changes associated to the three-dimensional (3D) full-field strain distribution computed via DVC. Finally, bone regeneration was investigated at organ level using in situ XCT imaging for the mineralised tissue; whilst the radiolucent cartilage matrix in the same region was studied through histological analysis.

Indentation was employed to assess the degradation of the mechanical properties of trabecular bone tissue in the sub-microscale (ex situ nanoindentation) as well as to induce plastic deformation at the microscale in cortical bone tissue (in situ XCT indentation). Specifically, nanoindentation was used to obtain the elastic modulus prior and post- XCT irradiation of tissue, on the surface of the specimens; and the damage induced in the whole volume was estimated by comparison with the 3D full-field strain distribution. Moreover, microcrack formation and prevention in the cortical bone was observed in axial and transverse orientation following plastic deformation. In particular, the microstructural morphology of the specimens was correlated to the crack initiation and strain accumulation in the volume. Microcrack formation in the trabecular and cortical bone was identified at regions of high strain accumulation. Alterations in the canal and pore network of cortical bone were associated to the strain accumulation during in situ loading. At organ level, in situ XCT microcompression was used to investigate the mechanical behaviour of the newly formed bone in femoral mid-shaft, where the diaphyseal fracture healing was studied under loading in the apparent elastic level. The strain accumulation in the fracture varied depending on the progress of the healing in the diaphysis, whereas the histological results showed the presence of soft tissues (i.e. cartilage matrix, skin and muscles) that contributed in the overall mechanics of the femur by sustaining the load.

In conclusion, the results of this work show the 3D full-field strain distribution in the microstructure of bone and the contribution of its mechanical properties in the microscale to its performance in the macroscale in mature and regenerated tissue under plastic and elastic deformation respectively.

Chapter 1 - Introduction

1.1 Thesis motivation

Bone is a heterogeneous and anisotropic material with a hierarchical structure [1–5], which consists of a variety of materials arranged at different length scales [6]. This variety in their arrangement affects bone mechanical, biological and chemical behaviour; thus, to understand and predict its behaviour, it is vital to investigate this complex architecture at the different scales. In general, there is a direct correlation between the material properties in the structural levels, where microstructural properties of bone determine its macrostructural behaviour [7]. In this study, the focus ranges between the sub-microstructure (1-10 μm) and the macrostructures as shown in Figure 1 [8]. Specifically, starting from the lamellae in the bone tissue, their Haversian systems and up to a macrostructure entailing both cortical and trabecular bone [9].

Techniques at different resolutions are employed to assess the bone structural levels [10]. Conventional mechanical testing on a variety of specimen sizes has been used extensively; one of the most popular methods to assess the mechanical properties at the sub-microstructure is nano/microindentation, scaling up to more conventional uniaxial compression at micro and macrostructural levels. Mechanical analysis at different dimensional scales is important as mechanical properties of bone highly depend on the structural level [11]. For instance, the tissue elastic modulus at the sub-microstructure of a trabecular femoral head, as estimated with indentation, has been reported as 21.3 ± 2.6 GPa, whereas the apparent modulus, from the stress-strain curves of cyclic compression, at the same area, accounts for 2.5 GPa [11]. The orientation of the microstructure also plays an important role in the mechanical properties. In fact, cortical bone in the axial direction has shown a greater Young's modulus than that of the transverse [12]. Specifically, in the axial direction of a long bone, it ranges between 23.45 ± 0.21 GPa whereas, transversely it is about 16.58 ± 0.32 GPa [12], justifying its anisotropic behaviour. Combining the mechanical properties with characterisation of the microarchitecture provides insights, which can help in predicting bone behaviour under different circumstances. The morphological properties at the cellular level have been widely studied through histomorphometric analysis. The histological 2D images are used to assess bone modelling, remodelling and degradation of diseased tissue (i.e. osteoporotic, osteoarthritic) [13–18]. The 3D morphology can be investigated through X-ray computed tomography (XCT) [19–21], that is used at different scales from nano/micro (high-resolution XCT) to macro levels [20]. In fact, characteristics such as bone volume (BV), trabecular bone thickness (Tb.th), trabecular spacing (Tb.Sp), cortical bone volume (Ct.BV), cortical thickness (Ct.Th) etc. have been identified using either laboratory XCT or synchrotron XCT systems [22–24].

However, as the above described techniques are able to understand bone mechanics at different scales they have to be performed individually and often destructive. In this sense, combination of mechanical testing and XCT imaging (in-situ and ex-situ) provides a more comprehensive insight on the bone structural characteristics at different dimensional scales and their relationship [11,25–28]. In particular, 3D full-field displacements and strains in bone, using tomographic datasets obtained during in situ XCT mechanics, could be evaluated using digital volume correlation (DVC) [29]. DVC analysis, using high-resolution images, has contributed so far to the understanding of microcrack formation and propagation in healthy and diseased bone tissue [30–33] as well as trying to identify the relationship between structural parameters, strain distribution and crack initiation in the whole bone [34]. However, to better understand the mechanical behaviour of the bone, the relation between strain distribution under load, morphology, defects in the structure should be examined at different dimensional scales. Furthermore, the regeneration of bone tissue using DVC has only been studied in the presence of biomaterials [35] and, to the best of the author's knowledge, the strain distribution in the regenerated tissue of a large defect (i.e. osteotomy gap) has never been reported. In order to perform in situ/ex situ mechanics of bone tissue using high-resolution XCT imaging in a laboratory system; long exposure times are required, particularly to investigate the sub-micron scale. This may induce tissue degradation due to the long exposure to radiation, as previously observed for SR-XCT experiments [36]. Therefore, it is important to assess this damage and to develop appropriate experimental protocols accounting for this aspect.

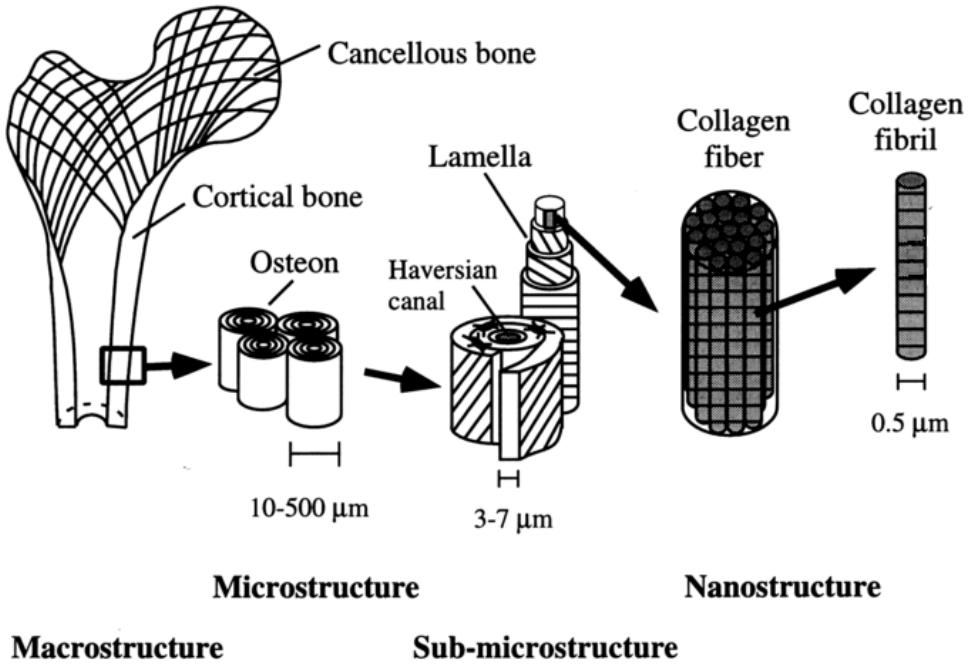

Figure 1: Hierarchical structural organisation of bone. Adapted from [8]

1.2 Aims and Objectives

The primary aim of this study is to examine bone at different scales using a combination of mechanical testing, XCT imaging and DVC analysis. As mentioned, to understand the behaviour of bone, its microstructure needs to be investigated. In order to assess bone at such levels, high-resolution XCT imaging is required; thus, it is important to understand how the radiation of a laboratory XCT system affects the bone properties at the sub-micron scale. Moreover, it is vital to characterise the relationship between morphology of the microstructure and tissue behaviour under loading to predict crack formation and propagation in the whole bone. To further analyse the connection between the micro and macroscale, it is essential to appreciate how the morphology of regenerated bone tissue at organ level is affecting the structure under loading. Hence, the objectives of this project are:

1. To assess the damage induced to the trabecular bone tissue mechanical properties and behaviour, due to irradiation in a laboratory XCT system at the sub-micron level.
2. To evaluate the strain distribution, induced by plastic deformation in cortical bone in relation to its microstructure.
3. To characterise regenerated tissue in fracture healing at the diaphysis of whole bone (rat femur) in the micro and macroscale.

1.3 Thesis outline

This thesis consists of six chapters, where the first one presents the motivation and aims of this project and outlines the structure of the thesis. The rest of the chapters include the following:

Chapter 2: literature review of the theoretical background related to this study. An overview of the bone anatomical and structural behaviour is presented first. This is followed by a description of high-resolution X-ray computed tomography (XCT) imaging with details on the laboratory and synchrotron systems used for bone imaging. The chapter closes with an elaborate report on bone mechanical behaviour and the techniques used in the studies involved [indentation, in situ XCT mechanics and digital volume correlation (DVC) analysis].

Chapter 3: evaluation of the effect of irradiation induced by a laboratory high-resolution XCT system on the sub-microstructure in trabecular bone tissue, by means of microindentation. Mechanical properties of the non-irradiated tissue were compared to the irradiated state to establish development of degradation patterns. 3D full-field strain maps computed via DVC at increasing irradiation stages were obtained for the investigation of the damage throughout the structure.

Chapter 4: examination of cortical bone behaviour during plastic deformation via in situ XCT indentation. The 3D morphological properties of cortical bone (canal and pore network) segmented

from the tomograms are studied in relation to crack formation and progression. The effect of the canal network orientation in the microstructure on crack formation is also assessed. The statistical difference in the mean canal and pore diameter between the in situ XCT indentation stages in each specimen was estimated using a non-parametric independent Kruskal-Wallis test. 3D full-field strain maps are computed using DVC to evaluate the deformation accumulated throughout the volume during indentation.

Chapter 5: characterisation of the 3D full-field strain in newly regenerated bone after fracture healing in the diaphysis of long bones under compressive loading. The regeneration ability of the osteotomy gaps in the diaphysis of rat femurs is investigated regarding its capacity to sustain the load. The strain in the mineralised regenerated tissue is computed by means of DVC. The cartilaginous matrix formation in the same region is observed using histological analysis.

Chapter 6: summary of the work presented in the thesis. Discussion of the contribution for the work presented and the limitations of this research project. Finally, prospective future work development is discussed.

References

[1] P. Augat, T. Link, T.F. Lang, J.C. Lin, S. Majumdar, H.K. Genant, Anisotropy of the elastic modulus of trabecular bone specimens from different anatomical locations, Med. Eng. Phys. 20 (1998) 124–131. doi:10.1016/S1350-4533(98)00001-0.

[2] J.P.P. Saers, Y. Cazorla-Bak, C.N. Shaw, J.T. Stock, T.M. Ryan, Trabecular bone structural variation throughout the human lower limb, J. Hum. Evol. 97 (2016) 97–108. doi:10.1016/j.jhevol.2016.05.012.

[3] E. Dall'Ara, C. Karl, G. Mazza, G. Franzoso, P. Vena, M. Pretterklieber, D. Pahr, P. Zysset, Tissue properties of the human vertebral body sub-structures evaluated by means of microindentation, J. Mech. Behav. Biomed. Mater. 25 (2013) 23–32. doi:10.1016/j.jmbbm.2013.04.020.

[4] M.E. Roy, J.Y. Rho, T.Y. Tsui, N.D. Evans, G.M. Pharr, Mechanical and morphological variation of the human lumbar vertebral cortical and trabecular bone, J. Biomed. Mater. Res. 44 (1999) 191–197. doi:10.1002/(SICI)1097-4636(199902)44:2<191::AID-JBM9>3.0.CO;2-G.

[5] C.E. Hoffler, K.E. Moore, K. Kozloff, P.K. Zysset, M.B. Brown, S.A. Goldstein, Heterogeneity of bone lamellar-level elastic moduli., Bone. 26 (2000) 603–9. http://www.ncbi.nlm.nih.gov/pubmed/10831932.

[6] A.M. Torres, J.B. Matheny, T.M. Keaveny, D. Taylor, C.M. Rimnac, C.J. Hernandez, Material heterogeneity in cancellous bone promotes deformation recovery after mechanical failure, Proc. Natl. Acad. Sci. 113 (2016) 2892–2897. doi:10.1073/pnas.1520539113.

[7] X. Cai, H. Follet, L. Peralta, M. Gardegaront, D. Farlay, R. Gauthier, B. Yu, E. Gineyts, C. Olivier, M. Langer, A. Gourrier, D. Mitton, F. Peyrin, Q. Grimal, P. Laugier, Anisotropic elastic properties of human femoral cortical bone and relationships with composition and microstructure in elderly, Acta Biomater. 90 (2019) 254–266. doi:10.1016/j.actbio.2019.03.043.

[8] R. Jae-young, L. Kuhn-Spearing, P. Zioupos, Mechanical Properties and the hierarchical structure of bone, Med. Eng. Phys. 20 (1998) 92–102. doi:10.1038/251673a0.

[9] J.D. Currey, Bones, 2nd ed., Princeton University Press, New Jersey, 2002.

[10] H.B. Hunt, E. Donnelly, Bone Quality Assessment Techniques: Geometric, Compositional, and Mechanical Characterization from Macroscale to Nanoscale, Clin. Rev. Bone Miner. Metab. 14 (2016) 133–149. doi:10.1007/s12018-016-9222-4.

[11] Y. Chevalier, D. Pahr, H. Allmer, M. Charlebois, P. Zysset, Validation of a voxel-based FE method for prediction of the uniaxial apparent modulus of human trabecular bone using macroscopic mechanical tests and nanoindentation., J. Biomech. 40 (2007) 3333–40. doi:10.1016/j.jbiomech.2007.05.004.

[12] C.H. Turner, J. Rho, Y. Takano, T.Y. Tsui, G.M. Pharr, The elastic properties of trabecular and cortical bone tissues are similar: Results from two microscopic measurement techniques, J. Biomech. 32 (1999) 437–441. doi:10.1016/S0021-9290(98)00177-8.

[13] W.T. Chen, D.C. Han, P.X. Zhang, N. Han, Y.H. Kou, X.F. Yin, B.G. Jiang, A special healing pattern in stable metaphyseal fractures, Acta Orthop. 86 (2015) 238–242. doi:10.3109/17453674.2014.1003127.

[14] M.L. Hillier, L.S. Bell, Differentiating human bone from animal bone: A review of histological methods, J. Forensic Sci. 52 (2007) 249–263. doi:10.1111/j.1556-4029.2006.00368.x.

[15] M. Zandi, A. Dehghan, F. Gheysari, L. Rezaeian, N. Mohammad Gholi Mezerji, Histological evaluation of the healing process of autografted mandibular bone defects in rats under treatment with zoledronate, European Association for Cranio-Maxillo-Facial Surgery, 2019. doi:10.1016/j.jcms.2018.11.015.

[16] D.R. Epari, H. Schell, H.J. Bail, G.N. Duda, Instability prolongs the chondral phase during bone healing in sheep, Bone. 38 (2006) 864–870. doi:10.1016/j.bone.2005.10.023.

[17] G.N. Duda, M. Sollmann, S. Sporrer, J.E. Hoffmann, J. Kassi, C. Khodadadyan, M. Raschke, Interfragmentary Motion in Tibial Osteotomies Stabilized With Ring Fixators, Clin. Orthop. Relat. Res. (2002) 162–172.

[18] A. Vetter, D.R. Epari, R. Seidel, H. Schell, P. Fratzl, G.N. Duda, R. Weinkamer, Temporal tissue patterns in bone healing of sheep, J. Orthop. Res. 28 (2010) 1440–1447. doi:10.1002/jor.21175.

[19] V. Cnudde, B. Masschaele, H.E. V. De Cock, K. Olstad, L. Vlaminck, J. Vlassendbroeck, M. Dieirick, Y.D. Witte, L. Van Hoorebeke, P. Jacobs, Virtual histology by means of high-resolution X-ray CT, J. Microsc. (2008) 476–485.

[20] D.W. Holdsworth, M.M. Thornton, Micro-CT in small animal and specimen imaging, Trends Biotechnol. 20 (2002) 34–39. doi:10.1016/S0167-7799(02)02004-8.

[21] T. Kustro, T. Kiss, D. Chernohorskyi, Y. Chepurnyi, Z. Helyes, A. Kopchak, Quantification of the mandibular defect healing by micro-CT morphometric analysis in rats, J. Cranio-Maxillofacial Surg. 46 (2018) 2203–2213. doi:10.1016/j.jcms.2018.09.022.

[22] C. Chappard, A. Basillais, L. Benhamou, A. Bonassie, B. Brunet-Imbault, N. Bonnet, F. Peyrin, Comparison of synchrotron radiation and conventional x-ray microcomputed tomography for assessing trabecular bone microarchitecture of human femoral heads, Med. Phys. 33 (2006) 3568–3577. doi:10.1118/1.2256069.

[23] P. Schneider, M. Stauber, R. Voide, M. Stampanoni, L.R. Donahue, R. Müller, Ultrastructural properties in cortical bone vary greatly in two inbred strains of mice as assessed by synchrotron light based micro- and nano-CT, J. Bone Miner. Res. 22 (2007) 1557–1570. doi:10.1359/jbmr.070703.

[24] M.L. Bouxsein, S.K. Boyd, B.A. Christiansen, R.E. Guldberg, K.J. Jepsen, R. Müller, Guidelines for assessment of bone microstructure in rodents using micro-computed tomography, J. Bone Miner. Res. 25 (2010) 1468–1486. doi:10.1002/jbmr.141.

[25] N.M. Harrison, P.F. McDonnell, D.C. O'Mahoney, O.D. Kennedy, F.J. O'Brien, P.E. McHugh, Heterogeneous linear elastic trabecular bone modelling using micro-CT attenuation data and

experimentally measured heterogeneous tissue properties, J. Biomech. 41 (2008) 2589–2596. doi:10.1016/j.jbiomech.2008.05.014.

[26] S. Hengsberger, J. Enstroem, F. Peyrin, P. Zysset, How is the indentation modulus of bone tissue related to its macroscopic elastic response? A validation study., J. Biomech. 36 (2003) 1503–9. doi:10.1016/S0021-9290(03)00131-3.

[27] T. Lowe, E. Avcu, E. Bousser, W. Sellers, P.J. Withers, 3D Imaging of indentation damage in bone, Materials (Basel). 11 (2018) 1–13. doi:10.3390/ma11122533.

[28] U. Wolfram, H.J. Wilke, P.K. Zysset, Valid μ finite element models of vertebral trabecular bone can be obtained using tissue properties measured with nanoindentation under wet conditions, J. Biomech. 43 (2010) 1731–1737. doi:10.1016/j.jbiomech.2010.02.026.

[29] B.K. Bay, T.S. Smith, D.P. Fyhrie, M. Saad, Digital volume correlation: Three-dimensional strain mapping using x-ray tomography, Exp. Mech. 39 (1999) 217–226. doi:10.1007/BF02323555.

[30] P. Sztefek, M. Vanleene, R. Olsson, R. Collinson, A.A. Pitsillides, S. Shefelbine, Using digital image correlation to determine bone surface strains during loading and after adaptation of the mouse tibia, J. Biomech. 43 (2010) 599–605. doi:10.1016/j.jbiomech.2009.10.042.

[31] B.C. Roberts, E. Perilli, K.J. Reynolds, Application of the digital volume correlation technique for the measurement of displacement and strain fields in bone: A literature review, J. Biomech. 47 (2014) 923–934. doi:10.1016/j.jbiomech.2014.01.001.

[32] F. Gillard, R. Boardman, M. Mavrogordato, D. Hollis, I. Sinclair, F. Pierron, M. Browne, The application of digital volume correlation (DVC) to study the microstructural behaviour of trabecular bone during compression, J. Mech. Behav. Biomed. Mater. 29 (2014) 480–499. doi:10.1016/j.jmbbm.2013.09.014.

[33] A.I. Hussein, P.E. Barbone, E.F. Morgan, Digital volume correlation for study of the mechanics of whole bones, Procedia IUTAM. 4 (2012) 116–125. doi:10.1016/j.piutam.2012.05.013.

[34] M.I.Z. Ridzwan, C. Sukjamsri, B. Pal, R.J. van Arkel, A. Bell, M. Khanna, A. Baskaradas, R. Abel, O. Boughton, J. Cobb, U.N. Hansen, Femoral fracture type can be predicted from femoral structure: A finite element study validated by digital volume correlation experiments, J. Orthop. Res. 36 (2018) 993–1001. doi:10.1002/jor.23669.

[35] M. Peña Fernández, E. Dall'Ara, A.J. Bodey, R. Parwani, A.H. Barber, G.W. Blunn, G. Tozzi, Full-Field Strain Analysis of Bone-Biomaterial Systems Produced by the Implantation of Osteoregenerative Biomaterials in an Ovine Model, ACS Biomater. Sci. Eng. 5 (2019) 2543–2554. doi:10.1021/acsbiomaterials.8b01044.

[36] O. Akkus, R.M. Belaney, P. Das, Free radical scavenging alleviates the biomechanical impairment of gamma radiation sterilized bone tissue, J. Orthop. Res. 23 (2005) 838–845. doi:10.1016/j.orthres.2005.01.007.

Chapter 2 - Background

2.1 The skeleton

The skeleton functions as a framework for the body by supporting, protecting and assisting its motion. Additionally, it is vital to its biomechanical and metabolic attributes and consists of many individual bones and cartilages. There are also bands of fibrous connective tissues (i.e. ligaments and tendons). It can be subdivided into two main entities; the axial, which includes the vertebral column and the skull and the appendicular, which includes the pelvic and pectoral area along with the limbs (i.e. long bones such as femur, tibia etc.) [1].

An overview of the vertebral column and femur is of central interest in this study.

2.1.1 Vertebral column and vertebrae

The vertebral column is the axis of the human body, on which the absorptive layer of tissue hangs forward, or downward and on which the sensory or processing layer (the central nervous system, which is shaped as the brain and spinal cord) lies. The axis bones grow arches devoted to surrounding the central nervous system. There are 33 separate vertebrae, which are categorized in five classes of shapes, from neck to “tail”, named correspondingly: cervical, thoracic, lumbar, sacral and coccygeal (Fig. 1). These vertebral regions are modified according to the role they play in maintaining upright posture and bipedal locomotion. They bear the weight of the body cumulatively from top to bottom, hence why the sacral vertebrae, which help transmit the weight across the hips and down into the legs, are wholly fused to one another. Conversely, the cervical vertebrae move quite loosely on one another, affording the head a wide range of motions [2].

A typical vertebra design is composed of a body and a neural arch, which sprouts off the body posteriorly. The neural arch begins as pedicles (or else as “tiny feet”), rising off the contour of the vertebral body and it continues as laminae on each side. The transition from pedicle to lamina is marked by a transverse growth of bone, called the transverse process. The laminae support articular surfaces that contact the laminae of both the vertebra above and the one below. The laminae arc toward themselves, meeting in the midline as a merger called the spinous process. These spines take on various lengths and angles of declination depending on where in the column they are located. They accommodate differences in weight load, calibrate the spinal cord, support the ribs and also prevent or allow movements thus, the cervical vertebrae tend to be small of body, long of spinous process and almost bereft of transverse projections. They also possess a hole on each side that allows the vertebral artery to reach the base of the brain in a well-protected route [3]. The bodies of lumbar vertebrae, which show the effects of increased weight-bearing, and the articular facets are rotated to be almost

perpendicular to the thoracic facets. This enables this part of the column to flex and extend, but not to side-bend easily. The older the bone gets, the more limitations appear [1].

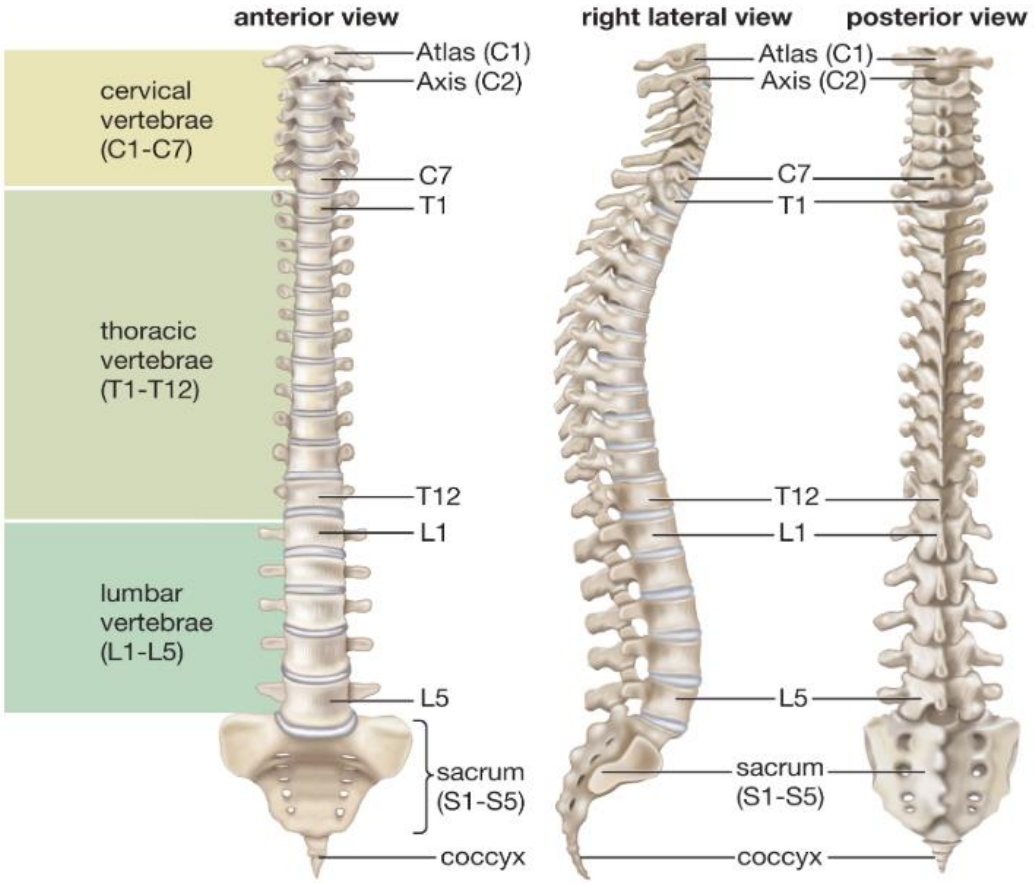

Figure 1: Human vertebral column [4]

2.1.2 The femur

The femur is the strongest and longest bone in the body, located in the lower limb and connecting the hip to the knee joint. Due to its unique structure it supports the various muscular and ligamentous attachments in this area, as well as extending the limb during movement. The proximal part of the femur is linked to the pelvic bone and the distal part articulates with the patella and the proximal end of the tibia [2]. The head of the femur is nearly spherical and projects anteriorly from the shaft of the bone, the femoral neck, to accommodate the muscle forces that pull against the top of the femur (Fig. 2). These are the trochanters, on which the muscles act on to balance the heavy truck against the strut of the lower limb during standing or movement. The generic shape of long bone consists of a cylindrical shaft, the diaphysis and two wider and round ends the epiphyses; the part connecting the two is called the metaphysis. The ends are wider than the middle since in most long bones they are part of joints [1,3].

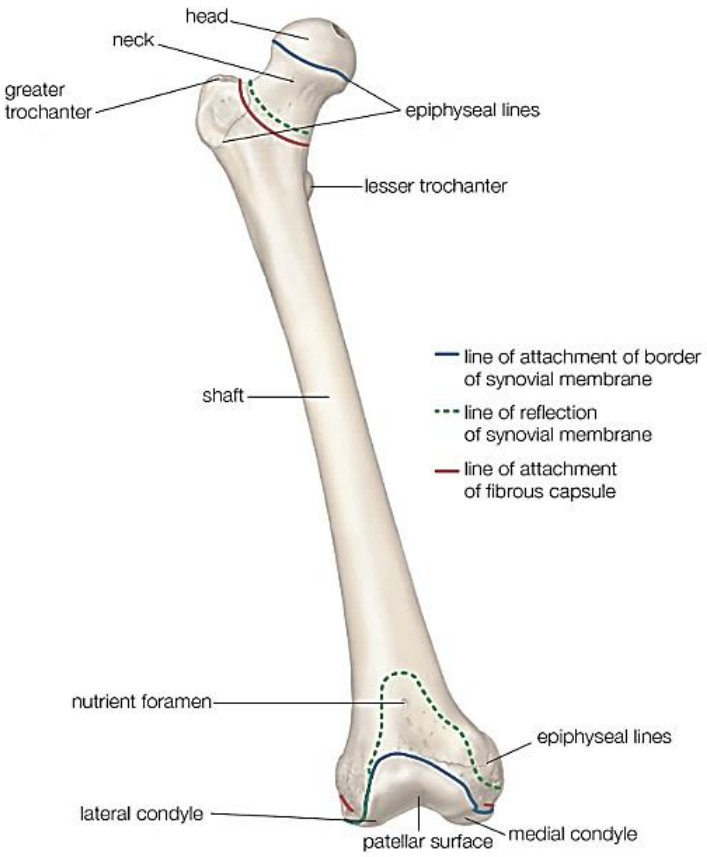

Figure 2: Anterior view of the right human femur [5]

2.2 Bone structure

2.2.1 Anatomic structure of bone

Bones can be categorised in three groups based on their morphology: short, long and flat. Short bones, such as vertebral bodies, have approximately the same dimension in all directions (trapezoidal, cuboidal, cuneiform or irregular shaped) and have rather thin cortices. Long bones, such as the femur and the tibia, have three apparent regions - the epiphysis, the metaphysis and the diaphysis (Fig. 3). The diaphysis is a tubular shaft in the middle of the bone with thick dense walls (cortical or compact bone) and is hollow-like in the middle (medullary cavity). The epiphysis is located at the proximal and distal ends of the bone and is filled with cancellous bone (spongy bone). The epiphyses meet the diaphysis at the metaphysis. The metaphysis is the narrow region that comprises of the epiphyseal plate, a layer of hyaline cartilage in growing bone, which after growth is replaced by the epiphyseal plate. The medullary cavity is surrounded by the endosteum that is responsible for bone growth, repair and remodeling. The outer surface is covered by the periosteum enclosing the nerves, lymphatic and

blood vessels that sustain the cortical bone. At last, flat bones, such as the ones in the cranium, have sandwich like structure, with layers of cortical bone on the outside surrounding trabecular bone [6].

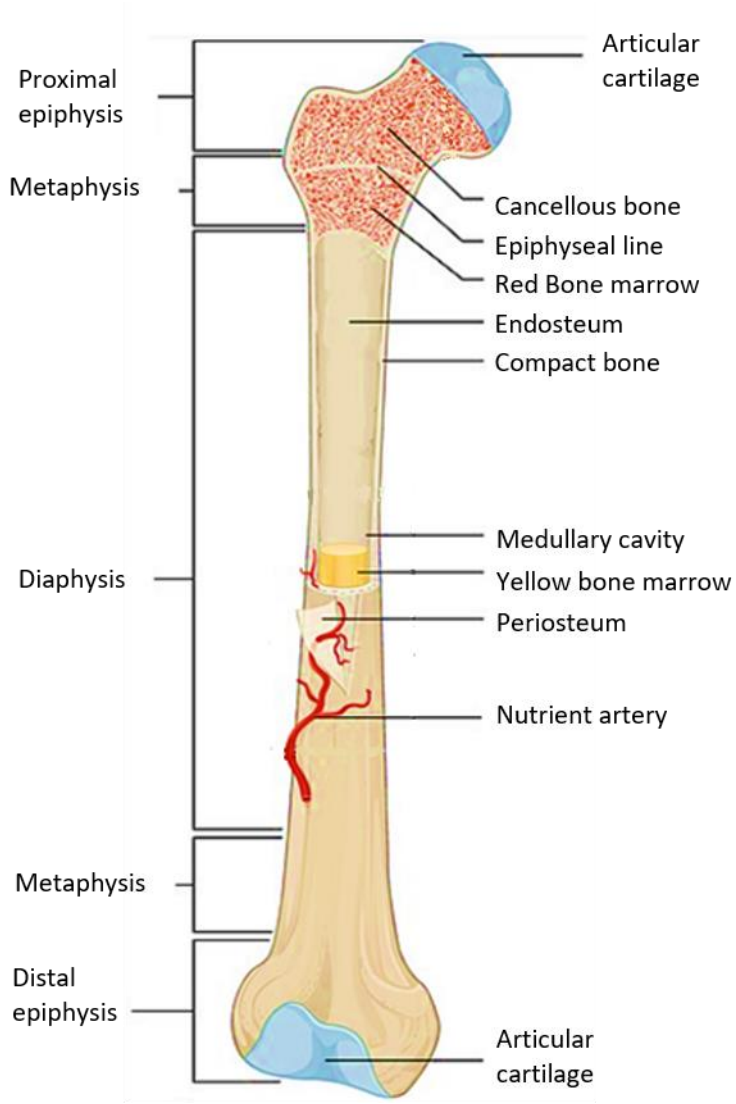

Figure 3: Structure of the femur identifying the anatomical elements. Image adapted from [7]

2.2.2 Microscopic structure of bone

An adult human skeleton has 80% of cortical bone and 20% of trabecular bone. Most bones in the skeleton contain both compact and cancellous bone; however, the bone function dictates their classification and concentration. In the human vertebra the cortical to trabecular bone ration is 25:75, the femoral head accounts to 50:50, whereas in the radial diaphysis it is 95:5 [8]. Both forms have the same matrix composition, however cortical bone is dense, solid and surrounds bone marrow. Trabecular bone has a honeycomb-like network of trabecular plates and rods, which provide large porous spaces for the red marrow [9]. Therefore, the real difference of the two is in their microstructure arrangement. The osteon, comprises the basic structural unit in the microscale that

surrounds the Haversian canal (20-100 μm diameter) [10]. In the trabecular bone, lamellae are composing an irregular and sinuous convolution, the trabeculae.

Cortical bone is a porous composite material composed of the aforementioned soft organic matrix that is hardened by the mineral phase. It consists of 70% mineral in the form of hydroxyapatite, 22% of type I collagen and 8% water by weight [11]. Its hierarchical structure extends over several organization levels, starting with the fibers in the nanoscale, which are consisting of collagen and hydroxyapatite fibrils. The mineralized fibers form the lamellae (sing. lamella) which are cylindrically shaped. It is a concentric complex of lamellae surrounding a canal that consists of blood vessels, nerves, and loose connective tissue called osteon or Haversian system. These assemblies include sublayers where the orientation of the fibers varies and resembles a twisted plywood structure [10]. The osteons are the main structural component in the microscale. The porosity of the cortical bone (5-10 %) involves the Haversian canals which are inter-connected by Volkmann's canals, the osteocyte lacunae and canaliculi and the resorption cavities [12]. The pores in the bone enclose soft tissues and fluids (i.e. blood vessels, cells as well as nerves) [13]. Cortical bone surrounds an organized microstructure of laminated bone which comprise multi-layer, multi-scale tubes that allow the physiological and biomechanical functions [14].

Trabecular bone, as stated, is an assembly of parallel sheets of lamellae arranged in the orientation of the trabeculae. The lamellae are forming groups named trabecular packets, which are separated from each one with cement lines. Trabecular bone remodeling is achieved by removing old bone from the surface of the bone and replacing it in the cavities left empty with trabecular packets. Osteons in the trabecular bone are present in trabeculae with thickness greater than 350 μm. These osteons can be found in the calcaneus, mastoid and the medial aspect of the proximal femur and are similar to those of the cortical bone. The size of the lamellae in these lead to believe that they have analogous properties to those of the cortical bone [13].

There are two distinct varieties of bone; the immature primary, woven bone and the mature secondary, lamellar bone. Woven bone is rarely seen in human healthy skeleton after the age of five, unless there is an injury that leads to new bone formation, neoplastic diseases or inflammation [12,15]. The main characteristic in woven bone is the irregular deposition of collagen fibrils whose diameter varies between 0.1-0.3 μm. This irregularity in the orientation of the fibrils makes woven bone more flexible, easily deformable and weaker than lamellar bone. It also has a lower mineral content and higher number of osteocytes [16].

The secondary or lamellar bone is found in adults and is more precisely arranged. The collagen fibrils in secondary bone are positioned in sheets, the lamellae, which are parallel to each other or

concentrically organized around a vascular canal. It forms after the remodeling of existing bone. Osteoclasts resorb the existing bone at its edge and are replaced by osteoblasts. This is where the Haversian canal forms due to partial filling of the osteoblasts. The Haversian system in the canals are linked together by the Volkmann's canals, which are perpendicular to the long axis [10,17].

2.2.3 Bone matrix composition

Bone is consisting of cells and extracellular matrix. The feature that differentiates bone from the rest of the connective tissues is the mineralization of its matrix, which creates a highly hard tissue able to support and protect the surrounding organs. The term matrix refers to the water and soft organic material, which for the most part is collagen where the mineral crystals are located. The mineral is calcium phosphate in the form of hydroxyapatite crystals, which are stored in bone and determine its mineral content. Therefore, not only does bone provide support and protection but it also contributes in the homeostatic regulation of the calcium levels in the blood. The bone matrix is soft organic material, largely collagen in which the mineral crystals are located. Except from type I collagen in the bone matrix (mentioned in the previous section), other types that can be found in lesser extent are: III, V, XI and XII [18]. The collagen molecules comprise 90% of the weight of proteins in the bone matrix. The other 10% consists of other non-collagenous proteins. These are vital to bone growth, development, remodeling and repair. Therefore, the mineralized tissue is obtained from both, the collagen and the ground substance. The non-collagenous proteins can be divided in four main categories namely as proteoglycan macromolecules, multi-adhesive glycoproteins, bone-specific vitamin K-dependent proteins, growth factors and cytokines [16].

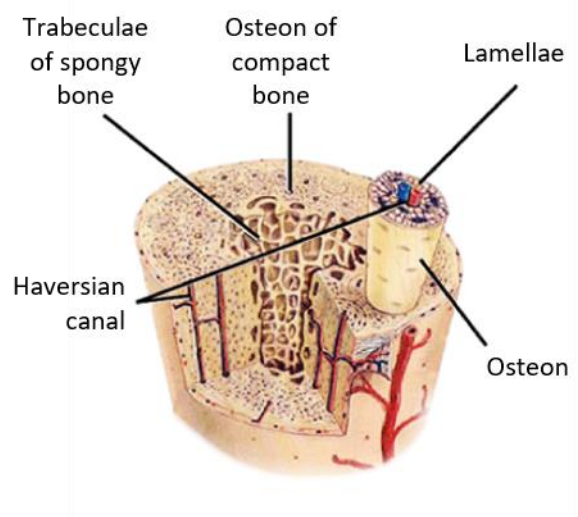

Figure 4: Human bone internal structure. Adapted from [7]

2.2.4 Osteoblasts

Osteoprogenitor cells also known as stem cells, produce osteoblasts that are responsible for the formation of new bone matrix and are derived from bone marrow, bone canals, the endosteum and periosteum. They initially form the collagenous matrix, osteoid, in which mineral is later deposited to and it becomes an osteocyte. Osteoblasts are located at the surfaces of bone tissue close to each other; they have a cuboidal to columnar shape and basophilic cytoplasm. Osteoblast populations are heterogeneous, that could justify the heterogeneity in trabecular bone microstructure in different regions in the skeleton [8].

2.2.5 Osteocytes

The osteocytes are derived from maturation of osteoblasts and are located in the lacunae; each lacuna contains one osteocyte. The lacunae in the bone matrix are between the lamellae and connected by a network of canaliculi, which allow contact between the cell processes of neighboring osteocytes and have approximately 0.2-0.3 μm diameter [16]. The connections between these cells is achieved by means of gap junction and permit small molecules to pass through [19].

2.2.6 Osteoclasts

Part of the mineralized bone matrix is also the osteoclasts, which are bone-resorbing cells found on the surface of bone where the tissue has been damaged or remodeling occurs [18]. They are obtained from the fusion of bone marrow-derived mononucleated cells.

2.2.7 Bone-lining cells

In the surface of the bone, there are bone-lining cells. They derive from osteoprogenitor cells and are considered inactive osteoblasts. They are also involved in propagating the activation of signal that initiates bone resorption and remodeling. [16]

2.3 Histology

Histology is the study of tissues, their appearance and arrangement in the constitution of organs. It has been extensively used in bone research to further characterize its physiological properties in cases such as skeletal development [20], disease diagnosis [21], examination fracture healing progress [22–25] and investigation of the micropenetration depth of indents in cartilage [26]. It has also been used in combination with X-ray tomography (XCT). Specifically, images of femoral head after ischemic injury where correlated to histology of the bony epiphysis and epiphyseal cartilage to assess the reparation progress [27]. Furthermore, Neldam et al. (2017) compared the histomorphometric 2D results to the

3D synchrotron XCT tomograms to evaluate the bone-to-implant contact in goat mandible. The combination between the two is beneficial due to the fact that XCT tomograms examine the mineralised 3D morphology of the bone structure, whereas histomorphology reviews the non-mineralised and low-mineralised regions of the tissue [28].

2.4 Bone formation

There are two processes for bone formation (ossification): direct (intramembranous) and indirect (endochondral).

2.4.1 Intramembranous ossification

Intramembranous ossification begins in the embryo and continues on to adolescence. Cortical and trabecular bone start forming from sheets of mesenchymal, which is undifferentiated connective tissue. Afterwards the mesenchymal cell in the skeleton of the foetus assemble differentiate into specific cells (i.e. capillaries or from osteogenic to osteoblasts). Intramembranous ossification in adolescent ends with the formation of the flat bones in the face [6].

2.4.2 Endochondral ossification

Endochondral ossification is the process during which bone forms and completely replaces hyaline cartilage. In endochondral ossification mesenchymal cells differentiation into chondroblasts instead of osteoblasts, which are cartilage cells that comprise the cartilaginous skeleton prior to bone. The perichondrium is then formed, from the cellular membrane enclosing the cartilage. Matrix is produced by the chondroblasts until they grow in size in the cartilaginous model. Once the matrix calcifies, the chondrocytes start dying due to lack of nutrients and the cartilage disintegrates. Blood vessels replace the empty space, carrying osteogenic cells that later become osteoblasts. These spaces develop into medullary cavities. The cartilage continues to grow and capillaries penetrate it; leading to the conversion of the perichondrium to the bone-producing periosteum. The produced osteoblasts develop the periosteal collar of cortical bone in the diaphysis. At the ends of the bone there is continues growth of chondrocytes and cartilage, increasing the length of the bone while cartilage is replaced in the diaphysis. Once the bone is fully formed, only the surfaces of the joints have cartilage (articular) and the epiphysis. After birth, the process is repeated for the epiphyseal areas [6].

2.5 Bone modelling and remodelling

Modelling and remodelling of bone are two processes the adult skeleton undergoes during life. Modelling is the procedure where bones alter their architecture (i.e. shape, size etc.) depending on

biomechanical forces. Osteoblasts and osteoclasts add or remove bone respectively, based on physiological influences or mechanical forces applied to the skeleton.

Bone remodelling occurs when bone develops to sustain bone strength. According to Wolff's law in 1892 the mechanical stress induced in the bones is dictating their architecture [29]. The remodelling occurs as a response to loading due to mechanotransduction. This is the process where forces are transformed into biochemical signals and afterwards into cellular response. Wolff's law describes the treatment of bone pathologies (i.e. osteoporosis, fracture healing) with the use of physical exercise. In fact, it promotes the use of strength and weight-bearing activities as a non-medicinal treatment for osteoporosis and a range of motions and stresses that can enhance the overall strength of a fractured bone. Since then, it has been shown that the relationship between exercise and bone mineral density is more complex and exercise alone is not sufficient [30].

In the remodeling phase, old bone is resorbed and afterwards replaced by new bone. Remodeling can be targeted in areas where repair is required or randomly. It consists of four subsequent phases; activation, resorption, reversal and formation [8]. Activation is the phase, which involves the admission of osteoclast predecessor to the surface of bone and their differentiation to osteoclasts. In resorption, the osteoclasts dissolve the mineral part of the bone matrix and release the collagen in it. The reversal stage consists of the termination of resorption and the introduction of formation. Here, the osteoblasts create unmineralised matrix, which as mentioned above, later becomes osteocytes. [20].

2.6 Bone fracture healing

In general, bone fracture occurs when an unforeseen load surpasses the physiological loading, causing stresses beyond the strength of the bone tissue. There are two primary factors for this type of injuries (traumatic fractures); fractures that appear by a muscular contraction "unprompted" (i.e. in elderly people with osteoporosis) and those caused by an external impact [12].

Fracture healing in bones is a highly complex process where not all of each aspects are completely understood. Bone is a tissue that can heal without leaving a fibrous scar [31]. Fracture healing encompasses a variety of repair processes that involve convoluted, well-coordinated phases instigated by fracture. It is highly dependent on the biological environment (fracture site) and mechanical stability of the tissue [32]. Instability and large movements of the fracture ends can interfere with the process. Therefore, optimal healing involves a degree of mechanical stability as well as proximity between the fracture ends [33]. There are two main types of bone healing; primary or secondary, depending on the amount of strain induced on the bone.

2.6.1 Primary Healing

Primary bone healing develops when there is open reduction and internal fixation surgery. It involves direct remodeling of lamellar bone, Haversian canals and blood vessels. It can happen by either contact healing, where the gap between the bone is less than 0.01 mm and the strain less than 2% [34]. Furthermore, contact healing causes generation of osteoblasts that cross the fracture line, creating longitudinal cavities. These are filled with osteocytes. Afterwards, there is a simultaneous development of bony union and Haversian systems, bridging the gap. The osteons in the mature area are then leading to remodeling of lamellar bone and healing of the fracture. Additionally, the process of healing starts with formation of lamellar bone, which is oriented perpendicularly to the long axis. Later, this is replaced by osteoprogenitor cells inside longitudinal osteons. The osteoblasts from these cells differentiate and form lamellar bone perpendicularly to the surfaces, but in order to strengthen the lamellar bone secondary healing is necessary [34].

2.6.2 Secondary Healing

In cases where the distance of the parts can be approximatively 800 μm to 1 mm, gap healing occurs. The space between the fracture ends is filled with intramembranous woven bone, which is later remodeled into mature bone [35]. When complete rigidity is not achieved due to the gap size, the healing process is known as secondary. Secondary (indirect) healing is the most frequent type of healing and involves both intramembranous and endochondral bone formation. It is generally improved by controlled micro-motion and weight-bearing. Indirect healing has three phases; inflammatory, reparative and remodelling (Fig. 5) [32,36,37]. It should be noted, that these phases are set as the framework of secondary fracture healing in an effort to depict the process and not a timeline, since they occur simultaneously at different regions of the same fracture [33,36]. Moreover, the most common skeletal site for secondary healing is in fractures of cortical tissue in the diaphyseal part of long bone [38].

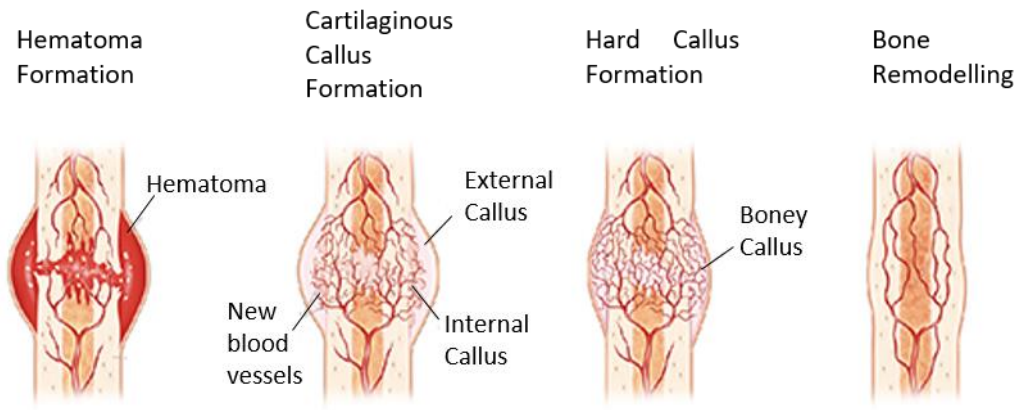

Figure 5: Stages of secondary fracture healing. Hematoma formation during the inflamatory phase, callus formation as part of the reparative phase and bone remodeling where complete healing of the fracture occurs. Adapted from [39]

2.6.2.1 Inflammatory

Shortly after the trauma, cells from the peripheral and intramedullary blood along with bone marrow cells, start to assemble in the region creating an hematoma [40]. An inflammatory response, required for the healing occurs and causes the hematoma to gather in the fractured region. This promotes the formation of callus. In the inflammatory phase, there is differentiation of mesenchymal cells to both osteoclasts and osteoblasts [41]. The osteoclasts contribute in the resorption of bone debris. Whereas the osteoblasts assist in the development of cartilaginous callus and angiogenesis (blood vessels creation) [36]. This phase occurs in the first 1 to7 days post-trauma [34].

2.6.2.2 Repair

The reparative stage of secondary healing can also be described as the proliferation and differentiation stage. It is defined by the differentiation of mesenchymal stem cells in the fracture site into ones with osteogenic capacity [36]. Hence, callus starts forming, becoming stiffer as it calcifies. Soft and hard callus is developed, simultaneously, in a combination of endochondral and intramembranous ossification [32,42]. After the hematoma a fibrin-rich granulation tissue is developed. The tissue formed in the area is exposed to high tissue strains, which encourages the differentiation of mesenchymal cells to chondrogenic leading to soft callus formation. The soft callus extends throughout the gap connecting the fracture ends and helps to stabilize the fracture during the calcification and remodeling processes that follow. During this endochondral ossification, the hypertrophic chondrocytes are enclosed by calcified matrix resulting in their removal and replacement by woven bone. The soft callus here is cartilaginous tissue [34,43]. At the same time with the soft callus development in the center of the fracture the hard callus is forming. The intramembranous ossification creates hard callus of woven bone beneath the periosteum, at some distance from the

gap, developing peripherally towards the fracture. The osteoblasts in the area synthesize type I collagen that contributes in the development of calcified tissue. Eventually, woven bone surrounds the outer surface of the site providing mechanical stability in the first stages of mineralisation [33].

2.6.2.3 Remodelling

The woven bone formed during the repair is a rigid structure that provides the biomechanical stability however, as mentioned before (Section 1.4), it does not have the biomechanical properties of lamellar bone. The collagen fibres in the woven bone are in a random orientation. This results in a much more isotropic behaviour, with less strength and stiffness [36]. The osteoclasts resorb the hard callus, while osteoblast generate lamellar bone [16]. The process starts approximately on the third week and may last years until full regeneration is accomplished. It is seen that remodeling occurs when there is electrical polarity in the region. To attain such polarity axial loading can be induced in long bones, causing osteoclastic and osteoblastic reactions [44]. As the woven bone is slowly replaced with lamellar bone over the duration of several months, the mechanical integrity and properties of the tissue are restored. Ultimately, leading to tissue formation indistinguishable from bone seen elsewhere [45].

2.6.3 Fracture Fixation

The outcome of fracture healing depends on a variety of elements; such us acuteness of the injury, fracture realignment and prior diseases in the bone (i.e. osteoporosis, osteoarthritis etc.). Optimal fracture healing is achieved when the natural healing process is not obstructed and there is the ideal biological and mechanical environment for repair. In fact, is cases of severe trauma surgical stabilisation of the bone fragments is used [46]. The objective of fracture fixation is to anatomically position the bone fragments and accomplish adequate stability to allow uncompromised facture healing [32]. The technique used to align the tissue prescribes the degree of interfragmentary movement happening under the external loading and muscle motions, factors that regulate the healing environment. Specifically, low interfragmentary movement leads to low interfragmentary strain, which causes the intramembranous bone formation. Moderate interfragmentary movement results in endochondral ossification and higher movement can prevent fracture healing [47]. Indeed, the critical strain tolerance for the fracture site is 2%, meaning that if the bone was deformed by more than 2%, the bone element would be obstructed or not able to achieve healing. According to Perren (2015), the structure of woven bone achieves bone bridging at approximately 10% strain [45]. In this case, the bone is strained less than the destructive 2%. The most commonly used fracture fixations are splinting and compression (Fig. 6) [35,46].

There are two types of splinting: internal and external. Internal splinting can be intramedullary nails or internal fixator plates. The first is required in fractures of long bones, positioned into the medullary cavity fixed in placed by screws/bolts at each one of the ends of the splint [46]. This can lead to an unstable fixation that raises the risk of delayed healing [48]. The internal fixator plates are securely positioned close to the bone surface with locked screws [35]. They allow some interfragmentary movement in the region opposite the fixator, enhancing the formation of callus. However, there is obstruction of the formation adjacent to the plates [47]. New designs have been developed for both techniques trying to optimise the healing [48,49].

The external splinting is applied by either plaster casts or braces; allowing a larger degree of interfragmentary movement. In cases of open tissue wound fracture, external fixators are used. External fixators are widely employed to sustain a defect in fracture healing studies. This is because they have minimum involvement with investigation to follow and are easy to implement. In addition, using an external fixator allows alteration to the mechanical environment in the duration of the experiment [25]. The interfragmentary stability in this instance depends on numerous factors such as the distance between the bone and the fixator, the spacing, diameter and number of the screws. For instance, Meeson et al. (2019) assessed a variety of mechanical environments regarding the interfragmentary strain and stiffness in the healing of three osteotomy induced gap sizes, in rat femurs [25]. It was observed that the 1 mm gap led to complete fracture healing, whereas the 2 mm and 3 mm led to delayed and non-union respectively. In fact, there are several studies investigating the regulation of stability (flexible to rigid) in inducing callus healing [50–53]. However, the biomechanics of the regenerated tissue in situation have only been explored in Finite Element (FE) models [54].

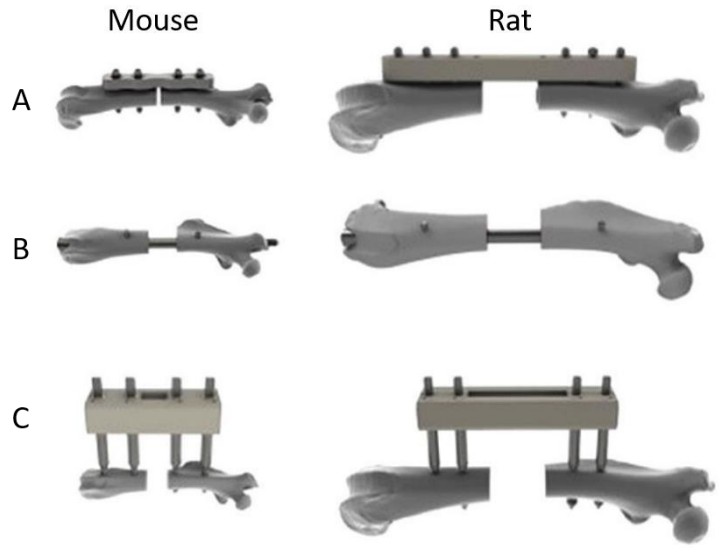

Figure 6: Standardised fracture fixation systems of mice and rat femurs. (A): Internal locking plate, (B) Locking nail, (C) External fixator (adapted from [55]).

2.6.4 Complications

A fracture is considered healed when there is adequate mechanical union to restore function. The progress can be monitored, clinically, with radiography by observing the calcified tissue in the union. A failed fracture healing is considered when the fracture ends do not meet: “non-union”; or healing progress is not as expected: “delayed-union” [56]. A non-union for human bone tissue can be defined as a 9-month old fracture that has shown no signs of healing advancement in the last three. In rats and mice time points are approximated to 15 and 12 weeks, respectively [55]. However, time has been proven to be a less important factor in the healing progress since different bone sites require different times (i.e. high energy diaphyseal injuries). Therefore, a broader definition would be “a symptomatic fracture with no apparent potential to heal without intervention”. Likewise, a delayed-union can be classified as “a fracture in which healing has not occurred in the expected time and the outcome remains uncertain”. At last, in some cases of non-union in humans there was development of pseudarthrosis, which consist of synovial membrane and has a form of a false joint [55]. A definition for pseudarthrosis would be: “a painless fracture that has failed to unite and has no potential to do so without intervention” [36].

2.7 High resolution X-ray Imaging

X-ray computed tomography (XCT) is an imaging method where individual projections (radiographs) recorded from different viewing directions are used to reconstruct the internal structure of the object of interest. Computed tomography offers an accurate map of the different absorption levels of x-rays inside an object, irrespective of the different phases in substructure or the variation in the density of the object. Micro-Computed Tomography (microCT or µCT) or otherwise know high-resolution XCT imaging is used for reconstruction of object’s internal volumes with the spatial and contrast resolution needed for numerous applications. It is widely used for biological, physical science or engineering problems. In fact, in 1989 Feldkamp et al. build a microCT scanner to investigate the trabecular bone 3D microstructure [57].

The distinction between a conventional and high-resolution X-ray microCT is in the spatial resolution achieved (microCT ≤ 100 µm). The microCT systems used nowadays, can reach an isotropic voxel size of a few nanometers, investigating structures smaller than mouse trabeculae that are in the range of 30 to 50 µm. High-resolution microCT has been extensively used to assess trabecular, cortical and whole bone morphology [58]

The principle of computed tomography is based on measuring the volume of an object by evaluating it from different directions and computing images from these data. X-rays transmitted from the source are either absorbed by the sample or reach the detector. The absorptivity of the object provides the

contrast, meaning uniform absorptivity in its geometry leads to a uniform grey level. To measure the distribution of X-rays in a radiograph the grey value pattern is exploited i.e. intensity, I. The initial intensity (I_0) is measured along with the intensity attenuated by the object (I), so as to compute the attenuation for each ray from source to detector [59]. The real attenuation depends on both the material and the energy spectrum of the X-ray source. The energy-dependent material constant in the exponent of this attenuation formula is called linear attenuation coefficient.

$$I = I_0 \times e^{-\mu \times d}$$

Equation 1: Intensity of the radiation in a homogeneous object with monochromatic radiation, where I_0 is the initial intensity, μ is the attenuation coefficient and d the absorber thickness [59].

$$I = I_0 \times e^{-\mu_1 \times d_1 - \mu_2 \times d_2 - \mu_3 \times d_3 - \cdots} = I_0 \times e^{-\int_0^d \mu \times ds}$$

Equation 2: Intensity of the radiation in an inhomogeneous objects with monochromatic radiation the formula considers the difference in the attenuation coefficient and thickness of the component [59].

$$I = \int_0^{E_{max}} I_0(E) \times e^{-\int_0^d \mu \times (E) \times ds} ds$$

Equation 3: Intensity of the radiation in inhomogeneous objects with polychromatic radiation [59].

An X-ray projection/image expresses an image of the sum of all the local attenuations along the X-ray beam path. A three-dimensional CT image, is obtained by acquiring a group of these two-dimensional images. In a microCT to obtain such images, a source and a detector are fixed in place while the object is rotating around its vertical axis. In a laboratory-based microCT the source is a microfocus X-ray tube whereas in a synchrotron X-ray microCT is an insertion devise. The detector is a charged-coupled device (CCD) camera with phospholayer that converts X-ray photons to visible light. The projections are then documented, in discrete points keeping the sampling distance between the neighbouring pixels, based on the number of pixels in the detector camera. In order to compute a quality image, there needs to be adequate number of projections values from all the directions. That implies that the minimum angular range of the projections is 180˚ and that each projection data point is extremely close to the next. Subsequently, the three-dimensional image is reconstructed by these two-dimensional projections [60,61].

However, microCT imaging depends on more than just the specimen imaging. It involves computation of a variety of parameters in addition to the two- and three-dimensional visualization. Starting with the sample, it needs to be fitted and fixed in the microCT system configuration. The correct placement of the sample ensures that it is in the field of view (FOV) and secure fixation that there are no motion artifacts. Orientation of the sample is also an important factor to consider, since positioning vertically

to the vial axis requires less measurement time. However, in a laboratory-based microCT vertical orientation can affect the image quality due to the beam hardening.

Integration time defines the quality of the tomogram. The longer the scan, the better the signal-to-noise ratio (SNR). Measuring time however, is also increased, along with the radiation dose, which can negatively affect the bone tissue properties [62] . Moreover, each microCT system has an integration time limit, set by the CCD saturation time of the detector. To improve the image quality each projection can be acquired numerous times and use the average for image reconstruction, a method known as frame averaging. Admittedly, the time and radiation dose are increased as well, however saturation of the CCD detector is avoided. The resolution of the images is determined by the sample features in question. For the selection of the optimal resolution, the dimensions of the sample should be considered since they are linearly coupled to each other. In addition, binning is employed to increase the SNR. It is a method where several pixels are averaged together in the CCD chip, improving the photon statistics [60].

Finally, reconstruction of the images has an impact on the image quality. There are different ways to reconstruct microCT imaging scans, such as Fourier-Based reconstruction, Sinogram, Cone-Beam and Filtered Back Projection. The most common way is using a Filtered Back Projection algorithm [63,64]. The main concept of this technique is that projections of the object are depicted at 45˚ intervals and run back through the image to attain an estimation to the original one. They correlate effectively in the areas which equate to the original image. An issue that can appear when running the image back is the star-like artefacts that cause blurring. Consequently, a filter is applied to eliminate the blurring known as ramp filter [63].

2.7.1 Laboratory X-ray microCT

A typical laboratory X-ray microCT system uses either an evacuated tube or a rotating anode as a source. An X-ray tube contains a filament, the cathode. This filament emits electrons in the form of a beam accelerated by a voltage up to 240 kV (or more in case of vacuum tube) aimed at the anode. The latter is a metal target manufactured from tungsten. The electron beam, that is produced, impacts the anode and the high kinetic energy of the electrons is converted into X-rays [65]. The current microCT systems function using a cone-beam [66]. The specimen is positioned between the source and detector onto a table that rotates in a specific angle (most commonly 180° or 360°) (Fig. 8). The spatial resolution of the system depends on the detector width, the geometric configuration and the spot size, which can be defined as the area on the target where the photons (X-rays) are produced [67]. Specifically, the spot size limits the image resolution. High-resolution X-ray sources with spot size as small as approximately 1 μm are available. The contrast resolution is determined by the X-ray flux and

detector element size [68]. In fact, in a laboratory high-resolution microCT system the contrast resolution is restricted by the limited X-ray flux emitted by the source.

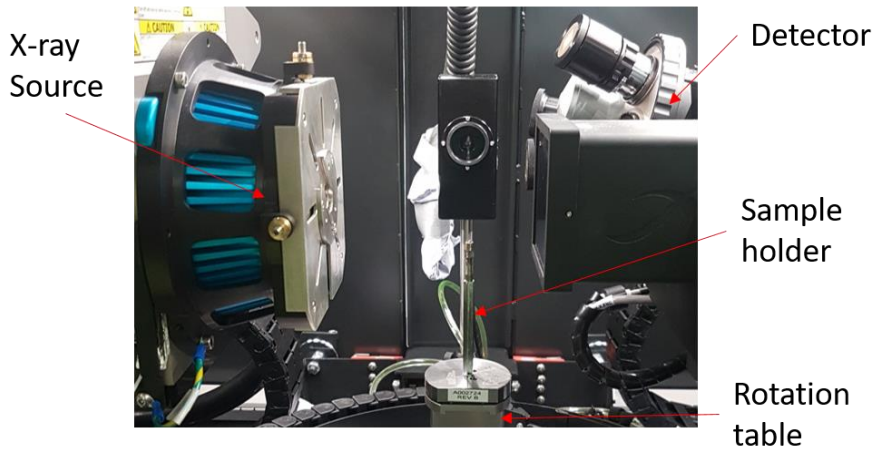

Figure 7: Zeiss Versa 510; high-resolution XCT system.

2.7.2 Synchrotron radiation X-ray microCT

A typical synchrotron (SR-) microCT system uses a parallel beam directly without focusing optics. It consists of the specimen rotator, X-ray phosphor, optical lens and CCD detector. The main part of the synchrotron source is the electron accelerator. The electrons are generated by an injector and pre-accelerated to a high energy, resembling to that of the speed of light. Then, they are guided towards a close path in a ultra-high-vacuum chamber (known as hutch) and kept there by a bending and focusing magnetic system. During the circulation in the close path, they emit X-rays that are accumulated in beamlines (Fig. 8). The X-rays are channelled in chambers for different experimental purposes [69]. A SR-microCT system has a monochromatic (or pink) X-ray beam, which is characterised by a high photon flux. This enables quantitative reconstruction eluding beam-hardening effects [66]. The X-ray source contains almost perfectly parallel rays, enabling 3D tomographic reconstruction via filtered backprojections algorithms. The high-photon flux accommodates for high spatial resolutions (micron and sub-micron level) without increasing the acquisition time. The spatial resolution in the reconstructed images depends on the spatial resolution of the detector due to the lack of magnification [70].

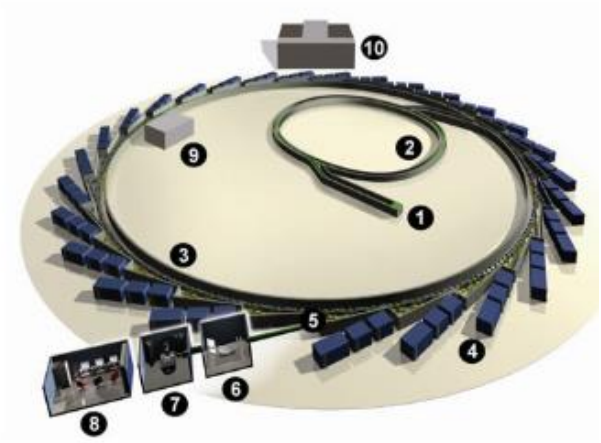

Figure 8: Diamond Light Source (Oxfordshire, UK) synchrotron machine. 1: Injection system- electron gun and Linac, 2: Booster Synchrotron- electrons are injected from the linac into the booster, 3: Storage Ring: Diamonds storage ring has twenty five strain sections forming a closed loop, 4: Beamlines- a beamline has four primary sections; a) the front end; b) the optics hutch; c) the experimental hutch and d) the control cabin, 5: front end; fitted into the storage ring where the synchrotron light is channelled into a beamline, 6: Optics hutch; the first room the beam of light enters, 7: Experimental Hutch where the experiment occurs, 8: Control Cabin where the experiment is monitored, 9: Radiofrequency Cavity which allows the beam to maintain a fixed orbit around the storage ring, 10: Diamond House which is the staff meeting rooms [71].

2.8 Bone characterization and mechanics

Bone has the ability to resist fracture due to its material properties, geometry, micro-architecture and spatial distribution [72]. Bone mechanical properties vary depending on the anatomical site, the age and the general health of the donor. These material properties, including strength, fracture toughness, elastic modulus, also depend on the composition and organization of the mineral and matrix components, as well as the occurrence of microdamage. Hydroxyapatite is directly connected of the stiffness of the cortical bone tissue. In addition, collage content contributes in the post-yield ductility. The geometric aspects of the bone involve the nano-, micro-, and macroscopic characteristics (i.e. cross-sectional properties of the whole organ/bone and trabecular tissue architecture respectively) [73].

2.7.3 Mechanical testing of bones

The mechanical properties of bone have been extensively measured by traditional mechanical testing techniques (i.e. tensile, compressive, bending, torsion, site-specific, indentation, pure shear, fracture mechanics, acoustic, micro- and nano- testing).

2.7.3.1 Whole bone testing

Studying whole bone structure is more complex than the investigation of cortical and trabecular bone individually, due to the fact that it comprises of both these tissues; its behaviour depends on the cortical thickness, the spatial distribution of trabecular bone, as well as the bone size and shape. Investigating the whole bone contributes in the understanding the biomechanical aspect of fracture occurrence and healing. However, mechanical testing in the macroscale is more feasible in cadaveric and animal tissues. Rodents have been proven one of the most pragmatic options for testing of long bones (i.e. femur, tibia) due to their skeleton size [23,58]. In addition to the long bones, vertebral bodies are tested depending on the nature of the study [74–76]. The main disadvantages of whole bone testing are that it is not feasible to simulating all the factors that affect the skeleton structural properties and that they are fundamentally destructive [72].

The loading conditions used in whole bone testing are one of the most important aspects, because they need to resemble as much as possible the physiological ones. In vivo loading involves impact conditions, muscle and joint contact forces (Fig. 9). The mechanical behaviour of whole bone is usually investigated via monotonic or cyclic loading, in axial compression/tension, bending and torsional loading modes. To achieve an accurate representation, it requires accurate estimation of the direction, magnitude and location of the forces and moments that are implemented ex vivo.

Compression testing on rat femur combined with digital volume correlation (DIC) analysis has shown that tensile strain in the diaphysis of the bone promotes crack propagation [77]. Furthermore, mice long bones have been used to assess the effects of aging in the tissue, showing bone mass reduction as result of cortical bone thickness and new bone formation decrease. The medullary cavity size increased along with the number of intracortical resorption cavities [78]. Micro-computed tomography has been proven a very useful tool when it comes to examining whole bone structures.

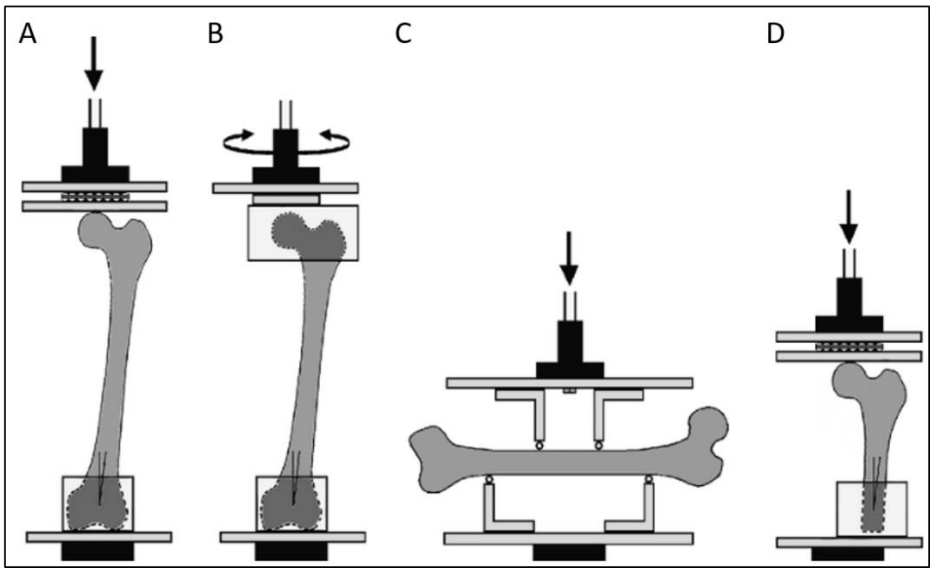

Figure 9: Whole femur mechanical testing with different load cell configurations: A) compressive cyclic or monotonic testing with the distal part of the femur fixed to the bottom plate, axially applied load; B) torsional testing with the proximal and distal part stabilised, rotation applied by the actuator; C) four-point bending testing with the femur positioned between the pins in both medial-lateral and anterior-posterior planes; D) axial compressive testing with the diaphysis rigidly fixed to the bottom platen and the femoral head loaded axially. Image adapted from [79].

2.7.3.2 Indentation of bone

Indentation is a mechanical testing method during which a diamond or ceramic tip with known geometry is applying a single static force onto a flat surface, recording the depth and size of the indent. In bone, it is performed at a variety of length scales giving information about the tissue biomechanical properties such as hardness, and elastic modulus that can then be mapped accordingly to the indentation site [80]. The tip morphology, loading rate, sample hydration, surface and orientation are controlled. Moreover, indentation readings depend on the test used to measure them. In order to establish comparable indentation values, international standard methods (ISO 14577) have been set in place based on the different scales at macro-, micro-, and nano-level [81]. Specimens can be embedded in resin and surface polishing is required prior to testing [82,83].

Table 1: Four most commonly used indentation tips: Spherical, Rockwell, Vickers and Berkovich [81]

Parameters	Spherical	Conical/ Rockwell	Vickers	Berkovich
Shape		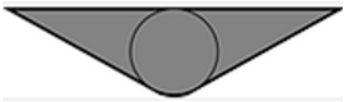		
Angle with the vertical axis	n/a	n/a	68°	65.3°
Contact area	$\pi \times \alpha^2$	$\pi \times \alpha^2$	$24.5044 \times d^2$	$24.56 \times d^2$

Microindentation is characterised by the indentation load (L < 2 N) and depth (h > 0.2 μm). There are two principal tests; the Vickers and Knoop. The main difference between the two is in the tip (Table 1), both have a pyramidal shaped, however the dimensions differ. The shape of the indentation imprint is used to measure the mechanical properties of the bone. It is used for hardness testing in individual trabeculae and osteons of bone. According to Evans et al. (1990) hardness testing is associated with the yield strength of the material instead of the Young's modulus, because the imprint of the indentation is related to the plastic flow in the material. Microhardness is used to quantify the physical effects of small scale spatial variation in the composition of bone. It has been used to identify the differences between the properties of interstitial and secondary osteonal bone, the variation of the properties of long bones along their length and of younger secondary osteons from older ones [84]. Microindentation also provides information on the microporosity correlated with the lacunae and degree of mineralisation. It has also been employed to identify intact from damaged bone [85], aged and osteoporotic tissue [82]. Furthermore, the micromechanical properties of femoral cortical bone in both axial and transverse direction have been identified in female and male donors confirming the anisotropy of the tissue [86]. Through microindentation and compression of micropillars it was seen that the strength and ductility of the tissue in the microscale is higher than in the macroscale [87]. However, when it comes to fracture toughness they appeared to be similar [88]. In fact, Vickers test has been used extensively to assess the fracture toughness by indenting directly next to pre-existing cracks [89]. It has however, raised a concern regarding the state of the volume under/near the indentation imprint, since lateral or cone cracks have been observed during Vickers indentation [90]. Microindentation protocols dictate a variety of holding time once the maximum load/depth has been reached to avoid the creep effect. In some cases holding time is set at 10-15 s [80,91] and in other at 30 s [86,92]. In Evans et al., (1990) the recovery effect of indentation due to removal of the load was investigated, proving that variation of loading around 10 seconds seems negligible whereas holding the sample for 5 secs showed higher values of the hardness.

Nanoindentation, as the name implies uses a nanoindenter tip. The displacement of the tip is continuously measured with high precision, providing a force-displacement curve (Fig. 10) [80]. The average pressure under load is representing the hardness, which is computed by dividing the maximum load with the indentation contact area. The reduced modulus, is produced by the plastic deformation (unloading part of the force-displacement curve). At last, the elastic modulus (E) is calculated using the reduced modulus (E_r), Poison's ration (v) of the sample and the indenter tip material properties. (Eq. 4), where E_t and v_t are elastic modulus and Poisson's ratio respectively of the tip [93].

$$\frac{1}{E_r} = \frac{1-\nu^2}{E} + \frac{1-{\nu_t}^2}{E_t}$$

Equation 4: Elastic modulus calculation using the Oliver-Pharr method [93].

The most commonly used tips in nanoindentation are the Berkovich and cube cornered [81]. The Berkovich tip is a three-sided pyramid with a face angle of 65.3° with the vertical axis. Likewise, the cube cornered has also a three-sided pyramidal shape, however the angle is equal to that of the corner of a cube. In cases of soft tissue (i.e. cartilage, artery tissue) a spherical tip can be used (diameter >50 μm) [26,94,95].

The sample preparation plays a significant role in the results. The surface roughness can affect the readings, same as the hydration status. Samples are usually polished with progressive grades of sand paper. Additionally, it has been shown that the indentation modulus in wet conditions decreases up to 40%. This is due to the fact that the mechanical properties of both cortical and trabecular bone depend on the water content [96].

Nanoindentation in bone has approximately 1 μm spatial resolution and is used to analyse the lamellar and interlamellar regions of the bone [97]. This spatial resolution, makes specimen preparation essential (i.e. surface polishing) as roughness or surface discrepancies affect the measurements [98]. Nanoindentation and nanoscratching have been used extensively to identify the mechanical properties of the cortical bone in all directions. Nanoindentation was used on both cortical and trabecular tissue to identify the degree of anisotropy [99,100]. Specifically, the elastic moduli of the osteonal and interstitial lamellae was measured, seeing that in the longitudinal direction it was 45% higher than the transverse [100]. Lewis and Nyman (2008) have reported the different elastic moduli from nanoindentation studies accounting for both skeletal site and hydration status of the tissue (Table 2) [101].

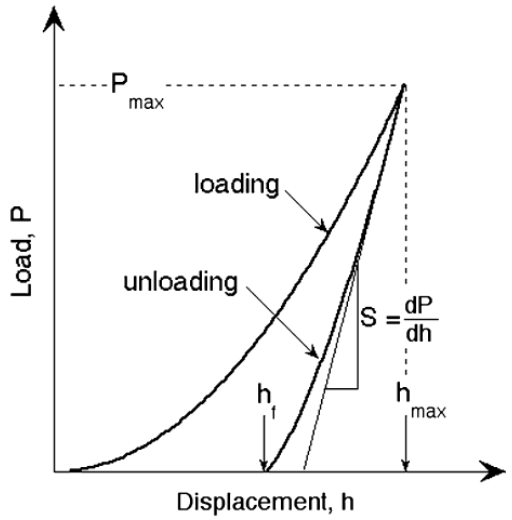

Figure 10: Typical representation of the Load-Displacement curve. P_{max} = maximum applied Load; h_{max} = penetration depth; h_c = contact depth (height of the contact between the sample and the tip); h_f = final depth; S = the elastic unloading stiffness [93].

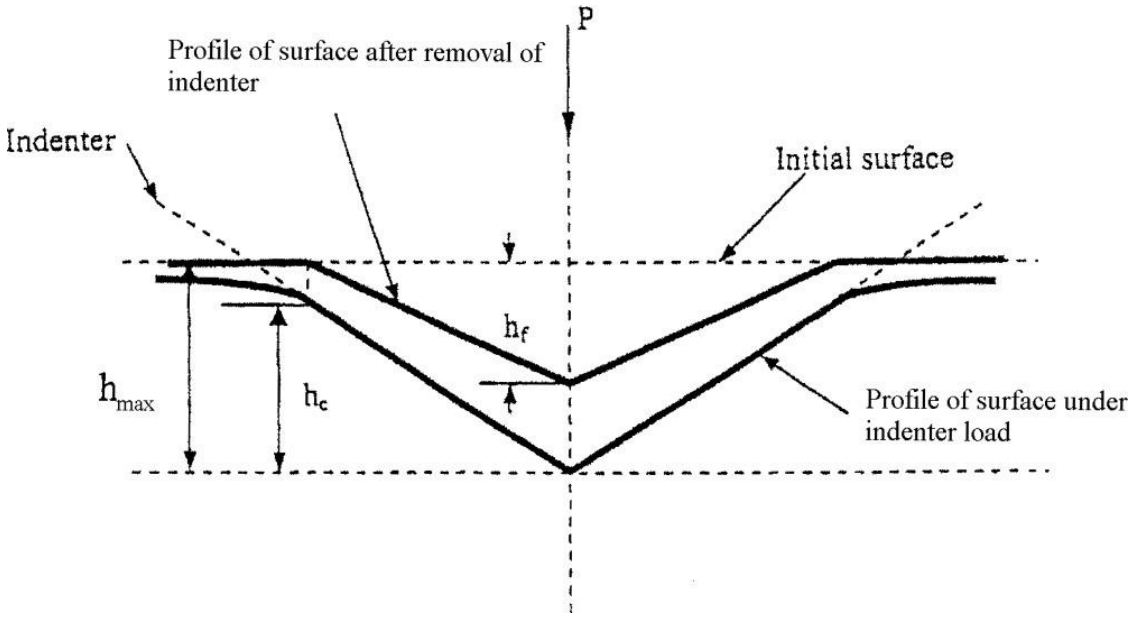

Figure 11: Representation of the indentation cross-section, made by a Berkovich tip. h_c = contact depth; h_{max} = maximum elastic displacement between the tip and the sample surface; P_{max} = maximum indentation load; h_f = permanent or final depth of indentation after the elastic displacements have fully recovered [101].

Table 2: Elastic Modulus (E) and Hardness (H) of Bone and Teeth tissue derived from Nanoindentation measurements (Table adjusted from [101]).

Tissue	**E (GPa)**	**H (GPa)**	**Reference**
Human trabecular, lamellar (L2 vertebra)			[102]
Cadaver of 92-year-old female	20.8*a* ± 1.8*b*	880 ± 200	
Cadaver of 63-year-old male	32.3 ± 2.7	970 ± 160	
Cadaver of 77-year-old male	22.9 ± 2.0	780 ± 100	
Cadaver of 64-year-old male	22.9 ± 1.8	850 ± 70	
Male human cortical tibia			[99]
Osteons (longitudinal, Lc)	22.4 ± 1.2	617 ± 39	
Interstitial lamellae (*L*)	25.7 ± 1.0	736 ± 44	
(Transverse, *Tc*,*d*)	16.6 ± 1.1	564 ± 34	
Human trabecular (*T*12 and *L*1 vertebrae)			
(*L*)	19.4 ± 2.3	618 ± 61	
(*T*)	15.0 ± 2.5	515 ± 82	
Mid-shaft of radius of 2-year-old thoroughbred horse *Equus caballus L*			[103]
Osteon (anterior, mid)	21.65 ± 0.59		
Osteon (anterior, outer)	16.48 ± 1.08		
Osteon (posterior, mid)	19.64 ± 0.58		
Osteon (posterior, outer)	15.12 ± 0.96		
Carp (*Cyprinus carpio*) rib bone			[104]
Proximal end (L)	8.25 ± 0.27		
Proximal end (T)	15.4 ± 1.24		
Distal end (L)	16.0 ± 0.76		
Distal end (T)	9.64 ± 0.39		
Rat tibia			[105]
Toothless mutation	17.97 ± 4.77	840 ± 60	
Osteoporosis mutation	21.88 ± 1.47	890 ± 50	
Incisors-absent mutation	22.02 ± 1.25	800 ± 30	
Cortical bone from femur of 4-months-old female mouse			[106]
C3H/HeJ strain	30.5 ± 0.80	1080 ± 30	
DBA/2J strain	28.5 ± 0.50	1110 ± 20	
C57BL/6J strain	26.6 ± 0.60	1070 ± 30	
Cancellous bone from left distal lateral femoral condyle of skeletally mature male New Zealand white rabbit			[98]
Lamellar bone tissue	26.6 ± 2.27	990 ± 140	
Interlamellar bone tissue	20.3 ± 2.09	950 ± 110	
Bovine femur			[107]
Osteons (wet)	21.1 ± 2.0	578 ± 52	
Osteons (dry)	24.4 ± 2.2	680 ± 102	
Interstitial lamellae (wet)	25.1 ± 1.6	730 ± 48	

Interstitial lamellae (dry)	27.5 ± 1.2	818 ± 49	
Distal left femur of adult dog			[108]
Trabecular bone	12.97 ± 4.15	530 ± 240	
Third molars from human subjects			[109]
Enamel	63.55*a* [62.09, 65.02]*e*	3510*a* [3380, 3630]*e*	
Intertubular dentin	19.65*a*[18.61, 20.69]*e*	830*a* [740, 920]*e*	
Mandibular third molars from human subjects			[110]
Cementum (ultrasectioned, dry specimens)	19.1 ± 2.7	640 ± 1000	
Cementum (ultrasectioned, wet specimens)	7.9 ± 1.3	200 ± 40	
Cementum (polished, dry specimens)	19.13 ± 1.15	860 ± 500	
Cementum (polished, wet specimens)	13.38 ± 0.91	380 ± 60	

2.7.3.3 Compressive Testing

Compressive tests have been applied in many occasions on bone [77,111–113] and even more so recently with in situ microcomputed tomography [9,114–117]. They are used to calculate the strain and stress induced by the load on the specimen. The specimens are loaded until failure to identify the yielding point and therefore, the Young's modulus. The load-displacement curve and associated stress-strain ones, are separated into two parts, same as with the indentation curve, the elastic and plastic deformation areas. As mentioned before, the elastic region represents the level of temporary deformation from which the bone can recover from once the load is released. It should be noted however, that bone is an anisotropic, heterogeneous material and its behaviour is not exclusively elastic. In particular it has shown a non-linear behaviour in the lower level of the pre-yielding elastic region [118].

Compressive test requires either cubical or cylindrical samples. The standard compression test set up has two fixed parallel platens. The specimen is placed between those for compression. The orientation of the bone specimen is similar to the anatomical one. Misalignment, leads to errors in the calculation of the mechanical properties [119,120]. In cases of wet conditions a water bath is used filled with saline solution [121,122]. The posterior and anterior boundaries of the sample need to be parallel to each other to avoid error in measurements, hence the use of end caps to both ends is recommended [123].

Strain measurements are taken based on the displacement reported in compression. There is a variety of ways to obtain the strain. One can get the strain by applying machine compliance correction [124–127], or by the use of extensometers [128–133]. In recent years the use of DIC and digital volume correlation (DVC) has become quite popular [75,77,117,134–141] (see Section 2.8.3).

2.7.3.4 In situ mechanics

In situ mechanics, or image-guided failure assessment (IGFA), is a technique that allows evaluation of fracture initiation and progression in the microscale as well as the monitoring of differences in their structure due to the loading [142]. Accurate failure analysis of the bone structure involves examination of its 3D volume. In situ mechanics engages the use of a microCT system for image acquisition of specimens in combination with a micromechanical loading device [76,115,117,140,143]. The latter is employed for step-wise mechanical testing. The loading device is placed in the microCT chamber and the step-wise mechanical testing (i.e. compression, indentation, tension etc.) is performed after each tomogram acquisition [14,144,145]. In fact, the first tomogram is obtained when the specimen is in the undeformed state. After applying the load and before the acquiring the images, the bone specimens are allowed to relax, considering their viscoelastic properties. In addition to the 3D imaging of the structure, the mechanical testing provides information about the behaviour of the sample. For example, in case of a compression/tension test the stress/strain curve is derived, whereas in indentation the elastic modulus is calculated. It should be noted however, that these curves can show discontinuity due to tissue relaxation [142]. Admittedly, it is a technique that has been extensively used to characterise healthy and diseased trabecular and cortical bone tissue at different dimensional scales and loading conditions [14,76,115,117,140,142,143,145].

2.8.1 Mechanical properties of cortical bone

Cortical bone has been identified as a major factor in bone strength and its structural indices as a fundamental indicator of bone loss and bone fragility. It contributes significantly to the mechanical strength of bone. Specifically, cortical bone stiffness is influenced by small changes in the density of the tissue in comparison to trabecular bone. Proximal femur fracture due to osteoporosis is mainly dictated by the reduction in the cortical bone mass rather than trabecular [146]. Thus, it is vital to understand cortical bone parameters that describe the geometry, mass and other strength-related properties. The material behaviour of cortical bone is considered anisotropic, meaning that its mechanical properties in the longitudinal direction are greater than in the radial and circumferential. However, strength and elastic modulus are similar in respect to the radial and circumferential direction. This is indicating that it can be treated as transversely isotropic [73]. Consequently, it behaves differently under longitudinal and transverse compressive loads. In the first, it experiences rapid hardening post-yielding followed by softening, whereas in the second the accumulated strains cause brittle fracture. Due to this anisotropy, cortical bone behaves differently in multiaxial loading compare to uniaxial. Multiaxial loading can cause significant decrease in the stiffness and fatigue life of the tissue in comparison to uniaxial [147]. Over the years, in order to fully comprehend the

anisotropy of cortical bone mechanical properties, the micro- and nanoscale have been investigated. The micromechanical behaviour of bone depends on a variety of factors. The size and distribution of the lacunae is one of those and it is known to influence the stiffness of the tissue. In cortical bone the average area of a lacuna is between 30 to 40 μm^2 and density is reported to be 460 g/mm^2 [148]. Cané et al. (1982) states that the size and number difference of lacunae (lacunae/mm^2) in cortical and trabecular bone (vertebral cortical bone: 52 μm^2, 577/mm^2) affects the bone tissue and hence cortical bone is stiffer [13]. Osteon mechanical properties vary depending on the orientation of collagen fibres, mineral density and loading modes. Specifically, shear loading stiffness accounts to approximately 4 GPa, whereas in tensile and compressive loading it ranges between 5-17 GPa [149,150]. Furthermore, the interfacial strength of cement lines is less than that of the osteonal lamellae (17.5 MPa and 30.4 MPa) [151,152]. The alignment of osteons also contributes to the effective toughening of the cortical bone, in an anisotropic way. That means that, a crack propagating vertical to the osteons (in the transverse orientation) has a higher probability of deflecting than if it was parallel to the osteon (longitudinal orientation) [153].

The osteocytes in bone are mechanosensitive, which entails regulating any permanent biological remodelling occurring in the bone tissue, thus allowing adaptations to the mechanical load that can be sustained [154]. The bone stiffness can be defined by the response of the osteocytes to a load induced by local strain. Therefore, the bone functional adaptation mechanisms can also be examined through a detailed analysis of the bone stiffness.

It should be noted, that cortical bone is a viscoelastic material and hence the strain and loading rates affect its behaviour, enhancing its brittleness as they increase [155]. When damage occurs to the tissue, there is degradation of its mechanical properties [156]. Damage can occur in either the meso-, micro or nanostructure of the bone. Microdamage increases the risk of fracture and it is proven to accumulate exponentially with age, especially in women [157,158]. However, microdamage does not always induce fragility to the bone. It has been seen that it can also contribute to its toughness. In particular, linear microcracks ahead of a larger crack strengthen the resistance to crack propagation [153].

Age is also a critical determinant in the mechanical properties. It can affect porosity, hypermineralisation and microdamage accumulation [159]. Tension and compression strength undergo 2% of reduction every 10 years after the third decade of someone's life and fracture toughness 4%. Whereas, tensile ultimate strain has a 10% reduction, from a 5% strain at the first 30 years to less than 1% for ages above 80 years [160,161]. The degradation of mechanical properties in bone due to aging are not always discernible from those of osteoporosis due to the pathology of the

disease. The cortical bone mass is reduced and the cavity area is increased. That causes reduction in the tensile ultimate and elastic modulus [162]. Other diseases affect cortical bone properties such as osteogenesis imperfecta, vitamin D deficiency and Paget's disease [138]. The first one is a genetic disease, where the bone toughness is reduced and the porosity of the bone increases leading to tissue brittleness [163]. Lastly, Vitamin D deficiency and Paget's disease can cause decrease in the stiffness and toughness as well affect the manner cracks propagate [164].

2.8.2 Mechanical properties of trabecular bone

Trabecular bone has higher porosity than cortical and that is the main factor which defines its mechanical properties at the apparent-level, followed by the arrangement of the trabecular network and properties of each trabecula at tissue-level [73]. In the long bones, it transfers mechanical loads from the joints to the cortical bone and in the vertebral bodies it is the predominant load bearing structure [165]. Its compressive strength is greater than the tensile one [166]. The yield in compression has been shown to be 0.7% of the total applied strain, however it can withstand up to 50% compressive strain when the loading and unloading does not exceed 3% [132]. The physiologic loads for human trabecular specimens are in the order of 1500 microstrain (με) at tissue level [73].

Trabecular architecture parameters have been investigated using high-resolution, three-dimensional techniques like micro-computed tomography (μCT), peripheral quantitative computed tomography (peripheral QCT) and micro-magnetic resonance (MRI) [58]. These parameters consist of trabecular thickness, spacing and number, connectivity density, structure model index (SMI; defining the differences between rod and plate architecture) and degree of anisotropy [167].

Trabecular bone is anisotropic due to the variation of elastic modulus and strength in its microstructure [73,165,168,169], therefore predicting its mechanical properties is difficult. It often shows an orthotropic behaviour that is characterising fully its elastic behaviour [170,171] and it has also been described as transversely isotropic in cases of vertebral bodies [172,173]. The elastic behaviour of trabecular bone is determined by the loading direction, anatomical site, geometry of the sample as well as the condition of the cartilage close to it [174].

Heterogeneity in the architecture and density of the tissue also affects the elastic behaviour and mechanical properties. Differences in the density of trabecular bone has been seen in the superior-inferior and posterior-anterior sites in vertebral bodies [175]. Apparent density is proportional to the square root of strength and modulus of trabecular bone [176]. The modulus of human trabeculae diverges from 10-3000 MPa and strength between 0.1 and 30 MPa. This fluctuation in the modulus and strength can be partially explained by the apparent density or volume fraction [177].

Nevertheless, it has been observed that in a single anatomic site, where the apparent density variations is less than an order magnitude the strength and modulus relation is linear [119].

The apparent modulus of trabecular tissue is decreased when overloading occurs leading to microscopic damage. In fact, microdamage has an effect on both the tissue and apparent level strains (Torres et al., 2016). Digital Image/Volume Correlation (DIC and DVC respectively) are techniques (see Section 3.3.5) that have been employed to investigate tissue-level deformations. Using DIC to analyse the bending of a single trabecula, it has been stated that tissue-level strain for compression is different from that of tension and that microcracks start forming at strain of 1.6% [179]. The tissue-level strains in combination with the heterogeneity in the tissue can lead to local yielding that can, in turn, cause reduction in the properties of the whole specimen [180]. In vitro, microdamage in trabecular tissue is common and it is increasing with age, similarly to cortical bone, and has been associated with volume fraction and architectural parameters [181].

Another reason for accumulation of residual strains at tissue-level, loss of stiffness and strength is cyclic compressive loading. As the magnitude of the strain increases, the damage accumulation due to fatigue grows and the modulus decreases [182]. The elastic modulus of trabecular bone is determined using a variety of tests; such are, tensile [183], ultrasonic measurements [184], nanoindentation [185]. Comparing the elastic modulus of trabecular to that of the cortical it is seen that first is approximately 10% less [150]. However, it has also been noticed that trabecular tissue can withstand larger deformations without complete loss of its load-bearing capability [183].

As in the cortical bone, age has a negative effect on the strength and modulus of trabecular bone. Except from the architectural change and density reduction, the degree of anisotropy in the structure of the tissue seems to be increasing [73]. Osteoarthritis is one of many diseases causing changes in the bone architecture indicating low mineral density and stiffness of the tissue [186].

2.8.3 Digital volume correlation

Digital volume correlation (DVC) is a method of computing the 3D full-field displacement and strain distribution between undeformed and deformed 3D volumes (Fig. 12). It is a technique that gives substance to strain measurements using the 3D visual information often obtained from in situ XCT mechanics. To be specific, it is a continuation of digital image correlation (DIC), which is a non-contact optical method used to measure in-plane displacement and strain fields in a variety of specimens under mechanical or thermal loading [113,187].

It was first developed by Bay et al. (1999), in an effort to measure the strain in trabecular bone tissue by determining the continuum level of displacement, under compression loading [188]. According to

the same study, DVC can be divided in three gradual processes; (a) acquisition of tomograms of samples in the loaded and unloaded state, (b) measurement of the resulting displacement field in the correlated volumes and (c) extraction of the strain tensors from the calculated displacement vector field. Acquisition of the tomograms is predominantly achieved through high-resolution X-ray microCT imaging, however, techniques such as confocal microscopy [189], micro-magnetic resonance imaging (microMRI) [190], high-resolution peripheral quantitative computed tomography (HR-pQCT) [191] and optical coherence tomography [192] have also been used. Images in the undeformed and deformed state are obtained using any of the aforementioned imaging modalities either after the applied load is removed or during. The discrete displacement in DVC is computed by correlating the reference (undeformed) volume to the target (deformed) one. The computation is based on the grey-level intensity values in the images, which depend on the detectable features of the specimen. Discrete points are defined in the reference where the displacement measurements are then executed. These points can be identified manually by the user or through meshing techniques. The measurement of the displacement field of the reference to the target image can be achieved in two ways: the local and global approach. In the first, the undeformed volume is divided into sub-volumes (usually cubic shaped) with size determined by the imaging scale. The advantage of this local approach is in the flexibility, however, in cases of large deformation there can be errors due to discontinuity [117,139] (Fig. 12). In the global approach a mesh is created, selecting the element size, and the displacement field is considered continuous [193]. A comparison between the two has shown that both give similar displacement uncertainties (0.009-0.094 voxel), however the second one has lower systematic errors [117].

The correlation of the images (target to reference) is determined by the DVC procedure. It entails the undeformed subvolume to deform predicated on an affine transformation; such as translation (most commonly used) [188,194,195], rotation, normal and shear strain [196,197]. The mapping of the reference feature to the respective point in the target image, is achieved by a correlation function, or otherwise known as objective function. This function defines the degree of correspondence between the two images. Such functions are the cross-correlation (CC), specifically direct correlation (DC) where the products of the voxel grey values of the initial and deformed tomograms are added directly [198]. Additionally, in cases of sub-voxel deformations, due to the implemented affine transformations, interpolation is needed between the voxel locations, so as to estimate the image data. In most studies tricubic interpolation is applied [188,195,196,199].

DVC is a relatively new technique and its accuracy and precision is being evaluated. It is highly determined by the quality of the images as well as errors in the displacement measurements. At tissue level such errors in the displacement have been estimated at 0.001 and 0.056 voxels for accuracy and

precision respectively [200]. Moreover, displacement errors can be attributed to the subvolume size. It has been observed that the larger the subvolume, the less the error. However, as mentioned above, the subvolume size is determined by the imaging scale. Therefore, it is up to the individual user to dictate the acceptable magnitude of the measuring error. Considering that, a method has been suggesting to minimise the systematic uncertainty error based on the zero-strain condition. In particular, two consecutive tomograms of the reference volume are acquired and registered, considering every non-zero value as error [201–203].

To conclude, DVC is a strain-measurement method with increasing popularity, that has been applied on cortical [204] and trabecular [141] as well as whole bone tissue [101,162] with the intention of characterising their mechanical properties and structural behaviour under mechanical testing.

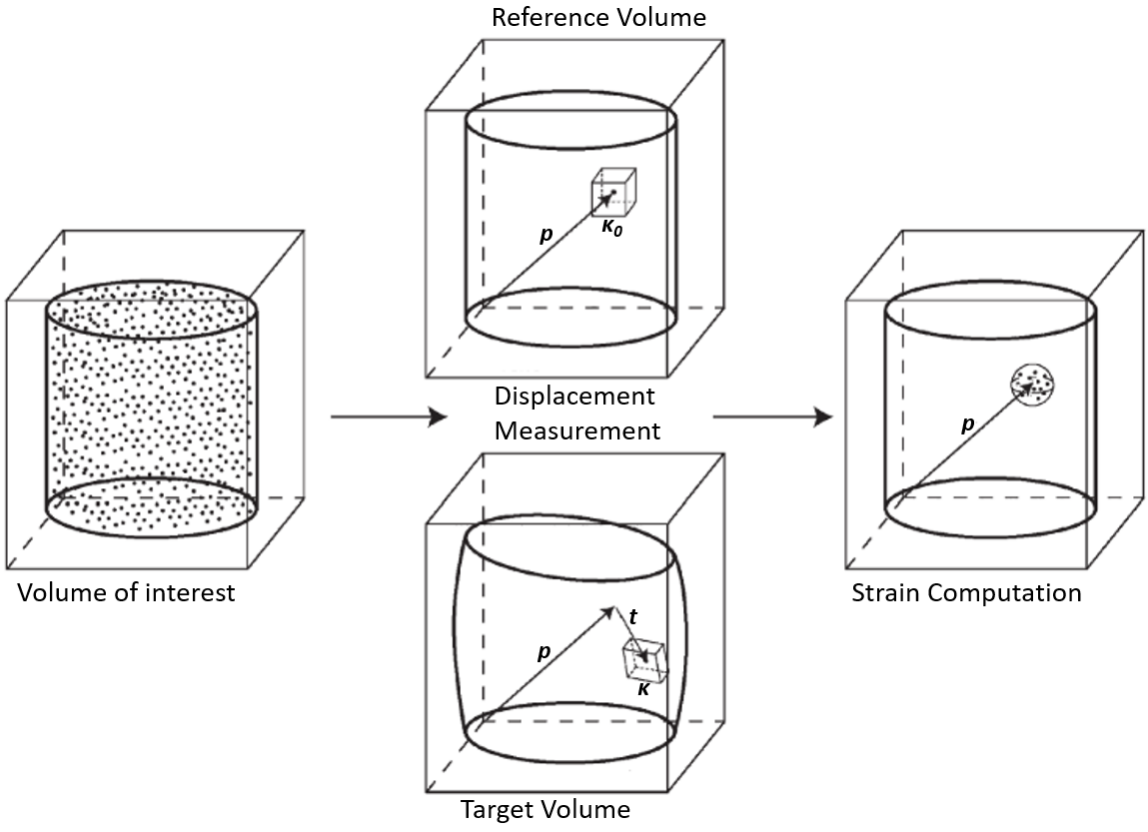

Figure 12: Digital volume correlation process. The volume of interest is specified and the measurement points are identified, the displacement is measured based on the correlation between the reference and target digital volumes and the strain is calculated at each point through approximation of the neighbouring deformation gradients. (p: points at location, κ_0 and κ: subvolumes, t: displacement vector). Adapted from [199].

References

[1] R.L. Drake, W. Vogl, A.W.M. Mitchel, Gray's anatomy for Students, 1st ed., Elsevier Churchill Livingstone, 2005.

[2] V. Singh, General Anatomy, Elsevier India, 2009.

[3] W.J. Hamilton, Textbook of human anatomy, 2nd ed., Macmillan London, 1976.

[4] A. Warren, Human skeleton, Encycl. Br. (2019). https://www.britannica.com/science/human-skeletal-system (accessed July 22, 2019).

[5] A. Warren, Human skeleton, Encycl. Br. (2019).

[6] G.J. Betts, P. DeSaix, E. Johnson, J.E. Johnson, O. Korol, D.H. Kruse, B. Poe, J.A. Wise, K.A. Young, Anatomy and Physiology, 2013. https://opentextbc.ca/anatomyandphysiology/.

[7] C. Rye, R. Wise, V. Jurukovski, J. DeSaix, J. Choi, Y. Avissar, Biology, 2013.

[8] B. Clarke, Normal bone anatomy and physiology., Clin. J. Am. Soc. Nephrol. 3 Suppl 3 (2008) 131–139. doi:10.2215/CJN.04151206.

[9] A. Levchuk, P. Schneider, M. Meier, P. Vogel, F. Donaldson, R. Müller, An Automated Step-Wise Micro-Compression Device for 3D Dynamic Image-Guided Failure Assessment of Bone Tissue on a Microstructural Level Using Time-Lapsed Tomography, Front. Mater. 5 (2018). doi:10.3389/fmats.2018.00032.

[10] X. Cai, H. Follet, L. Peralta, M. Gardegaront, D. Farlay, R. Gauthier, B. Yu, E. Gineyts, C. Olivier, M. Langer, A. Gourrier, D. Mitton, F. Peyrin, Q. Grimal, P. Laugier, Anisotropic elastic properties of human femoral cortical bone and relationships with composition and microstructure in elderly, Acta Biomater. 90 (2019) 254–266. doi:10.1016/j.actbio.2019.03.043.

[11] P. Augat, S. Schorlemmer, The role of cortical bone and its microstructure in bone strength, Age Ageing. 35 (2006) 27–31. doi:10.1093/ageing/afl081.

[12] M. Doblaré, J.M. García, M.J. Gómez, Modelling bone tissue fracture and healing: A review, Eng. Fract. Mech. 71 (2004) 1809–1840. doi:10.1016/j.engfracmech.2003.08.003.

[13] S.C. Cowin, Bone Mehcanics Handbook, Second Edi, CRC Press, 2001.

[14] T. Lowe, E. Avcu, E. Bousser, W. Sellers, P.J. Withers, 3D Imaging of indentation damage in bone, Materials (Basel). 11 (2018) 1–13. doi:10.3390/ma11122533.

[15] J.A. Buckwalter, M.J. Glimcher, R.R. Cooper, R. Recker, Bone Biology, (1995) 1256–1275.

[16] J.D. Currey, Bones, 2nd ed., Princeton University Press, New Jersey, 2002.

[17] M.L. Hillier, L.S. Bell, Differentiating human bone from animal bone: A review of histological methods, J. Forensic Sci. 52 (2007) 249–263. doi:10.1111/j.1556-4029.2006.00368.x.

[18] M.H. Ross, P. Wojciech, Histology a Text and Atlas With correlated cell and molecular biology, 5th ed., LIPPINCOTT WILLIAMS & WILKINS, Baltimore, 2006.

[19] L.C. Junqueira, J. Carneiro, Basic Histology text & atlas, 11th ed., McGraw-Hill companies, 2005.

[20] M.R. Allen, D.B. Burr, Bone Modeling and Remodeling, Basic Appl. Bone Biol. (2013) 75–90. doi:10.1016/B978-0-12-416015-6.00004-6.

[21] E.F. McCarthy, The histology of metabolic bone disease, Diagnostic Histopathol. 22 (2016) 378–383. doi:10.1016/j.mpdhp.2016.09.004.

[22] M. Zandi, A. Dehghan, F. Gheysari, L. Rezaeian, N. Mohammad Gholi Mezerji, Histological evaluation of the healing process of autografted mandibular bone defects in rats under treatment with zoledronate, European Association for Cranio-Maxillo-Facial Surgery, 2019. doi:10.1016/j.jcms.2018.11.015.

[23] L.J. Harrison, J.L. Cunningham, L. Strömberg, A.E. Goodship, Controlled induction of a pseudarthrosis: A study using a rodent model, J. Orthop. Trauma. 17 (2003) 11–21. doi:10.1097/00005131-200301000-00003.

[24] M.Z. Fathy, G.H. Ragab, M.M. Seif, S.M. Gadallah, S. Deeb, N.M. Safwat, Clinico-radiographic and histopathologic evaluation of iliac shaft fracture in dogs (an experimental study), Beni-Suef Univ. J. Basic Appl. Sci. 7 (2018) 165–170. doi:10.1016/j.bjbas.2017.09.001.

[25] R. Meeson, M. Moazen, A. Sanghani-Kerai, L. Osagie-Clouard, M. Coathup, G. Blunn, The influence of gap size on the development of fracture union with a micro external fixator, J. Mech. Behav. Biomed. Mater. 99 (2019) 161–168. doi:10.1016/j.jmbbm.2019.07.015.

[26] N.K. Simha, C.S. Carlson, J.L. Lewis, Evaluation of fracture toughness of cartilage by micropenetration, J. Mater. Sci. Mater. Med. 15 (2004) 631–639. doi:10.1023/B:JMSM.0000026104.30607.c7.

[27] D. Pringle, T.J. Koob, H.K.W. Kim, Indentation properties of growing femoral head following ischemic necrosis, J. Orthop. Res. 22 (2004) 122–130. doi:10.1016/S0736-0266(03)00135-9.

[28] C.A. Neldam, J. Sporring, A. Rack, T. Lauridsen, E.M. Hauge, H.L. Jørgensen, N.R. Jørgensen, R. Feidenhansl, E.M. Pinholt, Synchrotron radiation μCT and histology evaluation of bone-to-implant contact, J. Cranio-Maxillofacial Surg. 45 (2017) 1448–1457. doi:10.1016/j.jcms.2017.05.019.

[29] J. Wolff, Das Gesetz der Transformation der Knochen, Hirschwald, Berlin, 1892.

[30] A. Moayyeri, The Association Between Physical Activity and Osteoporotic Fractures: A Review of the Evidence and Implications for Future Research, Ann. Epidemiol. 18 (2008) 827–835. doi:10.1016/j.annepidem.2008.08.007.

[31] C. Ferguson, E. Alpern, T. Miclau, J.A. Helms, Does adult fracture repair recapitulate embryonic skeletal formation?, Mech. Dev. 87 (1999) 57–66. doi:10.1016/S0925-4773(99)00142-2.

[32] L. Claes, S. Recknagel, A. Ignatius, Fracture healing under healthy and inflammatory conditions, Nat. Rev. Rheumatol. 8 (2012) 133–143. doi:10.1038/nrrheum.2012.1.

[33] F. Loi, L.A. Córdova, J. Pajarinen, T. hua Lin, Z. Yao, S.B. Goodman, Inflammation, fracture and bone repair, Bone. 86 (2016) 119–130. doi:10.1016/j.bone.2016.02.020.

[34] R. Marsell, T.A. Einhorn, The biology of fracture healing, Injury. 42 (2011) 551–555. doi:10.1016/j.injury.2011.03.031.

[35] S.M. Perren, Evolution of the internal fixation of long bone fractures, J. Bone Jt. Surg. - Ser. B. 84 (2002) 1093–1110. doi:10.1302/0301-620X.84B8.13752.

[36] P.J. Harwood, J.B. Newman, A.L.R. Michael, (ii) An update on fracture healing and non-union, Orthop. Trauma. 24 (2010) 9–23. doi:10.1016/j.mporth.2009.12.004.

[37] L.C. Gerstenfeld, D.M. Cullinane, G.L. Barnes, D.T. Graves, T.A. Einhorn, Fracture healing as a post-natal developmental process: Molecular, spatial, and temporal aspects of its regulation, J. Cell. Biochem. 88 (2003) 873–884. doi:10.1002/jcb.10435.

[38] W.T. Chen, D.C. Han, P.X. Zhang, N. Han, Y.H. Kou, X.F. Yin, B.G. Jiang, A special healing pattern in stable metaphyseal fractures, Acta Orthop. 86 (2015) 238–242. doi:10.3109/17453674.2014.1003127.

[39] D.B. Harrell, E. Caradonna, L. Mazzucco, R. Gudenus, B. Amann, V. Prochazka, P. V. Giannoudis, C. Hendrich, M. Jäger, R. Krauspe, P. Hernigou, Non-hematopoietic essential functions of bone marrow cells: A review of scientific and clinical literature and rationale for treating bone defects, Orthop. Rev. (Pavia). 7 (2015) 122–128. doi:10.4081/or.2015.5691.

[40] P. Kolar, K. Schmidt-Bleek, H. Schell, T. Gaber, D. Toben, G. Schmidmaier, C. Perka, F. Buttgereit, G.N. Duda, The early fracture hematoma and its potential role in fracture healing, Tissue Eng. - Part B Rev. 16 (2010) 427–434. doi:10.1089/ten.teb.2009.0687.

[41] X. Yang, B.F. Ricciardi, A. Hernandez-Soria, Y. Shi, N. Pleshko Camacho, M.P.G. Bostrom, Callus mineralization and maturation are delayed during fracture healing in interleukin-6 knockout mice, Bone. 41 (2007) 928–936. doi:10.1016/j.bone.2007.07.022.

[42] K.N. Malizos, L.K. Papatheodorou, The healing potential of the periosteum molecular aspects, Injury. 36 (2005) S13–S19. doi:10.1016/j.injury.2005.07.030.

[43] T.A. Einhorn, The cell and molecular biology of fracture healing, Clin. Orthop. Relat. Res. (1998) 7–21. doi:10.1097/00003086-199810001-00003.

[44] B. Mavčič, V. Antolič, Optimal mechanical environment of the healing bone fracture/osteotomy, Int. Orthop. 36 (2012) 689–695. doi:10.1007/s00264-012-1487-8.

[45] S.M. Perren, Fracture healing: fracture healing understood as the result of a fascinating cascade of physical and biological interactions. Part II., Acta Chir. Orthop. Traumatol. Cech. 82 (2015) 13–21. http://www.ncbi.nlm.nih.gov/pubmed/25748657.

[46] T.P. Rüedi, W.M. Murphy, Ao Principles of Fracture Management, 2000. doi:https://dx.doi.org/10.1016/j.jss.2017.02.010.

[47] L. Claes, Biomechanical principles and mechanobiologic aspects of flexible and locked plating, J. Orthop. Trauma. 25 (2011) 4–7. doi:10.1097/BOT.0b013e318207093e.

[48] T. Wehner, R. Penzkofer, P. Augat, L. Claes, U. Simon, Improvement of the shear fixation stability of intramedullary nailing, Clin. Biomech. 26 (2011) 147–151. doi:10.1016/j.clinbiomech.2010.09.009.

[49] M. Bottlang, M. Lesser, J. Koerber, J. Doornink, B. Von Rechenberg, P. Augat, D.C. Fitzpatrick, S.M. Madey, J.L. Marsh, Far cortical locking can improve healing of fractures stabilized with locking plates, J. Bone Jt. Surg. - Ser. A. 92 (2010) 1652–1660. doi:10.2106/JBJS.I.01111.

[50] G.N. Duda, M. Sollmann, S. Sporrer, J.E. Hoffmann, J. Kassi, C. Khodadadyan, M. Raschke, Interfragmentary Motion in Tibial Osteotomies Stabilized With Ring Fixators, Clin. Orthop. Relat. Res. (2002) 162–172.

[51] P. Augat, J. Burger, S. Schorlemmer, T. Henke, M. Peraus, L. Claes, Shear movement at the fracture site delays healing in a diaphyseal fracture model, J. Orthop. Res. 21 (2003) 1011–1017. doi:10.1016/S0736-0266(03)00098-6.

[52] L. Claes, P. Augat, G. Suger, H.J. Wilke, Influence of size and stability of the osteotomy gap on the success of fracture healing, J. Orthop. Res. 15 (1997) 577–584. doi:10.1002/jor.1100150414.

[53] D.R. Epari, H. Schell, H.J. Bail, G.N. Duda, Instability prolongs the chondral phase during bone healing in sheep, Bone. 38 (2006) 864–870. doi:10.1016/j.bone.2005.10.023.

[54] T. Wehner, M. Steiner, A. Ignatius, L. Claes, C.M. Aegerter, Prediction of the time course of callus stiffness as a function of mechanical parameters in experimental rat fracture healing studies - A numerical study, PLoS One. 9 (2014) 1–16. doi:10.1371/journal.pone.0115695.

[55] P. Garcia, T. Histing, J. Holstein, W. Klein, M. Laschke, R. Matthys, A. Ignatius, B. Wildemann, J. Lienau, A. Peters, B. Willie, G. Duda, L. Claes, T. Pohlemann, M. Menger, Rodent animal models of delayed bone healing and non-union formation: a comprehensive review, Eur. Cells Mater. 26 (2013) 1–14. doi:10.22203/ecm.v026a01.

[56] M. Bhandari, G.H. Guyatt, M.F. Swiontkowski, P. Tornetta, S. Sprague, E.H. Schemitsch, A Lack of Consensus in the Assessment of Fracture Healing Among Orthopaedic Surgeons, 16 (2002) 562–566. doi:10.1097/01.BOT.0000031144.58425.CB.

[57] L.A. Feldkamp, S.A. Goldstein, M.A. Parfitt, G. Jesion, M. Kleerekoper, The direct examination of three-dimensional bone architecture in vitro by computed tomography, J. Bone Miner. Res. 4 (1989) 3–11. doi:10.1002/jbmr.5650040103.

[58] M.L. Bouxsein, S.K. Boyd, B.A. Christiansen, R.E. Guldberg, K.J. Jepsen, R. Müller, Guidelines for assessment of bone microstructure in rodents using micro-computed tomography, J. Bone Miner. Res. 25 (2010) 1468–1486. doi:10.1002/jbmr.141.

[59] S.R. Stock, MicroComputed Tomography Methodology and Applications, CRP Press, 2009.

[60] M. Stauber, R. Müller, Micro-Computed Tomography: A Method for the Non-Destructive Evaluation of the Three-Dimentional Structure of Biological Specimens, in: Osteoporos. Methods Protoc., Humana Press, 2008: pp. 273–292.

[61] W.A. Kalender, Computed Tomography, 3rd ed., Publicis Publishing, Erlangen, 2011.

[62] J.A. Meganck, B. Liu, Dosimetry in Micro-computed Tomography: a Review of the Measurement Methods, Impacts, and Characterization of the Quantum GX Imaging System, Mol. Imaging Biol. 19 (2017) 499–511. doi:10.1007/s11307-016-1026-x.

[63] A.J. Nygren, Filtered Back Projection, (1997). http://www.owlnet.rice.edu/~elec539/Projects97/cult/node2.html (accessed August 26, 2019).

[64] L.A. Feldkamp, L.C. Davis, J. w Kress, Practical cone-beam algorithm, America (NY). 1 (1984) 612–619.

[65] A. du Plessis, C. Broeckhoven, A. Guelpa, S.G. le Roux, Laboratory x-ray micro-computed tomography: A user guideline for biological samples, Gigascience. 6 (2017) 1–11. doi:10.1093/gigascience/gix027.

[66] C. Chappard, A. Basillais, L. Benhamou, A. Bonassie, B. Brunet-Imbault, N. Bonnet, F. Peyrin, Comparison of synchrotron radiation and conventional x-ray microcomputed tomography for assessing trabecular bone microarchitecture of human femoral heads, Med. Phys. 33 (2006) 3568–3577. doi:10.1118/1.2256069.

[67] Y. Yang, Y.C. Wu, L. Li, S.Y. Zhang, K.G. Dong, T.K. Zhang, M.H. Yu, X.H. Zhang, B. Zhu, F. Tan, Y.H. Yan, G. Li, W. Fan, F. Lu, Z.Q. Zhao, W.M. Zhou, L.F. Cao, Y.Q. Gu, Design and characterization of high energy micro-CT with a laser-based X-ray source, Results Phys. 14 (2019) 1–12. doi:10.1016/j.rinp.2019.102382.

[68] M.J. Paulus, S.S. Gleason, S.J. Kennel, P.R. Hunsicker, D.K. Johnson, High resolution X-ray computed tomography: An emerging tool for small animal cancer research, Neoplasia. 2 (2000) 62–70. doi:10.1038/sj.neo.7900069.

[69] P. Russo, Handbook of X-ray Imaging Physics and Technology, Taylor & Francis, 2018.

[70] M. Salomé, F. Peyrin, P. Cloetens, C. Odet, A.M. Laval-Jeantet, J. Baruchel, P. Spanne, A synchrotron radiation microtomography system for the analysis of trabecular bone samples, Med. Phys. 26 (1999) 2194–2204. doi:10.1118/1.598736.

[71] Diamond House, (n.d.). https://www.diamond.ac.uk/Science/Machine/Components/diamondhouse.html (accessed October 14, 2019).

[72] H.B. Hunt, E. Donnelly, Bone Quality Assessment Techniques: Geometric, Compositional, and Mechanical Characterization from Macroscale to Nanoscale, Clin. Rev. Bone Miner. Metab. 14 (2016) 133–149. doi:10.1007/s12018-016-9222-4.

[73] E.F. Morgan, G.U. Unnikrisnan, A.I. Hussein, Bone Mechanical Properties in Healthy and Diseased States, Annu. Rev. Biomed. Eng. 20 (2018) 119–143. doi:10.1146/annurev-bioeng-062117-121139.

[74] A.I. Hussein, P.E. Barbone, E.F. Morgan, Digital volume correlation for study of the mechanics of whole bones, Procedia IUTAM. 4 (2012) 116–125. doi:10.1016/j.piutam.2012.05.013.

[75] V. Danesi, G. Tozzi, L. Cristofolini, Application of digital volume correlation to study the efficacy of prophylactic vertebral augmentation, Clin. Biomech. 39 (2016) 14–24. doi:10.1016/j.clinbiomech.2016.07.010.

[76] G. Tozzi, V. Danesi, M. Palanca, L. Cristofolini, Elastic Full-Field Strain Analysis and Microdamage Progression in the Vertebral Body from Digital Volume Correlation, Strain. 52 (2016) 446–455. doi:10.1111/str.12202.

[77] S.A. Yavari, J. van der Stok, H. Weinans, A.A. Zadpoor, Full-field strain measurement and fracture analysis of rat femora in compression test, J. Biomech. 46 (2013) 1282–1292. doi:10.1016/j.jbiomech.2013.02.007.

[78] V.L. Ferguson, R.A. Ayers, T.A. Bateman, S.J. Simske, Bone development and age-related bone loss in male C57BL/6J mice, Bone. 33 (2003) 387–398. doi:10.1016/S8756-3282(03)00199-6.

[79] D. Merriman, Z. Gugala, R. Morris, R. Lindsey, The Effects of Intramedullary Reaming on Residual Long Bone Biomechanical Properties in a Composite Femur Model, Texas Orthop. J. 1 (2015) 59–70. doi:10.18600/toj.010207.

[80] E. Broitman, Indentation Hardness Measurements at Macro-, Micro-, and Nanoscale: A Critical Overview, Tribol. Lett. 65 (2017) 1–18. doi:10.1007/s11249-016-0805-5.

[81] A.C. Fischer-Cripps, Mechanical Engineering Series, 2006. doi:10.1007/b22134.

[82] P.K. Zysset, Indentation of bone tissue: A short review, Osteoporos. Int. 20 (2009) 1049–1055. doi:10.1007/s00198-009-0854-9.

[83] C.E. Hoffler, X.E. Guo, P.K. Zysset, S.A. Goldstein, An application of nanoindentation technique to measure bone tissue Lamellae properties., J. Biomech. Eng. 127 (2005) 1046–53. doi:10.1115/1.2073671.

[84] G.P. Evans, J.C. Behiri, J.D. Currey, W. Bonfield, Microhardness and Young's modulus in cortical bone exhibiting a wide range of mineral volume fractions, and in a bone analogue, J. Mater. Sci. Mater. Med. 1 (1990) 38–43. doi:10.1007/BF00705352.

[85] E. Dall'Ara, R. Schmidt, P. Zysset, Microindentation can discriminate between damaged and intact human bone tissue, Bone. 50 (2012) 925–929. doi:10.1016/j.bone.2012.01.002.

[86] M.J. Mirzaali, J.J. Schwiedrzik, S. Thaiwichai, J.P. Best, J. Michler, P.K. Zysset, U. Wolfram, Mechanical properties of cortical bone and their relationships with age, gender, composition and microindentation properties in the elderly, Bone. 93 (2016) 196–211. doi:10.1016/j.bone.2015.11.018.

[87] J. Schwiedrzik, R. Raghavan, A. Bürki, V. Lenader, U. Wolfram, J. Michler, P. Zysset, In situ micropillar compression reveals superior strength and ductility but an absence of damage in lamellar bone, Nat. Mater. 13 (2014) 740–747. doi:10.1038/nmat3959.

[88] A. Kataruka, K. Mendu, O. Okeoghene, J. Puthuvelil, A.T. Akono, Microscopic assessment of bone toughness using scratch tests, Bone Reports. 6 (2017) 17–25. doi:10.1016/j.bonr.2016.12.001.

[89] J.J. Kruzic, D.K. Kim, K.J. Koester, R.O. Ritchie, Indentation techniques for evaluating the fracture toughness of biomaterials and hard tissues, J. Mech. Behav. Biomed. Mater. 2 (2009) 384–395. doi:10.1016/j.jmbbm.2008.10.008.

[90] J.J. Kruzic, R.O. Ritchie, Determining the toughness of ceramics from vickers indentations using the crack-opening displacements: An experimental study, J. Am. Ceram. Soc. 86 (2003) 1433–1436. doi:10.1111/j.1151-2916.2003.tb03490.x.

[91] J. Zhang, G.L. Niebur, T.C. Ovaert, Mechanical property determination of bone through nano- and micro-indentation testing and finite element simulation, J. Biomech. 41 (2008) 267–275. doi:10.1016/j.jbiomech.2007.09.019.

[92] U. Wolfram, H.J. Wilke, P.K. Zysset, Valid μ finite element models of vertebral trabecular bone can be obtained using tissue properties measured with nanoindentation under wet conditions, J. Biomech. 43 (2010) 1731–1737. doi:10.1016/j.jbiomech.2010.02.026.

[93] W.C. Oliver, G.M. Pharr, Measurement of hardness and elastic modulus by instrumented indentation: Advances in understanding and refinements to methodology, J. Mater. Res. 19 (2004) 3–20. doi:10.1557/jmr.2004.19.1.3.

[94] A. Lundkvist, E. Lilleodden, W. Siekhaous, J. Kinney, L. Pruitt, M. Balooch, Viscoelastic properties of healthy human artery measured in saline solution by AFM based indentation technique, 436 (1997) 353–358.

[95] D.M. Ebenstein, L.A. Pruitt, Nanoindentation of biological materials, Nano Today. 1 (2006) 26–33. doi:10.1016/S1748-0132(06)70077-9.

[96] Ondrej jirousek, Nanoindentation of Human Trabecular Bone – Tissue Mechanical Properties Compared to, (2012) 259–284. doi:10.5772/50152.

[97] P.K. Zysset, X. Edward Guo, C. Edward Hoffler, K.E. Moore, S.A. Goldstein, Elastic modulus and hardness of cortical and trabecular bone lamellae measured by nanoindentation in the human femur, J. Biomech. 32 (1999) 1005–1012. doi:10.1016/S0021-9290(99)00111-6.

[98] E. Donnelly, S.P. Baker, A.L. Boskey, M.C.H. van der Meulen, Effects of surface roughness and maximum load on the mechanical properties of cancellous bone measured by nanoindentation, J. Biomed. Mater. Res. 77 (2006) 426–435.

[99] J.Y. Rho, M.E. Roy, T.Y. Tsui, G.M. Pharr, Elastic properties of microstructural components of human bone tissue as measured by nanoindentation, J. Biomed. Mater. Res. 45 (1999) 48–54. doi:10.1002/(SICI)1097-4636(199904)45:1<48::AID-JBM7>3.0.CO;2-5.

[100] G. Franzoso, P.K. Zysset, Elastic Anisotropy of Human Cortical Bone Secondary Osteons Measured by Nanoindentation, J. Biomech. Eng. 131 (2008) 021001. doi:10.1115/1.3005162.

[101] G. Lewis, J.S. Nyman, The use of nanoindentation for characterizing the properties of mineralized hard tissues: State-of-the art review, J. Biomed. Mater. Res. - Part B Appl. Biomater. 87 (2008) 286–301. doi:10.1002/jbm.b.31092.

[102] E. Donnelly, R.M. Williams, S.A. Downs, M.E. Dickinson, S.P. Baker, M.C.H. van der Meulen, Quasistatic and dynamic nanomechanical properties of cancellous bone tissue relate to collagen content and organization, J. Mater. Res. 21 (2006) 2106–2117. doi:10.1557/jmr.2006.0259.

[103] J.Y. Rho, J.D. Currey, P. Zioupos, G.M. Pharr, The anisotropic Young's modulus of equine secondary osteones and interstitial bone determined by nanoindentation, J. Exp. Biol. 204 (2001) 1775–1781.

[104] M.E. Roy, S.K. Nishimoto, J.Y. Rho, S.K. Bhattacharya, G.M. Pharr, The distribution of osteocalcin, degree of mineralization, and mechanical properties along the length of Cyprinus carpio rib bone, J. Mater. Sci. Mater. Med. 12 (2001) 699–702. doi:10.1023/A:1011268525937.

[105] T. Jämsä, J.Y. Rho, Z. Fan, C.A. MacKay, S.C. Marks, J. Tuukkanen, Mechanical properties in long bones of rat osteopetrotic mutations, J. Biomech. 35 (2002) 161–165. doi:10.1016/S0021-9290(01)00203-2.

[106] M.P. Akhter, Z. Fan, J.Y. Rho, Bone intrinsic material properties in three inbred mouse strains, Calcif. Tissue Int. 75 (2004) 416–420. doi:10.1007/s00223-004-0241-7.

[107] J.Y. Rho, G.M. Pharr, Effects of drying on the mechanical properties of bovine femur measured by nanoindentation, J. Mater. Sci. Mater. Med. 10 (1999) 485–488. doi:10.1023/A:1008901109705.

[108] E. Mittra, S. Akella, Y. Qin, The effects of embedding material, loading rate and magnitude, and penetration depth in nanoindentation of trabecular bone, (2006). doi:10.1002/jbm.a.

[109] G.W. Marshall, M. Balooch, R.R. Gallagher, S.A. Gansky, S.J. Marshall, Mechanical properties of the dentinoenamel junction: AFM studies of nanohardness, elastic modulus, and fracture, J. Biomed. Mater. Res. 54 (2001) 87–95. doi:10.1002/1097-4636(200101)54:1<87::AID-JBM10>3.0.CO;2-Z.

[110] S.P. Ho, H. Goodis, M. Balooch, G. Nonomura, S.J. Marshall, G. Marshall, The effect of sample preparation technique on determination of structure and nanomechanical properties of human cementum hard tissue, Biomaterials. 25 (2004) 4847–4857. doi:10.1016/j.biomaterials.2003.11.047.

[111] R.L. De Souza, M. Matsuura, F. Eckstein, S.C.F. Rawlinson, L.E. Lanyon, A.A. Pitsillides, Non-invasive axial loading of mouse tibiae increases cortical bone formation and modifies trabecular organization: A new model to study cortical and cancellous compartments in a single loaded element, Bone. 37 (2005) 810–818. doi:10.1016/j.bone.2005.07.022.

[112] Y. Chen, E. Dall'Ara, E. Sales, K. Manda, R. Wallace, P. Pankaj, M. Viceconti, Micro-CT based finite element models of cancellous bone predict accurately displacement once the boundary condition is well replicated: A validation study, J. Mech. Behav. Biomed. Mater. 65 (2017) 644–651. doi:10.1016/j.jmbbm.2016.09.014.

[113] S. Zhao, M. Arnold, R.L. Abel, J.P. Cobb, S. Ma, U. Hansen, O. Boughton, Standardizing Compression Testing for Measuring the Stiffness of Human Bone, Bone Jt. Res. 7 (2018) 524–538. doi:10.1302/2046-3758.78.BJR-2018-0025.R1.

[114] P. Sztefek, M. Vanleene, R. Olsson, R. Collinson, A.A. Pitsillides, S. Shefelbine, Using digital image correlation to determine bone surface strains during loading and after adaptation of the mouse tibia, J. Biomech. 43 (2010) 599–605. doi:10.1016/j.jbiomech.2009.10.042.

[115] R. Voide, P. Schneider, M. Stauber, P. Wyss, M. Stampanoni, U. Sennhauser, G.H. van Lenthe, R. Müller, Time-lapsed assessment of microcrack initiation and propagation in murine cortical bone at submicrometer resolution, Bone. 45 (2009) 164–173. doi:10.1016/j.bone.2009.04.248.

[116] M. Giorgi, E. Dall'Ara, Variability in strain distribution in the mice tibia loading model: A preliminary study using digital volume correlation, Med. Eng. Phys. 62 (2018) 7–16. doi:10.1016/j.medengphy.2018.09.001.

[117] K. Madi, G. Tozzi, Q.H. Zhang, J. Tong, A. Cossey, A. Au, D. Hollis, F. Hild, Computation of full-field displacements in a scaffold implant using digital volume correlation and finite element analysis, Med. Eng. Phys. 35 (2013) 1298–1312. doi:10.1016/j.medengphy.2013.02.001.

[118] E.F. Morgan, O.C. Yeh, W.C. Chang, T.M. Keaveny, Nonlinear behavior of trabecular bone at small strains, J. Biomech. Eng. 123 (2001) 1–9. doi:10.1115/1.1338122.

[119] E.F. Morgan, T.M. Keaveny, Dependence of yield strain of human trabecular bone on anatomic site, J. Biomech. 34 (2001) 569–577. doi:10.1016/S0021-9290(01)00011-2.

[120] E. Perilli, M. Baleani, C. Öhman, R. Fognani, F. Baruffaldi, M. Viceconti, Dependence of mechanical compressive strength on local variations in microarchitecture in cancellous bone of proximal human femur, J. Biomech. 41 (2008) 438–446. doi:10.1016/j.jbiomech.2007.08.003.

[121] H. Follet, K. Bruyère-Garnier, F. Peyrin, J.P. Roux, M.E. Arlot, B. Burt-Pichat, C. Rumelhart, P.J. Meunier, Relationship between compressive properties of human os calcis cancellous bone and microarchitecture assessed from 2D and 3D synchrotron microtomography, Bone. 36 (2005) 340–351. doi:10.1016/j.bone.2004.10.011.

[122] L. Karim, D. Vashishth, Heterogeneous glycation of cancellous bone and its association with bone quality and fragility, PLoS One. 7 (2012). doi:10.1371/journal.pone.0035047.

[123] T.M. Keaveny, X.E. Guo, T.A. McMahon, E.F. Wachtel, W.C. Hayes, Trabecular bone exhibits fully linear elastic behavior and yields at low strains, J. Biomech. 27 (2004) 1127–1136. doi:10.1016/0021-9290(94)90053-1.

[124] M. Zhu, T.S. Keller, D.M. Spengler, Effects of specimen load-bearing and free surface layers on the compressive mechanical properties of cellular materials, J. Biomech. 27 (1994) 57–66. doi:10.1016/0021-9290(94)90032-9.

[125] T.D. Brown, A.B. Ferguson, Mechanical property distributions in the cancellous bone of the human proximal femur, Acta Orthop. 51 (1980) 429–437. doi:10.3109/17453678008990819.

[126] A.K. Aiyangar, J. Vivanco, A.G. Au, P.A. Anderson, E.L. Smith, H.L. Ploeg, Dependence of anisotropy of human lumbar vertebral trabecular bone on quantitative computed tomography-based apparent density, J. Biomech. Eng. 136 (2014) 1–10. doi:10.1115/1.4027663.

[127] T.S. Keller, Predicting the Compressive Mechanical Behaviour of Bone, J Blomechamcs. 27 (1994). https://ac.els-cdn.com/0021929094900566/1-s2.0-0021929094900566-

main.pdf?_tid=8d666fce-c80c-4a37-aca9-81273747ef91&acdnat=1533750486_d321f579a14cb021bc34d7ab9d4d47f3.

[128] C. Öhman, E. Dall'Ara, M. Baleani, S.V.S. Jan, M. Viceconti, The effects of embalming using a 4% formalin solution on the compressive mechanical properties of human cortical bone, Clin. Biomech. 23 (2008) 1294–1298. doi:10.1016/j.clinbiomech.2008.07.007.

[129] F. Linde, I. Hvid, F. Madsen, The effect of specimen geometry on the mechanical behavior of trabecular bone specimens, J. Biomech. 25 (1991) 359–368. doi:10.4028/www.scientific.net/SSP.185.129.

[130] P. Augat, T. Link, T.F. Lang, J.C. Lin, S. Majumdar, H.K. Genant, Anisotropy of the elastic modulus of trabecular bone specimens from different anatomical locations, Med. Eng. Phys. 20 (1998) 124–131. doi:10.1016/S1350-4533(98)00001-0.

[131] U. Hansen, P. Zioupos, R. Simpson, J.D. Currey, D. Hynd, The effect of strain rate on the mechanical properties of human cortical bone, J. Biomech. Eng. 130 (2008) 1–8. doi:10.1115/1.2838032.

[132] T.M. Keaveny, E.F. Wachtel, D.L. Kopperdahl, Mechanical behavior of human trabecular bone after overloading, J. Orthop. Res. 17 (1999) 346–353. doi:10.1002/jor.1100170308.

[133] C. Öhman, M. Baleani, E. Perilli, E. Dall'Ara, S. Tassani, F. Baruffaldi, M. Viceconti, Mechanical testing of cancellous bone from the femoral head: Experimental errors due to off-axis measurements, J. Biomech. 40 (2007) 2426–2433. doi:10.1016/j.jbiomech.2006.11.020.

[134] S. Oliviero, M. Giorgi, E. Dall'Ara, Validation of finite element models of the mouse tibia using digital volume correlation, J. Mech. Behav. Biomed. Mater. 86 (2018) 172–184. doi:10.1016/j.jmbbm.2018.06.022.

[135] L. Duchemin, V. Bousson, C. Raossanaly, C. Bergot, J.D. Laredo, W. Skalli, D. Mitton, Prediction of mechanical properties of cortical bone by quantitative computed tomography, Med. Eng. Phys. 30 (2008) 321–328. doi:10.1016/j.medengphy.2007.04.008.

[136] I. Kalouche, J. Crépin, S. Abdelmoumen, D. Mitton, G. Guillot, O. Gagey, Mechanical properties of glenoid cancellous bone, Clin. Biomech. 25 (2010) 292–298. doi:10.1016/j.clinbiomech.2009.12.009.

[137] H. Sugita, M. Oka, J. Toguchida, T. Nakamura, T. Ueo, T. Hayami, Anisotropy of osteoporotic cancellous bone, Bone. 24 (1999) 513–516. doi:10.1016/S8756-3282(99)00021-6.

[138] V. Vardakastani, D. Saletti, W. Skalli, P. Marry, J.M. Allain, C. Adam, Increased intra-cortical porosity reduces bone stiffness and strength in pediatric patients with osteogenesis imperfecta, Bone. 69 (2014) 61–67. doi:10.1016/j.bone.2014.09.003.

[139] G. Tozzi, E. Dall'Ara, M. Palanca, M. Curto, F. Innocente, L. Cristofolini, Strain uncertainties from two digital volume correlation approaches in prophylactically augmented vertebrae: Local analysis on bone and cement-bone microstructures, J. Mech. Behav. Biomed. Mater. 67 (2017) 117–126. doi:10.1016/j.jmbbm.2016.12.006.

[140] G. Tozzi, Q.H. Zhang, J. Tong, Microdamage assessment of bone-cement interfaces under monotonic and cyclic compression, J. Biomech. 47 (2014) 3466–3474. doi:10.1016/j.jbiomech.2014.09.012.

[141] M. Peña-Fernández, S. Cipiccia, E. Dall'Ara, A.J. Bodey, R. Parwani, M. Pani, G.W. Blunn, A.H. Barber, G. Tozzi, Effect of SR-microCT radiation on the mechanical integrity of trabecular bone using in situ mechanical testing and digital volume correlation., J. Mech. Behav. Biomed. Mater. 88 (2018) 109–119. doi:10.1016/j.jmbbm.2018.08.012.

[142] A. Nazarian, R. Müller, Time-lapsed microstructural imaging of bone failure behavior, J. Biomech. 37 (2004) 55–65. doi:10.1016/S0021-9290(03)00254-9.

[143] P.J. Thurner, P. Wyss, R. Voide, M. Stauber, M. Stampanoni, U. Sennhauser, R. Müller, Time-lapsed investigation of three-dimensional failure and damage accumulation in trabecular bone using synchrotron light, Bone. 39 (2006) 289–299. doi:10.1016/j.bone.2006.01.147.

[144] Y. Vertyagina, M. Mostafavi, C. Reinhard, R. Atwood, T.J. Marrow, In situ quantitative three-dimensional characterisation of sub-indentation cracking in polycrystalline alumina, J. Eur. Ceram. Soc. 34 (2014) 3127–3132. doi:10.1016/j.jeurceramsoc.2014.04.002.

[145] G. Tozzi, Q.H. Zhang, J. Tong, 3D real-time micromechanical compressive behaviour of bone-cement interface: Experimental and finite element studies, J. Biomech. 45 (2012) 356–363. doi:10.1016/j.jbiomech.2011.10.011.

[146] P. Schneider, M. Stauber, R. Voide, M. Stampanoni, L.R. Donahue, R. Müller, Ultrastructural properties in cortical bone vary greatly in two inbred strains of mice as assessed by synchrotron light based micro- and nano-CT, J. Bone Miner. Res. 22 (2007) 1557–1570. doi:10.1359/jbmr.070703.

[147] W.T. George, D. Vashishth, Susceptibility of aging human bone to mixed-mode fracture increases bone fragility, Bone. 38 (2006) 105–111. doi:10.1016/j.bone.2005.08.002.

[148] V. Canè, G. Marotti, G. Volpi, D. Zaffe, S. Palazzini, F. Remaggi, M.A. Muglia, Size and density of osteocyte lacunae in different regions of long bones, Calcif. Tissue Int. 34 (1982) 558–563. doi:10.1007/BF02411304.

[149] A. Ascenzi, P. Baschieri, A. Benvenuti, The torsional properties of single selected osteons, J. Biomech. 27 (1994). doi:10.1016/0021-9290(94)90260-7.

[150] H.H. Bayraktar, E.F. Morgan, G.L. Niebur, G.E. Morris, E.K. Wong, T.M. Keaveny, Comparison of the elastic and yield properties of human femoral trabecular and cortical bone tissue, J. Biomech. 37 (2004) 27–35. doi:10.1016/S0021-9290(03)00257-4.

[151] R.F. Bigley, L. V. Griffin, L. Christensen, R. Vandenbosch, Osteon interfacial strength and histomorphometry of equine cortical bone, J. Biomech. 39 (2006) 1629–1640. doi:10.1016/j.jbiomech.2005.05.006.

[152] X.N. Dong, X. Zhang, X.E. Guo, Interfacial strength of cement lines in human cortical bone., Mech. Chem. Biosyst. 2 (2005) 63–8. http://www.ncbi.nlm.nih.gov/pubmed/16783927.

[153] R.K. Nalla, J.S. Stölken, J.H. Kinney, R.O. Ritchie, Fracture in human cortical bone: Local fracture criteria and toughening mechanisms, J. Biomech. 38 (2005) 1517–1525. doi:10.1016/j.jbiomech.2004.07.010.

[154] R. Jae-young, L. Kuhn-Spearing, P. Zioupos, Mechanical Properties and the hierarchical structure of bone, Med. Eng. Phys. 20 (1998) 92–102. doi:10.1038/251673a0.

[155] P. Zioupos, U. Hansen, J.D. Currey, Microcracking damage and the fracture process in relation to strain rate in human cortical bone tensile failure, J. Biomech. 41 (2008) 2932–2939. doi:10.1016/j.jbiomech.2008.07.025.

[156] M.T. Fondrk, E.H. Bahniuk, D.T. Davy, A Damage Model for Nonlinear Tensile Behavior of Cortical Bone, J. Biomech. Eng. 121 (1999) 533. doi:10.1115/1.2835084.

[157] A.C. Courtney, W.C. Hayes, L.J. Gibson, Age-related differences in post-yield damage in human cortical bone. Experiment and model, J. Biomech. 29 (1996) 1463–1471. doi:10.1016/0021-9290(96)84542-8.

[158] R. Zebaze, E.J. Atkinson, Y. Peng, M. Bui, A. Ghasem-Zadeh, S. Khosla, E. Seeman, Increased Cortical Porosity and Reduced Trabecular Density Are Not Necessarily Synonymous With Bone Loss and Microstructural Deterioration, JBMR Plus. 3 (2019) e10078. doi:10.1002/jbm4.10078.

[159] P. Zioupos, J.D. Currey, A. Casinos, Tensile fatigue in bone: Are cycles-, or time to failure, or both, important?, J. Theor. Biol. 210 (2001) 389–399. doi:10.1006/jtbi.2001.2316.

[160]. R.K. Nalla, J.J. Kruzic, J.H. Kinney, R.O. Ritchie, Effect of aging on the toughness of human cortical bone: Evaluation by R-curves, J. Mech. Behav. Biomed. Mater. 4 (2004) 1240–1246. doi:doi:10.1016/j.bone.2004.07.016.

[161] K.J. Koester, H.D. Barth, R.O. Ritchie, Effect of aging on the transverse toughness of human cortical bone: Evaluation by R-curves, J. Mech. Behav. Biomed. Mater. 4 (2011) 1504–1513. doi:10.1016/j.jmbbm.2011.05.020.

[162] R. Dickenson, W. Hutton, J. Stott, The Mechanical Properties of Osteoporosis, J. Bone. 63-B (1981) 233–238. http://web.jbjs.org.uk/content/63-B/2/233.full.pdf.

[163] A. Carriero, E.A. Zimmermann, A. Paluszny, S.Y. Tang, H. Bale, B. Busse, T. Alliston, G. Kazakia, R.O. Ritchie, S.J. Shefelbine, How tough is brittle bone? Investigating osteogenesis imperfecta in mouse bone, J. Bone Miner. Res. 29 (2014) 1392–1401. doi:10.1002/jbmr.2172.

[164] E.A. Zimmermann, B. Busse, R.O. Ritchie, The fracture mechanics of human bone: influence of disease and treatment, Bonekey Rep. 4 (2015). doi:10.1038/bonekey.2015.112.

[165] R. Oftadeh, M. Perez-Viloria, J.C. Villa-Camacho, A. Vaziri, A. Nazarian, Biomechanics and Mechanobiology of Trabecular Bone: A Review, J. Biomech. Eng. 137 (2015) 010802. doi:10.1115/1.4029176.

[166] T.M. Keaveny, E.F. Wachtel, C.M. Ford, W.C. Hayes, Differences between the tensile and compressive strengths of bovine tibial trabecular bone depend on modulus, J. Biomech. 27 (1994) 1137–1146. doi:10.1016/0021-9290(94)90054-X.

[167] T. Hildebrand, A. Laib, R. Müller, J. Dequeker, P. Rüegsegger, Direct Three-Dimensional Morphometric Analysis of Human Cancellous Bone: Microstructural Data from Spine, Femur, Iliac Crest, and Calcaneus, J. Bone Miner. Res. (2006). doi:10.1359/jbmr.1999.14.7.1167.

[168] T.M. Keaveny, T.P. Pinilla, R.P. Crawford, D.L. Kopperdahl, A. Lou, Systematic and random errors in compression testing of trabecular bone, J. Orthop. Res. 15 (1997) 101–110. doi:10.1002/jor.1100150115.

[169] M.J. Ciarelli, S.A. Goldstein, J.L. Kuhn, D.D. Cody, M.B. Brown, Evaluation of orthogonal mechanical properties and density of human trabecular bone from the major metaphyseal regions with materials testing and computed tomography, J. Orthop. Res. 9 (1991) 674–682. doi:10.1002/jor.1100090507.

[170] P.K. Zysset, R.W. Goulet, S.J. Hollister, A Global Relationship Between Trabecular Bone Morphology and Homogenized Elastic Properties, J. Biomech. Eng. 120 (1998) 640. doi:10.1115/1.2834756.

[171] G. Yang, J. Kabel, B. Van Rietbergen, A. Odgaard, R. Huiskes, S.C. Cowin, Anisotropic Hooke's law for cancellous bone and wood, J. Elast. 53 (1998) 125–146. doi:10.1023/A:1007575322693.

[172] J.P.P. Saers, Y. Cazorla-Bak, C.N. Shaw, J.T. Stock, T.M. Ryan, Trabecular bone structural variation throughout the human lower limb, J. Hum. Evol. 97 (2016) 97–108. doi:10.1016/j.jhevol.2016.05.012.

[173] A. Odgaard, J. Kabel, B. van Rietbergen, M. Dalstra, R. Huiskes, Fabric and Elastic Principal Directions of Cancellous Related, J. Biomech. 30 (1997) 487–495.

[174] J.S. Day, M. Ding, J.C. Van der Linden, I. Hvid, D.R. Summer, H. Weinans, A decreased subchondral trabecular bone tissue elastic modulus is associated with pre-arthritic cartilage damage, J. Orthop. Res. 19 (2001) 914–918. doi:10.1016/S0736-0266(01)00012-2.

[175] X. Banse, J.P. Devogelaer, E. Munting, C. Delloye, O. Cornu, M. Grynpas, Inhomogeneity of human vertebral cancellous bone: Systematic density and structure patterns inside the vertebral body, Bone. 28 (2001) 563–571. doi:10.1016/S8756-3282(01)00425-2.

[176] D.S. Weaver, Skeletal tissue mechanics, 2000. doi:10.1002/1096-8644(200007)112:3<435::aid-ajpa12>3.3.co;2-z.

[177] E.F. Morgan, H.H. Bayraktar, T.M. Keaveny, Trabecular bone modulus-density relationships depend on anatomic site, J. Biomech. 36 (2003) 897–904. doi:10.1016/S0021-9290(03)00071-X.

[178] A.M. Torres, J.B. Matheny, T.M. Keaveny, D. Taylor, C.M. Rimnac, C.J. Hernandez, Material heterogeneity in cancellous bone promotes deformation recovery after mechanical failure, Proc. Natl. Acad. Sci. 113 (2016) 2892–2897. doi:10.1073/pnas.1520539113.

[179] R. Jungmann, M.E. Szabo, G. Schitter, R. Yue-Sing Tang, D. Vashishth, P.K. Hansma, P.J. Thurner, Local strain and damage mapping in single trabeculae during three-point bending tests, J. Mech. Behav. Biomed. Mater. 4 (2011) 523–534. doi:10.1016/j.jmbbm.2010.12.009.

[180] E.F. Morgan, O.C. Yeh, T.M. Keaveny, Damage in trabecular bone at small strains, Eur. J. Morphol. 42 (2005) 13–21. doi:10.1080/09243860500095273.

[181] F.M. Lambers, A.R. Bouman, E. V. Tkachenko, T.M. Keaveny, C.J. Hernandez, The effects of tensile-compressive loading mode and microarchitecture on microdamage in human vertebral cancellous bone, J. Biomech. 47 (2014) 3605–3612. doi:10.1016/j.jbiomech.2014.10.011.

[182] T.L.A. Moore, L.J. Gibson, Fatigue Microdamage in Bovine Trabecular Bone, J. Biomech. Eng. 125 (2004) 769. doi:10.1115/1.1631584.

[183] R. Carretta, B. Luisier, D. Bernoulli, E. Stüssi, R. Müller, S. Lorenzetti, Novel method to analyze post-yield mechanical properties at trabecular bone tissue level, J. Mech. Behav. Biomed. Mater. 20 (2013) 6–18. doi:10.1016/j.jmbbm.2012.12.003.

[184] J.Y. Rho, R.B. Ashman, C.H. Turner, Young's modulus of trabecular and cortical bone material: Ultrasonic and microtensile measurements, J. Biomech. 26 (1993) 111–119. doi:10.1016/0021-9290(93)90042-D.

[185] C.H. Turner, J. Rho, Y. Takano, T.Y. Tsui, G.M. Pharr, The elastic properties of trabecular and cortical bone tissues are similar: Results from two microscopic measurement techniques, J. Biomech. 32 (1999) 437–441. doi:10.1016/S0021-9290(98)00177-8.

[186] D.J. Hunter, L. Gerstenfeld, G. Bishop, A.D. David, Z.D. Mason, T.A. Einhorn, R.A. Maciewicz, P. Newham, M. Foster, S. Jackson, E.F. Morgan, Bone marrow lesions from osteoarthritis knees are characterized by sclerotic bone that is less well mineralized, Arthritis Res. Ther. 11 (2009) 1–9. doi:10.1186/ar2601.

[187] L. Grassi, S.P. Väänänen, S.A. Yavari, J.S. Jurvelin, H. Weinans, M. Ristinmaa, A.A. Zadpoor, H. Isaksson, Full-field strain measurement during mechanical testing of the human femur at physiologically relevant strain rates, J. Biomech. Eng. 136 (2014) 1–8. doi:10.1115/1.4028415.

[188] B.K. Bay, T.S. Smith, D.P. Fyhrie, M. Saad, Digital volume correlation: Three-dimensional strain mapping using x-ray tomography, Exp. Mech. 39 (1999) 217–226. doi:10.1007/BF02323555.

[189] C. Franck, S. Hong, S.A. Maskarinec, D.A. Tirrell, G. Ravichandran, Three-dimensional full-field measurements of large deformations in soft materials using confocal microscopy and digital volume correlation, Exp. Mech. 47 (2007) 427–438. doi:10.1007/s11340-007-9037-9.

[190] A. Benoit, S. Guérard, B. Gillet, G. Guillot, F. Hild, D. Mitton, J.N. Périé, S. Roux, 3D analysis from micro-MRI during in situ compression on cancellous bone, J. Biomech. 42 (2009) 2381–2386. doi:10.1016/j.jbiomech.2009.06.034.

[191] S.E. Basler, T.L. Mueller, D. Christen, A.J. Wirth, R. Müller, G.H. van Lenthe, Towards validation of computational analyses of peri-implant displacements by means of experimentally obtained displacement maps, Comput. Methods Biomech. Biomed. Engin. 14 (2011) 165–174. doi:10.1080/10255842.2010.537263.

[192] J. Fu, F. Pierron, P.D. Ruiz, Elastic stiffness characterization using three-dimensional full-field deformation obtained with optical coherence tomography and digital volume correlation, J. Biomed. Opt. 17 (2012) 1–7. doi:10.1117/1.JBO.

[193] F. Comini, M. Palanca, L. Cristofolini, E. Dall'Ara, Uncertainties of synchrotron microCT-based digital volume correlation bone strain measurements under simulated deformation, J. Biomech. 86 (2019) 232–237. doi:10.1016/j.jbiomech.2019.01.041.

[194] R. Zauel, Y.N. Yeni, B.K. Bay, X.N. Dong, D.P. Fyhrie, Comparison of the linear finite element prediction of deformation and strain of human cancellous bone to 3D digital volume correlation measurements, J. Biomech. Eng. 128 (2006) 1–6. doi:10.1115/1.2146001.

[195] L. Liu, E.F. Morgan, Accuracy and precision of digital volume correlation in quantifying displacements and strains in trabecular bone, J. Biomech. 40 (2007) 3516–3520. doi:10.1016/j.jbiomech.2007.04.019.

[196] T.S. Smith, B.K. Bay, M.M. Rashid, of Freedom during Minimization L , y, Methods. 42 (2002).

[197] E. Verhulp, B. Van Rietbergen, R. Huiskes, A three-dimensional digital image correlation technique for strain measurements in microstructures, J. Biomech. 37 (2004) 1313–1320. doi:10.1016/j.jbiomech.2003.12.036.

[198] M. Peña-Fernández, A.H. Barber, G.W. Blunn, G. Tozzi, Optimization of digital volume correlation computation in SR-microCT images of trabecular bone and bone-biomaterial systems, J. Microsc. 272 (2018) 213–228. doi:10.1111/jmi.12745.

[199] B.K. Bay, Methods and applications of digital volume correlation, J. Strain Anal. Eng. Des. 43 (2008) 745–760. doi:10.1243/03093247JSA436.

[200] I. Jandejsek, O. Jiroušek, D. Vavřík, Precise strain measurement in complex materials using digital volumetric correlation and time lapse micro-CT data, Procedia Eng. 10 (2011) 1730–1735. doi:10.1016/j.proeng.2011.04.288.

[201] M. Palanca, A.J. Bodey, M. Giorgi, M. Viceconti, D. Lacroix, L. Cristofolini, E. Dall'Ara, Local displacement and strain uncertainties in different bone types by digital volume correlation of synchrotron microtomograms, J. Biomech. 58 (2017) 27–36. doi:10.1016/j.jbiomech.2017.04.007.

[202] M. Palanca, G. Tozzi, L. Cristofolini, The use of digital image correlation in the biomechanical area: A review, Int. Biomech. 3 (2016) 1–21. doi:10.1080/23335432.2015.1117395.

[203] M. Palanca, G. Tozzi, L. Cristofolini, M. Viceconti, E. Dall'Ara, Three-Dimensional Local Measurements of Bone Strain and Displacement: Comparison of Three Digital Volume Correlation Approaches, J. Biomech. Eng. 137 (2015) 071006. doi:10.1115/1.4030174.

[204] D. Christen, A. Levchuk, S. Schori, P. Schneider, S.K. Boyd, R. Müller, Deformable image registration and 3D strain mapping for the quantitative assessment of cortical bone microdamage, J. Mech. Behav. Biomed. Mater. 8 (2012) 184–193. doi:10.1016/j.jmbbm.2011.12.009.

Effect of radiation-induced damage of trabecular bone tissue evaluated using microindentation and digital volume correlation

Aikaterina Karali[1], Enrico Dall'Ara[2], Jurgita Zekonyte[1], Alexander P. Kao[1], Gordon Blunn[3], Gianluca Tozzi[1]

[1]School of Mechanical and Design Engineering, University of Portsmouth, Portsmouth, UK

[2]Departement of Oncology and Metabolism and Insigneo institute for in silico medicine, Sheffield, UK

[3]School of Pharmacy and Biomedical Sciences, University of Portsmouth, UK

Keywords: Microindentation, Digital Volume Correlation (DVC), tissue irradiation, X-ray computed tomography (XCT), trabecular bone.

Abstract

Exposure to X-ray radiation for an extended amount of time can cause damage to the bone tissue and therefore affect its mechanical properties. Specifically, high-resolution X-ray Computed Tomography (XCT), in both synchrotron and lab-based systems, has been employed extensively for evaluating bone micro-to-nano architecture. However, to date, it is still unclear how long exposures to X-ray radiation affect the bone, particularly in relation to lab-XCT systems. Microindentation has been widely used to identify local mechanical properties such as hardness and elastic modulus of bone and other biological tissues, often in combination with XCT imaging. The purpose of this study is therefore to use microindentation and XCT-based investigative tools such as digital volume correlation (DVC) to assess the microdamage induced by long exposure of trabecular bone tissue to X-ray radiation and how this affects its local mechanical properties. Trabecular bone specimens were indented before and after X-ray exposures of 33 and 66 hours, where variation of elastic modulus was evaluated at every stage. The resulting elastic modulus was affected by the irradiation displaying a decrease in the specimens with crack formation after the first long X-ray exposure and an increase in the ones with crack formation after the second exposure. High strain concentration from DVC was also present around the damaged tissue largely exceeding 10000 με. The outcomes of this study show the importance of designing appropriate XCT-based experiments also in lab systems to avoid degradation of the bone tissue mechanical properties due to irradiation and will help to inform future studies that may require long X-ray exposure for in situ experiments or generation of reliable subject-specific computational models.

Introduction

Bone is an anisotropic, heterogeneous material, with hierarchical structure [1–6]. In order to evaluate the mechanical behaviour of bone, the hierarchical relationship in its material structures at the different length scales needs to be understood [7,8]. The microstructural properties of bone determine its macrostructural behaviour [4,9], therefore it is important to study its mechanical properties at the micro level.

The mechanical properties at tissue level are not affected by shape, size, and porosity of the bone [10,11]. Thus, microindentation testing is proven an effective way of evaluating bone tissue properties (elastic modulus and hardness). Microindentation has been used extensively in the last few decades to characterise trabecular bone in axial, longitudinal and transverse directions [3,12–14]. Moreover, it has been combined with a variety of techniques to better inform computational models [1,15,16] and enhance the understanding of the relation between microscopic and macroscopic bone properties [17].

More specifically, X-ray computed tomography (XCT) and indentation have been integrated at different scales (nano and micro) to characterise the bone morphology and mechanical properties. In 2003 Hengsberger et al., estimated the local anisotropic elastic constants of cortical bone using synchrotron X-ray computed tomography (SR-XCT) to calculate the porosity prior to obtaining the apparent longitudinal modulus via nanoindentation [3]. Different regions of the same samples were used for nanoindentation and imaging, to ensure that mechanical properties of the tissue were not compromised by the radiation. Furthermore, Harrison et al. (2008) proposed an approach of finite element (FE) modelling trabecular bone by determining the heterogenity of the tissue modulus aquired from nanoindentation and matching it with the heterogenity in the grey levels of lab-based XCT scans [18]. They used different parts of the same sample, similar to Hengsberger et al. (2003). In their case, the specimens were sliced in two parts prior to the procedure, one part was used for the nanoindentation and the other for the imaging, so as not to compromise the mechanical intergrity of the tissue. More recently, Lowe et al., (2018) performed an in situ high-resolution XCT microindentation in dried mouse femoral head, using a lab-XCT system, to visualise and track plastic deformation and crack propagation; an experiment that lasted 52 hours [19]. Conventional lab-based XCTs use polychromatic x-ray cone beam, whereas sychroton CTs use monochromatic parallel beam. That means that the radiation of sychrotron systems is more aggressive compare to conventional XCTs, that have limited amount of photons [20]. However, to optimise the quality of a lab-based XCT high-resolution scan a higher signal-to-noise ratio (SNR) is need, and thus the acquisition time is increased. This leads to an increasing of the irradiation in the tissue that negatively affects its

mechanical properties [21]. The radiation affects the collagen network resulting in a cross-linking reaction that degrades the structural integrity of the collagen fibres [22].

High-resolution XCT has been also combined with in situ mechanical testing (4D evaluations) and employed to study bone micromechanical properties and behaviour [23,24]. In these studies, the deformation induced by compression was analysed using digital volume correlation (DVC). DVC is a three-dimensional technique where the full-field strain distribution is derived on the measured displacement field, which is computed based on the differential variation of grey level intensity for XCT images of the material undergoing in situ step-wise loading. The technique and its principles are widely documented in literature [24–26]. DVC analysis has been improving through the years, becoming more accurate in computing the strain distribution in deformed bone at both apparent and tissue level [26–30]; thus, providing enough confidence in its use to evaluate initiation and development of microdamage in the tissue due to mechanical and/or other factors. Recently, Peña-Fernández et al. (2018a) assessed the influence of the radiation dose on the trabecular bone tissue by variating the exposure times within a SR-XCT system [31]. It was noticed that highly irradiated specimens developed more microcracks within the tissue. Another study [32] retained the bone tissue integrity by performing in situ SR-XCT, while controlling the temperature at 23˚C and 0˚C. It was observed that the decrease in the temperature promoted tissue preservation, as there were no visilbe microcracks. This was due to the reduction of the cross-linking reactions, of highly reactive oxygen free radicals produced by high-energy X-ray radiation, within the collagen fibres. The advantage of the temperature reduction was also seen in the DVC analysis of the specimens, where at 0˚C the strain levels were lower.

However, to the best of the authors knowledge an assessment of how XCT radiation in a lab-system can promote bone tissue degradation and how this is linked to potential variation of local mechanical properties has not been proposed yet. Therefore, the aim of this study is to evaluate trabecular bone tissue damage induced by X-ray irradiation by combining microindentation and high-resolution XCT, using DVC to confirm the increased strain levels corresponding to microdamage (i.e. formation of microcracks) induced in the trabeculae by prolonged X-ray exposure.

Materials and Methods

A schematic diagram with detailed description of the experimental protocol is given in Fig.1.

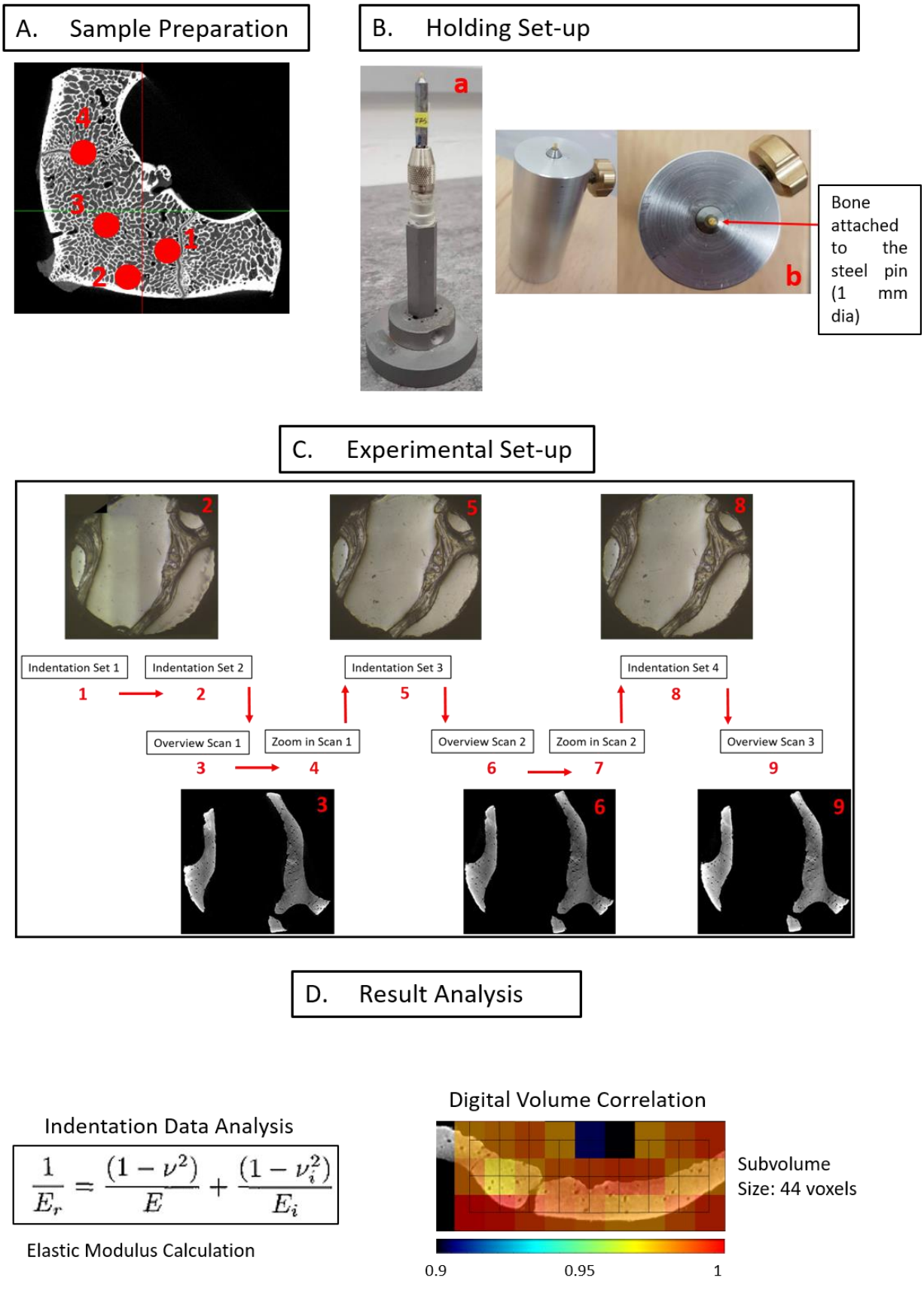

Figure 1: A. Bone plugs (D= 3mm) extracted from the anterior part of the vertebral body in positions indicated by the red dots (n=1 in position 1, n=2 in position 2, n=1 in position 3 and n=1 in position 4). B. Holding setup for the (a) XCT system and (b) microindenter. **C**. Experimental testing outline guided by red arrows for step sequence. The first indentation set was performed on D= 3mm samples, then the sample diameter was reduced to 1 mm for the remaining tests. Indentation location (1,2,5,8) and XCT details of trabeculae after each indentation set (3,6,9) are also shown. **D**. (a) Oliver-Pharr elastic modulus formula was using the indentation data of the trabecular bone, (b) DVC analysis performed on the XCT images.

Sample Preparation

Slices of bone in 5 mm height were cut using a diamond band saw (Exact GmbH, Germany) under constant irrigation from three porcine lumbar vertebrae. Seven bone plugs, of 3 mm diameter, were cored from different locations within the slices along the axial direction (Fig.1A). The specimens (S1-S7) were dried at room temperature overnight, then, they were embedded in epoxy resin (Epofix, Struers, Denmark) and polished with progressive grades of sandpapers and Alumina paste using distilled water as a lubricant [33].

Microindentation Settings

Indentations were performed in dry condition on the embedded and polished samples using a NanoTest Platform 3 (Micro Materials, UK) nanoindenter, using a Berkovich tip. To maintain the consistency between the NanoTest Platmorm and the subsequent XCT scanning, a mounting set up was designed where the sample was fixed onto a steel pin (Fig.1B). Depth control indentation mode was chosen, with the maximum depth set at 2.5 µm [34]. To minimise the creep effect, a 30s holding time was introduced between the loading and unloading stage. Both the loading and unloading rate was set at 0.8 mN/s [34]. Although a nanoindenter instrument was used, this indentation is defined as microindentation due to the micron size of the indents. The elastic moduli were calculated using the Oliver and Pharr method [35], considering a local isotropy poison's ratio of 0.3 [18]. All the indents closer to the edges of the trabeculae were discarted from the analysis.

X-ray Computed Tomography imaging

At defined indentation steps, as reported in Fig. 1C, the samples were XCT imaged (Versa 510, Zeiss, USA). As shown in Table 1 the overview scan was performed at 1.86 µm of voxel size, which allows the whole geometry of the sample to be in the field of view (FOV) (Fig.2), whereas in the higher-resolution zoom in scan the voxel size was reduced to 0.13 µm. The images were reconstructed and each 3D dataset consisted of 991 images (984x1009 pixels, 32-bit grey levels). After conversion of the images to 8-bit, they were rigidly registered using Fiji (ImageJ 1.52p, USA) and cropped to parallelepipeds in the center of the specimens. To reduce the noise in the images a mean filter was applied. At last, to reduce artifacts from the epoxy surrounding the trabeculae the datasets were segmented by introducing a zero-intensity value in the epoxy voxels [27,32].

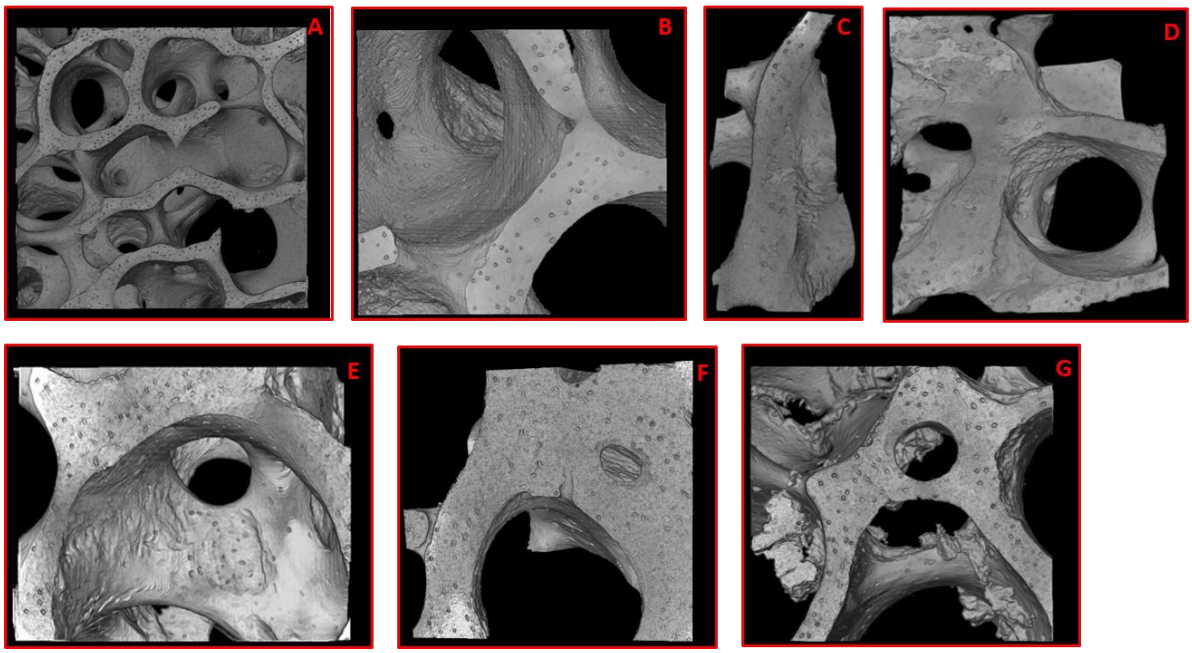

Figure 2: XCT images showing the indentation sites, (A): D = 3 mm mechanics control sample (S1), (B): D = 1 mm imaging control sample (S2), (C-E) D = 1 mm samples following the main experimental protocol S3-7. All samples showed no visible damage after the first image acquisition (h_3).

Experimental Protocol

Prior to the XCT imaging, to evaluate the effect the X-ray radiation had on the tissue, the first indentation set was executed. The diameter of each sample was 3 mm, an average number of 30 indents was performed in specific locations identified using the integrated optical microscope inside the nanoindenter. The three following indentation sets on the same samples, where the diameter was reduced by means of milling to 1 mm, consisted of 3 indents each; keeping a minimum distance of 20 µm from previous indents [9,33]. The diameter of the samples was reduced to facilitate the high-resolution XCT imaging. The specimens were exposed to radiation for several hours (h_x, *x* represents the number of hours), depending on the acquisition time of the tomograms. The first overview scan, to visualise the trabecular microstructure at and underneath the indentation site, was done after the 2nd indentation set (h_3), directly followed by a higher-resolution scan on a single indent location (h_{33}). Similarly, to examine the effect of exposure to radiation in the trabeculae, a 2nd pair of scans was executed after the 3rd indentation set (h_{66}). The final overview scan was taken to fully appreciate the effect the radiation has on the trabeculae (h_{69}).

The first sample (S1) was tested as control for the mechanics. Overview scans were obtained and the sample was indented after each overview tomogram to assess the effect of h_3, h_6 and h_9 irradiation on the mechanical properties of the tissue. Initially, its diameter was 10 mm due to the epoxy

surrounding the bone. The epoxy was then removed by means of milling after the first indentation set and the diameter remained 3 mm throughout the rest of the process (Fig.3), to allow a larger number of indentations in each set.

The temperature was monitored, to ensure no cracks were forming due to expansion or contraction. A thermocouple was attached onto a sample aligned with the X-ray beam and an overview and high-resolution scan were acquired. It should be noted that the tomograms from these scans were not used for the analysis, only the temperature readings were of interest.

Furthermore, indentations were randomly placed on the epoxy surrounding the trabeculae on S3, S5 and S7 throughout the protocol to calculate the effect of radiation on the epoxy.

Digital Volume Correlation

DVC on the XCT images (sequential overview scans) was computed using sum of differential correlation with a multi-pass processing, 74 to 44 voxels of subvolume size (DaVis 10.0.5, LaVison, Göttingen, Germany). The error uncertainty was calculated using two approaches complimentary to each other. Overview scans for a 1 mm sample (S2) were obtained sequentially without the high-resolution scans and removing the sample form the XCT microscope for indentation. These tomograms were used to compute the error uncertainty as well as the strain induced by radiation at h_9. The second approach was by virtually translating the 1st overal scan images 10 pixels in each direction [26,27]. This method was applied to the rest of the 1 mm sampled in order not to add additional repeated scans and therefore inducing more exposure to X-rays. The correlation coefficient was filtered at 0.9 and a geometric mask used to reduce the error uncertainty. The 1st, 3rd principal strains (ε_{p1}, ε_{p3}) and the maximum shear strain (γ_{max}) were computed to evaluate the radiation damage.

Table 1: XCT scanning specifications used in this study for overview and higher-resolution imaging

	Overview Scan	**Higher-resolution Zoom in Scan**
Objective	4X	40X
Binning	2	1
kVolt/Watt	60/5	80/7
Filter	Air	Air
Projections	2001	2101
Exposure time (s)	1.5	46
Pixel size (µm)	1.86	0.13

Results

The elastic modulus of the S1, which had not been exposed to the high-resolution zoom in scan irradiation, showed a similar median throughout the four different indentation sets (Fig 3.B). The median/SD E in the first step resulted in 15.8 ± 1.8 GPa and after the 6 hours of exposure to radiation it was 14.19 ± 2.1 GPa. In fact, also observing the indents individually, there was no increase in the elastic modulus locally (Fig 3. A). Furthermore, by observation of the three overview scans there were no visible cracks.

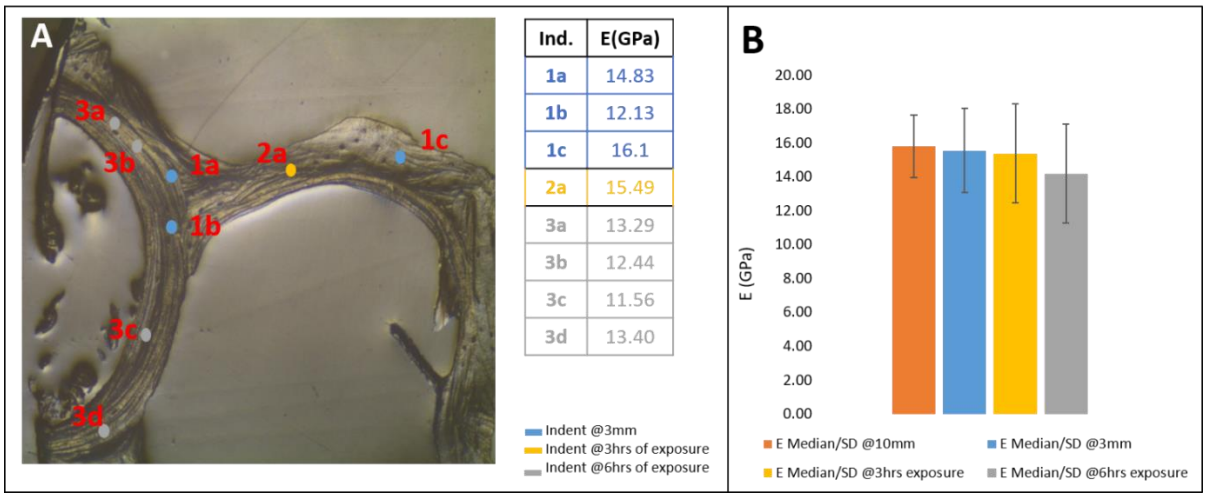

Figure 3: Mechanics control sample indentation (S1): (A) Trabeculae under optical microscope, with different sets of indents identified and coloured respectively (blue: indents at h_0 when specimen diameter was D = 3 mm, yellow: indents after h_3 and D= 3 mm grey: indents after h_6 and D= 3 mm). (B) Median/SD of elastic modulus of indentation sets (orange: median when specimen diameter was D= 10 mm, blue: median when specimen diameter was D = 3 mm, yellow: median after h_3 and D= 3 mm, grey: median after h_6 and D= 3 mm).

The samples which were exposed up to 69 hours to radiation during the scanning showed a change in the elastic modulus. As seen in Figure 4B, the median/SD of the elastic modulus at the initial state of the sample (33 indents) (D=3 mm) was 10.74 ±1.85 GPa, which reached after h_{66} a maximum value of 16.33 GPa. S4 (Fig. 5A) showed a decrease in the moduli. More specifically, the median/SD of the first indentation set (30 indents at h_0) was 14.24±2.69 GPa. The maximum indent elastic moduli value in the last set (6 indents at h_{66}) was 7.99 GPa and the minimum 4.88 GPa. Similarly, the median/SD elastic modulus of S5 (Fig. 5B) in the initial set (26 indents at h_0) was 14.26 ±2.48 GPa and at the last indentation set, the maximum value of elastic modulus decreased to 7.39 GPa (3 indents at h_{66}). The bone structure in S6 (Fig. 5C) allowed a larger number of indents in the first and last sets, 42 and 5 respectively. The median/SD of the initial set was 14.89 ± 2.26 GPa and in the last set it reached a maximum value of 24.48 GPa. In S7 (Fig. 5D) the median/SD of the first set (36 indents at h_0) was 14.79 ±2.93 GPa and the maximum elastic moduli value in the last set (4 indents at h_{66}) was 22.34 GPa.

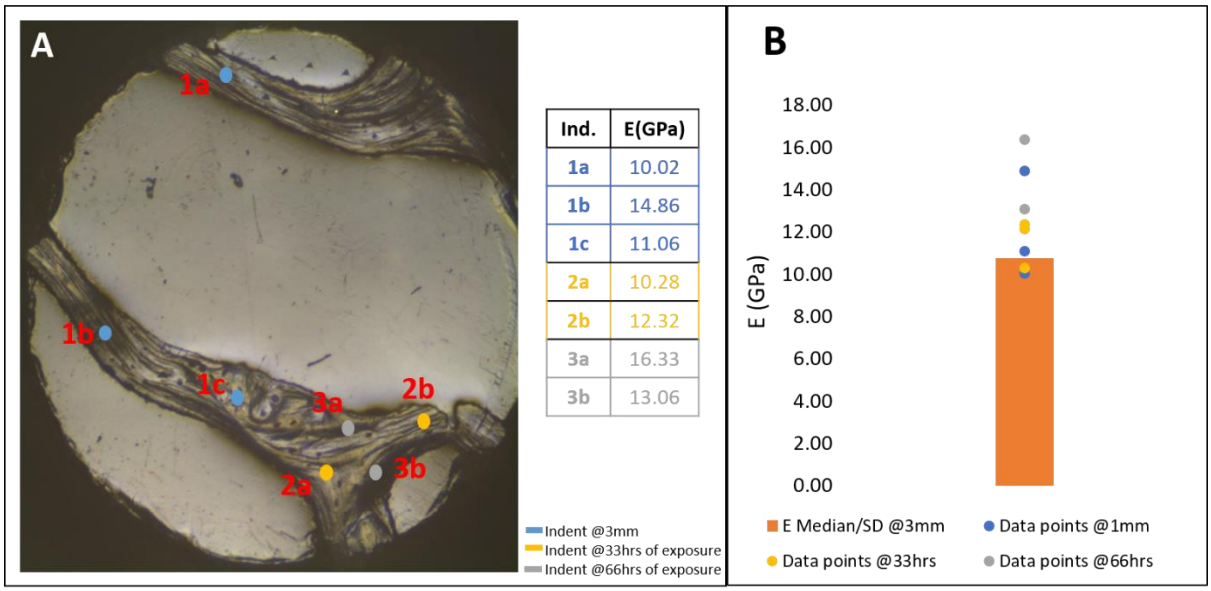

Figure 4: S3: (A) Trabeculae under optical microscope, with different sets of indents identified and coloured respectively (blue: indents at h_0 when specimen diameter was D = 1 mm, yellow: indents after h_{33} and D = 1 mm, grey: indents after h_{66} and D = 1 mm). (B) Median/SD of elastic modulus of trabeculae at h_0 (orange) and elastic modulus of each indent for the following indentation sets at increasing exposure to X-ray radiation (blue: h_0 and D = 1 mm, yellow: h_{33} and D = 1 mm, grey: h_{66} and D = 1 mm).

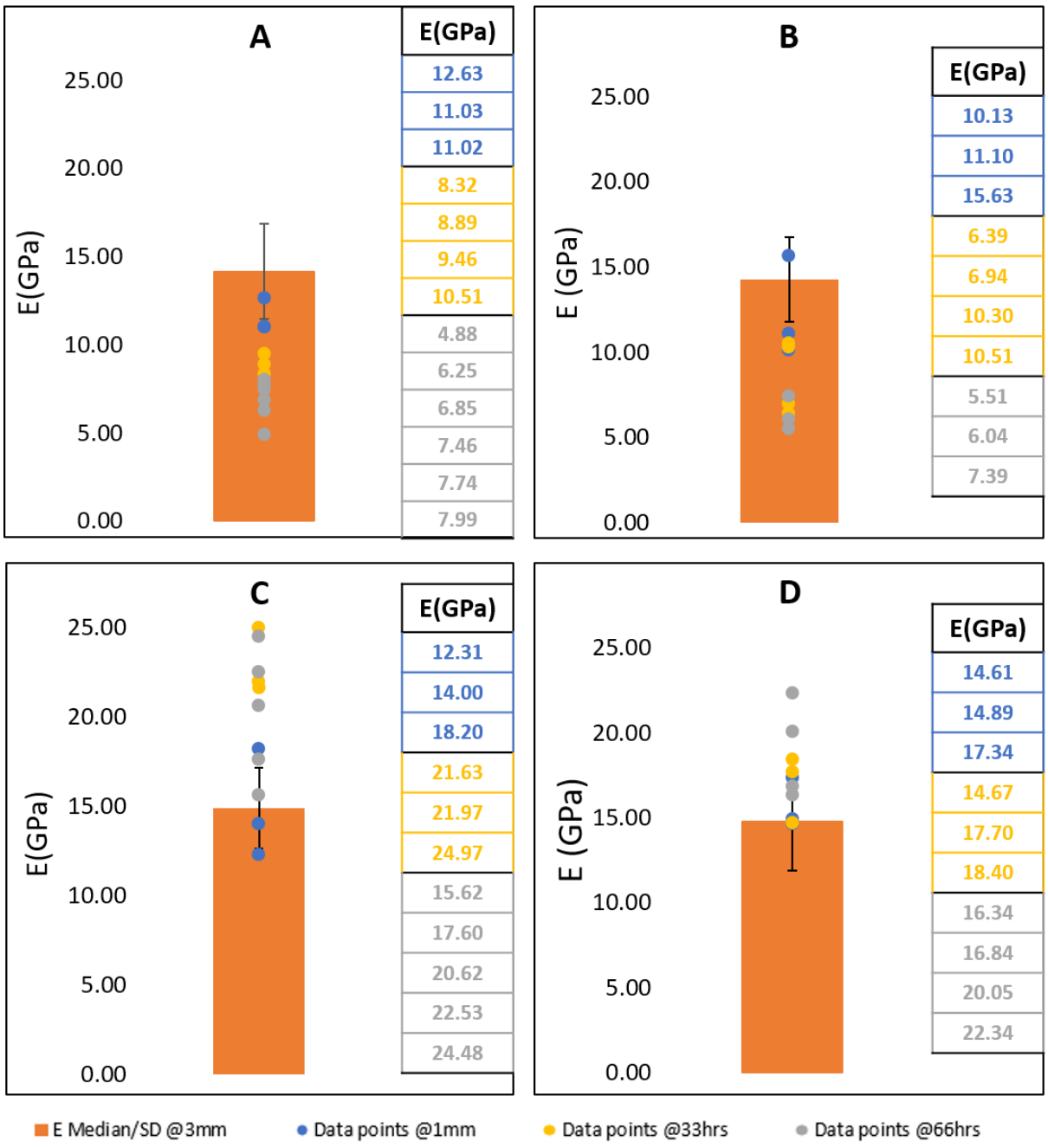

Figure 5*:* Median/SD elastic modulus at zero exposure to radiation (orange) and elastic modulus of each indent of the following indentation sets at increasing exposure to X-ray radiation stating their values for the remaining samples (A) S4, (B) S5, (C) S6 and (D) S7.

DVC was used to assess the strain induced on the tissue at increasing levels of X-ray exposure. The analysis on S4 for the 3rd principal strain (ε_{p3}) showed higher values around the areas where cracks were formed at h_{36}, which were even further damaged at h_{69} (Fig. 6A). Similar pattern appeared for the max shear strain (γ_{max}). The strain initially reached 10000 με around the cracks, approaching 20000 με at h_{69} in the same area without further crack opening (Fig. 6B).

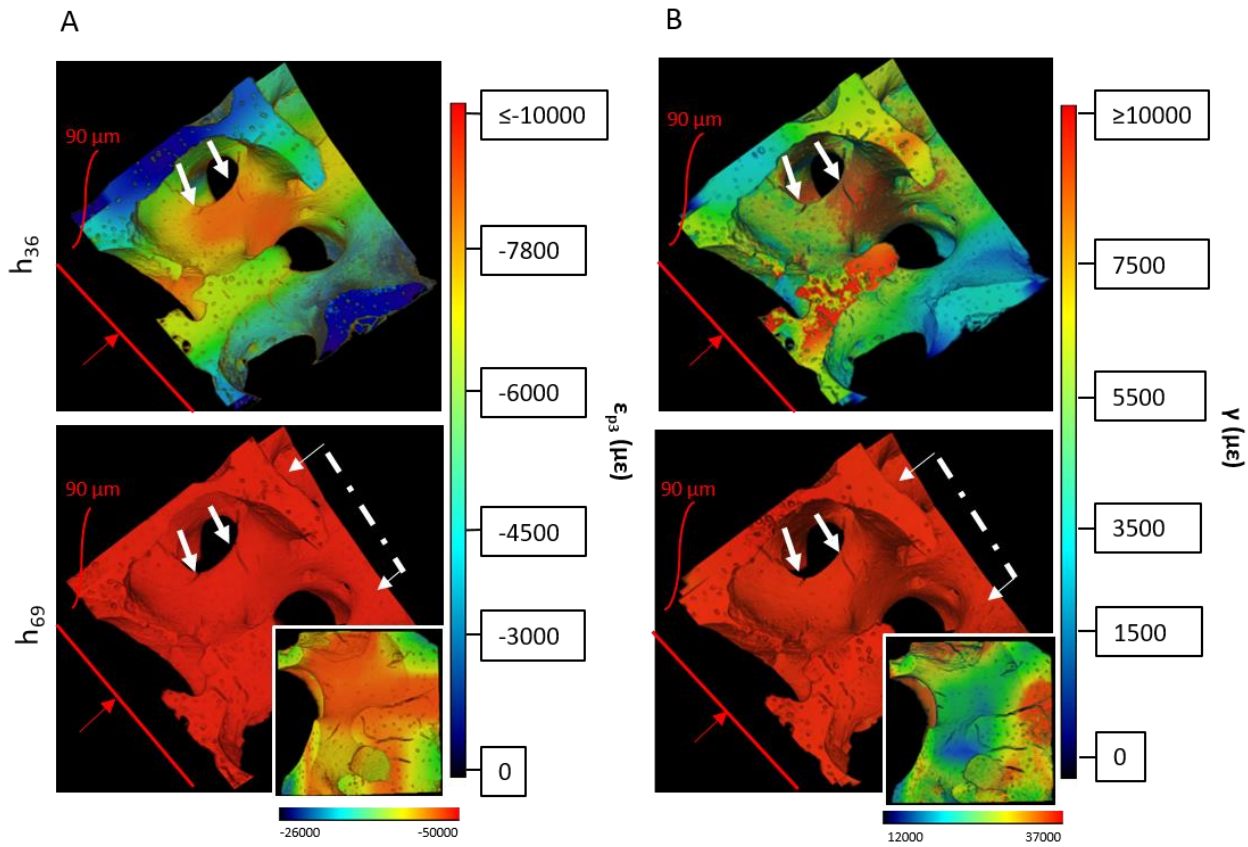

Figure 6: DVC analysis of S4, where red line identifies the indentation plane and red arrow direction (90 μm apart from the represented volume). A) 3rd principal strain (ε_{p3}) at h_{36} and h_{69} reaching ~-8000 με at areas of crack formation (white arrows) and exceeding -10000 με throughout the volume, respectively. b) maximum shear strain (γ_{max}) at the same time points, reaching strains over 30000 με around the cracks (white arrows) after h_{69}. Maximum strain distribution around cracks at h_{69} for cross section are reported at the bottom right corner.

S5 was the sample with the largest crack formation; at h_{69} the 3rd principal strain (ε_{p3}) in the trabeculae exceeds absolute strains of 10000 με (Fig. 7A). An increase of strain between the h_{36} and h_{69} also occurred regarding the max shear strain (γ_{max}), which exceeded 10000 με at the last stage (Fig. 7B).

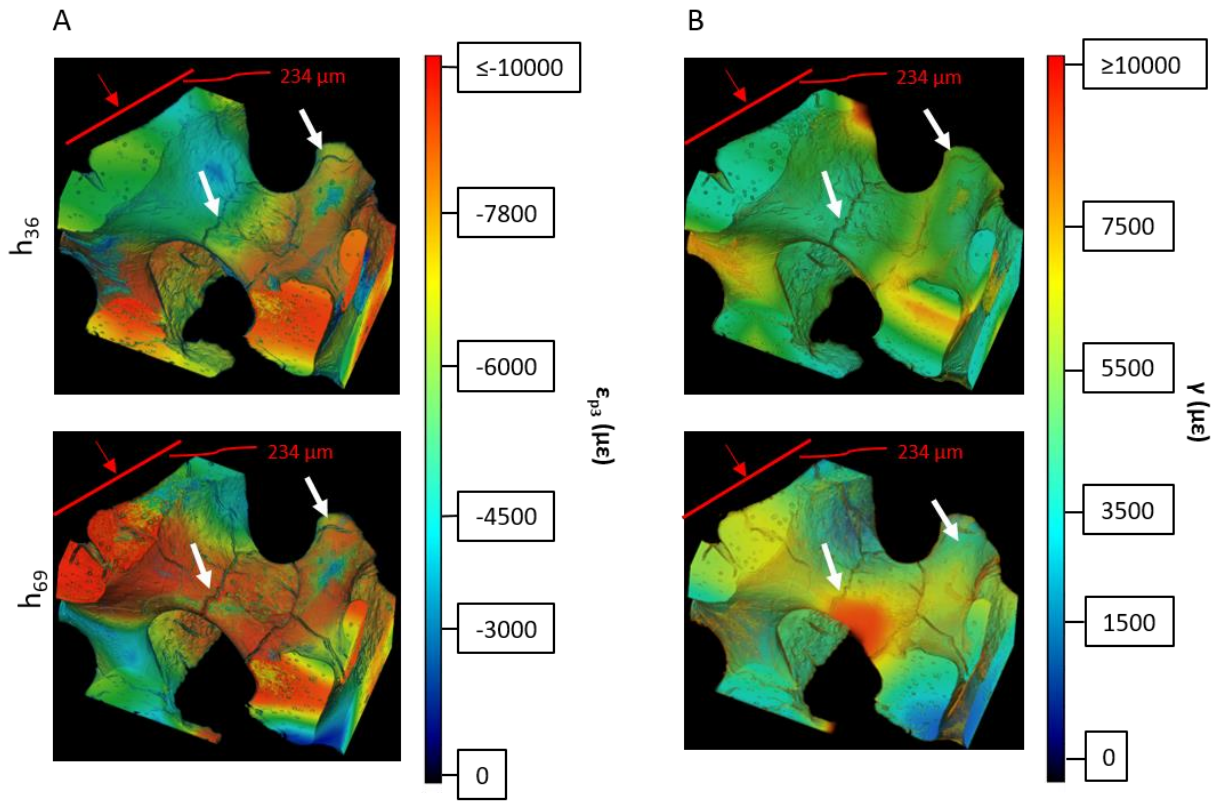

Figure 7*:* DVC analysis of S5, where red line identifies the indentation plane and red arrow direction (234 µm apart from represented the volume). A) 3rd principal strain (ε_{p3}) at 36 and 69 hours of exposure to radiation reaching ~-8000 µε at areas of crack formation (white arrows) and exceeding -10000 µε at crack propagation, respectively. B) maximum shear strain (γ_{max}) at the same time points, reaching ~5500 µε around the cracks (white arrows) at 36 hours and approaching ~9000 µε after 69 hours.

Crack formation is also visible in the higher-resolution zoom in XCT of the trabecular bone. Particularly, in S3 cracks are forming at h_{66} (Fig. 8B), starting from the edges of the tissue propagating to the centre. In S4 however, there is crack formation from the first zoom in scan (Fig.8C). As seen in Fig.8C one of the cracks is starting gradually from the edge of the trabecula and at h_{66} it reaches the closest lacuna opening further (Fig.8D). Whereas the second crack is starting from a lacuna in the middle of the structure at h_{33} propagating towards the boarders at h_{66}.

In addition to the XCT image acquisition, the temperature was monitored during the imaging and it was noticed that, in the overview scan (h_3) the temperature increased by 2˚C and remained at the same level through the zoom in scan (h_{33}).

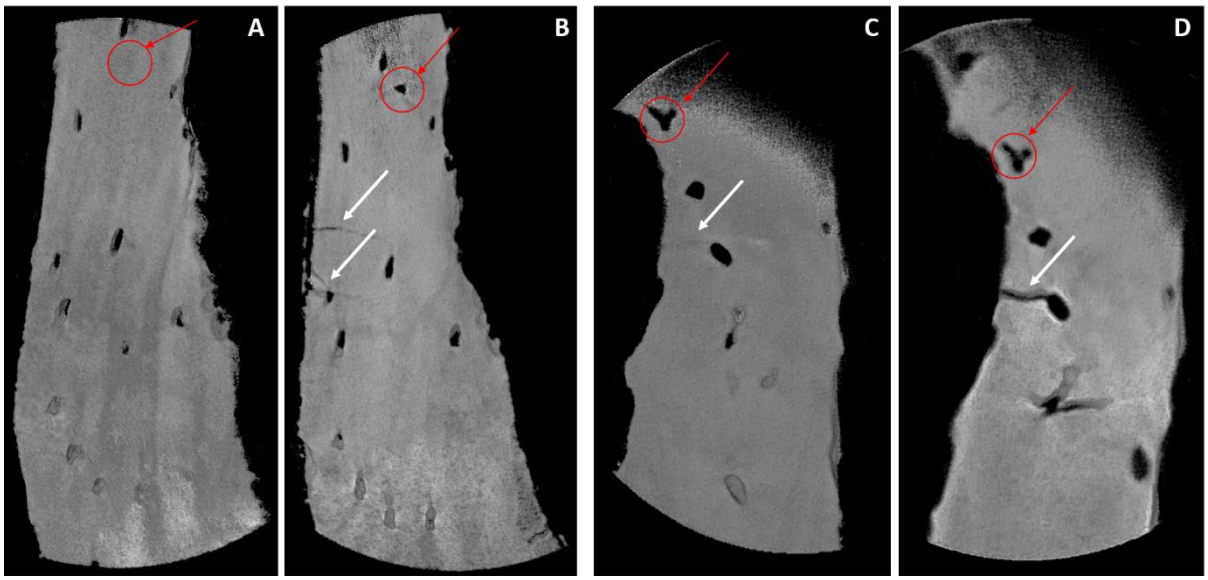

Figure 8: High-resolution Zoom in Scans (0.18 µm pixel size) of S3 (A, B) and S4 (C, D) at h_{33} and h_{66}; (A, B): the indent was applied in the 3rd indentation set and crack formation appeared after h_{33}. (C, D): the indent was applied in the 1st indentation set and crack formation started at h_{33}, propagating further at h_{66}; red arrows pointing at indentation imprint on the surface of the bone, white arrows showing cracks due to irradiation

Discussion

The aim of the present study was to investigate the effect of high-resolution XCT radiation on the trabecular tissue at the micro level. High-resolution XCT has been extensively used to assess the microstructure of trabecular bone [36–38]. However, to investigate features in the micro/ nano-scale, such as the imprints of indentation to potentially extract important and more localised mechanical properties of bone tissue (i.e. via DVC), high-resolution and long exposure scans are required [19,39]. In fact, the long exposure to radiation is known to affect the mechanical properties of the tissue [21,40], as exposure time in XCT imaging is directly related to the quality of the imaging and thus this impacts on the signal-to-noise ratio (SNR) and therefore on the overall quality of the image [20].

In this study, microindentation was performed to assess the bone tissue mechanical properties throughout the indentation process. In addition, high-resolution XCT imaging was employed to visualise the region of indentation and the internal volume underneath the individual indents for subsequent DVC analysis.

The average elastic modulus obtained from all the specimens at h_0 was 14.5 ± 3.11 GPa, which is in line with values reported in literature for dry vertebral trabecular bone, 15.4 ± 1 GPa [1] and 13.4 ± 2 GPa [41]. The difference in the two can be attributed to the nature of the bone; porcine and human, as well as the fact that in the first study they used both thoracic and lumbar vertebrae.

It was observed that (Fig.5), after the first long exposure scan (h_{33}), there is a change in the mechanical properties of approximately 2 GPa, which can also be attributed to the bone anisotropy [6]. However,

after 69 hours of scanning, the effect of the radiation is more distinct. In S3, S6 and S7 there is an increase in elastic modulus, indicating that the tissue has become stiffer and more brittle. This is even more apparent when comparing individual values of neighbouring indents at h_0 and h_{66} as shown in Fig.4. Specifically, 1c and 3a in Fig. 4A (indents at h_0 and h_{66} respectively), which are 140 μm away from each other; have a 5.24 GPa difference in the individual calculated elastic modulus. In S6 at h_0 and specimen diameter 3 mm, there were two indents with elastic modulus 19.11 and 18.87 GPa at a 80 μm distance. In the middle of these two at a 30 μm distance two consequent indents were placed at h_{33} with elastic moduli of 21.63 and 21.97 respectively (Fig.5C). This shows a distinct increase of approx. 2GPa even after the first high-resolution zoom in scan. This trend, however, does not seem to correspond to all the samples, since S4 and S5 displayed a decrease in the elastic modulus (≈ 4 GPa) (Fig.5 A, B). In fact in S5, the indent with modulus 10.13 GPa (h_0) (Fig.5B) has a 30 μm distance from indent with modulus 7.39 GPa (h_{66}) in the middle of the same trabecula. Dall'Ara et al.(2012) reported how severe damage due to compressive deformation (ranging from 12-53%) in the trabeculae reduced the indentation moduli and therefore elastic modulus by 55%. To such extent, the high-resolution zoom in tomograms of the tissue showed details in the structure of the trabeculae with clear microdamage formation that was not visible in the overview tomograms due to the larger voxel size. The timing of the microcrack formation might be directly related to the elastic modulus measurements from the microindentation data. In S3 the cracks start forming at h_{66} where the modulus is increased, making the tissue stiffer. Whereas in S4, the cracks form at h_{33} and at h_{66} the modulus is decreased leading to tissue failure as previously observed.

From the overview scans it was observed that crack formation occurred in all the samples after the first long exposure followed by crack propagation in the second one (Figs.6,7). At h_{36}, the tissue experienced strain (ε_{p1}, γ_{max}) exceeding 5000 με, with microcracks formation. After that, the microcracks propagate further, surpassing 10000 με (ε_{p1}, γ_{max}). This trend of increasing strain is consistent to the one reported in Peña-Fernández et al. (2018b), where the tissue was exposed to synchrotron X-ray (SR-XCT) radiation. In that case, ε_{p1} reached 1500 με after the second scanned and it increased to 5000 με after the fifth one. However, bone specimens of that study [30] were exposed for approximately 80 min to the radiation of the monochromatic pink beam, whereas here they were exposed (polychromatic X-ray) for 69 hours. Also, the hydration status of the tissue might also affect the strain and microcrack accumulation, since in the current study the specimens were embedded in epoxy resin and kept dehydrated throughout the procedure. However, the irradiation difference cannot be assessed with certainty since the dose of radiation could not be computed in this study, as the information needed for the dose estimation could not be disclosed by the lab-XCT manufacturer. The dose of radiation in a laboratory-based XCT system depends on the energy, the pixel size, detector

filter, exposure time and number of projections [43]. Particularly, in higher-resolution scans where bone morphological measurement are need, an increased dose is required [44]. An experiment performed on mice hindlimb with an XCT tomogram in vivo of 19 min total scan duration, showed trabecular bone loss with total radiation 776 mGy [45]. In a different study it was observed that the trabecular bone volume of mice was reduced after irradiation of 712 mGy almost weekly (1, 2, 3 and 5 weeks) [46]. At last, single radiation doses of 15-20 Gy at the abdomen of mice led to femoral and tibial bone mass loss 7 days post-irradiation [47]. The mechanical properties degradation in trabecular bone specimens, due to irradiation, has been assessed in a SR-XCT system before [30]. At 32.9 kGy radiation dose the apparent bone volume decreased and the strain, obtain through DVC, increased compared to the specimens irradiated at 4.7 kGy [30].

The strain distribution in the overview tomograms (DVC control, S2) did not exceed 2000 με for ε_{p1} and γ_{max} and -1800 μm for ε_{p3}, values that are associated to physiological loads in trabecular bone [11,29]. Thus, It is assumed that 9 hours of exposure to radiation did not lead to crack initiation and degradation of the mechanical properties.

The initiation of microcracks from the edges of the trabeculae could be either a result of the effect of the X-ray radiation to the mechanical properties of the bone, or the epoxy surrounding the tissue. In this sense, the radiation-thermal effects on mechanical properties of epoxy film polymer have been previously investigated [48] for samples exposed to different rates of X-ray radiation, ranging from 0 to 300 kGy. The Young's modulus of the epoxy at zero exposure was 4.84 MPa, it reached 5.86 MPa at 100 kGy and 5.34 MPa at 300 kGy. At higher irradiation dose, the mechanical properties decreased due to the polymer chain scission reactions. In the case of the current study, the elastic modulus of the epoxy resin surrounding the bone was measured throughout the process and showed no significant difference during all the stages of the protocol, with a median of 3.8 ± 0.038 GPa. It can be therefore assumed that the movement of the polymer chains remained relatively the same, since it has been shown that an increase in the movement accounts for decrease in the modulus. Hence, the cracks forming in the lacunae (Fig.8) should be attributed to the radiation and not the potential contraction or expansion of the epoxy resin.

This study has a number of limitations. The number of indents obtained after the specimen diameter was reduced at 1 mm was limited due to the tissue surface available. Therefore, in order to generalise the findings, the protocol should be implemented on a larger number of specimens in the future. Furthermore, the signal-to-noise ratio (SNR) in the high-resolution zoom in scans was not adequate to achieve an accurate DVC analysis of the specimens. High-resolution scans using SR-XCT provide a

better SNR, making it easier to track changes in the volume but at a higher flux and increased tissue damage [30].

Conclusions

In conclusion, this study presents an experimental approach to evaluate the degradation in the trabecular bone mechanical properties due to X-ray irradiation combining microindentation and XCT imaging. Specimens that exhibited crack formation from the first high-resolution zoom in scan experienced a decrease in the elastic modulus that can be related to severe tissue damage. Conversely, specimens with crack formation at a later stage displayed an increase in the elastic modulus. The DVC analysis in all the specimens shows higher strain accumulation as the exposure time is increased, with peak values in correspondence to the cracks. The findings of this study can be used to inform experimental protocols in the future, to avoid damage of the tissue due to irradiation in long XCT-based experiments.

Acknowledgments

The authors would like to acknowledge Mr Geoff Britton for his assistance with the sample preparation and experimental set up, Dr Dave Hollis (LaVision Ltd) for advice on DVC computation and Ms Yordana Shopova for proofreading the manuscript. The Insigneo Institute (University of Sheffield) provided the equipment for the sample preparation. The Zeiss Global Centre (University of Portsmouth) provided XCT imaging and DVC capability to conduct this study. Nanoindentation equipment provided by School of Mechanical and Design Engineering (University of Portsmouth). This study is part of a PhD programme funded by the Faculty of Technology (University of Portsmouth).

References

[1] U. Wolfram, H.J. Wilke, P.K. Zysset, Valid μ finite element models of vertebral trabecular bone can be obtained using tissue properties measured with nanoindentation under wet conditions, J. Biomech. 43 (2010) 1731–1737. doi:10.1016/j.jbiomech.2010.02.026.

[2] G. Franzoso, P.K. Zysset, Elastic Anisotropy of Human Cortical Bone Secondary Osteons Measured by Nanoindentation, J. Biomech. Eng. 131 (2008) 021001. doi:10.1115/1.3005162.

[3] S. Hengsberger, J. Enstroem, F. Peyrin, P. Zysset, How is the indentation modulus of bone tissue related to its macroscopic elastic response? A validation study., J. Biomech. 36 (2003) 1503–9. doi:10.1016/S0021-9290(03)00131-3.

[4] R. Oftadeh, M. Perez-Viloria, J.C. Villa-Camacho, A. Vaziri, A. Nazarian, Biomechanics and Mechanobiology of Trabecular Bone: A Review, J. Biomech. Eng. 137 (2015) 010802. doi:10.1115/1.4029176.

[5] J.G. Swadener, J.Y. Rho, G.M. Pharr, Effect of anisotropy on elastic moduli measured by nanoindentation in human tibial cortical bone, J. Biomed. Mater. Res. 57 (2001) 108–112. doi:10.1002/1097-4636(200110)57:1<108::AID-JBM1148>3.0.CO;2-6.

[6] P.K. Zysset, A review of morphology-elasticity relationships in human trabecular bone: Theories and experiments, J. Biomech. 36 (2003) 1469–1485. doi:10.1016/S0021-9290(03)00128-3.

[7] R. Jae-young, L. Kuhn-Spearing, P. Zioupos, Mechanical Properties and the hierarchical structure of bone, Med. Eng. Phys. 20 (1998) 92–102. doi:10.1038/251673a0.

[8] J.A. Buckwalter, M.J. Glimcher, R.R. Cooper, R. Recker, Bone Biology, (1995) 1256–1275.

[9] U. Wolfram, H.-J. WILKE, P.K. ZYSSET, Transverse Isotropic Elastic Properties of Vertebral Trabecular Bone Matrix Measured Using Microindentation Under Dry Conditions (Effects of Age, Gender, and Vertebral Level), J. Mech. Med. Biol. 10 (2010) 139–150. doi:10.1142/s0219519410003241.

[10] N. Rodriguez-Florez, M.L. Oyen, S.J. Shefelbine, Insight into differences in nanoindentation properties of bone, J. Mech. Behav. Biomed. Mater. 18 (2013) 90–99. doi:10.1016/j.jmbbm.2012.11.005.

[11] H.B. Hunt, E. Donnelly, Bone Quality Assessment Techniques: Geometric, Compositional, and Mechanical Characterization from Macroscale to Nanoscale, Clin. Rev. Bone Miner. Metab. 14 (2016) 133–149. doi:10.1007/s12018-016-9222-4.

[12] P.K. Zysset, X. Edward Guo, C. Edward Hoffler, K.E. Moore, S.A. Goldstein, Elastic modulus and hardness of cortical and trabecular bone lamellae measured by nanoindentation in the human femur, J. Biomech. 32 (1999) 1005–1012. doi:10.1016/S0021-9290(99)00111-6.

[13] C.E. Hoffler, K.E. Moore, K. Kozloff, P.K. Zysset, M.B. Brown, S.A. Goldstein, Heterogeneity of bone lamellar-level elastic moduli., Bone. 26 (2000) 603–9. http://www.ncbi.nlm.nih.gov/pubmed/10831932.

[14] P.K. Zysset, Indentation of bone tissue: a short review, Osteoporos. Int. 20 (2009) 1049–1055. doi:10.1007/s00198-009-0854-9.

[15] R. Lucchini, D. Carnelli, M. Ponzoni, E. Bertarelli, D. Gastaldi, P. Vena, Role of damage mechanics in nanoindentation of lamellar bone at multiple sizes: Experiments and numerical modeling, J. Mech. Behav. Biomed. Mater. 4 (2011) 1852–1863. doi:10.1016/j.jmbbm.2011.06.002.

[16] J. Zhang, M.M. Michalenko, E. Kuhl, T.C. Ovaert, Characterization of indentation response and stiffness reduction of bone using a continuum damage model, J. Mech. Behav. Biomed. Mater. 3 (2010) 189–202. doi:10.1016/j.jmbbm.2009.08.001.

[17] M.J. Mirzaali, J.J. Schwiedrzik, S. Thaiwichai, J.P. Best, J. Michler, P.K. Zysset, U. Wolfram, Mechanical properties of cortical bone and their relationships with age, gender, composition and microindentation properties in the elderly, Bone. 93 (2016) 196–211. doi:10.1016/j.bone.2015.11.018.

[18] N.M. Harrison, P.F. McDonnell, D.C. O'Mahoney, O.D. Kennedy, F.J. O'Brien, P.E. McHugh, Heterogeneous linear elastic trabecular bone modelling using micro-CT attenuation data and experimentally measured heterogeneous tissue properties, J. Biomech. 41 (2008) 2589–2596. doi:10.1016/j.jbiomech.2008.05.014.

[19] T. Lowe, E. Avcu, E. Bousser, W. Sellers, P.J. Withers, 3D Imaging of indentation damage in bone, Materials (Basel). 11 (2018) 1–13. doi:10.3390/ma11122533.

[20] C. Chappard, A. Basillais, L. Benhamou, A. Bonassie, B. Brunet-Imbault, N. Bonnet, F. Peyrin, Comparison of synchrotron radiation and conventional x-ray microcomputed tomography for assessing trabecular bone microarchitecture of human femoral heads, Med. Phys. 33 (2006) 3568–3577. doi:10.1118/1.2256069.

[21] O. Akkus, R.M. Belaney, P. Das, Free radical scavenging alleviates the biomechanical impairment of gamma radiation sterilized bone tissue, J. Orthop. Res. 23 (2005) 838–845. doi:10.1016/j.orthres.2005.01.007.

[22] H.D. Barth, E.A. Zimmermann, E. Schaible, S.Y. Tang, T. Alliston, R.O. Ritchie, Characterization of the effects of x-ray irradiation on the hierarchical structure and mechanical properties of human cortical bone, Biomaterials. 32 (2011) 8892–8904. doi:10.1016/j.biomaterials.2011.08.013.

[23] G. Tozzi, Q.H. Zhang, J. Tong, Microdamage assessment of bone-cement interfaces under monotonic and cyclic compression, J. Biomech. 47 (2014) 3466–3474. doi:10.1016/j.jbiomech.2014.09.012.

[24] G. Tozzi, V. Danesi, M. Palanca, L. Cristofolini, Elastic Full-Field Strain Analysis and Microdamage Progression in the Vertebral Body from Digital Volume Correlation, Strain. 52 (2016) 446–455. doi:10.1111/str.12202.

[25] B.K. Bay, T.S. Smith, D.P. Fyhrie, M. Saad, Digital volume correlation: Three-dimensional strain mapping using x-ray tomography, Exp. Mech. 39 (1999) 217–226. doi:10.1007/BF02323555.

[26] G. Tozzi, E. Dall'Ara, M. Palanca, M. Curto, F. Innocente, L. Cristofolini, Strain uncertainties from two digital volume correlation approaches in prophylactically augmented vertebrae: Local analysis on bone and cement-bone microstructures, J. Mech. Behav. Biomed. Mater. 67 (2017) 117–126. doi:10.1016/j.jmbbm.2016.12.006.

[27] M. Palanca, G. Tozzi, L. Cristofolini, M. Viceconti, E. Dall'Ara, Three-Dimensional Local Measurements of Bone Strain and Displacement: Comparison of Three Digital Volume Correlation Approaches, J. Biomech. Eng. 137 (2015) 071006. doi:10.1115/1.4030174.

[28] M. Palanca, L. Cristofolini, E. Dall'Ara, M. Curto, F. Innocente, V. Danesi, G. Tozzi, Digital volume correlation can be used to estimate local strains in natural and augmented vertebrae: An organ-level study, J. Biomech. 49 (2016) 3882–3890. doi:10.1016/j.jbiomech.2016.10.018.

[29] M. Palanca, A.J. Bodey, M. Giorgi, M. Viceconti, D. Lacroix, L. Cristofolini, E. Dall'Ara, Local displacement and strain uncertainties in different bone types by digital volume correlation of synchrotron microtomograms, J. Biomech. 58 (2017) 27–36. doi:10.1016/j.jbiomech.2017.04.007.

[30] M. Peña-Fernández, S. Cipiccia, E. Dall'Ara, A.J. Bodey, R. Parwani, M. Pani, G.W. Blunn, A.H. Barber, G. Tozzi, Effect of SR-microCT radiation on the mechanical integrity of trabecular bone using in situ mechanical testing and digital volume correlation., J. Mech. Behav. Biomed. Mater. 88 (2018) 109–119. doi:10.1016/j.jmbbm.2018.08.012.

[31] M. Peña-Fernández, A.H. Barber, G.W. Blunn, G. Tozzi, Optimization of digital volume correlation computation in SR-microCT images of trabecular bone and bone-biomaterial systems, J. Microsc. 272 (2018) 213–228. doi:10.1111/jmi.12745.

[32] M. Peña-Fernández, E. Dall'Ara, A.P. Kao, A.J. Bodey, A. Karali, G.W. Blunn, A.H. Barber, G. Tozzi, Preservation of bone tissue integrity with temperature control for in situ SR-MicroCT experiments, Materials (Basel). 11 (2018). doi:10.3390/ma11112155.

[33] E. Dall'Ara, C. Karl, G. Mazza, G. Franzoso, P. Vena, M. Pretterklieber, D. Pahr, P. Zysset, Tissue properties of the human vertebral body sub-structures evaluated by means of microindentation, J. Mech. Behav. Biomed. Mater. 25 (2013) 23–32. doi:10.1016/j.jmbbm.2013.04.020.

[34] U. Wolfram, H.J. Wilke, P.K. Zysset, Rehydration of vertebral trabecular bone: Influences on its anisotropy, its stiffness and the indentation work with a view to age, gender and vertebral level, Bone. 46 (2010) 348–354. doi:10.1016/j.bone.2009.09.035.

[35] W.C. Oliver, G.M. Pharr, Measurement of hardness and elastic modulus by instrumented indentation: Advances in understanding and refinements to methodology, J. Mater. Res. 19 (2004) 3–20. doi:10.1557/jmr.2004.19.1.3.

[36] F. Levrero-Florencio, L. Margetts, E. Sales, S. Xie, K. Manda, P. Pankaj, Evaluating the macroscopic yield behaviour of trabecular bone using a nonlinear homogenisation approach, J. Mech. Behav. Biomed. Mater. 61 (2016) 384–396. doi:10.1016/j.jmbbm.2016.04.008.

[37] S. Judex, S. Boyd, Y.X. Qin, L. Miller, R. Müller, C. Rubin, Combining high-resolution micro-computed tomography with material composition to define the quality of bone tissue., Curr. Osteoporos. Rep. 1 (2003) 11–19. doi:10.1007/s11914-003-0003-x.

[38] F. Gillard, R. Boardman, M. Mavrogordato, D. Hollis, I. Sinclair, F. Pierron, M. Browne, The application of digital volume correlation (DVC) to study the microstructural behaviour of trabecular bone during compression, J. Mech. Behav. Biomed. Mater. 29 (2014) 480–499. doi:10.1016/j.jmbbm.2013.09.014.

[39] M. Peña Fernández, E. Dall'Ara, A.J. Bodey, R. Parwani, A.H. Barber, G.W. Blunn, G. Tozzi, Full-Field Strain Analysis of Bone-Biomaterial Systems Produced by the Implantation of Osteoregenerative Biomaterials in an Ovine Model, ACS Biomater. Sci. Eng. 5 (2019) 2543–2554. doi:10.1021/acsbiomaterials.8b01044.

[40] H.D. Barth, M.E. Launey, A.A. MacDowell, J.W. Ager, R.O. Ritchie, On the effect of X-ray irradiation on the deformation and fracture behavior of human cortical bone, Bone. 46 (2010) 1475–1485. doi:10.1016/j.bone.2010.02.025.

[41] M.E. Roy, J.Y. Rho, T.Y. Tsui, N.D. Evans, G.M. Pharr, Mechanical and morphological variation of the human lumbar vertebral cortical and trabecular bone, J. Biomed. Mater. Res. 44 (1999) 191–197. doi:10.1002/(SICI)1097-4636(199902)44:2<191::AID-JBM9>3.0.CO;2-G.

[42] E. Dall'Ara, R. Schmidt, P. Zysset, Microindentation can discriminate between damaged and intact human bone tissue, Bone. 50 (2012) 925–929. doi:10.1016/j.bone.2012.01.002.

[43] J.A. Meganck, B. Liu, Dosimetry in Micro-computed Tomography: a Review of the Measurement Methods, Impacts, and Characterization of the Quantum GX Imaging System, Mol. Imaging Biol. 19 (2017) 499–511. doi:10.1007/s11307-016-1026-x.

[44] L. Arentsen, S. Hui, Characterization of rotating gantry micro-CT configuration for the in vivo evaluation of murine trabecular bone, Microsc. Microanal. 19 (2013) 907–913. doi:10.1017/S1431927613001396.

[45] K. Laperre, M. Depypere, N. van Gastel, S. Torrekens, K. Moermans, R. Bogaerts, F. Maes, G. Carmeliet, Development of micro-CT protocols for in vivo follow-up of mouse bone architecture without major radiation side effects, Bone. 49 (2011) 613–622. doi:10.1016/j.bone.2011.06.031.

[46] R.J. Klinck, G.M. Campbell, S.K. Boyd, Radiation effects on bone architecture in mice and rats resulting from in vivo micro-computed tomography scanning, Med. Eng. Phys. 30 (2008) 888–895. doi:10.1016/j.medengphy.2007.11.004.

[47] D. Jia, D. Gaddy, L.J. Suva, P.M. Corry, Rapid Loss of Bone Mass and Strength in Mice after Abdominal Irradiation, Radiat. Res. 176 (2011) 624–635. doi:10.1667/rr2505.1.

[48] A.T. Nguyen, P.M. Visakh, O.B. Nazarenko, C.S. Chandran, T. V. Melnikoca, Effect of electron beam irradiation on thermal and mechanical properties of epoxy polymer, Conf. Ser. Mater. Sci. Eng. 168 (2017) 1–7. doi:10.1088/1757-899X/168/1/012073.

Mechanical and morphometric evaluation of cortical bone through in situ XCT indentation

Aikaterina Karali[1], Alexander P. Kao[1], Jurgita Zekonyte[1], Gordon Blunn[2], Gianluca Tozzi[1]

[1]School of Mechanical and Design Engineering, University of Portsmouth, Portsmouth, UK

[2]School of Pharmacy and Biomedical Sciences, University of Portsmouth, UK

Keywords: Digital Volume Correlation (DVC), X-ray computed tomography (XCT), in situ mechanics, indentation, cortical bone microstructure.

Abstract

Cortical bone structure is hierarchical and therefore its mechanical behaviour depends on its microstructural properties. X-ray computed tomography (XCT) has been widely used to identify the microstructural properties of the cortical tissue (i.e. pore network, Haversian and Volkmann's canals). However, the connection between the microstructural properties and the cortical bone behaviour during plastic deformation is unclear. Hence, the purpose of this study is to investigate the behaviour of the canal network in cortical bone specimens regarding the strain induced by plastic deformation. In situ XCT indentation was used to introduce a deformation on the surface of the specimen and digital volume correlation (DVC) was employed to assess the three-dimensional (3D) full-field strain distribution in the volume. The region of the imprint was under tensile strain, whereas the volume underneath, was under compressive strain. Canal loss was displayed in region of higher compressive strains exceeding -20000 με and crack formation occurred in specimens were Haversian canals were parallel to the indentation tip. The results of this study outlined the relation between the microstructural mechanical behaviour of cortical bone to plastic deformation, providing information on cortical bone fracture initiation.

Introduction

Cortical bone is a load-bearing hard tissue with hierarchical structure from nano to macroscale [1,2]. It determines bone strength and it is an indicator of bone loss and fragility [3]. The details of its structural organisation affect macroscopic mechanical behaviour and ability to resist fracture [4]. Assessing and preventing bone fracture has been one of the predominant aims in bone research [5–9]. Fracture involves initiation and propagation of cracks to the point of failure. The ability of bone tissue to resist crack formation is vital in sustaining load without fracturing [10]. In fact, resisting fracture and sustaining microdamage involves a variety of mechanisms at different scales [11]. Its mechanical behaviour in the macroscale is affected by the stiffness in the mesoscale (millimetre-scale) [2,12]. For instance, investigation of the mesoscopic level has been useful in assessing stress and strain distribution in long bones with osteoporotic fractures [13]. Tissue porosity at the submicrometer scale in the cortical bone has been shown to cause discontinuities and affect its mechanical behaviour [14] by largely affecting its ability to resist deformation [15]. Porosity in the cortical bone refers to the canal network (i.e. Haversian and Volkmann's canals), osteocyte lacunar and canalicular system [16]. In fact, differences in the cortical porosity have been associated with increased fracture risk [17]. The microstructural properties influence fracture behaviour; either by acting as constrains in the crack propagation or defects in stress concentration [14,18–20]. This also depends on the orientation of the load. Nalla et al. (2005) [10] investigated the strain-controlled mechanism for the onset of fracture in bone. It was observed that the impact of the properties in the microstructure is more dominant in the transverse direction due to the fact that the cement lines deflect the crack along the length.

Three-dimensional analysis (3D) of the microstructure of cortical bone has been completed successfully with the use of either laboratory based or synchrotron radiation (SR) x-ray Computed Tomography (XCT) imaging providing information on the porosity of the structure [21]. Cai et al. (2019) [16] used SR-XCT to study the vascular pore and mineral content phenotypes in femoral cortical bone specimens. Moreover, micro-compression and SR-XCT have been combined to investigate the canal network under loading in femoral cortical bones [22]. Both studies concluded that the canal surfaces were acting as starting points for crack formation.

In the recent years, digital volume correlation (DVC) has been employed to compute the 3D full-field strain concentration in correspondence of bone microcracks using high-resolution XCT images [23–25]. DVC has been also used to assess the strain distribution around the intracortical canals in mice femoral bone under micro-compression during SR-XCT imaging [26]. A cross-sectional notch was introduced in the diaphysis of the femur, similar to Voide et al. (2009) [22], and the strain in two

different regions of the bone containing microcracks was computed. In all specimens cracks occurred at the canal surface and high shear and tensile strains were found it those areas.

Indentation has been extensively used to characterise bone mechanical properties at the micro- and nanoscale [27–29]. Plastic deformation due to indentation testing usually occurs when using pointed indentation tips; i.e. Vickers [30]. In fact, the plastic deformation due to the indentation is sustained by compressive and tensile strains in the whole volume rather than just the area under the indenter [31]. In that sense, in situ 3D X-ray nanoCT indentation has been recently used on an elephant tusk to investigate the relation between the plastic deformation and the microstructure [32]. Elephant dentin is an anisotropic material with hierarchical microstructure. At the mesoscale, it includes dentinal tubules that follow a wavy path. The plastic deformation resulted in crack formation that was studied regarding the tubules location. It was seen that when the tubules where parallel to the indentation tip large crack propagated towards the axial direction following the tubules orientation. Conversely, when the tubules where at 45° and 70° angle, less crack formation was observed. DVC on the volume under the indentation surface of the specimens showed the highest compressive strain in specimens with tubules at 45° and the lowest in those with 70°.

To the best of the author's knowledge, an investigation of crack initiation and propagation of cortical bone tissue due to plastic deformation via in situ XCT indentation and DVC has not been reported. Therefore, the purpose of this study was to investigate the strain distribution in the cortical bone tissue due to plastic deformation accumulated during indentation. In addition, strain distribution and microdamage initiation/progression were coupled with detailed analysis of the canal and pore network in the microstructure, both axially and transversely. A strong correlation between the strain distribution, microstructural phenotypes of crack formation and prevention was observed.

Methodology

Sample preparation

Bovine femoral bone harvested from a single animal bred and slaughtered for alimentary purposes was used in this study. The bone was cleaned and soft tissues removed using surgical tools. Cylindrical cortical bone specimens were extracted from the same region in the diaphysis of the femur (D = 4 mm, H = 6 mm), six in the transverse and six in the axial direction with respect to the long vertical axis of the bone. The specimens were cut using a diamond drill bit in a pillar drill (Pacera, Meddings Machine tools, UK) under constant water irrigation and 800 grade sandpaper was used to polish the top surface using distilled water as lubricant. Brass endcaps were used on the distal and intracortical part for both axial and transverse specimens. All specimens were kept frozen at -20°C and thawed for approximately 2 h in saline solution at room temperature before testing.

In situ Indentation and Imaging

A custom-made indentation set up was designed for the purposes of this experiment. The top plate of the XCT in situ loading stage (CT5000, Deben, UK) was adjusted to attach a Vickers' pyramidal diamond tip. A bottom cylindrical steel plate was designed to fit in the loading stage chamber with a recess in the middle to secure the sample with its end cup. The tip was fixed in the middle of the top plate aligned with the middle of the bone. Initially, the jaws of the loading stage were fully open and two consecutive XCT (Versa 510, Zeiss, USA) tomograms were taken prior to the in situ step-wise indentation to allow for DVC error analysis. After each indentation step a tomogram was acquired. The exposure time was set at 3 s/projection, 110/9 kV/W, resulting in a voxel size of 4.2 µm. The field of view (FOV) included all the specimen diameter and approximately half of its height (4.2 x 4.2 mm).

The loading stage was set in depth control and the displacement rate was 0.1 mm/min. The specimens were divided in three different groups of four, two axial and two transverse specimens in each group. In the first group (S1-2 axial, S3-4 transverse) the specimens were indented once at a displacement of 0.4 mm. The second group (S5-6 axial, S7-8 transverse) involved two indentation steps; first reaching 0.2 mm and then increasing the depth to 0.4 mm in the same location. The third group included three steps at 0.2 mm, 0.3 mm, and 0.4 mm displacement (S9-S12). These indentation stages are annotated as I_0, I_2, I_3, I_4 for 0 mm, 0.2 mm, 0.3 mm and 0.4 mm displacement, respectively.

The loading stage used here is not a conventional set up for indentation and does not automatically recognise contact with the surface of the specimen. Instead, the initial contact of the tip with the specimen was identified by the user, as the point where an increase in the force, of more than 0.3 N, occurred and the loading continued until it reached the desired displacement. Therefore, the

measurements mentioned above are not the plastic depth of indentation, rather the displacement of the loading stage actuator.

Image post-processing

The 3D datasets were obtained from the tomograms after reconstruction, at 32-bit gray levels), and all the imaging post-processing was performed using Fiji (ImageJ, USA). The images were converted to 8-bit and rigidly registered to the first scan prior to indentation. Parallelepipeds containing the whole specimen were cropped discarding images with zero grayscale value images at the top of the tomographic dataset, to be used for the DVC analysis. The artefacts and noise in the images were removed by creating a dataset specific mask. Using a plug-in (BoneJ), a purifying cycle was run in the binary images of each dataset [33]. The mask was applied by implementing an arithmetic and logical operation between the original and purified dataset.

Bone morphometry

A second set of parallelepipeds in the middle of the bone volume under the indent were cropped using Fiji (ImageJ, USA). The size of the parallelepipeds varied among the specimens due to the discrepancies in the borders of their volume (i.e. uneven edges, coarse surfaces etc.), the mean volume was 13 ± 2.27 mm^3. The binary images of the datasets were imported into Avizo 9.7.0 (ThermoFischer Scientific, USA). The void in the cortical bone volume was segmented using the wand function and the intracortical porosity, pore and canal network were determined. The canal network identifies the Haversian and Volkmann's canals. The porosity represents the percentage of pores and the canal network volume. Properties such as the number of canals (N.Ca), canal diameter (Ca.Dm), number of pores (N.Po) and pore diameter (Po.Dm) were obtained to evaluate how incremental indentation relates to changes in morphology. The statistical difference in the mean Ca.Dm and mean Po.Dm between the in situ XCT indentation stages in each sample was estimated using a non-parametric independent Kruskal-Wallis test using SPSS Statistics 25 (IBM, US).

Digital Volume Correlation

A local DVC approach was used in the cropped parallelepipeds (Davis 10.0.3, LaVision, UK). A multi-step pass processing (128 to 48 voxels/subvolume) was employed for the strain computation. The first two tomograms obtained prior to the indentation were used to calculate the error uncertainty (MAER = 700 ± 256 με, SDER = 664 ± 287 με) [34,35]. The first and third principal full-field strains (ε_{p1} and ε_{p3} respectively) were obtained.

Results

Microcracks were formed in four of the axial specimens (S1, S2, S5, and S9). The transverse samples did not show any large crack formation. In fact, in all the specimens that showed microcrack development, this started at the end of the indentation pile-up. S1 and S2 were indented in one step (I_4) whereas S6 and S9 went through two (I_2, I_4) and three (I_2, I_3, I_4) indentation steps, respectively. In all specimens, pile-up of the bone was observed and it was more dominant in the ones that showed crack formation. It was seen that microcrack initiated when the ends of the pile-up were located in close proximity to a Haversian canal, propagating further following the side of the pyramidal shaped imprint.

The effective depth of indentation was measured from the 3D images (Fig.1). The minimum effective depth was observed in S3 and S4 at 0.07 mm. The largest imprint displacement occurred in S2, at 0.19 mm, followed by S1 at 0.18 mm. Furthermore, S5 and S9 achieved 0.15 mm final depth. From the segmentation of the reversed volume in the area underneath the imprint, loss of the original canals was observed (Fig.1). In the specimens where fracture occurred, the microcrack was visible at the side of the imprint as well as distortion of the original network. Distortion was also present in those that did not crack. Specifically, as shown in Fig. 1, the network in S8 and S12 appears different. The alteration in S12 was not related to any canal loss; instead the load had a compressive affect in the horizontal canals reducing the distance between them (Fig. 1).

Specimen	Indentation Depth (mm)	Imprint Region at I_0	Imprint Region at I_4
S1	0.18	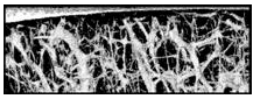	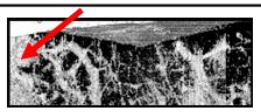
S8	0.12	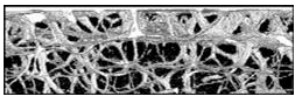	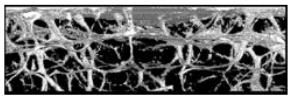
S9	0.15	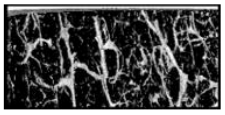	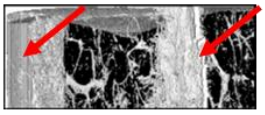
S12	0.10		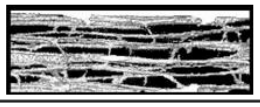

Figure 1: Representation of the canal network underneath the indentation area, before (I_0) and after the defect (I_4), showing the effective indentation depth [(S1, S9) depth (brown font) identifying the cracked axial specimens; (S8, S11): transverse specimens]. Red arrows are showing the microcracks.

The global porosity was calculated after every indentation stage. It varied among the specimens and it was observed that none of the specimens with the highest porosity values developed crack. The highest porosity was found is S12 (9%), followed by S7, S10, S3 and S8 (7.6%. 5.1%, 4.8% and 3.72% respectively). The four specimens that formed microcracks had a mean porosity value of 1.46%. The porosity in the rest of the samples ranged between 1.53% and 1.68%. S1, S2, S9 showed higher porosity values after microcrack formation. However, in S5 despite the fact that a microcrack developed at I_4, the porosity is reduced. The remaining samples displayed a general decrease, with the exception of S4 and S10. The porosity in S4 increased by 0.41% after I_4 and in S10 by 0.83% after I_2.

The distortion and microcracks were also visible in the canal network for the rest of the volume (Fig. 2). In S1 the canal network appeared to be thicker and more connections between the canals are created due to the cracking. This was also observed in the N.Ca that increased from 365 to 1531 from I_0 to I_4. The N.Po also increased in this particular sample by 445. Similarly, the porosity rise in S4 occurred due to the increase of the N.Ca by 50. The N.Ca in S5 after I_2 is halved with major N.Ca reduction at the borders of the specimen (from 696 to 320). In S9, there is both loss of canals (Fig. 2) and porosity increase after microcrack formation. The N.Ca in S9 was reduced from 403 to 395 after I4; however, the N.Po in the final stage was twice as much (183 to 458). In addition, in S10 the larger porosity in I_2 was the result of both the N.Ca increasing by 50 and the Ca.Dm widening; in an individual canal, it was seen that the diameter increased from 242 to 256 μm.

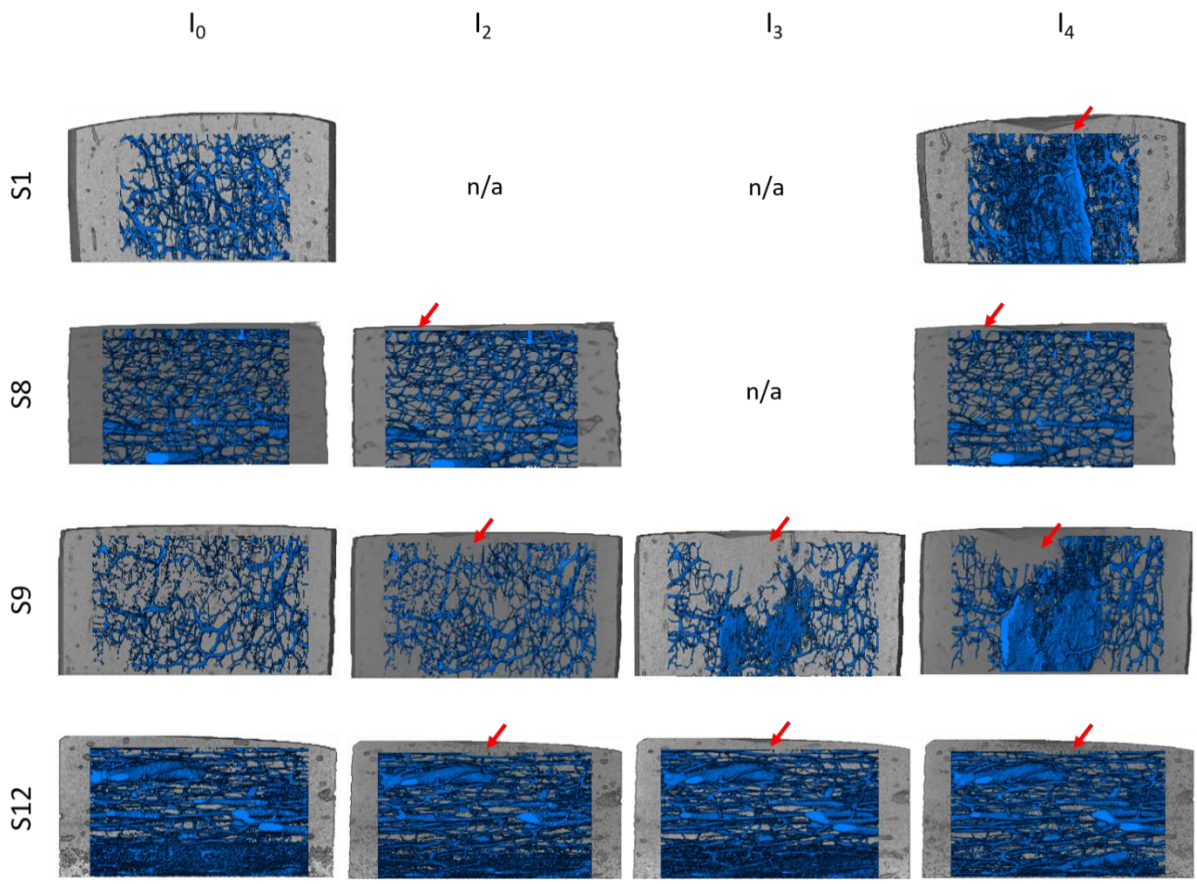

Figure 2: Illustration of the segmented canal network underneath the defect area of S1, S9 (cracked, axial specimens) and S8, S12 (transverse specimens) at the initial state I_0 and after the different stages of indentation. Microcrack formation was observed in S1 at I_4 and in S9 it initiates at I_3, propagating further at I_4. n/a: indentation stages not applicable; Red arrows are pointing at the alterations in the canal network throughout the indentation stages.

Statistical significance in the mean Ca.Dm and Po.Dm of each sample within their indentation stages was found in all the specimens that developed microcracks (Fig.3). In all the cases with fracture the mean Ca.Dm increased and mean Po.Dm decreased. Significant difference ($p < 0.0001$) in the mean Ca.Dm was also found in S12. The comparison between the mean Po.Dm however showed no significance. Conversely, statistical significance in the mean Po.Dm, but not in the mean Ca.Dm, was observed in S11.

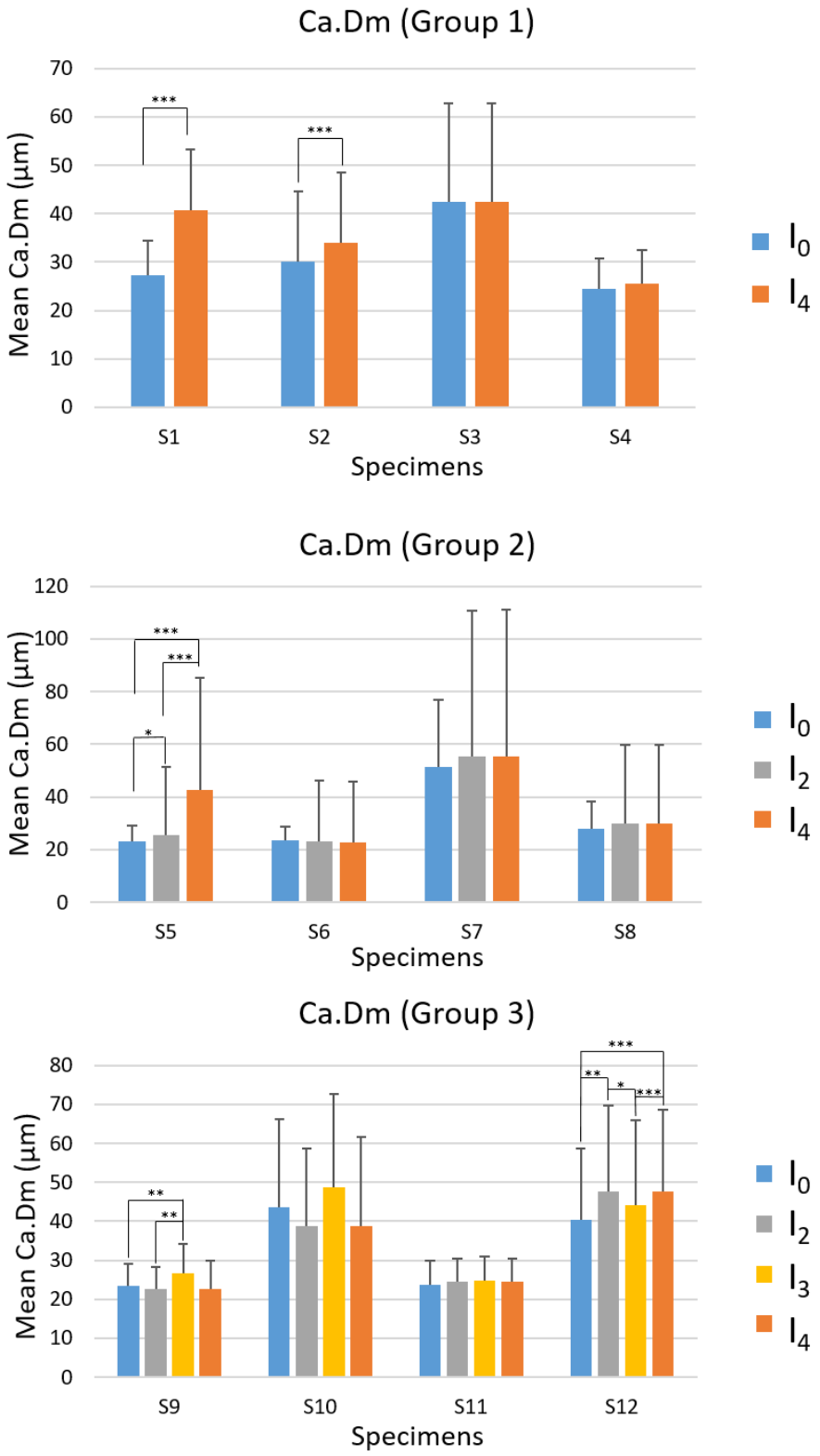

* p < 0.05, ** p < 0.001, *** p < 0.0001

Figure 3: Graphical analysis of the mean canal network diameter (Ca.Dm) of all the specimens in the different groups. Blue bar: mean Ca.Dm at I_0 prior to defect; grey bar: mean Ca.Dm at I_2 after 0.2 mm tip displacement; yellow bar: mean Ca.Dm at I_3 after 0.3 mm tip displacement; orange bar: mean Ca.Dm at I_4 after 0.4 mm tip displacement. The significant difference between the indentation stages was estimated with a Kruskal-Wallis test.

The imprint left on the bone surface after the last indentation step was approximately ¼ of its area, resulting in a global compression effect on the specimens, as shown in the strain maps (Fig.4). The ε_{p1} and ε_{p3} where computed using DVC. The strain maps showed a combination of tension and compression throughout the specimen volume. Specifically, ε_{p3} illustrated a reduced compressive strain in the region of the imprint (see also Appendix). The specimens extracted in the axial direction (S1, S2) experienced strain reaching -26000 με under and on the side of the pile-up. In the region of the microcrack formation for both these specimens the strain is locally ~-14000 με (Fig.4). In S3, compressive strain is concentrated under the indent in the middle of the volume (~-20000 με) and in the rest of the specimens remained under -4000 με. The strain map in S4 presented high compressive strains on the borders of the specimen locally of ~-26000 με; however, no microcracks were observed. In the second group only one of the two axial specimens fractured under the indentation load (S5) and only after I_4. In the first indentation (I_2), high compressive strain concentration was observed on one side of the imprint; reaching ~-26000 με locally. In I_4, microcrack is formed at the opposite side attaining ~-14000 με. The rest of the specimens extracted in transverse direction (S6-8) experienced similar values of εp_3 at I_2 not exceeding -4000 με overall, with some compressive strain concentration in the borders of their volume. At I_4, however, the strain in the axial specimen (S6) increased; compressive strain reached -28000 με around the pile-up region. Similarly to the second group, in the third one only one of the axial specimens failed (S9) (Fig.4). Both axial specimens showed similar behaviour at I_2 not surpassing overall -5000 με. The strain in S9 however, started to increase from the one side in I_3, causing microcrack formation in the opposite side after the last indent repetition (Fig.4). S10 exhibited elevated compressive strain local concentration at I_4 especially in the imprint region reaching -18000 με. The last two specimens, that were from the transverse direction, did not display any crack formation. In S11 εp_3 was increasing locally in multiple regions with the highest strain occurring in the borders (~-20000 με) during I_3. In fact, at I_4 it followed the same pattern rising overall with values adjacent to the indent of approximately -26000 με. At last, S12 showed the same strain pattern in all three indentation stages (Fig.4). There were high compressive values laterally on the one side of the specimen achieving ~-29000 με. At I_3 and I_4 there was an isolated strain concentration at the other side of the specimen and in the region of the imprint.

In the first group ε_{p1} displayed the same trend in all the specimens (see also Appendix). High strain values were distributed in the imprint region (maximum value ~27000 με) following the shape of the imprint. In S1 and S2 however, the strain continued to the distal part of the volume decreasing in magnitude (~ 16000 με). S5 (transverse), presented elevated tensile strain values at I_2 in the region of the imprint (~ 30000 με). At I_4 however the strain decreased and crack appeared adjacent to the

imprint. Tensile strain, at the same magnitude (~28000 με) also appeared in the distal part of S5 opposite to the crack in both I_2 and I_4. S6, at I_2, demonstrated a uniform strain map following the shape of the indent (pyramidal distribution) with peak value in the middle of the imprint (10000 με). It increased to 27000 με in I_4 maintaining the same trend. S7 exhibited the least tensile strain in all the specimens and remained at approx. 3000 με overall in all the stages. S8 experienced the same trend as S6, where tension was present at the imprint region rising in I_4; however, the distribution here showed a circular trend around the imprint. In the last group, the tensile strain varied around the specimens. S9 experienced concentration of strain only around the imprint. Specifically, the magnitude increased with the increase of the depth until microcrack formation in I_4, where it attained ~30000 με. S10 displayed maximum ε_{p1} strain of ~6000 με at I_2 in the indent region. At I_3 the strain was uniformly distributed around the volume at ~8000 με. It increased at the last stage in the indented area at one side of the specimen reaching ~23000 με. I_2 and I_3 appeared similar in the last two specimens. Specifically, tensile strain concentration was present in one side of the specimens (~20000 and ~260000 με for S11 and S12, respectively). Furthermore, an increase in the strain was observed in S12 at I_3 around the imprint (~23000 με). For I_4, S11 the tensile strain expanded towards the centre of the volume and the indentation region (~27000 με). In S12 however, the distribution remained the same similar to the previous two stages with a slight increase of strain in the opposite boarder as well.

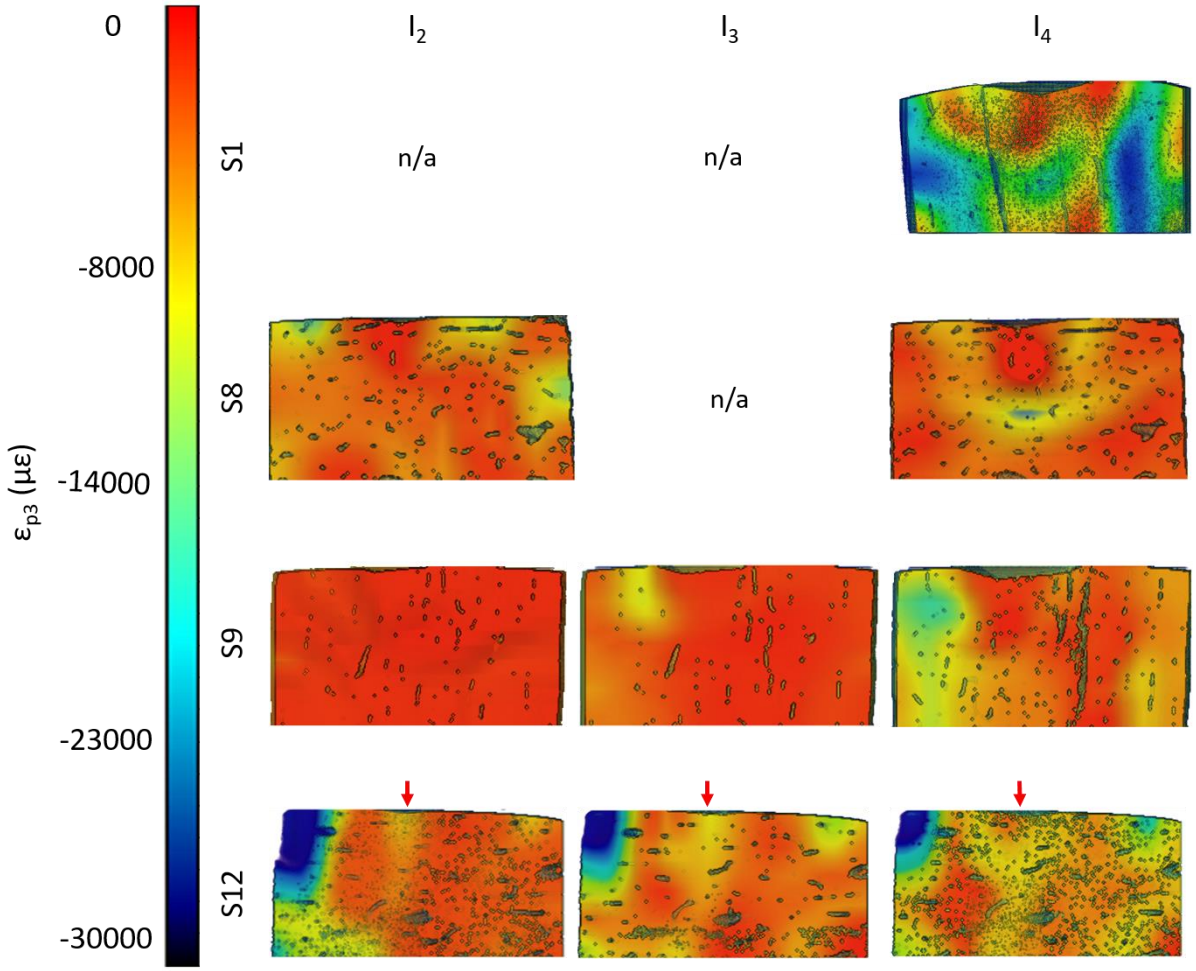

Figure 4: Visualisation of the strain maps (ε_{p3}) in axial (S1, S9) and transverse (S8, S12) specimens with different indentation stages. In all specimens, higher compressive strain values appeared on the sides. S1 experienced a combination of low and high compressive strain values reaching ~-26000 με closer to the borders of its volume. In the rest of the specimens, the strain was increasing steadily as the depth of the defect increased. n/a: indentation stages not applicable; Red arrows pointing at the indentation site

Discussion

The aim of this study was to investigate the behaviour of cortical bone microstructure after plastic deformation achieved by in situ XCT indentation in the axial and transverse orientation, in relation to the strain distribution (calculated via DVC) in the region.

Overall, in all the specimens, the canal network directly under the imprint is compressed, where the pile-up observed in the tomograms was localised around the indent and resulted in the deformation of the volume and thus strain concentration. It was observed that samples with higher porosity values did not crack. In the ones with intermediate levels of porosity (i.e. S3, S7, S8 and S10) the distribution of the strain in the overall volume was uniform and less in magnitude compared to the remaining specimens (maximum value: -4000 με). This phenomenon is dominant in the transverse samples. Specifically, in S7 where the porosity is 7.6 % and maximum canal diameter 295.5 μm at I_0. There was almost no tensile strain present after I_4 (mean ε_{p1} = 2500 ± 500 με). The porosity decreased slightly by 0.08 and 0.25 % at I_2 and I_4, respectively and there was Ca.Dm widening. The combination of the two helped maintain bone integrity. This is in accordance with findings from Zebaze et al. (2019) [36], where it was found that high porosity levels in cortical bone does not necessarily lead to fracture.

Additionally, the orientation of the network has been deemed a major factor in the formation and prevention of microcracks [10]. In the current study, S1 and S2 both experienced microcrack formation. These specimens were in axial direction where the indentation was performed in one stage and large deformation was introduced in the structure, without allowing relaxation to occur. However, this procedure was also completed for S3 and S4, where crack formation was avoided. This can be attributed to the fact that the first two were extracted from the axial direction along the long axis of the femur, whereas the last two from the transverse [37]. Observing the morphometry in S2, it was observed that a Harversian canal (Ca.Dm = ~200 μm) was adjacent to the borders of the imprint longitudinally, creating a weakness point, resulting in fracture. In Group 2 only one of the axial specimens failed under applied load (S5) in the last indentation stage, I_4. The morphometry in S5 and S6 was very similar. In fact, at I_0 the N.Ca is 696 and 659, and N.Po. is 263 and 230 for S5 and S6, respectively. The mean Ca.Dm was also similar (Fig. 3), at approximately 23 μm for both. The principal difference found however, was the canal network distribution under the indentation area. In S5, there was a canal located under the edges of the imprint. It can be assumed that with the large strain concentration in this region, due to the indentation pile-up, the canal created a weakness point leading to crack formation [30]. A similar behaviour occurred in S9, where microcrack initiated at I_3, propagating further at I_4 (Fig. 2). A canal was located under the surface and when the imprint periphery

size increased, reaching that point, microcrack formation occurred, which then expanded towards the inferior part of the volume.

In cases where a Harversian canal was directly under the indent tip at contact, failure was avoided (S10). This could be considered as a mechanism that prevents crack propagation. In fact, it is known that bone plasticity ahead of a crack dissipates energy and reduces the strain locally [38]. Although, with the resolution used in this study osteons are not visible, they are known to deflect crack formation [38]. Furthermore, in the transverse direction the Harversian canals, which are perpendicular to the indent, assisted in maintaining the structural integrity, hence no crack formation occurred. The lack of fracture in the transverse specimens was better understood when observing the morphology variation along with the mechanical behaviour. The change of the N.Ca and N.Po in the specimens throughout the indentation stages was representative of the strain distribution in the transverse samples. Specifically, in regions where the N.Ca was reduced, there was high compressive strain and when the N.Ca increased there was a high tensile strain.

This was more obvious in the case of S12, where at I_0 the N.Ca resulted in 1285. The N.Ca was reduced at I_2 to 918, increased to 1000 at I_3 and finally reaching 897 in the last stage (I_4). These values were in accordance to the strain, reaching values of compressive strain of ~-29000 με at I_2 in the border of the specimen where most of the loss occurs. At I_3, tensile strain increased in the opposite side (~23000 με), leading to believe that there was an opening of the canals augmenting their number. In the last stage, the strain distribution expanded throughout the volume with combination of tensile and compressive values. The effect of the load in the structure is clear from the N.Ca and pore network distribution. Specifically, presence of larger pores is dominant in regions of high strain concentration (either tensile or compressive). The distribution in the pore network follows that of the canals. This observation produced evidence that the defect location in respect to the canal and pore network was a major determinant in fracture initiation. As seen from S12, large pores and canals surrounding the indentation region (defect) were allowing uniform deformation in the structure that prevented large crack formation. Instead, strain was concentrated in these areas and not directly in the defect region.

The canal network influence in the mechanical behaviour has been previously investigated in regards to axial compressive loading in mice femur [22]. Specifically, a transverse notch was artificially introduced in the diaphysis of the bone, in situ SR-XCT microcompression was applied to the specimens and morphometric properties such as canal volume (Ca.V) and thickness (Ca.Th) were estimated. It was observed that the cracks were initiated at the canal surface, propagating towards the endosteal and periosteal. In a different study with similar mice models under micro-compression, DVC was computed for regions of microcrack formation [26]. In both cases it was observed that canals

act as stress raisers and encourage crack formation axially. However, in both these cases the notch in the bone has created a residual deformation to the canal network prior to testing. In the present study the network is intact prior to the plastic deformation. Furthermore, both axial and transverse orientation were examined.

In situ XCT Indentation has been previously employed for evaluation of plastic deformation in a specimen [32]. In particular, in has been used to investigate the behaviour of tubules in elephant tusk [32]. In that study the elephant dentin tubules were running parallel to the length of the tusk and three different tubules orientation with respect to the indentation axis were examined. Consistent to the results found in the present study, tubules parallel to the indentation tip created a weakness point for the structure leading to larger crack formation. For tubules at 70°, crack propagation is prevented and tiny cracks due to the contact with the tip deflect horizontally, in the axial direction. The orientation of the bone canal network is more complex than that of the tubules, however; the canals seemed to behave in the same manner regarding the axial and transverse alignment.

This study has a number of limitations. A small number of specimens were tested and in order to generalise the findings and the conditions at which fracture occurs, the protocol should be implemented in a larger group. Furthermore, although the canal network in the structure was intact prior to the testing, the morphometry and mechanical behaviour of the microstructure should also be investigated in whole bone specimens. Resistance of bone to microcracks highly depends on metabolic diseases and aging [16,39–41]. Thus, it is vital to assess these phenotypes in diseased tissue. At last, in the resolution of these datasets, the role of osteons could not be assessed as well potential sites of microcrack formation.

Conclusions

This paper presented the first study combining the plastic strain accumulation and canal network distortion in cortical bone using in situ XCT indentation and DVC. Fracture development as a result of plastic deformation was obtained in the axial and transverse orientation of the intracortical microstructure. It was observed that crack formation was predominant in the axial direction, whereas when the Harversian canals were perpendicular to the vertical axis of the tip they acted in preventing fracture. Furthermore, the indentation testing caused deformation, and hence strain distribution, in the whole volume of the specimen, affecting the canal and pore network of the structure underneath the surface. The importance of the canal network regarding the deformation was seen in the strain accumulation patterns. 3D strain maps were introduced to analyse tomographic images of the cortical bone microstructure during plastic deformation. In areas of canal loss, compressive strain was

observed and widening of the canals was accompanied by tensile strain. Tensile strain was also present in the indentation imprint.

Acknowledgments

The authors wish to thank Mr Geoff Britton for his assistance with the sample preparation and experimental set up and Dr Dave Hollis (LaVision Ltd) for advice on DVC computation. The Zeiss Global Centre (University of Portsmouth) provided XCT imaging and DVC capability to conduct this study. This study is part of a PhD programme funded by the Faculty of Technology (University of Portsmouth).

References

[1] K. Tai, H.J. Qi, C. Ortiz, Effect of mineral content on the nanoindentation properties and nanoscale deformation mechanisms of bovine tibial cortical bone, J. Mater. Sci. Mater. Med. 16 (2005) 947–959. doi:10.1007/s10856-005-4429-9.

[2] R. Jae-young, L. Kuhn-Spearing, P. Zioupos, Mechanical Properties and the hierarchical structure of bone, Med. Eng. Phys. 20 (1998) 92–102. doi:10.1038/251673a0.

[3] R. Chapurlat, In vivo evaluation of bone microstructure in humans: Clinically useful?, Bonekey Rep. 5 (2016) 1–5. doi:10.1038/bonekey.2016.40.

[4] P. Augat, S. Schorlemmer, The role of cortical bone and its microstructure in bone strength, Age Ageing. 35 (2006) 27–31. doi:10.1093/ageing/afl081.

[5] G.W. Marshall, M. Balooch, R.R. Gallagher, S.A. Gansky, S.J. Marshall, Mechanical properties of the dentinoenamel junction: AFM studies of nanohardness, elastic modulus, and fracture, J. Biomed. Mater. Res. 54 (2001) 87–95. doi:10.1002/1097-4636(200101)54:1<87::AID-JBM10>3.0.CO;2-Z.

[6] A. Raeisi Najafi, A.R. Arshi, M.R. Eslami, S. Fariborz, M.H. Moeinzadeh, Micromechanics fracture in osteonal cortical bone: A study of the interactions between microcrack propagation, microstructure and the material properties, J. Biomech. 40 (2007) 2788–2795. doi:10.1016/j.jbiomech.2007.01.017.

[7] M. Unal, A. Creecy, J.S. Nyman, The Role of Matrix Composition in the Mechanical Behavior of Bone, Curr. Osteoporos. Rep. 16 (2018) 205–215. doi:10.1007/s11914-018-0433-0.

[8] P. Zioupos, U. Hansen, J.D. Currey, Microcracking damage and the fracture process in relation to strain rate in human cortical bone tensile failure, J. Biomech. 41 (2008) 2932–2939. doi:10.1016/j.jbiomech.2008.07.025.

[9] U. Hansen, P. Zioupos, R. Simpson, J.D. Currey, D. Hynd, The effect of strain rate on the mechanical properties of human cortical bone, J. Biomech. Eng. 130 (2008) 1–8. doi:10.1115/1.2838032.

[10] R.K. Nalla, J.S. Stölken, J.H. Kinney, R.O. Ritchie, Fracture in human cortical bone: Local fracture criteria and toughening mechanisms, J. Biomech. 38 (2005) 1517–1525. doi:10.1016/j.jbiomech.2004.07.010.

[11] H.B. Hunt, E. Donnelly, Bone Quality Assessment Techniques: Geometric, Compositional, and Mechanical Characterization from Macroscale to Nanoscale, Clin. Rev. Bone Miner. Metab. 14 (2016) 133–149. doi:10.1007/s12018-016-9222-4.

[12] Q. Grimal, G. Rus, W.J. Parnell, P. Laugier, A two-parameter model of the effective elastic tensor for cortical bone, J. Biomech. 44 (2011) 1621–1625. doi:10.1016/j.jbiomech.2011.03.006.

[13] D. Rohrbach, Q. Grimal, P. Varga, F. Peyrin, M. Langer, P. Laugier, K. Raum, Distribution of mesoscale elastic properties and mass density in the human femoral shaft, Connect. Tissue Res. 56 (2015) 120–132. doi:10.3109/03008207.2015.1013627.

[14] F. Donaldson, D. Ruffoni, P. Schneider, A. Levchuk, A. Zwahlen, P. Pankaj, R. Müller, Modeling microdamage behavior of cortical bone, Biomech. Model. Mechanobiol. 13 (2014) 1227–1242. doi:10.1007/s10237-014-0568-6.

[15] I.S. Hage, R.F. Hamade, Intracortical stiffness of mid-diaphysis femur bovine bone: lacunar–canalicular based homogenization numerical solutions and microhardness measurements, J. Mater. Sci. Mater. Med. 28 (2017). doi:10.1007/s10856-017-5924-5.

[16] X. Cai, H. Follet, L. Peralta, M. Gardegaront, D. Farlay, R. Gauthier, B. Yu, E. Gineyts, C. Olivier, M. Langer, A. Gourrier, D. Mitton, F. Peyrin, Q. Grimal, P. Laugier, Anisotropic elastic properties of human femoral cortical bone and relationships with composition and microstructure in elderly, Acta Biomater. 90 (2019) 254–266. doi:10.1016/j.actbio.2019.03.043.

[17] K.L. Bell, N. Loveridge, J. Power, N. Garrahan, B.F. Meggitt, J. Reeve, Regional differences in cortical porosity in the fractured femoral neck, Bone. 24 (1999) 57–64. doi:10.1016/S8756-3282(98)00143-4.

[18] U. Wolfram, J.J. Schwiedrzik, M.J. Mirzaali, A. BÜRKI, P. Varga, C. Olivier, F. Peyrin, P.K. Zysset, Characterizing microcrack orientation distribution functions in osteonal bone samples, J. Microsc. 264 (2016) 268–281. doi:10.1111/jmi.12440.

[19] P. Augat, T. Link, T.F. Lang, J.C. Lin, S. Majumdar, H.K. Genant, Anisotropy of the elastic modulus of trabecular bone specimens from different anatomical locations, Med. Eng. Phys. 20 (1998) 124–131. doi:10.1016/S1350-4533(98)00001-0.

[20] P. Zioupos, Recent developments in the study of failure of solid biomaterials and bone: “Fracture” and “pre-fracture” toughness, Mater. Sci. Eng. C. 6 (1998) 33–40. doi:10.1016/S0928-4931(98)00033-2.

[21] D.M.L. Cooper, A.L. Turinsky, C.W. Sensen, B. Hallgrímsson, Quantitative 3D analysis of the canal network in cortical bone by micro-computed tomography, Anat. Rec. - Part B New Anat. 274 (2003) 169–179. doi:10.1002/ar.b.10024.

[22] R. Voide, P. Schneider, M. Stauber, P. Wyss, M. Stampanoni, U. Sennhauser, G.H. van Lenthe, R. Müller, Time-lapsed assessment of microcrack initiation and propagation in murine cortical bone at submicrometer resolution, Bone. 45 (2009) 164–173. doi:10.1016/j.bone.2009.04.248.

[23] M. Peña-Fernández, E. Dall’Ara, A.P. Kao, A.J. Bodey, A. Karali, G.W. Blunn, A.H. Barber, G. Tozzi, Preservation of bone tissue integrity with temperature control for in situ SR-MicroCT experiments, Materials (Basel). 11 (2018). doi:10.3390/ma11112155.

[24] F. Gillard, R. Boardman, M. Mavrogordato, D. Hollis, I. Sinclair, F. Pierron, M. Browne, The application of digital volume correlation (DVC) to study the microstructural behaviour of trabecular bone during compression, J. Mech. Behav. Biomed. Mater. 29 (2014) 480–499. doi:10.1016/j.jmbbm.2013.09.014.

[25] G. Tozzi, V. Danesi, M. Palanca, L. Cristofolini, Elastic Full-Field Strain Analysis and Microdamage Progression in the Vertebral Body from Digital Volume Correlation, Strain. 52 (2016) 446–455. doi:10.1111/str.12202.

[26] D. Christen, A. Levchuk, S. Schori, P. Schneider, S.K. Boyd, R. Müller, Deformable image registration and 3D strain mapping for the quantitative assessment of cortical bone microdamage, J. Mech. Behav. Biomed. Mater. 8 (2012) 184–193. doi:10.1016/j.jmbbm.2011.12.009.

[27] J. Zhang, G.L. Niebur, T.C. Ovaert, Mechanical property determination of bone through nano- and micro-indentation testing and finite element simulation, J. Biomech. 41 (2008) 267–275. doi:10.1016/j.jbiomech.2007.09.019.

[28] L. Yin, S. Venkatesan, D. Webb, S. Kalyanasundaram, Q.H. Qin, 2D and 3D mapping of microindentations in hydrated and dehydrated cortical bones using confocal laser scanning microscopy, J. Mater. Sci. 47 (2012) 4432–4438. doi:10.1007/s10853-012-6301-x.

[29] Z. Fan, J.Y. Rho, Effects of viscoelasticity and time-dependent plasticity on nanoindentation measurements of human cortical bone, J. Biomed. Mater. Res. - Part A. 67 (2003) 208–214. doi:10.1002/jbm.a.10027.

[30] A.C. Fischer-Cripps, Mechanical Engineering Series, 2006. doi:10.1007/b22134.

[31] A.C. Fischer-Cripps, The Hertzian contact surface, J. Mater. Sci. 34 (1999) 129–137. doi:10.1023/A:1004490230078.

[32] X. Lu, M.P. Fernández, R.S. Bradley, S.D. Rawson, M. O'Brien, B. Hornberger, M. Leibowitz, G. Tozzi, P.J. Withers, Anisotropic crack propagation and deformation in dentin observed by four-dimensional X-ray nano-computed tomography, Acta Biomater. 96 (2019) 400–411. doi:10.1016/j.actbio.2019.06.042.

[33] M. Doube, M.M. Klosowski, I. Arganda-Carreras, F.P. Cordelières, R.P. Dougherty, J.S. Jackson, B. Schmid, J.R. Hutchinson, S.J. Shefelbine, BoneJ: Free and extensible bone image analysis in ImageJ, Bone. 47 (2010) 1076–1079. doi:10.1016/j.bone.2010.08.023.

[34] M. Palanca, A.J. Bodey, M. Giorgi, M. Viceconti, D. Lacroix, L. Cristofolini, E. Dall'Ara, Local displacement and strain uncertainties in different bone types by digital volume correlation of synchrotron microtomograms, J. Biomech. 58 (2017) 27–36. doi:10.1016/j.jbiomech.2017.04.007.

[35] M. Palanca, L. Cristofolini, E. Dall'Ara, M. Curto, F. Innocente, V. Danesi, G. Tozzi, Digital volume correlation can be used to estimate local strains in natural and augmented vertebrae: An organ-level study, J. Biomech. 49 (2016) 3882–3890. doi:10.1016/j.jbiomech.2016.10.018.

[36] R. Zebaze, E.J. Atkinson, Y. Peng, M. Bui, A. Ghasem-Zadeh, S. Khosla, E. Seeman, Increased Cortical Porosity and Reduced Trabecular Density Are Not Necessarily Synonymous With Bone Loss and Microstructural Deterioration, JBMR Plus. 3 (2019) e10078. doi:10.1002/jbm4.10078.

[37] A. Basillais, S. Bensamoun, C. Chappard, B. Brunet-Imbault, G. Lemineur, B. Ilharreborde, M.C. Ho Ba Tho, C.L. Benhamou, Three-dimensional characterization of cortical bone

microstructure by microcomputed tomography: Validation with ultrasonic and microscopic measurements, J. Orthop. Sci. 12 (2007) 141–148. doi:10.1007/s00776-006-1104-z.

[38] R.O. Ritchie, M.J. Buehler, P. Hansma, Plasticity and toughness in bone, Phys. Today. (2009). www.physicstoday.org.

[39] E.A. Zimmermann, B. Busse, R.O. Ritchie, The fracture mechanics of human bone: influence of disease and treatment, Bonekey Rep. 4 (2015). doi:10.1038/bonekey.2015.112.

[40] S. Mori, R. Harruff, W. Ambrosius, D.B. Burr, Trabecular bone volume and microdamage accumulation in the femoral heads of women with and without femoral neck fractures, Bone. 21 (1997) 521–526. doi:10.1016/S8756-3282(97)00200-7.

[41] E.A. Zimmermann, E. Schaible, H. Bale, H.D. Barth, S.Y. Tang, P. Reichert, B. Busse, T. Alliston, J.W. Ager, R.O. Ritchie, Age-related changes in the plasticity and toughness of human cortical bone at multiple length scales, Proc. Natl. Acad. Sci. 108 (2011) 14416–14421. doi:10.1073/pnas.1107966108.

Micromechanical evaluation of regenerated bone in rat femurs using digital volume correlation

Aikaterina Karali[1], Alexander P. Kao[1], Richard Meeson[2], Marta Roldo[3], Gordon Blunn[3], Gianluca Tozzi[1]

[1]School of Mechanical and Design Engineering, University of Portsmouth, Portsmouth, UK

[2]University College London, Stanmore, UK

[3]School of Pharmacy and Biomedical Sciences, University of Portsmouth, UK

Keywords: Digital Volume Correlation (DVC), bone regeneration, X-ray computed tomography (XCT), in situ mechanics, rat femur, histological analysis.

Abstract

The mechanical behaviour of the regenerated tissue in fracture healing is a key factor for whole bone to withstand loading. However, to date it is still unclear how newly formed bone performs under loading. X-ray Computed Tomography (XCT) has been used to assess the progress of the mineralised tissue in bone regeneration. Furthermore, in-situ XCT mechanics combined with digital volume correlation (DVC) have been extensively implemented to understand the mechanical behaviour and full-field three-dimensional (3D) strain distribution in bone at the apparent level. The purpose of this study is to use in-situ XCT mechanical testing and DVC to investigate the load-bearing capacity and strain distribution in the regenerated diaphyseal bone tissue of rat femoral specimens. Rat femurs with 1 and 2 mm osteotomy gap where tested under step-wise compression in the apparent elastic region. High strain concentration was present in the mineralised newly formed bone exceeding 20000 με. Histological analysis was completed for observation of the unmineralised tissues in the fractured region. The variation in the 3D strain distribution at the regenerated bone region that are directly related to the presence of unmineralised tissue seen in the histological images. The outcomes of this study contribute in understanding regenerated bone mechanical behaviour under loading.

Introduction

Bone fracture healing is a complex process that has been investigated extensively throughout the years [1–5]. It is influenced by both the local biological and mechanical environment [6]. Optimal fracture healing involves local mechanical stability along with close proximity in the fracture ends, since instability and large movements can negatively affect the healing. However, some micromotion is necessary, as completely rigid fixation has shown only partial fracture healing [1,6]. In cases where the two fracture ends are not in contact, secondary fracture healing occurs. Secondary fracture healing can be described by three basic steps; inflammation, cellular proliferation and differentiation, and remodelling [7]. These phases occur in different locations at different rates. In the second step, intramembranous woven bone is deposited in the void between the ends, and it is later replaced in the remodelling process by mature bone [1]. Intramembranous and endochondral ossification can also happen simultaneously leading to formation of both soft and hard callus (uncalcified and calcified/woven bone respectively). It has been shown that hard callus starts forming in the inner layer of periosteum at a certain distance from the fracture site, progressing towards the gap, predominantly at the periphery [2,3]. Whereas, soft callus is forming centrally [6]. The combination of these two actions increases the fracture stiffness and stability. Any defect that cannot heal spontaneously without intervention is a critical size defect. It was recognised that defects without complete healing after 52 weeks would remain as such. In humans, non-healed defects are those induced by trauma or ablative oncological surgery [8]. The first studies to assess critical size defects were by Schmitz and Hollinger (1985) [9], and Hollinger and Kleinschmidt (1990) [10]. A standardised method to stabilise a critical size defect is requiring the use of external fixators [11–14]. They ensure alignment of the bone fragments and allow control over the degree of interfragmentary movement, which develops under external loading and muscle activity. Intramembranous bone formation is induced by low interfragmentary strain (IFS) [1]. A moderate interfragmentary movement leads to endochondral ossification, whereas a high one obstructs fracture healing [15].

Histology has been widely used to assess bone healing at the microscale throughout the entire healing process [16,17] to identify the type of defect [18,19], as well as to evaluate fixation efficiency [20,21]. It is employed to classify the mineralised and unmineralised tissue formation throughout the healing stages [16,19]. In fact, the mineralisation percentage in the fracture in the duration of the healing, provides information on different fixation designs [19] as well as bone grafts [18]. However, this technique, other than being destructive, is capable of investigating only selected two-dimensional (2D) regions of the tissue. Macroscopically, fracture healing has been also analysed in a three-dimensional (3D) manner with the use of radiography and high-resolution X-ray computed tomography (XCT). It is mainly employed for examination of the mineralised tissue development and fracture healing

progress [22–26]. Furthermore, investigation of bone regeneration mechanics using high-resolution XCT imaging has been completed formerly, in femoral condyles defects injected with different bone grafts. The regeneration progress along with the mechanical behaviour under in-situ step-wise compressive loading in the new tissue were examined [27].

Healing in the human tibia has been investigated under bending to measure the deflection of the bone in vivo [28]. It was observed that for deflection of more than 1°, the theoretical ultimate strength of the fracture can be compared within the first week of healing. Evans et al. (1988) calculated the fracture stiffness during healing using a transducer located onto the external fixator. The fracture stiffness was obtained by considering the system stiffness (fracture and fixator) as a ratio of the force and deflection. To avoid the errors in measurement induced by the fixator stiffness, another study [29] mounted U-shaped strain gauges onto the pins of each fragment on both fracture ends in sheep tibia. The load was applied by a cell implemented on to the external fixator parallel to the bone. Conversely, the fixator pin loosening in the bone affected the readings.

Digital volume correlation (DVC) is gaining increased popularity in the experimental computation of full-field strain in bone. Specifically, images at different stages in the mechanical testing are obtained by XCT (3D-DVC) and correlated to measure the full-field strain at tissue [30,31] and bone apparent level [32–34]. Moreover, DVC has been used on long bones to better understand the 3D full-field strain distribution of experiments in vivo on mice tibia [35]. In fact, the mice tibiae were scanned in the preloaded and loaded conditions within an in-vivo XCT system and DVC performed on these tomograms to identify the precision error of local strains in the whole tibia. Additionally, in the study of Peña Fernández et al. (2018) DVC was achieved, computing the full-filed 3D strain at tissue level in bone specimens that consisted of mature and new bone as well as the biomaterial [27]. Digital image correlation (DIC) has also been employed to identify the 2D strain on the surface of intact whole bone [36]. Specifically, Yavari et al. used DIC to examine 3D surface strains in the linear elastic region of rat femora during compression testing until failure, in order to investigate strain-based fracture criteria [37].However, to the best of the authors' knowledge, the investigation of internal strain distribution in the regenerated bone of healed fracture models using DVC is missing.

Therefore, the aim of this study is to assess the load-bearing capacity and the full-field strain distribution in the regenerated diaphyseal bone tissue using DVC. Furthermore, histology is used to assess the regeneration status of both calcified and uncalcified tissue in the region.

Methodology

Sample preparation

Seven Wistar rat female femurs with osteotomy in the diaphysis of 1 mm and 2 mm gap (S1-S4 and S5-S6, respectively) were used in this study. The gap was stabilised with a Stanmore Micro-External-Fixator (SMExF) [21]. The animals were sacrificed 5 weeks postoperative and the femurs were extracted and fixed in formalin solution (10% buffered formaldehyde). Both ends were embedded in Poly(methyl methacrylate) (PMMA) and Acetyl endcaps [38]. The average height of the femurs was 38±2.3 mm, consequently the tissue in between the endcaps was 20±2.3 mm. The fixator was removed prior to the in-situ mechanical testing.

High-resolution XCT imaging

High-resolution XCT was performed using the Zeiss Versa 510 system (Zeiss, Germany). The system operated at 110V/9kW and 1601 projections with exposure time of 3 s were acquired over a 360°, resulting in a 12 μm voxel size. The resulting field of view (FOV) included the osteotomy gap and 2 out of the 4 holes induced by the fixator pin (12000 x 12000 μm).

In situ XCT mechanics

A preliminary test was conducted in order to document damage induced by fixator removal as well as the apparent elastic region of the sample, in order to plan the following step-wise in situ XCT experiments. One 1 mm osteotomy gap sample (S1) was XCT imaged before and after removal of the fixator, then uniaxially compressed in situ with a loading device (CT5000, Deben, UK) until failure and finally XCT imaged post-failure. It was shown that removal of the fixator did not cause any visible damage to the sample (Fig.1A) and the yielding occurred at ~1.2mm displacement (Fig.1B, C).

For the in situ step-wise compression testing the bone was kept hydrated throughout the process by wrapping the tissue with a gauze immersed in saline solution and then paraffin film to avoid leakage. The distal end of the femur was fixed on the bottom plate. An initial pre-load of 7 ± 2.7 N was applied and two consecutive tomograms were acquired to allow DVC error analysis. The specimens were then step-wise compressed to 0.5 mm and 1 mm displacements, as dictated by the preliminary experiment, within their apparent elastic region. Following the application of each displacement step, the specimens were allowed to relax for 15 min, to allow for stress relaxation, before acquiring XCT images [39].

Image post-processing

The 3D datasets obtained from the tomograms after reconstruction, consisted of 1010 projection images (1004x1024 pixels, 32-bit grey levels). They were converted to 8-bit and rigidly registered using

Fiji (ImageJ, USA). Parallelepipeds were cropped in the centre of the dataset ensuring that the osteotomy and one of the pin holes were in the region of interest (ROI) (Fig. 3, Fig. 4). Artefacts in the images were removed by applying a mask to each dataset. The mask was created by running a purifying cycle on the binary image of each dataset with BoneJ plug-in. An arithmetic and logical operation was executed between the original dataset and the purified images to remove the noise using the same software.

Digital Volume Correlation

A local approach DVC analysis was performed for the cropped volumes (Fig. 2, Fig. 3) using Davis 10.0.3 (LaVision, UK). A multi-step pass processing (128 to 48 voxels/subvolume) was used to compute the strain. That was followed by a vector post-processing, where the correlation coefficient was thresholded to 0.8. The first two consecutive datasets where the pre-load was applied were used for the calculation of the error uncertainty (MAER = 287 ± 150 με) [33,40,41]. The 1st, 3rd principal (ε_{p1} and ε_{p3} respectively) and shear (γ) strains were computed.

Histological analysis

After in situ testing the specimens were decalcified in formic acid, dehydrated in increasing concentration of ethanol (50%, 75%, 85%, 95%, 100%) and cleared in xylene (C_8H_{10}). Then, they were infiltrated with paraffin wax for 30 hours and embedded in wax horizontally with the pin holes oriented vertically. Thin slices of 5 μm were cut from the middle of each specimen using Leica RM2235 rotary microtome (Leica Biosystems, UK) [21]. The paraffin wax was removed from the slices and they were stained using Hematoxylin & Eosin (H&E) staining [42,43]. The osteotomy gap region was located under 10x magnification lens and the tissue was analysed 50x magnification lens using Olympus BX40 (Leica Biosystems, UK). The soft (i.e. cartilaginous matrix, skin, muscles, fibrous) and hard (i.e. cortical, woven bone) tissue were identified in the periosteal, intracortical and intramedullary zones.

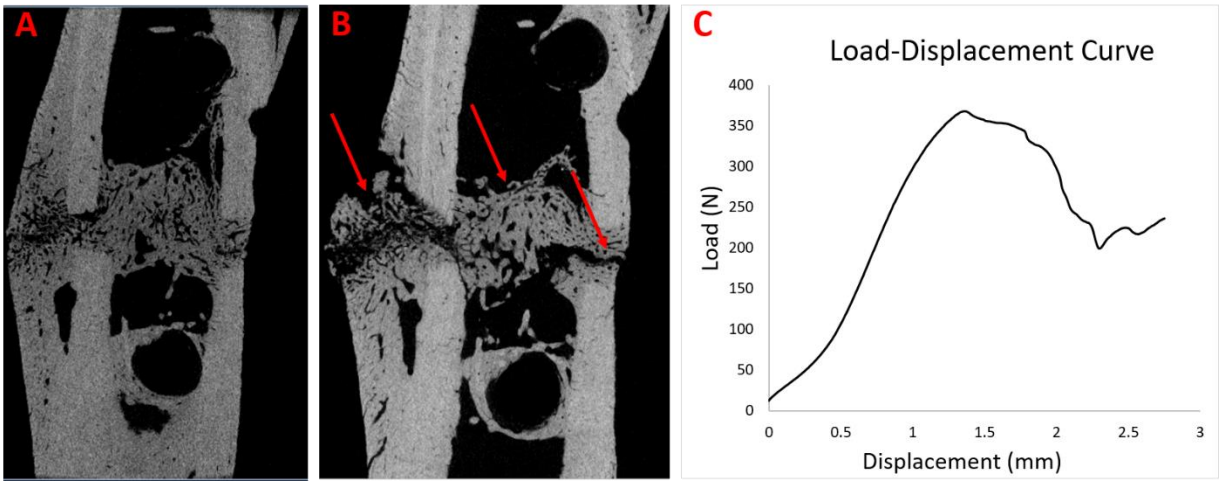

Figure 1: XCT tomograms of S1 before (A) and after (B) compression until failure, (C) Load-Displacement Curve for the compression. Red arrows pointing at cracks forming in the regenerated bone tissue.

Results

The XTC images showed differences in the morphology of the regenerated mineralised tissue. Only S1 showed complete healing after 5 weeks (Fig.1A). In S2, S3, S4 (1 mm gap, Fig. 2A-C) and S5 (2 mm gap, Fig. 3A) partial healing was shown, whereas S6 (Fig.3B) formed a non-union.

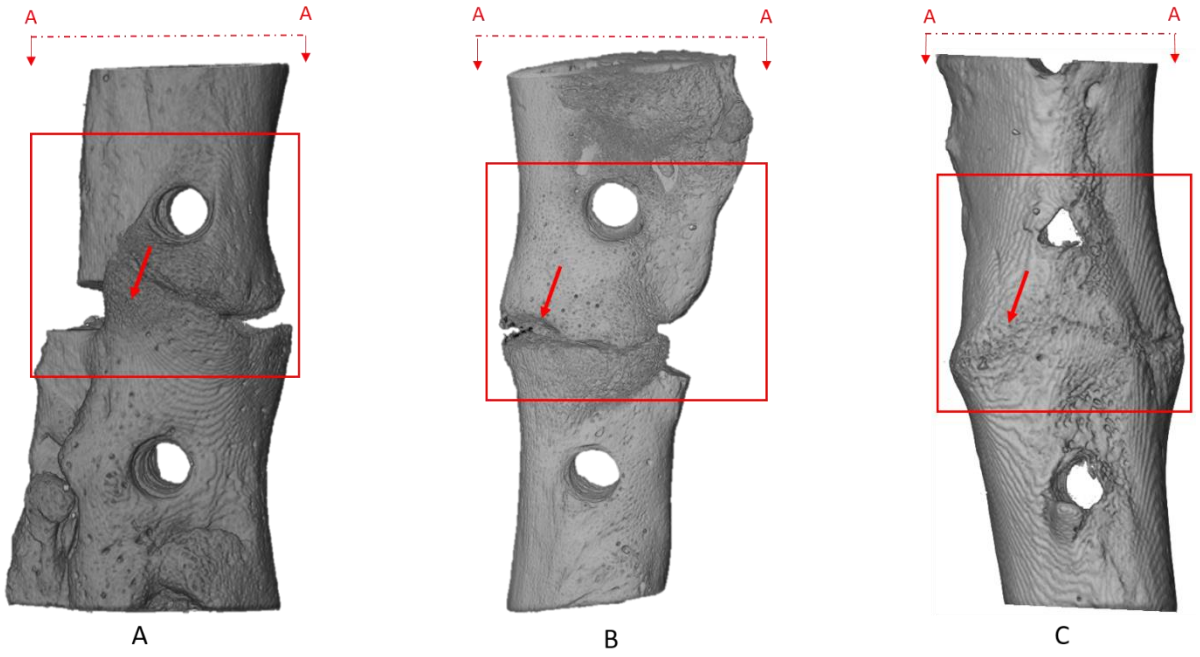

Figure 2: XCT images of rat femurs with 1mm osteotomy gap (red arrow) under 7 ± 27 N pre-load, red square outlining the ROIs of S2 (A), S3 (B) and S4 (C) cropped during the image post-processing.

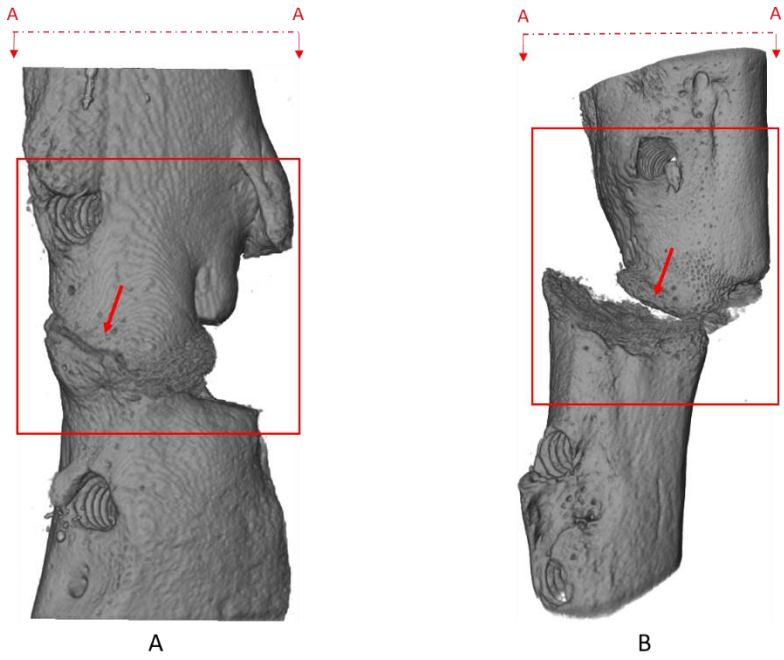

Figure 3: XCT images of rat femurs with 2 mm osteotomy gap (red arrow) under 7 ± 27 N pre-load, red square outlining the ROIs of S5 (A) and S6 (B) cropped during the image post-processing.

The strain induced on the regenerated tissue throughout the compression steps was assessed using DVC. Based on the distribution of the first and third principal strain (ε_{p1} and ε_{p3}, respectively) in S2-S5 a combination of tension and compression was seen (Figs. 4A-C; 5A) illustrating an overall buckling in the structure. Specifically, in S2 (Fig. 4A) compressive strains are accumulated laterally (≈ -30000 με) in the first compression step; prompting contact between the two fracture ends at the second compression step, where the volume of the tissue under compression is increased, not exceeding -32000 με (Fig. 4). The load in S3 (Fig. 4B) was primarily maintained by the woven bone leading to less than -2000 με at ΔL = 0.5 mm and inducing compressive strains locally in regions with less hard tissue formation levels (≈ -28000 με). At ΔL = 1.0 mm, ε_{p3} in S3 (Fig. 4B) resulted in similar trends as before; however, the strain induced in the woven bone reached a value of -5000 με. The strain distribution in S4 (Fig. 4C) was similar throughout its volume ranging between -1000 to -4000 με after the first compression step. The hard callus peripherally of the periosteum sustained the load, reaching -43000 με locally in the second compression step. In S6 (Fig.6A), the strain was concentrated in the middle of the woven bone locally in the first compression step, spreading laterally in the regenerated tissue on the second step. The behaviour of S7 (Fig. 5A) is different compared to the first; since the compression induced a sliding-like effect on the two parts of the fracture. The strain in the woven bone laterally shows a decrease of approximately 10000 με going from ≈ -20000 με to ≈ -30000 με (Fig. 6).

Focusing on the 1st principal strain (ε_{p1}) the increase of the strain is clear as the displacement is increased in all the samples (Appendix). However, a wide variation of the strain concentrations was observed locally. S2 experience higher strain level in the borders of the specimen where there was lack of woven bone maximum ≈ 29000 με). Conversely, in S3 and S4 strain concentration was present in the woven bone (exceeding 20000 με). The 2 mm osteotomy gap samples exhibit different strain distributions due to their morphology. S5 exhibits an increase in the stain inferiorly, not exceeding 15000 με. The results for S6 is different from the rest since it is observed in the XCT images that there is no radiopaque callus bridging the osteotomy region. The DVC analysis shows higher strain levels on the surface of the proximal fracture end (maximum ≈ 18000 με).

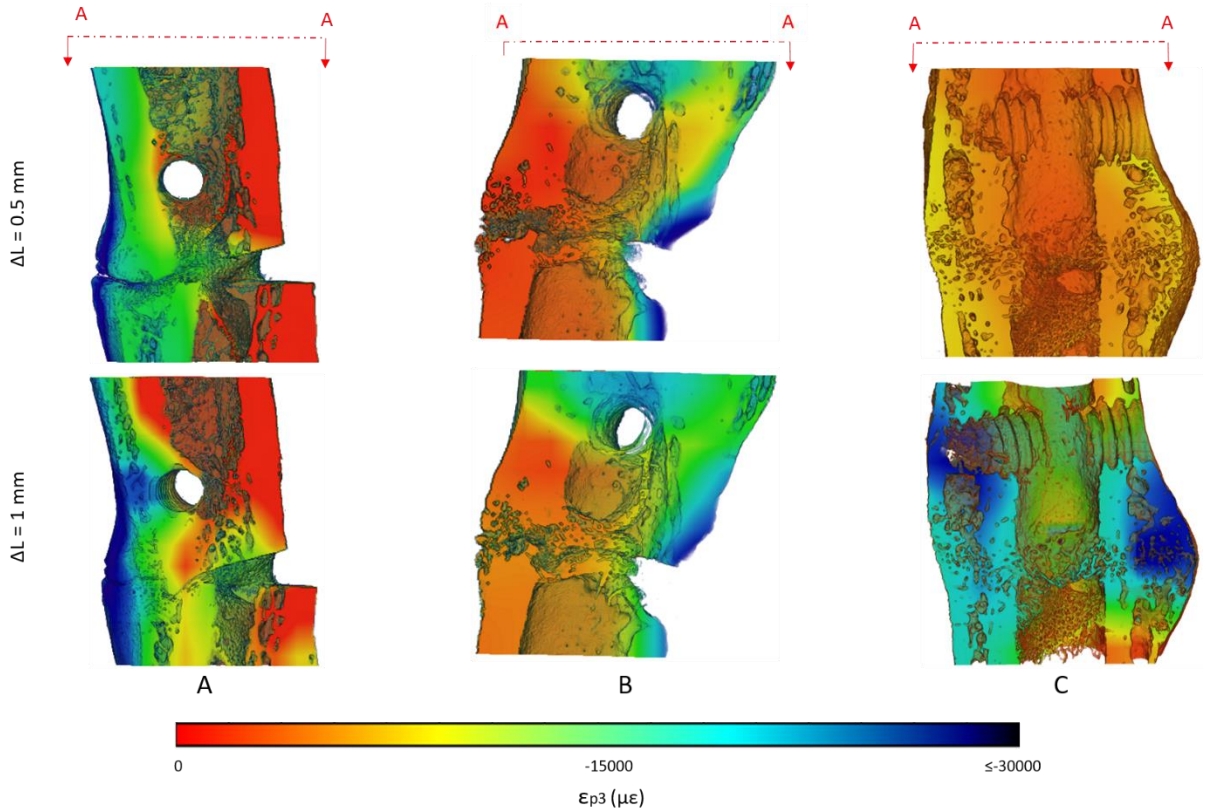

Figure 4: DVC analysis of 1 mm osteotomy gap, showing ε_{p3} of cross sections (A-A) in the ROIs of S2 (A), S3 (B) and S4 (C) in the first and second compression steps (top and bottom row, respectively)

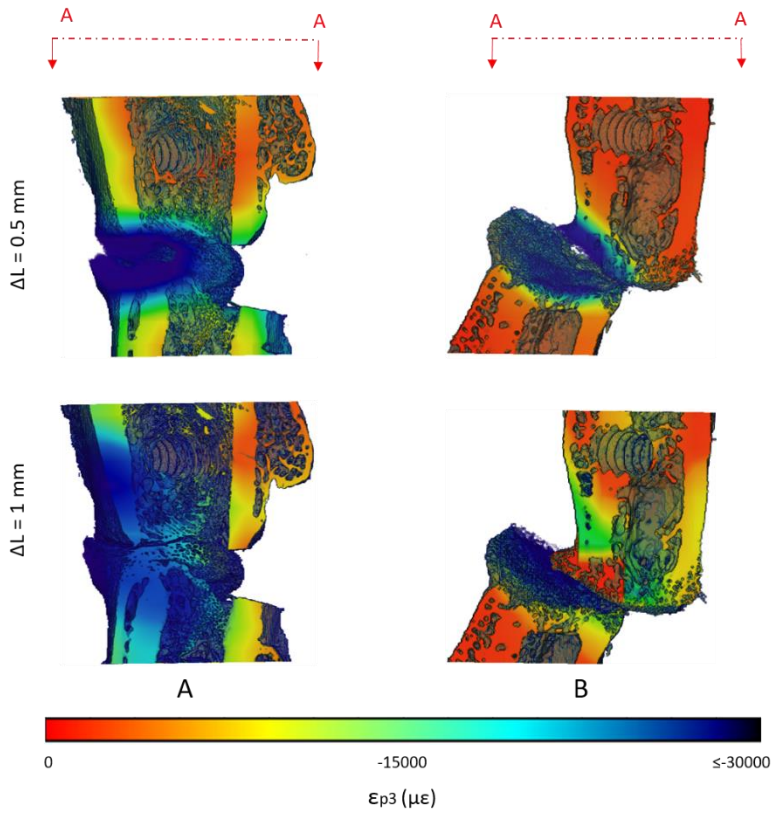

Figure 5: DVC analysis of 2 mm osteotomy gap, showing ε_{p3} of cross sections (A-A) in the ROIs of S6 (A) and S7 (B) in the first and second compression step (top and bottom row respectively)

Histological results were attained to gain more information on the radiolucent tissues. From the 5 µm mid-sagittal slides in S2, S3, S4 and S5 (Figs.6-9) it was observed fracture healing in progress. Hard and soft callus formation were occurring simultaneously, with mineralisation of the tissue being dominant laterally. In the higher magnification images, it was observed an advanced endochondral ossification (disorganised woven bone) extracortically and on the surfaces of the cortical bone (Fig.6-9). Cartilage matrix was observed intercortically of the osteotomy gaps, with mineralised chondrocytes (Fig.6, 7, 9). The histology in S4 also showed evidence of fibrous tissue intercortically (Fig.8). S6 was classified as a non-union based on the histology (Fig.10). Woven bone was found to be present at the surface of the both fracture ends, along with the cartilage matrix in the middle of the osteotomy gap. However, there was no bridging between the two.

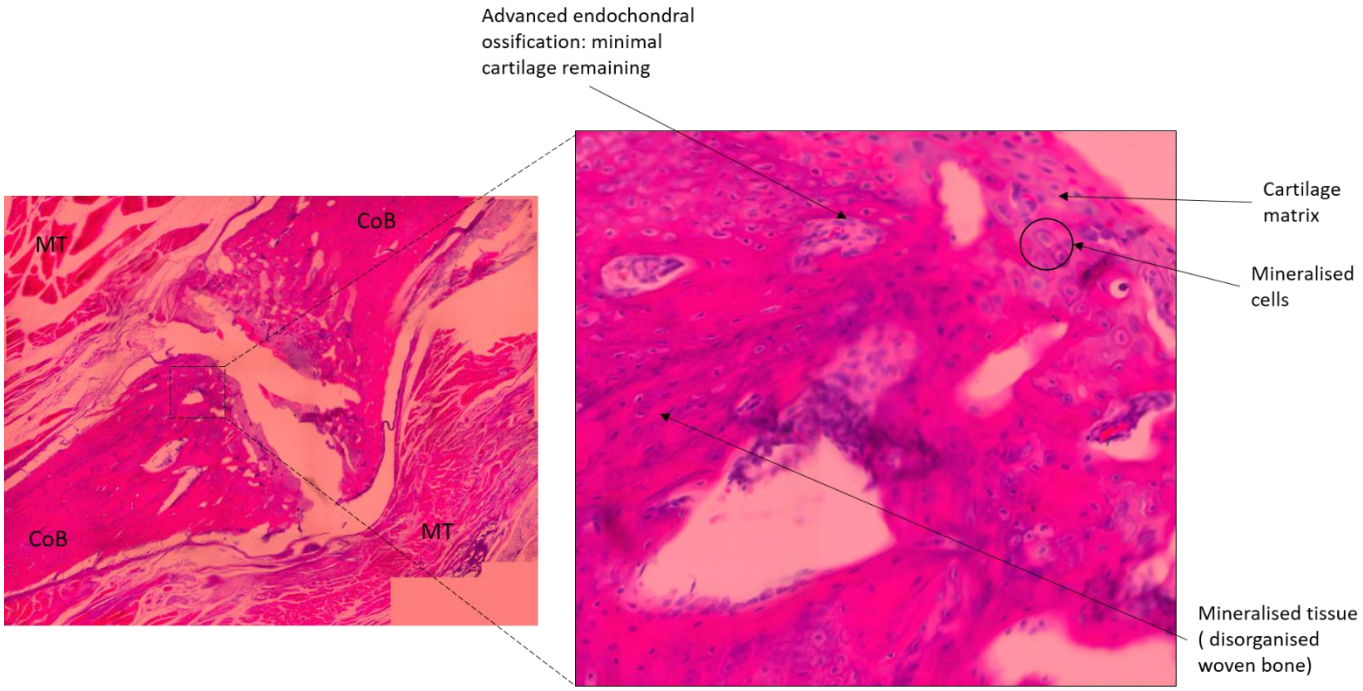

Figure 6: S2 Histology images of fracture healing in progress of 1 mm osteotomy gap. Images shown at x10 and x50 magnification; MT: muscular tissue, CoB: cortical bone.

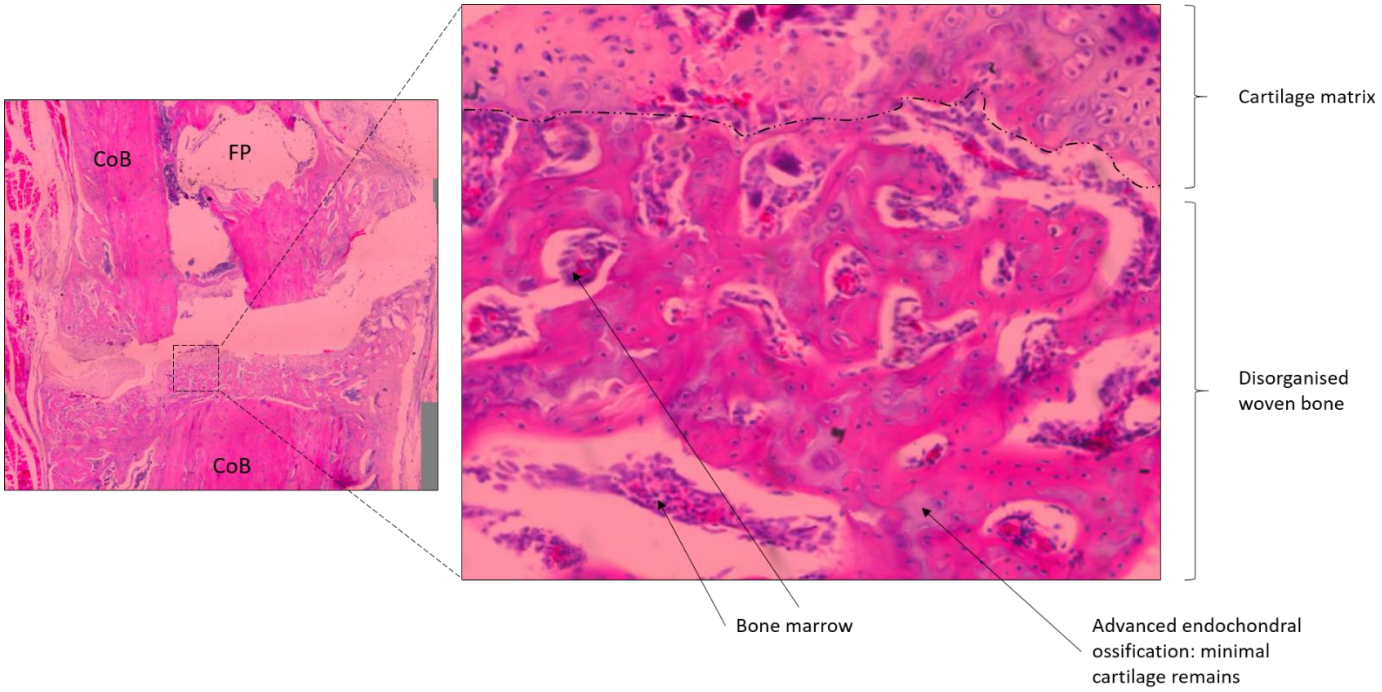

Figure 7: S3 Histology images of fracture healing in progress of 1 mm osteotomy gap. Images shown at x10 and x50 magnification; CoB: cortical bone, FP: fixator pin location.

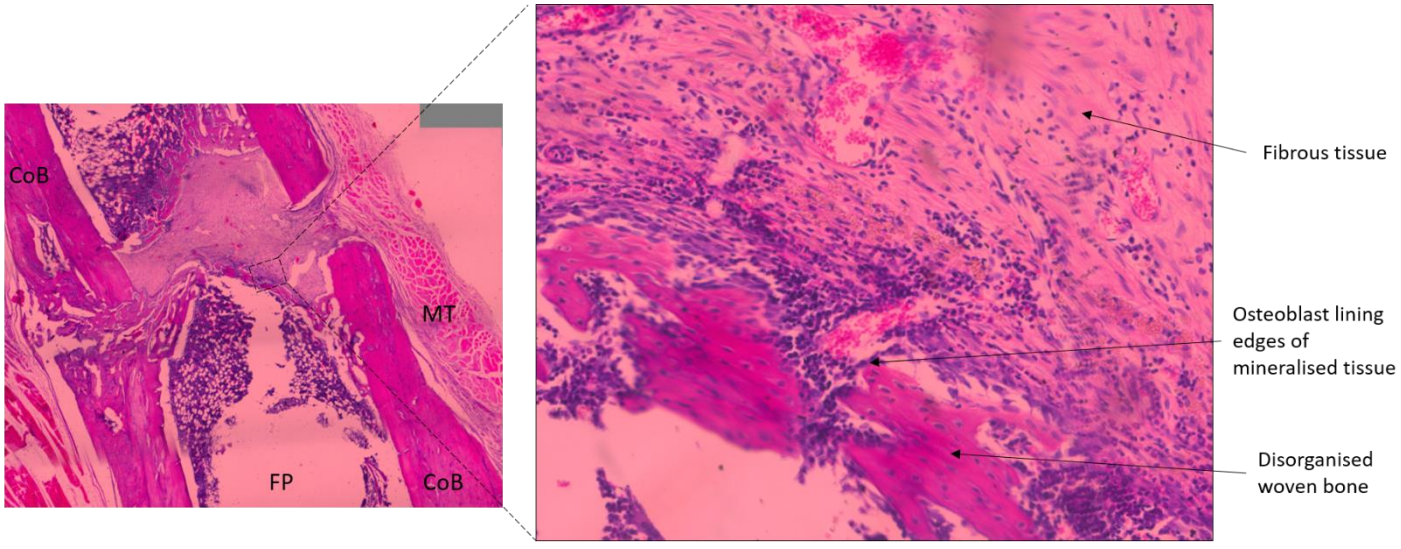

Figure 8: S4 Histology images of fracture healing in progress of 1 mm osteotomy gap. Images shown at x10 and x50 magnification; MT: muscular tissue, CoB: cortical bone, FP: fixator pin location

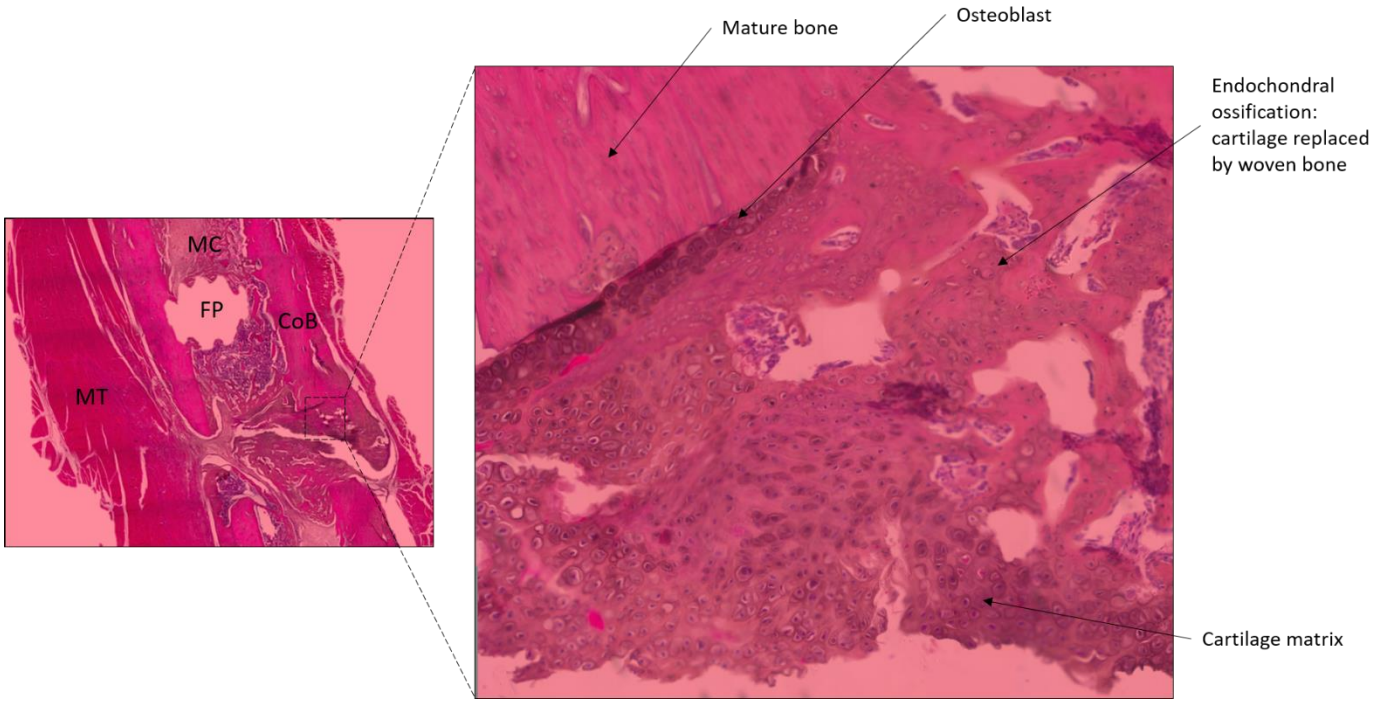

Figure 9: S5 Histology images of fracture healing in progress of 2 mm osteotomy gap. Images shown at x10 and x50 magnification; MT: muscular tissue, MC: marrow cavity, CoB: cortical bone, FP: fixator pin location.

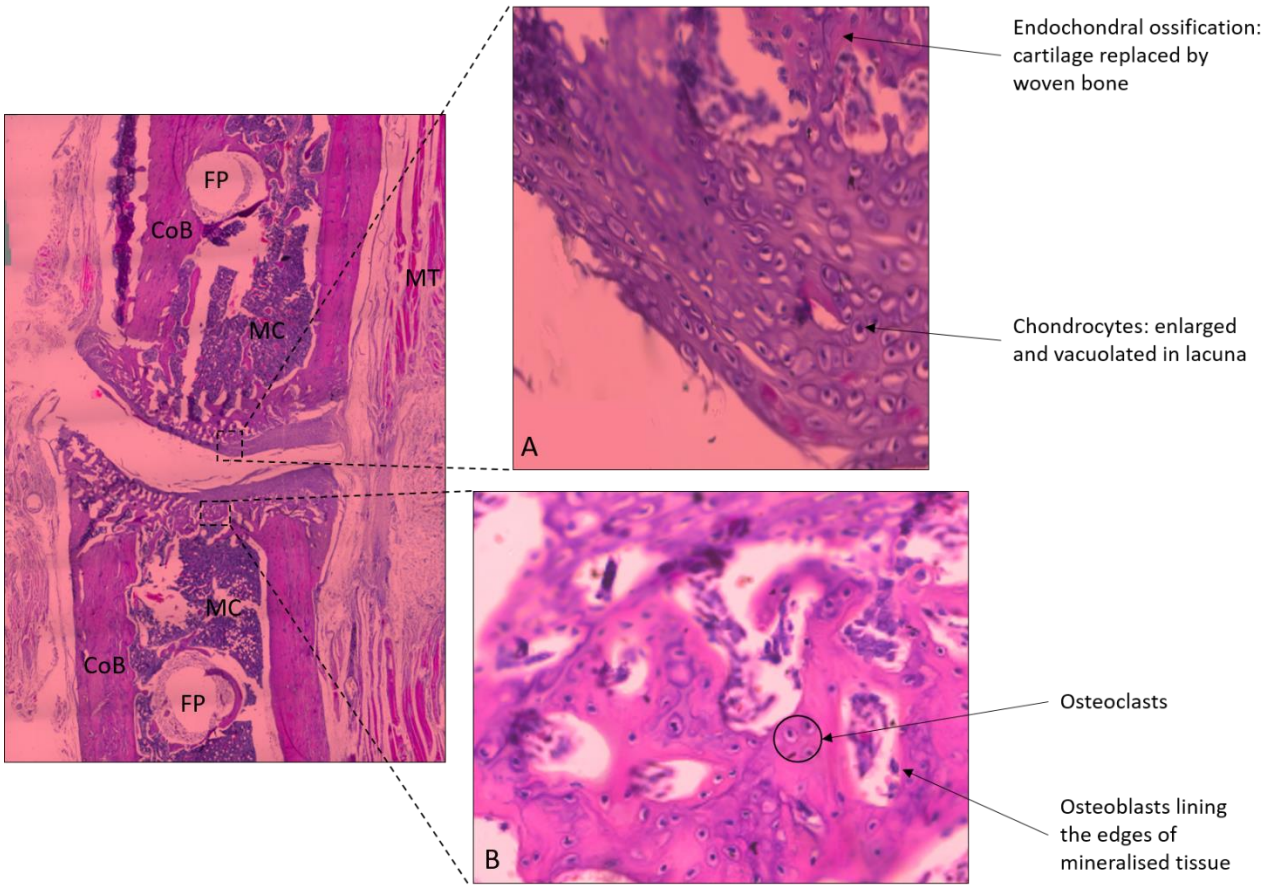

Figure 10: S6 Histology images of pseudarthrosis of 2 mm osteotomy gap. Images shown at x10 and x50 magnification; MT: muscular tissue, MC: marrow cavity, CoB: cortical bone, FP: fixator pin location. (A): Cartilage matrix, (B): region of endochondral ossification.

Discussion

XCT images showed that the fracture healing status differed in all 6 samples, having complete (S1, Fig.1A) and partial (S2-S4, Fig.2A-C and S5, Fig.3A) healing, as well as non-union (S6, Fig.3B). The tissue formation patterns throughout the healing process highly depended on the duration of the healing, gap size and intramembranous strain induced by the fixator [21,44,45]. In fact, as seen in sheep tibia, an early stage of healing a semi-rigid fixation lead to higher levels of callus formation compare to a rigid one. However, after two weeks callus densification is more advanced with rigid-fixation, due to the more stable mechanical environment [44]. It was also observed that the healing is influenced by the location of the external fixator. In fact, the side of bone adjacent to the fixation displayed a slower callus development [44]. This has been apprehended on the reduced interfragmentary movement closer to the fixator site [15].

The IFS induced by the SMExF in this study has been evaluated previously in similar rat femur models [21]. It was determined that for the 1 mm and 2 mm osteotomy gaps, the IFS accounted for 11.2 ± 13 and 6.1 ± 1.2% N/mm respectively, whilst the stiffness remained the same. In both this study and the one of Meeson et al. (2019) [21] the 2 mm gap samples exhibited a reduced healing compared to that of the 1 mm. Conversely, to Perren theory [1] where IFS needs to be below 2% to stimulate fracture healing, in Meeson et al. (2019) the reduction in the IFS and increase in the gap size inhibited the healing [21]. The variation in the tissue formation affected the strain distribution under the two displacement conditions. It has been shown that the intermittent tissue calcification during endochondral ossification and continuing growth of callus volume, increased the fracture stiffness and stability [6].

This clarified the divergence in the strain levels of the tissue. In the 1 mm osteotomy gap samples (Fig. 5) at ΔL = 0.5 mm, S2 exhibited high strain accumulation laterally. Compressive strain (≈ -30000 με) appeared in the area with visually higher levels of hard callus formation. From the histology images it was seen that area under tension is filled with cartilage matrix and mineralised chondrocytes (Fig. 6). This was promoted by an unstable interfragmentary mechanical environment, where the woven bone sustained the compressive load causing the cartilage matrix to tension. S3 and S4 displayed lower strain levels compared to S2 in the first compression step reaching -4000 and -5000 με, respectively (Fig. 4). Specifically, it is realised that lower strain was distributed when woven bone was present in either side of the gap, maintaining a stable mechanical environment. The callus formation in S4 supported the compressive load at ΔL = 1.0 mm without signs of buckling and concentration of compressive strain is experienced on both sides of the fracture (Fig. 4). The behaviour of S3 and S4 is better understood from the histology images. S3 illustrates an even distribution of soft and hard callus

formation in the osteotomy gap. As seen in the higher magnification images (Fig. 7) with soft callus formation and advanced endochondral ossification where the cartilage matrix mineralised into woven bone. The combination of the two provided the mechanical support in the overall structure under loading [2,28]. However, the fact that endochondral ossification was more dominant on one side instigated the buckling effect. In the case of S4 the XCT images showed high levels of woven bone formation extra- and intracortically and it could be assumed that the bone was at the beginning of the remodelling stage in the fracture healing (Fig. 2) [22]. Only a small region presented no hard callus formation. The histology images of that area showed presence of fibrous tissue along with osteoblast in close proximity (Fig. 8).

S5 showed increased levels of compressive strain localised in the intracortical callus in the first compression step, which extended towards the rest of the callus as well as the cortical cortex of the fracture ends in the second step. In this case of 2 mm osteotomy gap, union has formed, providing interfragmentary mechanical stability [2]. At the second compression step the distal side of the fracture with the delayed endochondral ossification exhibited less strain levels in the order of -6000 με. The histological analysis showed presence of cartilage matrix in that area that helped load transfer in these regions (Fig. 9) [46]. Although the maximum value of strain is decreased at ΔL = 1.0 mm, the volume under higher compressive strain levels increased thus maintaining the higher load. The last specimen S6 was a clear case of non-union. The load was conveyed between the two fracture ends through contact and sustained by the skin and muscles surrounding the bone. This assumption is made through observation of the specimen status post-XCT imaging and histological analysis (Fig. 3, 10). By contact, the fracture ends of the specimen appeared to be more flexible than the rest and visually there was no tearing of the skin surrounding the bone. From the histological images endochondral ossification was detected; however, there was no bridging. Both ends were surrounded by cartilage matrix. The sliding-like effect of the compressive load deformed the interfragmentary mineralised tissue reaching locally a maximum of approximately -30000 με (Fig. 5B).

Control samples were not available for comparison of the mechanics of intact and whole bone during fracture healing. However, the strain induced via compression on healthy young and mature rat femurs has been measured previously using DIC on the surface on the diaphysis [37]. The full-field measurements before failure displayed high levels of strain in the diaphysis reaching approx. -11000 με in the younger specimens and -17000 με in the mature ones. Furthermore, full-field strain distribution using DVC in long bones under physiological loading conditions (not exceeding 13 N of total load) exhibited higher strain level in the proximal and distal end of the bone [35]. Specifically, the highest and lowest ε_{p3} values in the mid-shaft region in all the specimens reached -17000 ± 2390 and -7504 ± 4347 με. In the current study, the strains obtained for the fracture site at the first

compression step in S4 were one order of magnitude lower than the ones presented in both these studies [35,37]. Overall, the first specimen group only locally in the extracortical woven bone exhibited higher values of strain than that mentioned in Giorgi and Dall'Ara. The full-field strain measurements in the second group displayed higher values (-43000 με), which can be attributed to the larger osteotomy gap and therefore axial volume of woven bone.

The mechanical behaviour of the soft tissue (cartilage matrix, muscles and skin) in the fracture site cannot be quantified with XCT-based evaluations. The cartilage matrix, where endochondral ossification occurred, should have experienced similar deformation as the woven bone around it. However, in areas of intramembranous ossification the strain was unknown. Characterisation of the mechanical properties of the callus formed via intramembranous ossification is vital in the understanding of factors determining healing process and mechanical stability [25]. In fact, the heterogeneity of an external callus formed during healing (next to the periosteum) has been assessed by means of nanoindentation [16]. The indentation modulus across the mineralised tissue showed an increase over the first 6 weeks of healing at the rate of 2.5 GPa/week. Additionally, after 6 and 9 weeks it was found to reach approximately 13 GPa, which was considerably less than that of the neighbouring cortical bone tissue (28 GPa). Nanoindentation of the newly formed woven bone has been performed to investigate the spatial and temporal differences of its elastic modulus [17]. The study demonstrated the heterogeneity of the indentation modulus with a coefficient of variation ranging from 18 to 60%. The mechanical behaviour of intervertebral discs, which consist hyaline cartilage, has been previously examined through DIC [47]. More specifically, whole vertebral elements were compressed and the vertebral discs connecting the bodies showed higher levels of strain compared to that of the vertebral bodies. In fact, under lateral bending the side of the intervertebral disk under tension ε_1 reached a maximum of 143000 με; during flexion ε_1 varied between 12000 and 87000 με. The strain values for the vertebral discs were below 500 and 600 με for bending and flexion respectively. The differences in strain magnitude between the bone and the cartilage represent the more elastic behaviour of the second. The mechanical properties of woven bone in fracture sites have been also compared to that of the adjacent mature bone by means of nanoindentation. The indentation modulus obtained from the mineralised callus after 6 weeks of healing was between 10 to 13 GPa, considerably less than that of the cortical bone adjacent to it, 28 ± 1.0 GPa [16]. The high full-field strain measurements on the surface of cartilaginous vertebral discs [47] and the lower values of indentation modulus [16] can explain the high strain values attained in new regenerated tissue under compression in all six specimens for the current study. 3D full-field strain concentration in regenerated tissue has been examined in cylindrical trabecular bone specimens that included osteoregenerative grafts [27]. DVC analysis was performed in regions which included the interface between the native bone tissue and

grafts. In the case of this study there are no biomaterials introduced to the structure; however, a correlation can be made in the strain values of regenerated tissue between the two studies. The specimen with the largest amount of new bone formation displaced higher compressive strain levels in the regenerated tissue compared to bone graft reaching a maximum of -15000 με.

Limitations should be considered in this study. A limited number of samples for both 1 mm and 2 mm osteotomy gaps were available and the ex situ analysis is representative of a single time point. Therefore, generalisation of the current results will require further analysis. Nevertheless, the differences observed in the bone formation for both osteotomy gaps were indicative of the local strain distribution induced in vivo during the remodelling phase. Despite the fact that mechanics of bone tissue may be altered by the fixation process, it has been shown that fixation should not alter the elastic properties of bone [48]. In the future, to better understand the behaviour of new bone formation in fracture healing, fresh bones should be tested following the same procedure.

Conclusions

This study presented an approach to evaluate the full-field strain distribution, within the regenerated tissue of two different osteotomy gaps in the diaphysis of rat femurs, induced by compression loading in the apparent elastic region. The regenerated mineralised tissue was evaluated via high-resolution XCT imaging and the soft callus formation was examined through histology. All specimens were at a different stage of healing progress leading to variability in the strain values under loading. The histological analysis showed endochondral ossification in all the specimens however, in the last one bridging of the tissue was not present. Overall, it was observed that in the specimens with partial regeneration the newly formed bone was able to withstand high strain values (ε_{p3} between -30000 and -40000 με). In the case of non-union the strain accumulation reached a maximum of -30000 με (ε_{p3}), the cartilaginous and soft tissues in the region of the osteotomy gap sustained the load.

Acknowledgments

The authors gratefully acknowledge Dr Robin Rumney, Ms Lowrie Vayro, Ms Amanda Chase and Ms Julie Rogers (School of Pharmacy and Biomedical Sciences, University of Portsmouth) for their assistance in the histology protocol, Mr Geoff Britton and Mr Robert Elliot (School of Mechanical and Design Engineering, University of Portsmouth) for their help with the experimental set up. The Zeiss Global Centre (University of Portsmouth) provided XCT imaging and DVC capability to conduct this study. This study is part of a PhD programme funded by the Faculty of Technology (University of Portsmouth).

This study was partially funded by the Medical Research Council (grant no., UK: MR/N002318/1)

References

[1] S.M. Perren, Physical and biological aspects of fracture healing with special reference to internal fixation, Clin. Orthop. Relat. Res. (1979) 175–196. http://journals.lww.com/corr/Citation/1979/01000/Physical_and_Biological_Aspects_of_Fracture.27.aspx.

[2] F. Loi, L.A. Córdova, J. Pajarinen, T. hua Lin, Z. Yao, S.B. Goodman, Inflammation, fracture and bone repair, Bone. 86 (2016) 119–130. doi:10.1016/j.bone.2016.02.020.

[3] L. Claes, S. Recknagel, A. Ignatius, Fracture healing under healthy and inflammatory conditions, Nat. Rev. Rheumatol. 8 (2012) 133–143. doi:10.1038/nrrheum.2012.1.

[4] Z. Zhao, D. Yang, X. Ma, H. Zhao, C. Nie, Z. Si, Successful Repair of a Critical-Sized Bone Defect in the Rat Femur with a Newly Developed External Fixator, Tohoku J. Exp. Med. 219 (2009) 115–120. doi:10.1620/tjem.219.115.

[5] B. McKibbin, The biology of fracture healing in long bones, J. Bone Jt. Surg. 60-B (1978) 150–162. doi:10.1007/978-1-4471-5451-8_139.

[6] P.J. Harwood, J.B. Newman, A.L.R. Michael, (ii) An update on fracture healing and non-union, Orthop. Trauma. 24 (2010) 9–23. doi:10.1016/j.mporth.2009.12.004.

[7] R. Marsell, T.A. Einhorn, The biology of fracture healing, Injury. 42 (2011) 551–555. doi:10.1016/j.injury.2011.03.031.

[8] S. Ochandiano Caicoya, Bone cavity filling with alloplastic material in maxillofacial surgery, Rev Esp Cir Oral y Maxilofac. 1 (2007) 21–32. doi:10.4321/S1130-05582007000100003.

[9] J.P. Schmitz, J.O. Hollinger, The Critical Size Defect as an Experimental Model for Craniomandibulofacial Nonunions, Clin. Orthop. Relat. Res. (1985) 299–308.

[10] J.O. Hollinger, J.C. Kleinschmidt, The critical size defect as an experimental model to test bone repair materials., J. Craniofac. Surg. 1 (1990).

[11] L. Claes, R. Grass, T. Schmickal, B. Kisse, C. Eggers, H. Gerngroß, W. Mutschler, M. Arand, T. Wintermeyer, A. Wentzensen, Monitoring and healing analysis of 100 tibial shaft fractures, Langenbeck's Arch. Surg. 387 (2002) 146–152. doi:10.1007/s00423-002-0306-x.

[12] S.J. Kaplan, W.C. Hayes, P. Mudan, J.L. Lelli, A.A. White, Monitoring the healing of a tibial osteotomy in the rabbit treated with external fixation, J. Orthop. Res. 3 (1985) 325–330. doi:10.1002/jor.1100030309.

[13] F.G. Lippert, C. Hirsch, The three dimensional measurement of tibia fracture motion by photogrammetry, Clin. Orthop. Relat. Res. 105 (1974) 130–143.

[14] K. Seide, N. Weinrich, M.E. Wenzl, D. Wolter, C. Jürgens, Three-dimensional load measurements in an external fixator, J. Biomech. 37 (2004) 1361–1369. doi:10.1016/j.jbiomech.2003.12.025.

[15] L. Claes, Biomechanical principles and mechanobiologic aspects of flexible and locked plating, J. Orthop. Trauma. 25 (2011) 4–7. doi:10.1097/BOT.0b013e318207093e.

[16] I. Manjubala, Y. Liu, D.R. Epari, P. Roschger, H. Schell, P. Fratzl, G.N. Duda, Spatial and temporal variations of mechanical properties and mineral content of the external callus during bone healing, Bone. 45 (2009) 185–192. doi:10.1016/j.bone.2009.04.249.

[17] J. Mora-Macías, A. Pajares, P. Miranda, J. Domínguez, E. Reina-Romo, Mechanical characterization via nanoindentation of the woven bone developed during bone transport, J. Mech. Behav. Biomed. Mater. 74 (2017) 236–244. doi:10.1016/j.jmbbm.2017.05.031.

[18] M. Zandi, A. Dehghan, F. Gheysari, L. Rezaeian, N. Mohammad Gholi Mezerji, Histological evaluation of the healing process of autografted mandibular bone defects in rats under treatment with zoledronate, European Association for Cranio-Maxillo-Facial Surgery, 2019. doi:10.1016/j.jcms.2018.11.015.

[19] D.R. Epari, H. Schell, H.J. Bail, G.N. Duda, Instability prolongs the chondral phase during bone healing in sheep, Bone. 38 (2006) 864–870. doi:10.1016/j.bone.2005.10.023.

[20] L. Claes, P. Augat, S. Schorlemmer, C. Konrads, A. Ignatius, C. Ehrnthaller, Temporary distraction and compression of a diaphyseal osteotomy accelerates bone healing, J. Orthop. Res. 26 (2008) 772–777. doi:10.1002/jor.20588.

[21] R. Meeson, M. Moazen, A. Sanghani-Kerai, L. Osagie-Clouard, M. Coathup, G. Blunn, The influence of gap size on the development of fracture union with a micro external fixator, J. Mech. Behav. Biomed. Mater. 99 (2019) 161–168. doi:10.1016/j.jmbbm.2019.07.015.

[22] H. Isaksson, I. Gröngröft, W. Wilson, C.C. Van Donkelaar, B. Ven Rietbergen, A. Tami, R. Huiskes, K. Ito, Remodeling of fracture callus in mice is consistent with mechanical loading and bone remodeling theory, J. Orthop. Res. 27 (2009) 664–672. doi:10.1002/jor.20725.

[23] E.F. Morgan, Z.D. Mason, K.B. Chien, A.J. Pfeiffer, G.L. Barnes, T.A. Einhorn, L.C. Gerstenfeld, Micro-computed tomography assessment of fracture healing: Relationships among callus structure, composition, and mechanical function, Bone. 44 (2009) 335–344. doi:10.1016/j.bone.2008.10.039.

[24] T. Kustro, T. Kiss, D. Chernohorskyi, Y. Chepurnyi, Z. Helyes, A. Kopchak, Quantification of the mandibular defect healing by micro-CT morphometric analysis in rats, J. Cranio-Maxillofacial Surg. 46 (2018) 2203–2213. doi:10.1016/j.jcms.2018.09.022.

[25] S.J. Shefelbine, U. Simon, L. Claes, A. Gold, Y. Gabet, I. Bab, R. Müller, P. Augat, Prediction of fracture callus mechanical properties using micro-CT images and voxel-based finite element analysis, Bone. 36 (2005) 480–488. doi:10.1016/j.bone.2004.11.007.

[26] Y. Gabet, R. Müller, E. Regev, J. Sela, A. Shteyer, K. Salisbury, M. Chorev, I. Bab, Osteogenic growth peptide modulates fracture callus structural and mechanical properties, Bone. 35 (2004) 65–73. doi:10.1016/j.bone.2004.03.025.

[27] M. Peña Fernández, E. Dall'Ara, A.J. Bodey, R. Parwani, A.H. Barber, G.W. Blunn, G. Tozzi, Full-Field Strain Analysis of Bone-Biomaterial Systems Produced by the Implantation of Osteoregenerative Biomaterials in an Ovine Model, ACS Biomater. Sci. Eng. 5 (2019) 2543–2554. doi:10.1021/acsbiomaterials.8b01044.

[28] T.E. Jørgensen, Measurements of stability of crural fractures treated with hoffmann osteotaxis: 2.measurements on crural fractures, Acta Orthop. 43 (1972) 207–218. doi:10.3109/17453677208991258.

[29] R. Hente, J. Cordey, S.M. Perren, In vivo measurement of bending stiffness in fracture healing, Biomed. Eng. Online. 2 (2003) 1–16. doi:10.1186/1475-925X-2-8.

[30] F. Gillard, R. Boardman, M. Mavrogordato, D. Hollis, I. Sinclair, F. Pierron, M. Browne, The application of digital volume correlation (DVC) to study the microstructural behaviour of trabecular bone during compression, J. Mech. Behav. Biomed. Mater. 29 (2014) 480–499. doi:10.1016/j.jmbbm.2013.09.014.

[31] M. Peña-Fernández, S. Cipiccia, E. Dall'Ara, A.J. Bodey, R. Parwani, M. Pani, G.W. Blunn, A.H. Barber, G. Tozzi, Effect of SR-microCT radiation on the mechanical integrity of trabecular bone using in situ mechanical testing and digital volume correlation., J. Mech. Behav. Biomed. Mater. 88 (2018) 109–119. doi:10.1016/j.jmbbm.2018.08.012.

[32] E. Dall'Ara, M. Peña-Fernández, M. Palanca, M. Giorgi, L. Cristofolini, G. Tozzi, Precision of Digital Volume Correlation Approaches for Strain Analysis in Bone Imaged with Micro-Computed Tomography at Different Dimensional Levels, Front. Mater. 4 (2017). doi:10.3389/fmats.2017.00031.

[33] G. Tozzi, V. Danesi, M. Palanca, L. Cristofolini, Elastic Full-Field Strain Analysis and Microdamage Progression in the Vertebral Body from Digital Volume Correlation, Strain. 52 (2016) 446–455. doi:10.1111/str.12202.

[34] D. Christen, A. Levchuk, S. Schori, P. Schneider, S.K. Boyd, R. Müller, Deformable image registration and 3D strain mapping for the quantitative assessment of cortical bone microdamage, J. Mech. Behav. Biomed. Mater. 8 (2012) 184–193. doi:10.1016/j.jmbbm.2011.12.009.

[35] M. Giorgi, E. Dall'Ara, Variability in strain distribution in the mice tibia loading model: A preliminary study using digital volume correlation, Med. Eng. Phys. 62 (2018) 7–16. doi:10.1016/j.medengphy.2018.09.001.

[36] P. Sztefek, M. Vanleene, R. Olsson, R. Collinson, A.A. Pitsillides, S. Shefelbine, Using digital image correlation to determine bone surface strains during loading and after adaptation of the mouse tibia, J. Biomech. 43 (2010) 599–605. doi:10.1016/j.jbiomech.2009.10.042.

[37] S.A. Yavari, J. van der Stok, H. Weinans, A.A. Zadpoor, Full-field strain measurement and fracture analysis of rat femora in compression test, J. Biomech. 46 (2013) 1282–1292. doi:10.1016/j.jbiomech.2013.02.007.

[38] T.M. Keaveny, X.E. Guo, T.A. McMahon, E.F. Wachtel, W.C. Hayes, Trabecular bone exhibits fully linear elastic behavior and yields at low strains, J. Biomech. 27 (2004) 1127–1136. doi:10.1016/0021-9290(94)90053-1.

[39] K. Madi, G. Tozzi, Q.H. Zhang, J. Tong, A. Cossey, A. Au, D. Hollis, F. Hild, Computation of full-field displacements in a scaffold implant using digital volume correlation and finite element analysis, Med. Eng. Phys. 35 (2013) 1298–1312. doi:10.1016/j.medengphy.2013.02.001.

[40] M. Palanca, A.J. Bodey, M. Giorgi, M. Viceconti, D. Lacroix, L. Cristofolini, E. Dall'Ara, Local displacement and strain uncertainties in different bone types by digital volume correlation of synchrotron microtomograms, J. Biomech. 58 (2017) 27–36. doi:10.1016/j.jbiomech.2017.04.007.

[41] M. Palanca, G. Tozzi, L. Cristofolini, M. Viceconti, E. Dall'Ara, Three-Dimensional Local Measurements of Bone Strain and Displacement: Comparison of Three Digital Volume Correlation Approaches, J. Biomech. Eng. 137 (2015) 071006. doi:10.1115/1.4030174.

[42] L.C. Junqueira, J. Carneiro, Basic Histology text & atlas, 11th ed., McGraw-Hill companies, 2005.

[43] M.H. Ross, P. Wojciech, Histology a Text and Atlas With correlated cell and molecular biology, 5th ed., LIPPINCOTT WILLIAMS & WILKINS, Baltimore, 2006.

[44] A. Vetter, D.R. Epari, R. Seidel, H. Schell, P. Fratzl, G.N. Duda, R. Weinkamer, Temporal tissue patterns in bone healing of sheep, J. Orthop. Res. 28 (2010) 1440–1447. doi:10.1002/jor.21175.

[45] M.J. Gómez-Benito, J.M. García-Aznar, J.H. Kuiper, M. Doblaré, Influence of fracture gap size on the pattern of long bone healing: A computational study, J. Theor. Biol. 235 (2005) 105–119. doi:10.1016/j.jtbi.2004.12.023.

[46] M.S. Ghiasi, J. Chen, A. Vaziri, E.K. Rodriguez, A. Nazarian, Bone fracture healing in mechanobiological modeling: A review of principles and methods, Bone Reports. 6 (2017) 87–100. doi:10.1016/j.bonr.2017.03.002.

[47] M. Palanca, M. Marco, M.L. Ruspi, L. Cristofolini, Full-field strain distribution in multi-vertebra spine segments: An in vitro application of digital image correlation, Med. Eng. Phys. 52 (2018) 76–83. doi:10.1016/j.medengphy.2017.11.003.

[48] J. Wieding, E. Mick, A. Wree, R. Bader, Influence of three different preservative techniques on the mechanical properties of the ovine cortical bone, Acta Bioeng. Biomech. 17 (2015) 137–146. doi:10.5277/ABB-00067-2014-03.

Chapter 6 - Synopsis

6.1 Discussion

The main aim of this PhD thesis is to investigate bone mechanical properties at different scales to provide a better understanding of its mechanical behaviour. Bone is an anisotropic [1–3], heterogeneous [4–6], hierarchical [7–9] material and its structure implies that the microstructural mechanical properties can predict the macrostructural behaviour [10]. Therefore, in order to better understand bone mechanics a multiscale investigation is essential. This project has been a combination of three main studies evaluating the native trabecular (Chapter 3), cortical bone (Chapter 4) leading up to mechanics at organ level and investigation of regenerated bone tissue (Chapter 5).

Laboratory-based X-ray computed tomography (XCT) and digital volume correlation analysis (DVC) were the two main techniques used throughout this work. The combination of the two has been previously employed for bone at both apparent and tissue level [11–14]. Specifically, the Versa Xradia 510 (Zeiss, USA) at the Zeiss Global Centre (University of Portsmouth) was used for the XCT imaging in all the studies involved. DVC analysis was implemented to assess the three-dimensional (3D) full-filed strain in bone due to the respective mechanical tests (DaVis 10.0.3, LaVision, UK).

XCT imaging has been used extensively in this study to characterise the morphology of bone. The resolution capabilities of the equipment were investigated reaching 0.13 µm voxel size for imaging of a single trabecula. In fact, the original aim of the first study was to examine the plastic deformation of microindentation imprint on trabecular bone using in situ XCT mechanics and DVC. However, it was observed that high-resolution XCT required longer exposure times to obtain a high signal-to-noise-ratio for good quality images, which are essential in morphological and DVC analysis [15]. Nonetheless, the long exposure to the radiation was observed to affect bone structural and mechanical properties [16–18]; therefore, it was deemed essential to first investigate the degradation of mechanical properties in the sub-microscale due to the irradiation. Microindentation at 2.5 µm depth was performed using a nanoindenter on the surface of trabecular bone pre- and post-irradiation. Additionally, high-resolution XCT imaging and DVC analysis were employed to assess the damage due to the irradiation in the 3D volume of the specimens underneath the indented areas. Tomograms of the specimens were acquired at two different resolutions; at 1.86 µm where an overview of the whole specimen volume was obtained and at 0.13 µm where a zoom in, focusing on a single trabecula was completed. The control specimens that were exposed to the radiation of the overview scan, did not show any change in the elastic modulus nor strain accumulation higher than 2000 µε. That lead to the conclusion that at 1.86 µm voxel size and 60 kV with total exposure time of approximately 9 hours, the irradiation did not affect the bone mechanics at the micro-level. In the specimens exposed to the

high-resolution XCT imaging with long exposure times (total exposure of 69 hours), large crack formation was present corresponding to strain values that exceeded 10000 με in both the third principal and shear strain (ε_{p3} and γ_{max} respectively). High-resolution XCT imaging with long exposure times such as the one used here are essential in evaluating the microstructure of bone [15]. In fact in situ indentation has been achieved previously using a Histron nanomechanical testing rig inside a Zeiss Xradia 520 Versa XCT, in order to evaluate crack formation in nanoindentation of mice femoral head [19]. The overall imaging time was 52 hours with a pixel size ranging between 2-3 μm. Evidently, this type of imaging is vital in understanding bone mechanics at the microlevel, however the mechanics can be affected by the irradiation. This was also observed in the elastic modulus attained here, where trabeculae with less damage accumulation displayed an increase of elastic modulus (from 19.11 to 21.97 GPa after 66 hours of irradiation), whereas those with more damage a decrease (from 10.13 to 7.39 GPa after 66 hours of irradiation). It is therefore vital to preserve the mechanical properties when examining the behaviour of bone, hence, the rest of the studies involved here did not exceed 10 hours of imaging p/experiment as well as 1.86 μm voxel size. A complementary study, assessing the effect of temperature in the preservation of cortical and trabecular bone tissue integrity during irradiation in SR-XCT, has been produced in the duration of this PhD project [20]. Microdamage was observed in trabecular bone at room temperature whereas at 0° no microcracks formed neither in cortical, nor in trabecular bone. The strain developed in the tissue due to irradiation was computed using DVC. High levels of residual strain ($\varepsilon_{p1} \approx 3500$ με) were displayed in areas of microcrack formation in trabecular bone at room temperature. In the cortical bone, although no crack formation was observed, high levels of strain accumulation ($\varepsilon_{p1} \approx 4000$ με) was seen around the Haversian and Volkmann's canals. From both lab-XCT and SR-XCT studies, emerged the necessity of carefully designing in situ experiment in order to obtain meaningful mechanical information that would not be (or minimally) affected by exposure to X-ray radiation.

Eventually, to avoid tissue degradation and examine progressive bone plastic deformation via indentation, the indent and voxel size were increased. An experimental set-up was designed for in situ indentation using a Vickers tip and cortical bone microstructure was studied using in situ indentation in the microscale, while the XCT imaging was performed using 4 μm voxel size. In comparison to the trabecular bone, where specimens were retrieved in the axial direction, the cortical bone specimens were extracted from both transverse and axial directions (with respect to the long bone axis). This is essential in order to understand the influence of microstructure orientation on the behaviour of bone during plastic deformation. In accordance with the findings of Basillais et al. (2007) [21], microcracks occurred in the axial specimens, whereas the transversely cut ones did not display any crack formation. This was due to the orientation of the larger canals in the structure (Haversian canals) [22],

that were perpendicular to the indentation tip. Moreover, DVC was performed to assess the plastic deformation in the region of indentation, as well as the deformation induced to the microstructure of the cortical bone due to the testing. Tensile strain values reached 29000 με in the imprint region and compressive strain up to -26000 με underneath this region locally. The strain accumulation in the rest of the volume varied depending on the distribution of the cortical bone canal network. In fact, strain distribution related to canal network and osteocyte lacunae in cortical bone has been previously investigated [23]. An artificial notch was introduced in the diaphysis of the femur transversely and the bone was step-wise compressed (in situ SR-XCT) until failure. Tensile strain, exceeding 15% was accumulated around the osteocyte lacunae where microcrack formation occurred, whereas the rest of the volume was experiencing shear strain locally [23]. Although strain values reported in the study of Christen et al. (2012) are greater compare to the ones observed here, both studies show tensile strain concentration around canals where microfracture occurred.

At last, mechanical behaviour at organ level was examined with in situ XCT step-wise compression testing and the 3D full-field elastic deformation induced in the bone was evaluated using DVC analysis. The regeneration of the tissue in the osteotomy gap was not complete at the time of femur extraction and the irregular shape of the tissue in this region led to high local strains. The DVC results displayed a combination of compressive and tensile strain reaching ~-30000 and ~29000 με respectively, after the second step of compression in the newly formed woven bone. It should be noted that DVC at organ level (mice tibia) has been previously studied for bone under physiological condition reaching minimum principal strain approximately -17000 με in the mid-shaft [24]. The differences found in these values and the ones reported here for the newly formed bone, can be attributed not only to irregular shape of the tissue but also to its mineralisation state. The radiolucent soft tissues in the rat femurs were studied using histological analysis. Using 50x magnification lens in the microscope (Olympus BX40, Leica Biosystems, UK) details of the cells in the osteotomy gap were acquired. Cartilage matrix was present, in areas not observable in the XCT tomograms, connecting the woven bone in the osteotomy gap and allowing for load transfer between the fracture ends. The sporadic advanced endochondral ossification detected was evidence of healing in progress [25] leading to the assumption that if more time was allowed for healing it would have reached full resorption.

6.2 Conclusions

A multi-scale study of bone mechanics was completed, where the sub-micron, microstructure and organ level mechanics were investigated. A variety of methods were employed for the mechanical characterisation at the different scales i.e. submicron, microscale and mechanics at organ level. Indentation was performed in both the trabecular and cortical bone studies. In the first, depth control

microindentation was completed, and the elastic modulus of bone was attained with a depth of indentation of 2.5 μm, the size of approximately three lamellae. In situ XCT indentation was carried out on the cortical bone, in the microscale, where a Vickers tip was mounted on a loading stage (CT5000, Deben, UK) using a custom made set up. The total displacement of the tip was 0.4 mm and the technique was used to induce plastic deformation in a known geometry of the cortical bone specimen. In the last part of this study, rat femurs, with diaphyseal fracture healing, were examined using in situ XCT compression, using the same loading stage as before. The mechanical behaviour of the mineralised woven bone in the fracture was evaluated via DVC from the XCT datasets and the non-mineralised soft tissues were studied through histological analysis.

In this work, an investigation of native and regenerated bone mechanical properties has been carried out using a range of experimental techniques. The following main conclusions are drawn:

- Laboratory-based XCT radiation caused degradation in bone mechanical properties at tissue level. It was observed that exposure for approximately 9 hours is unlikely to induce damage, thus experimental protocols should consider exposure time as a major factor in their methodology.
- Optimisation between exposure time and resolution in imaging is also essential for high-quality tomograms, which are used for morphological and DVC analysis of bone.
- The strain accumulation in the tissue showed an increase with the increase of the irradiation, due to the high-resolution XCT imaging, exceeding 10000 με.
- Cortical bone microstructure is a significant determinant in its mechanical behaviour. The orientation and arrangement of its canals (i.e. Haversian and Volkmann's) as well as the pore distribution encourage or prevent fracture, when plastic deformation occurs.
- The change in the canal network parameters (i.e. number, diameter size) can be attributed to the compressive and tensile strain applied during indentation, hence supporting the argument of its importance in bone structural integrity. Tensile strain was accompanied by widening of the canal diameters and increase in the number of canals locally. Additionally, compressive strain was observed when canal loss occurred.
- The strain distribution in the regenerated woven bone of fracture healing resulted highly dependent on the presence of mineralised tissue. Specimens with higher level of mineralisation showed a more uniform distribution of the strain.
- Combination of compressive and tensile strain was observed in all the specimens since healing was in progress exceeding 30000 με.

- Histological results provided information on the non-mineralised, radiolucent tissue in the fracture as well as the progress in the regeneration process.
- Overall, DVC has been deemed a reliable method to measure the 3D full-field deformation in the tissue and apparent level of bones.
- The mechanics of native and regenerated tissue were examined with techniques addressing primarily the microscale. The mechanical behaviour of native bone shows consistent patterns of strain, whereas woven bone mechanics is highly dependent on the degree of mineralisation. Moreover, in the case of bone with diaphyseal fracture healing, organ level mechanics are dictated by the healing progress.

6.3 Future work

Degradation of mechanical properties due to irradiation

Although the degradation of the mechanical properties has been identified, the dose of radiation induced on bone should also be evaluated either computationally or experimentally with dosimeters. Furthermore, it could be of great interest to assess the point at which degradation in the mechanical properties of tissue occurs in different laboratory-based XCT imaging scenarios. In fact, the increased use of XCT imaging systems in bone evaluation demands knowledge of such limitation. These will provide valuable information for in situ XCT experimental protocols requiring long X-ray exposures.

Microstructural morphology evaluation of cortical bone

It has been proven over the years that mechanical behaviour of cortical bone depends on its morphological arrangement. To better understand bone mechanics and inform computational models, the canal and pore network should be examined in organ level at a higher XCT resolution. Organ level mechanics can allow investigation of behaviour under physiological and high-energy impact response in the whole bone. Additionally, higher resolution has the advantage of examining the nanoscale mechanical behaviour of the tissue and its connection to the macrostructural response.

Mechanical behaviour of fracture healing at organ level

The experimental protocol applied in this work should be implemented in specimens at different time-points and post-operative. This will allow characterisation of the mechanics of the regenerated tissue at different stages assessing its ability to sustain load. Specimens at the resorption stage of the healing, where woven tissue is becoming lamellar bone, should also be evaluated in order to assess and understand the mechanical behaviour of the tissue during this stage, were there is no non-mineralised cartilage matrix present. Moreover, after the in situ XCT compression the specimens could be prepared for nano-/microindentation to obtain the elastic modulus at that scale, which was not

possible in the specimens used here since they were fixed in formalin solution. This will enhance the understanding of bone regeneration and its mechanical behaviour.

References

[1] U. Wolfram, H.J. Wilke, P.K. Zysset, Rehydration of vertebral trabecular bone: Influences on its anisotropy, its stiffness and the indentation work with a view to age, gender and vertebral level, Bone. 46 (2010) 348–354. doi:10.1016/j.bone.2009.09.035.

[2] G. Franzoso, P.K. Zysset, Elastic Anisotropy of Human Cortical Bone Secondary Osteons Measured by Nanoindentation, J. Biomech. Eng. 131 (2008) 021001. doi:10.1115/1.3005162.

[3] R. Oftadeh, M. Perez-Viloria, J.C. Villa-Camacho, A. Vaziri, A. Nazarian, Biomechanics and Mechanobiology of Trabecular Bone: A Review, J. Biomech. Eng. 137 (2015) 010802. doi:10.1115/1.4029176.

[4] C.E. Hoffler, K.E. Moore, K. Kozloff, P.K. Zysset, M.B. Brown, S.A. Goldstein, Heterogeneity of bone lamellar-level elastic moduli., Bone. 26 (2000) 603–9. http://www.ncbi.nlm.nih.gov/pubmed/10831932.

[5] A.M. Torres, J.B. Matheny, T.M. Keaveny, D. Taylor, C.M. Rimnac, C.J. Hernandez, Material heterogeneity in cancellous bone promotes deformation recovery after mechanical failure, Proc. Natl. Acad. Sci. 113 (2016) 2892–2897. doi:10.1073/pnas.1520539113.

[6] K.J. Goodwin, N.A. Sharkey, Material properties of interstitial lamellae reflect local strain environments, J. Orthop. Res. 20 (2002) 600–606. doi:10.1016/S0736-0266(01)00152-8.

[7] S. Pathak, S.J. Vachhani, K.J. Jepsen, H.M. Goldman, S.R. Kalidindi, Assessment of lamellar level properties in mouse bone utilizing a novel spherical nanoindentation data analysis method, J. Mech. Behav. Biomed. Mater. 13 (2012) 102–117. doi:10.1016/j.jmbbm.2012.03.018.

[8] A. Sharir, M.M. Barak, R. Shahar, Whole bone mechanics and mechanical testing, Vet. J. 177 (2008) 8–17. doi:10.1016/j.tvjl.2007.09.012.

[9] J. Rho, K.-S. Liisa, Z. Peter, Mechanical Properties and the hierarchical structure of bone, Nature. 20 (1998) 92–102. doi:10.1038/251673a0.

[10] X. Cai, H. Follet, L. Peralta, M. Gardegaront, D. Farlay, R. Gauthier, B. Yu, E. Gineyts, C. Olivier, M. Langer, A. Gourrier, D. Mitton, F. Peyrin, Q. Grimal, P. Laugier, Anisotropic elastic properties of human femoral cortical bone and relationships with composition and microstructure in elderly, Acta Biomater. 90 (2019) 254–266. doi:10.1016/j.actbio.2019.03.043.

[11] G. Tozzi, V. Danesi, M. Palanca, L. Cristofolini, Elastic Full-Field Strain Analysis and Microdamage Progression in the Vertebral Body from Digital Volume Correlation, Strain. 52 (2016) 446–455. doi:10.1111/str.12202.

[12] Y. Chen, E. Dall'Ara, E. Sales, K. Manda, R. Wallace, P. Pankaj, M. Viceconti, Micro-CT based finite element models of cancellous bone predict accurately displacement once the boundary condition is well replicated: A validation study, J. Mech. Behav. Biomed. Mater. 65 (2017) 644–651. doi:10.1016/j.jmbbm.2016.09.014.

[13] E. Dall'Ara, D. Barber, M. Viceconti, About the inevitable compromise between spatial resolution and accuracy of strain measurement for bone tissue: A 3D zero-strain study, J. Biomech. 47 (2014) 2956–2963. doi:10.1016/j.jbiomech.2014.07.019.

[14] M. Palanca, A.J. Bodey, M. Giorgi, M. Viceconti, D. Lacroix, L. Cristofolini, E. Dall'Ara, Local displacement and strain uncertainties in different bone types by digital volume correlation of synchrotron microtomograms, J. Biomech. 58 (2017) 27–36. doi:10.1016/j.jbiomech.2017.04.007.

[15] J.A. Meganck, B. Liu, Dosimetry in Micro-computed Tomography: a Review of the Measurement Methods, Impacts, and Characterization of the Quantum GX Imaging System, Mol. Imaging Biol. 19 (2017) 499–511. doi:10.1007/s11307-016-1026-x.

[16] H.D. Barth, M.E. Launey, A.A. MacDowell, J.W. Ager, R.O. Ritchie, On the effect of X-ray irradiation on the deformation and fracture behavior of human cortical bone, Bone. 46 (2010) 1475–1485. doi:10.1016/j.bone.2010.02.025.

[17] H.D. Barth, E.A. Zimmermann, E. Schaible, S.Y. Tang, T. Alliston, R.O. Ritchie, Characterization of the effects of x-ray irradiation on the hierarchical structure and mechanical properties of human cortical bone, Biomaterials. 32 (2011) 8892–8904. doi:10.1016/j.biomaterials.2011.08.013.

[18] M. Peña-Fernández, S. Cipiccia, E. Dall'Ara, A.J. Bodey, R. Parwani, M. Pani, G.W. Blunn, A.H. Barber, G. Tozzi, Effect of SR-microCT radiation on the mechanical integrity of trabecular bone using in situ mechanical testing and digital volume correlation., J. Mech. Behav. Biomed. Mater. 88 (2018) 109–119. doi:10.1016/j.jmbbm.2018.08.012.

[19] T. Lowe, E. Avcu, E. Bousser, W. Sellers, P.J. Withers, 3D Imaging of indentation damage in bone, Materials (Basel). 11 (2018) 1–13. doi:10.3390/ma11122533.

[20] M. Peña-Fernández, E. Dall'Ara, A.P. Kao, A.J. Bodey, A. Karali, G.W. Blunn, A.H. Barber, G. Tozzi, Preservation of bone tissue integrity with temperature control for in situ SR-MicroCT experiments, Materials (Basel). 11 (2018). doi:10.3390/ma11112155.

[21] A. Basillais, S. Bensamoun, C. Chappard, B. Brunet-Imbault, G. Lemineur, B. Ilharreborde, M.C. Ho Ba Tho, C.L. Benhamou, Three-dimensional characterization of cortical bone microstructure by microcomputed tomography: Validation with ultrasonic and microscopic measurements, J. Orthop. Sci. 12 (2007) 141–148. doi:10.1007/s00776-006-1104-z.

[22] J.D. Currey, Bones, 2nd ed., Princeton University Press, New Jersey, 2002.

[23] D. Christen, A. Levchuk, S. Schori, P. Schneider, S.K. Boyd, R. Müller, Deformable image registration and 3D strain mapping for the quantitative assessment of cortical bone microdamage, J. Mech. Behav. Biomed. Mater. 8 (2012) 184–193. doi:10.1016/j.jmbbm.2011.12.009.

[24] M. Giorgi, E. Dall'Ara, Variability in strain distribution in the mice tibia loading model: A preliminary study using digital volume correlation, Med. Eng. Phys. 62 (2018) 7–16. doi:10.1016/j.medengphy.2018.09.001.

[25] U. Simon, P. Augat, M. Utz, L. Claes, A numerical model of the fracture healing process that describes tissue development and revascularisation, Comput. Methods Biomech. Biomed. Engin. 14 (2011) 79–93. doi:10.1080/10255842.2010.499865.

Appendix

Chapter 4 - In situ XCT indentation

1st principal strain

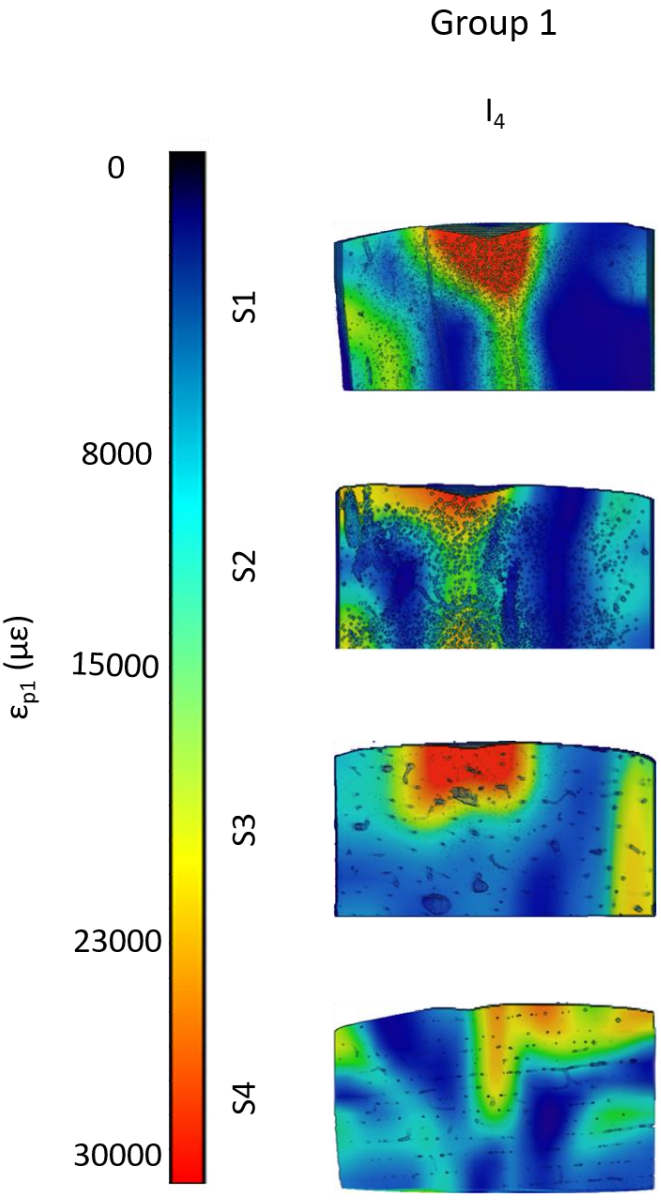

Figure A1: Visualisation of the strain maps (ε_{p1}) in axial (S1, S2) and transverse (S3, S4) specimens with one indentation step (I_4, Group 1). In all specimens, higher tensile strain values appeared on the imprint region. S1, S2, S3 experienced a combination of low and high tensile strain values reaching ~30000 με closer to the imprint. In S4, the strain was increasing steadily as the depth of the defect increased.

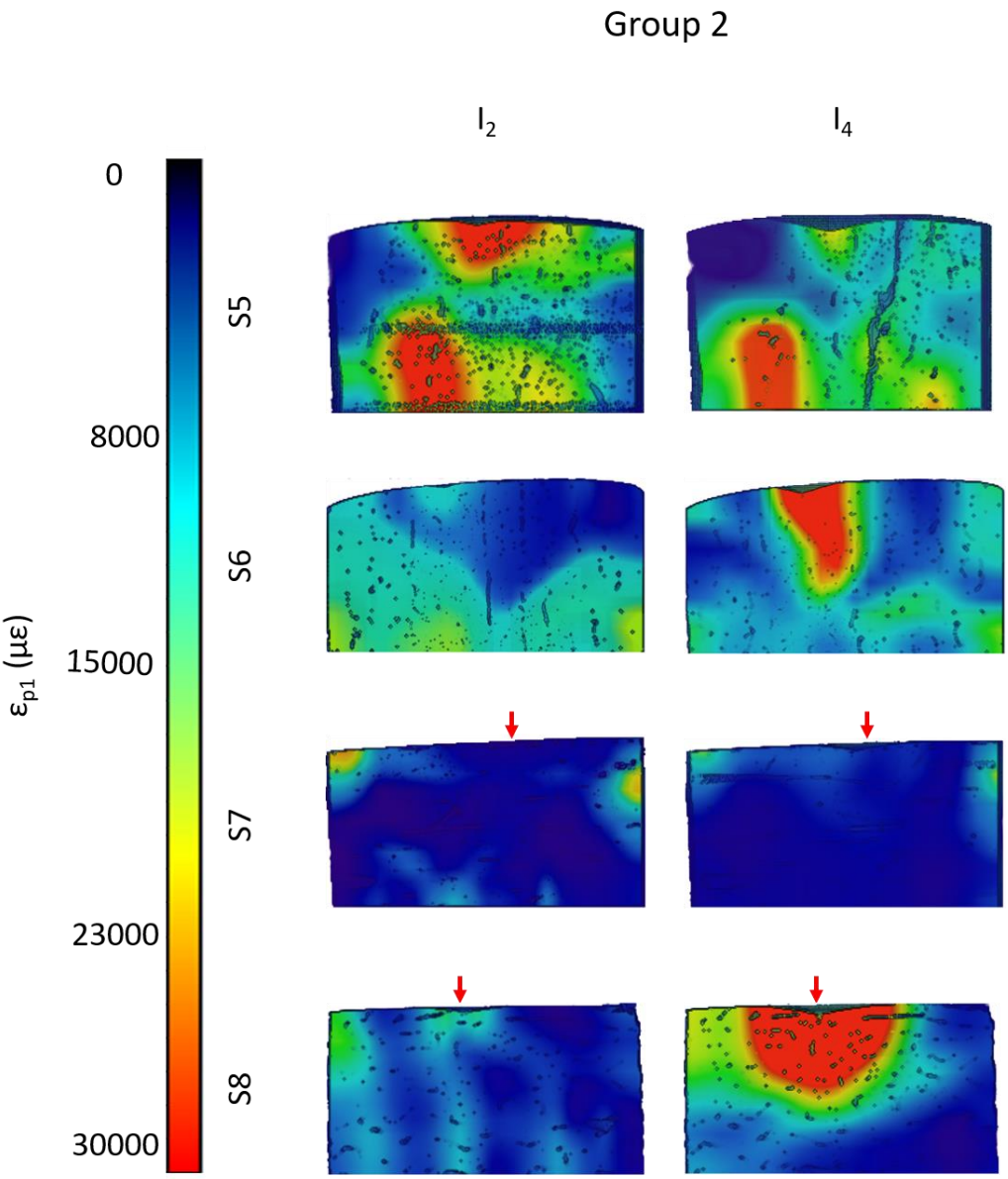

Figure A2: Visualisation of the strain maps (ε_{p1}) in axial (S5, S6) and transverse (S7, S8) specimens with two indentation steps (I_2 and I_4, Group 2). In S5 tensile strain reached 30000 με at I_2 leading to crack formation at I_4. S6 and S8 experienced high tensile strain values reaching ~30000 με closer to the imprint. In S7, the strain remained almost the same at I_2 and I_4 steadily as the depth of the defect increased. Red arrows pointing at indentation imprint

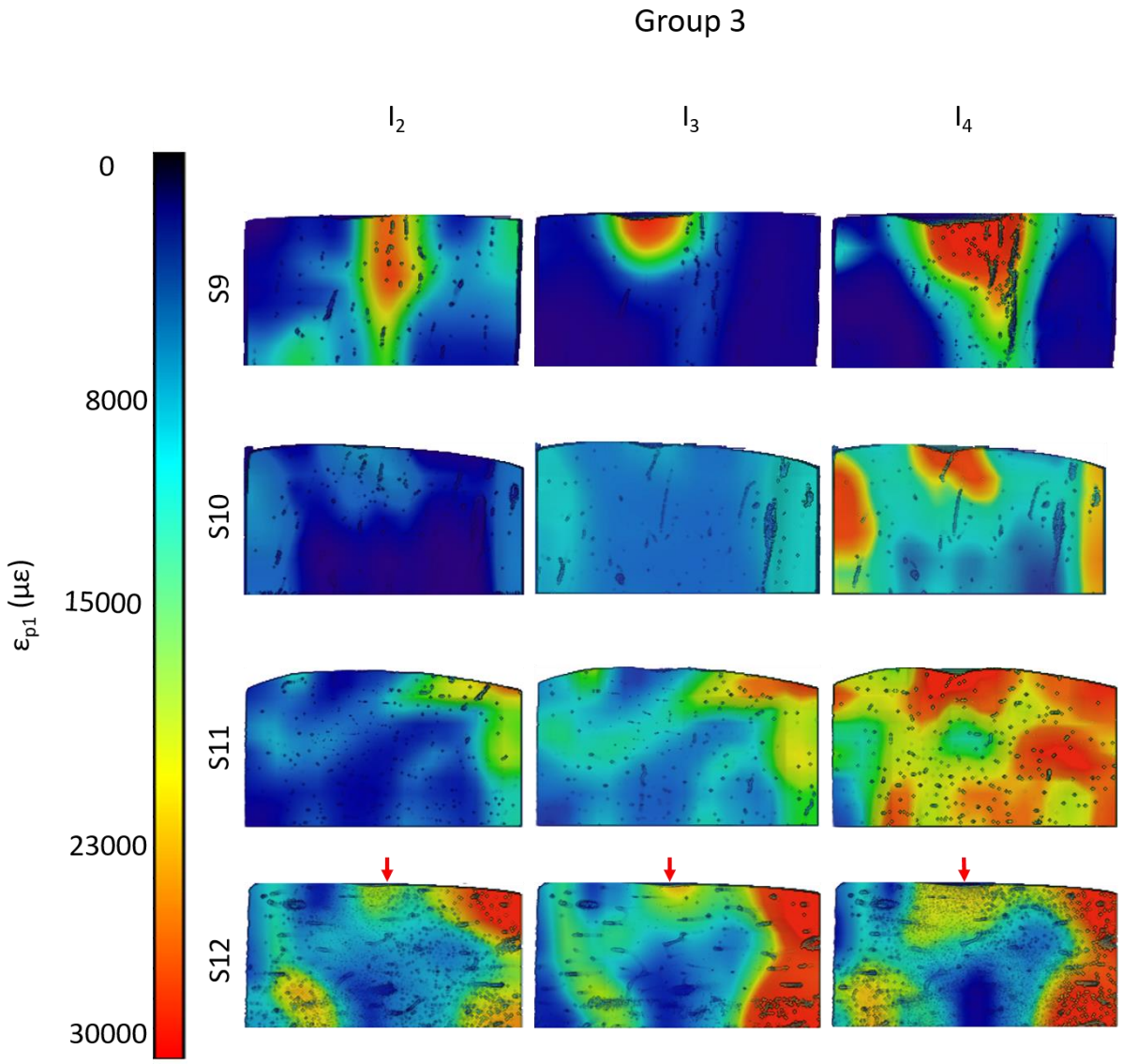

Figure A3: Visualisation of the strain maps (ε_{p1}) in axial (S9, S10) and transverse (S11, S12) specimens with three indentation steps (I_2, I_3 and I_4, Group 3). In S9 tensile strain reached 26000 με at I_2 leading to crack formation at I_4. Tensile strain in S10 increased at I_4 reaching 23000 με in the imprint area and on the sides. S11 and S12 experienced high tensile strain values in the borders of the specimens exceeding ~20000 με. The strain expanded towards the centre of the specimens at I_4.

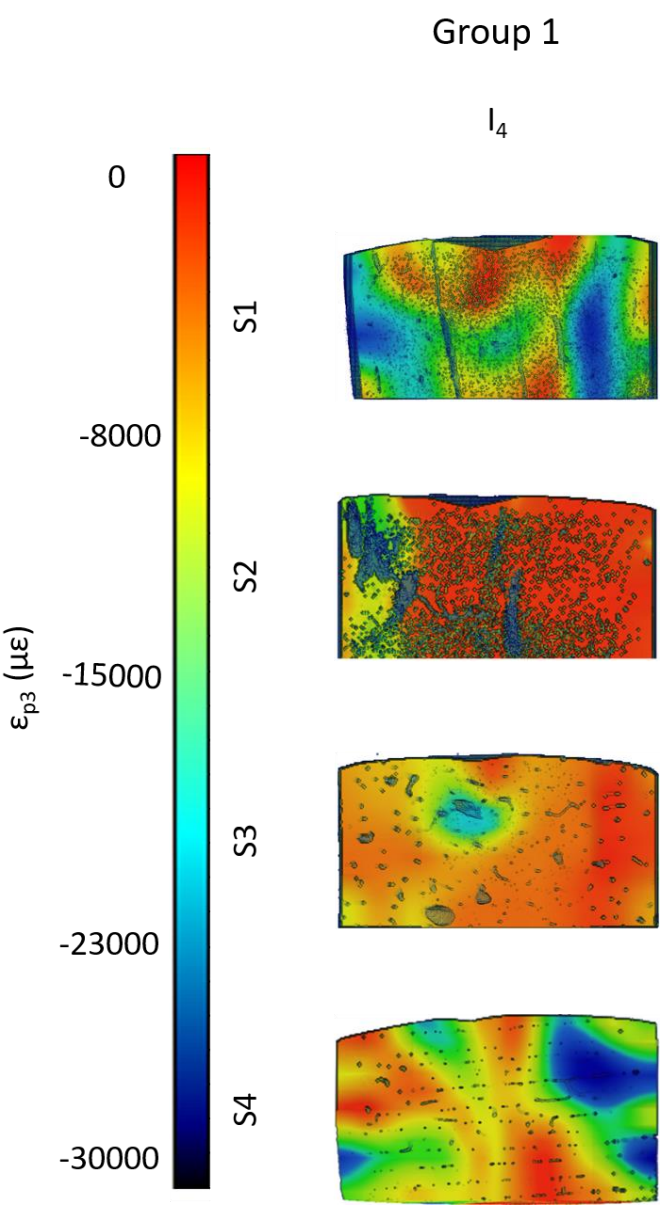

Figure A4: Visualisation of the strain maps (ε_{p3}) in axial (S1, S2) and transverse (S3, S4) specimens with one indentation step (I_4, Group 1). S1 and S2 experienced a combination of low and high compressive strain values reaching ~-14000 με locally at the microcracks. In S3 compressive strain of ~-20000 με was present underneath the indentation region. In S4 a combination of high and low compressive strain was displayed with highest values in the borders reaching ~-26000 με.

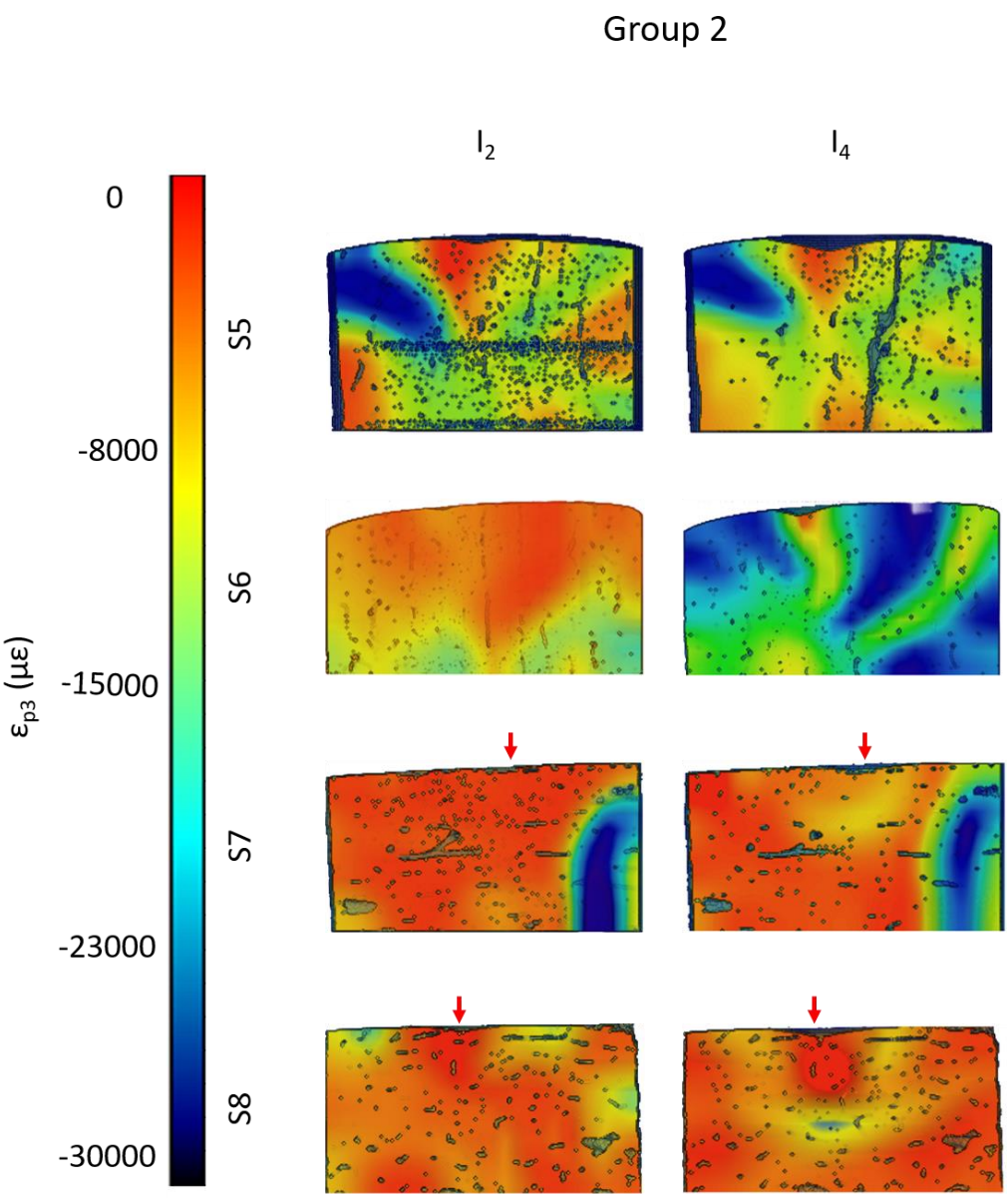

Figure A5: Visualisation of the strain maps (ε_{p3}) in axial (S5, S6) and transverse (S7, S8) specimens with two indentation steps (I_2 and I_4, Group 2). In S5 microcrack formed at I_4 indentation stage, with high concentration of compressive strain at the borders (~-26000 με). S6-8 showed similar values of ε_{p3} at I_2 not exceeding -4000 με overall, with some compressive strain concentration in the borders of their volume. S6 experienced an increase at I_4 reaching ~-28000 με around the imprint area. In S7 and S8 the area underneath the imprint displayed compressive strain of ~-9000 με and ~-16000 με respectively.

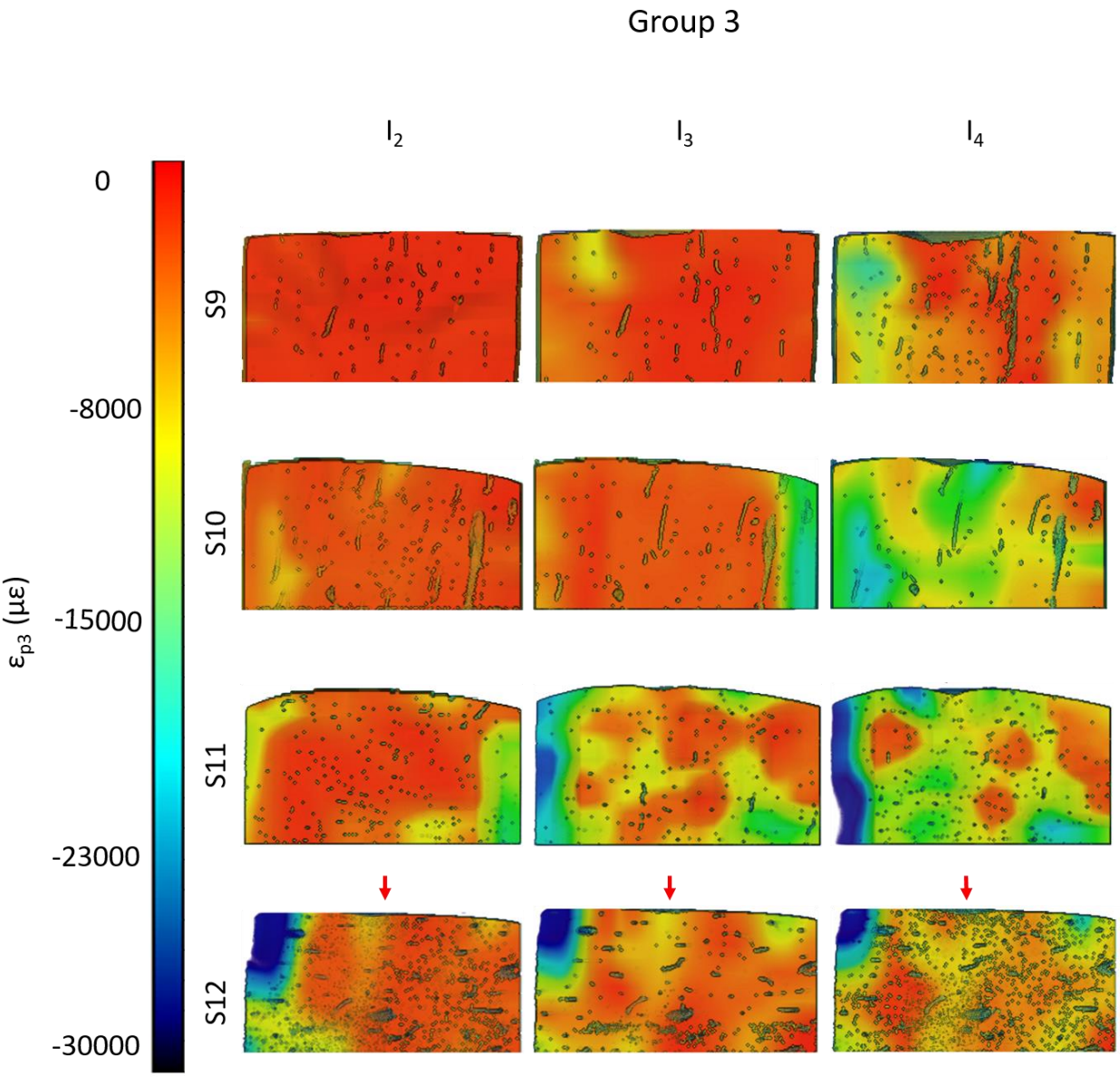

Figure A6: Visualisation of the strain maps (ε_{p3}) in axial (S9, S10) and transverse (S11, S12) specimens with three indentation steps (I_2, I_3 and I_4, Group 3). In S11 microcrack formed at I_4 indentation stage, with high concentration of compressive strain at the borders (~-14000 με). S10 exhibited elevated compressive strain at the indentation site at I_4 (-18000 με). In S11 and S12 the strain reached maximum values of strain ~-26000 με and ~-29000 με respectively locally.

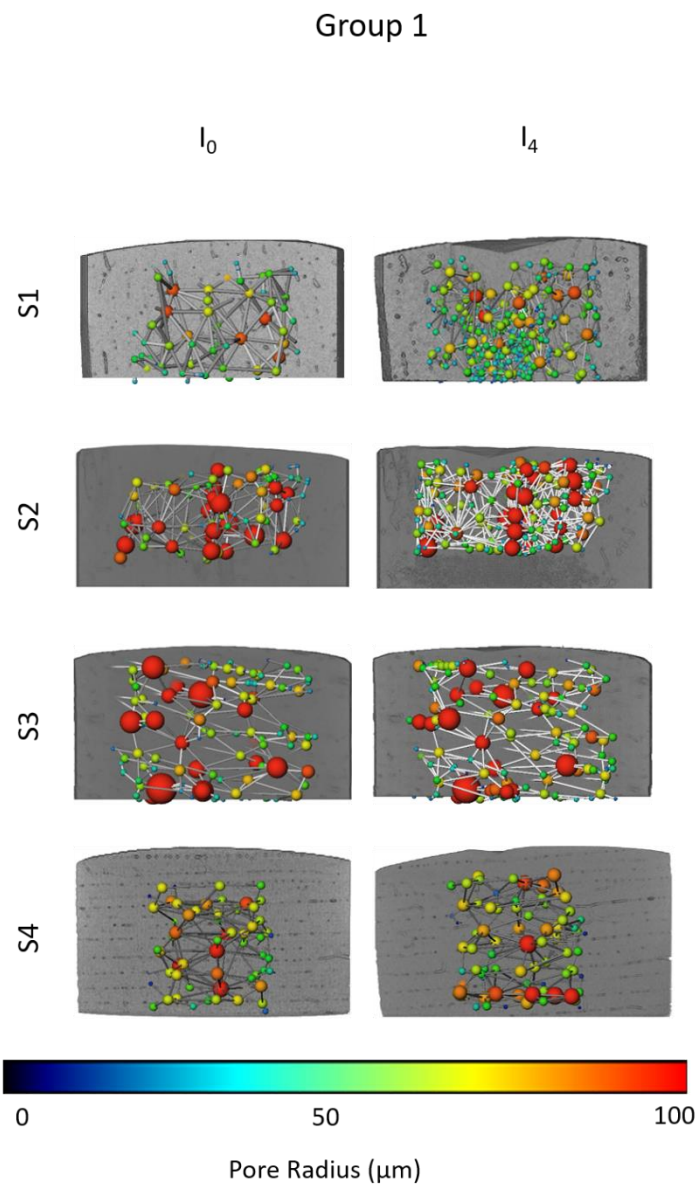

Figure A7: Visualisation of pore network in the middle of the volume of Group 1 with one indentation stage, axial specimens: S1, S2, transverse specimens: S3, S4. S1 and S2 formed microcracks at I_4.

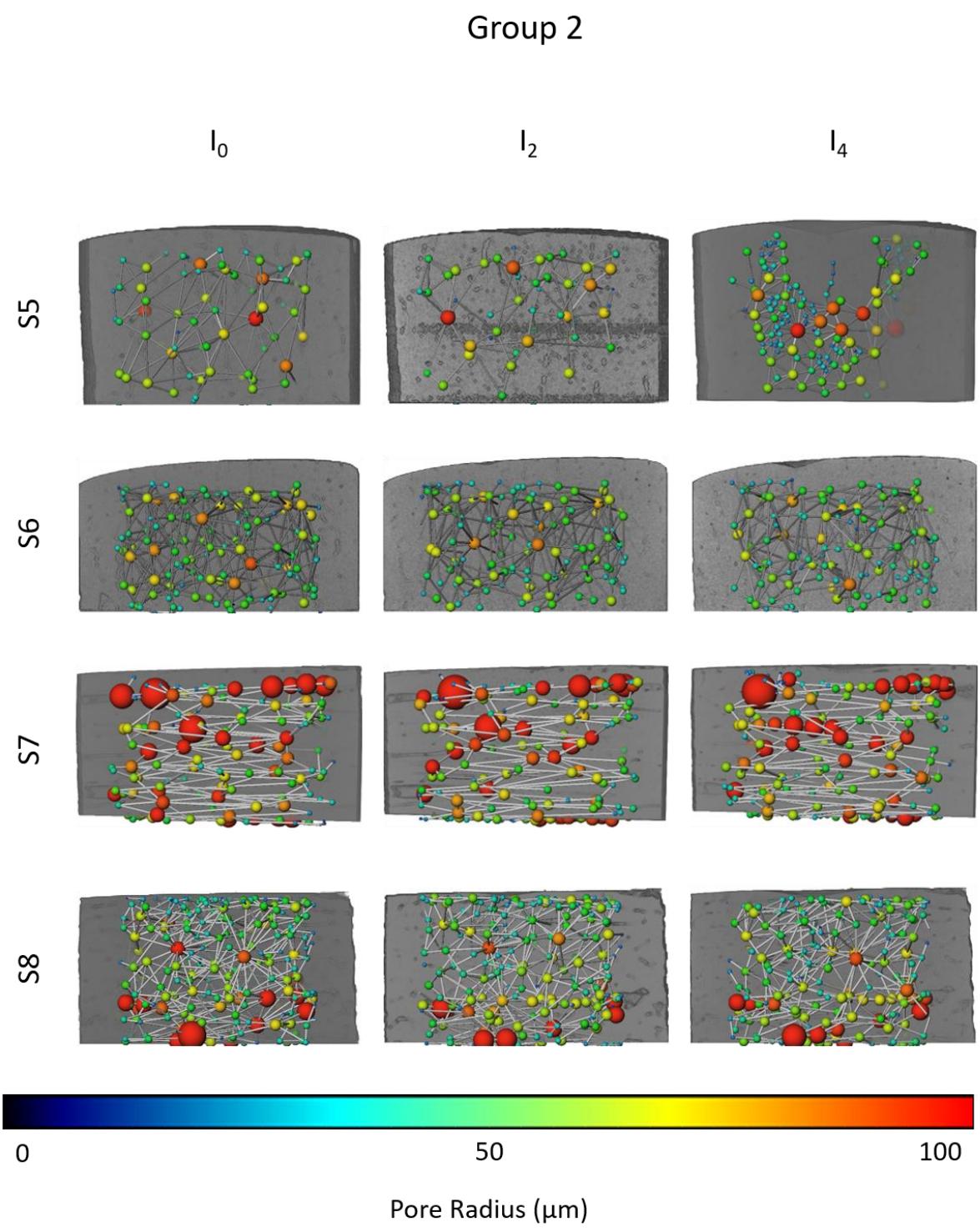

Figure A8: Visualisation of pore network in the middle of the volume of Group 2 with two indentation stages, axial specimens: S5, S6, transverse specimens: S7, S8. S5 formed microcracks at I_4.

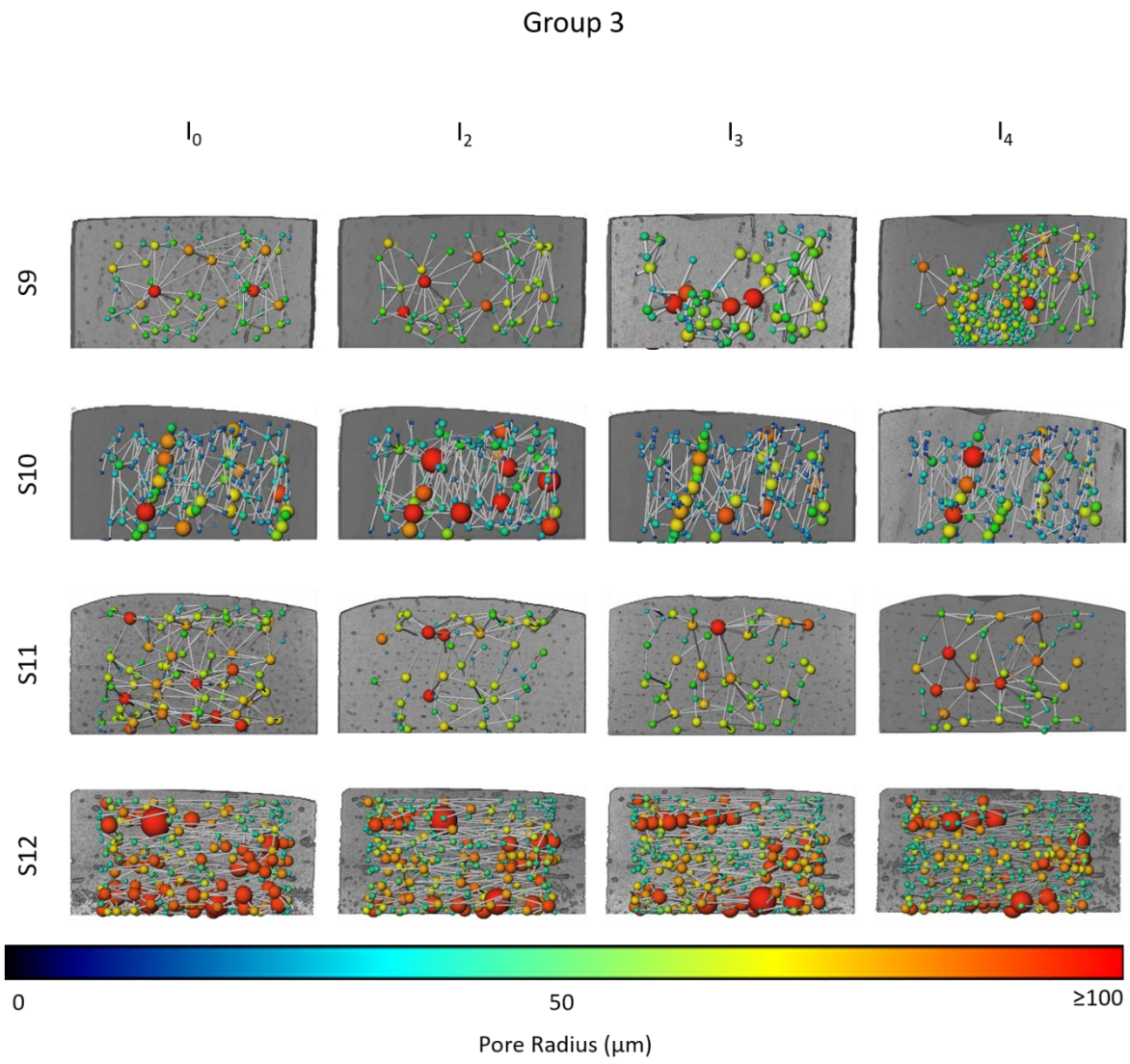

Figure A9: Visualisation of pore network in the middle of the volume of Group 3 with three indentation stages, axial specimens: S9, S10, transverse specimens: S11, S12. S9 formed microcracks at I_3 propagating further at I_4.

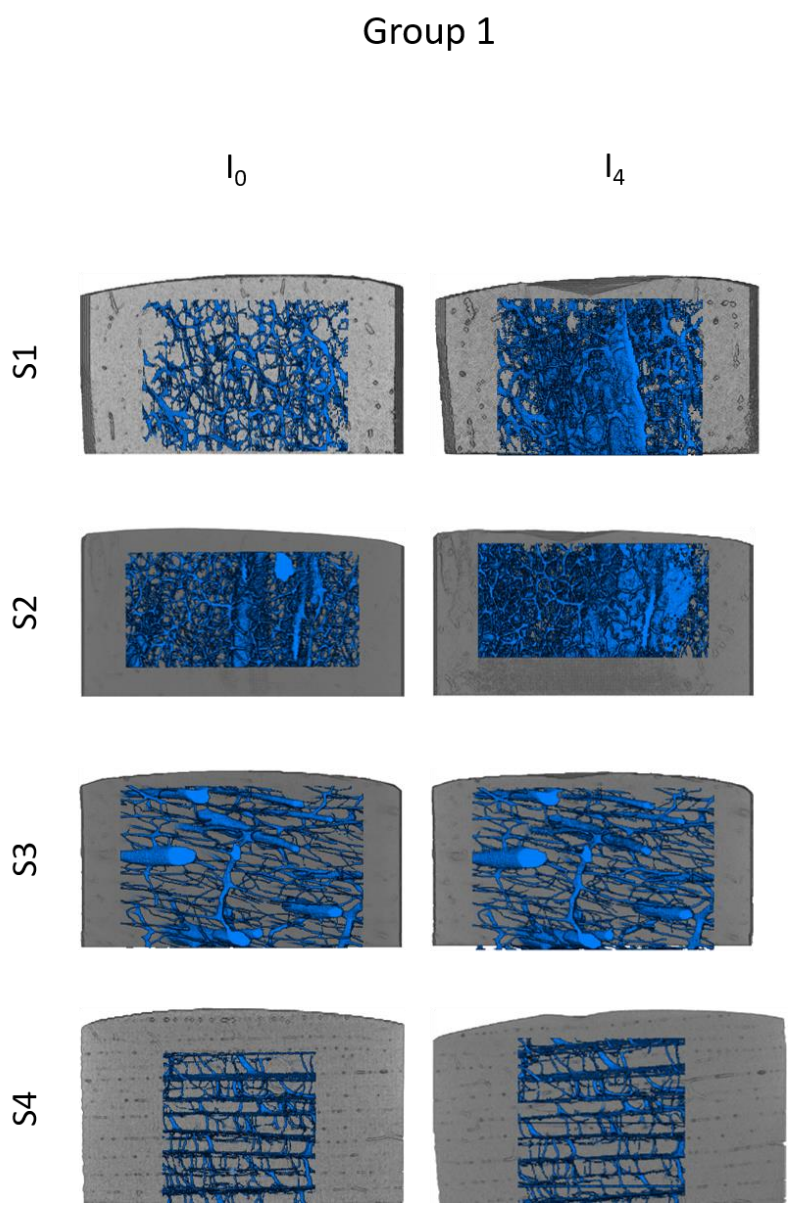

Figure A10: Visualisation of canal network in the middle of the volume of Group 1 with one indentation stage (I_4), axial specimens: S1, S2, transverse specimens: S3, S4. S1 and S2 formed microcracks at I_4. Haversian canals perpendicular to the indentation surface shown at S3 and S4

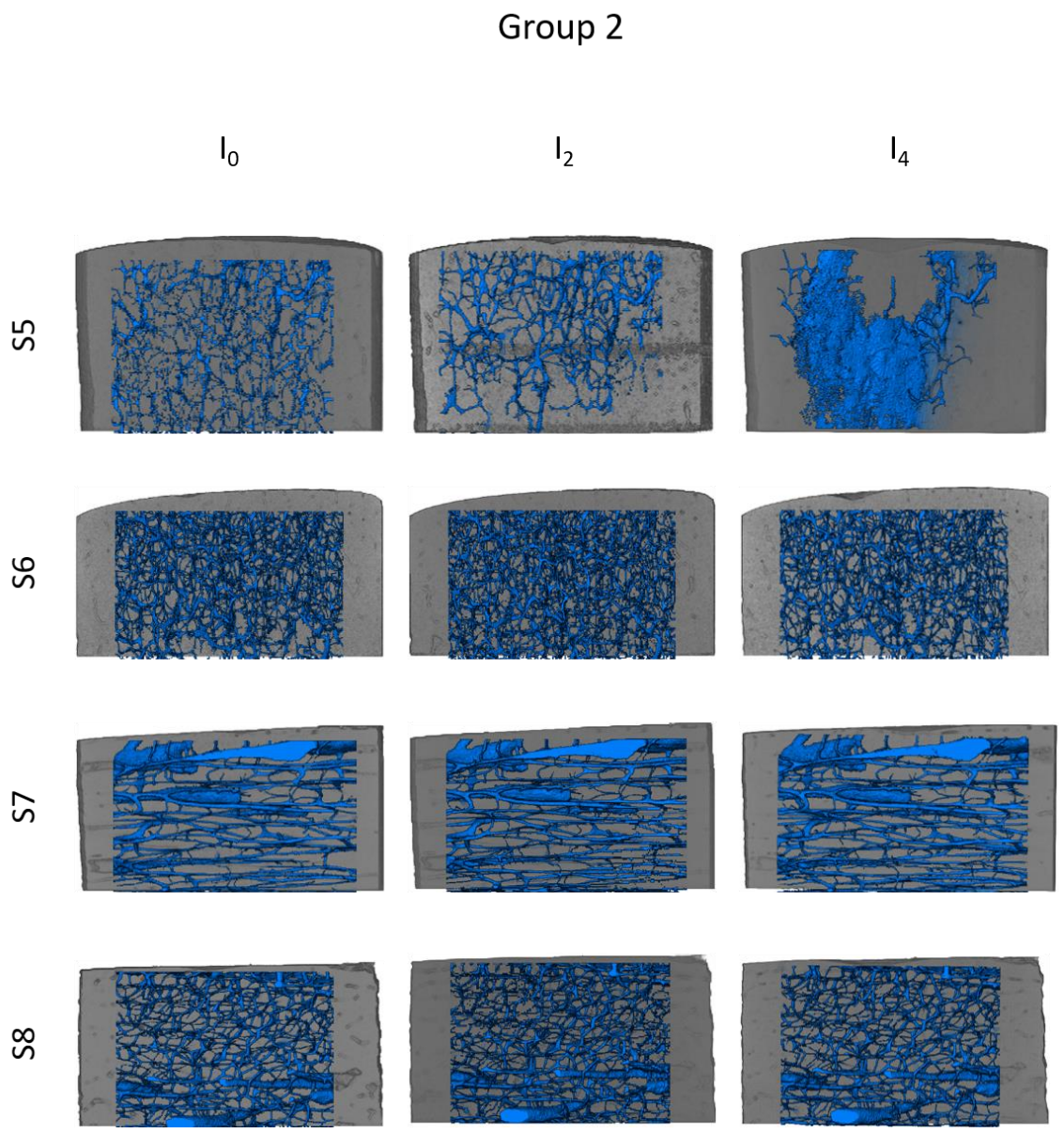

Figure A11: Visualisation of canal network in the middle of the volume of Group 2 with two indentation stages (I_2 and I_4), axial specimens: S5, S6, transverse specimens: S7, S8. S5 formed microcracks at I_4. Haversian canals perpendicular to the indentation surface shown at S7 and S8.

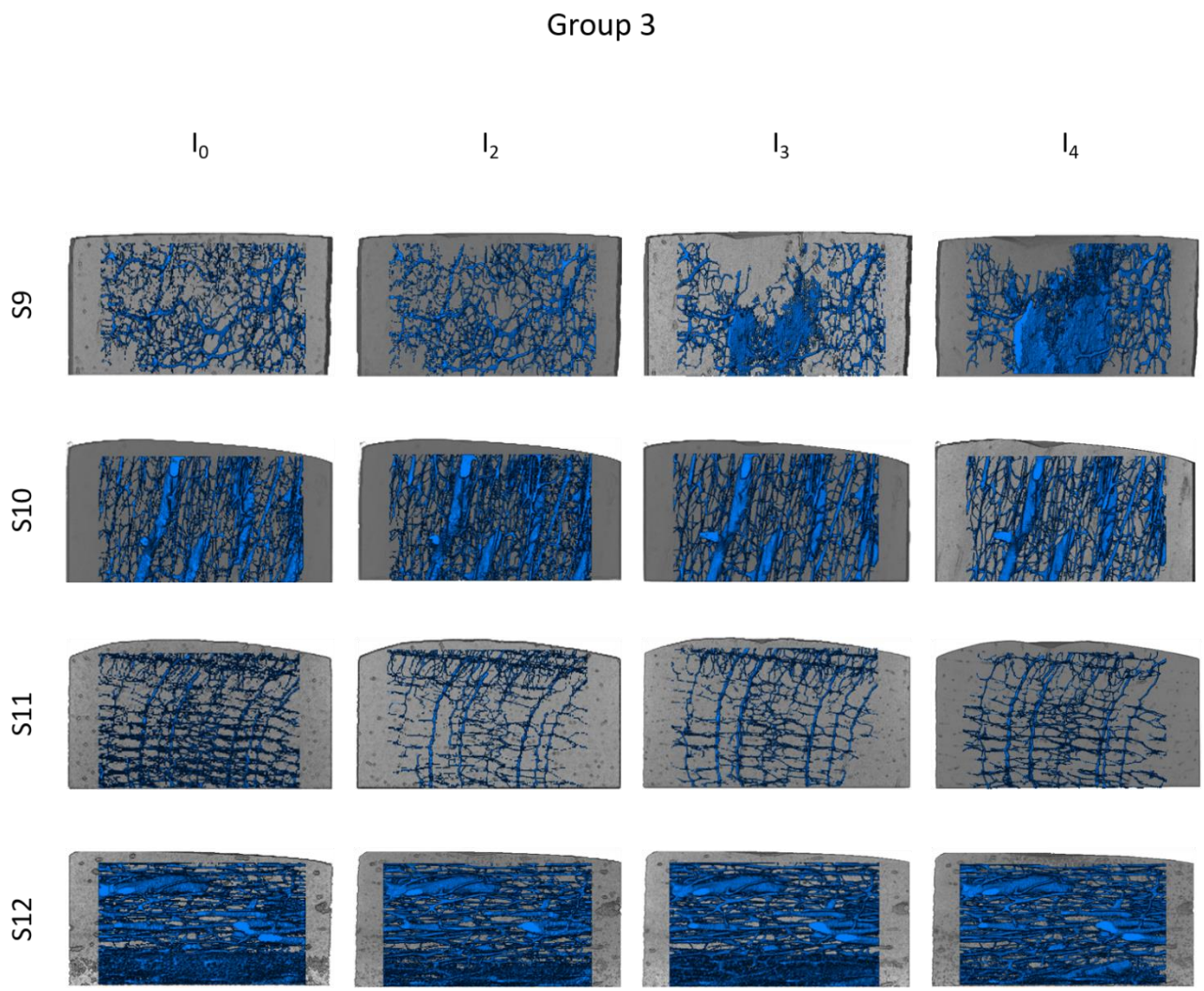

Figure A12: Visualisation of canal network in the middle of the volume of Group 3 with two indentation stages (I_2, I_3 and I_4), axial specimens: S9, S10, transverse specimens: S11, S12. S9 formed microcracks at I_3 propagating further at I_4. Haversian canals perpendicular to the indentation surface shown at S12.

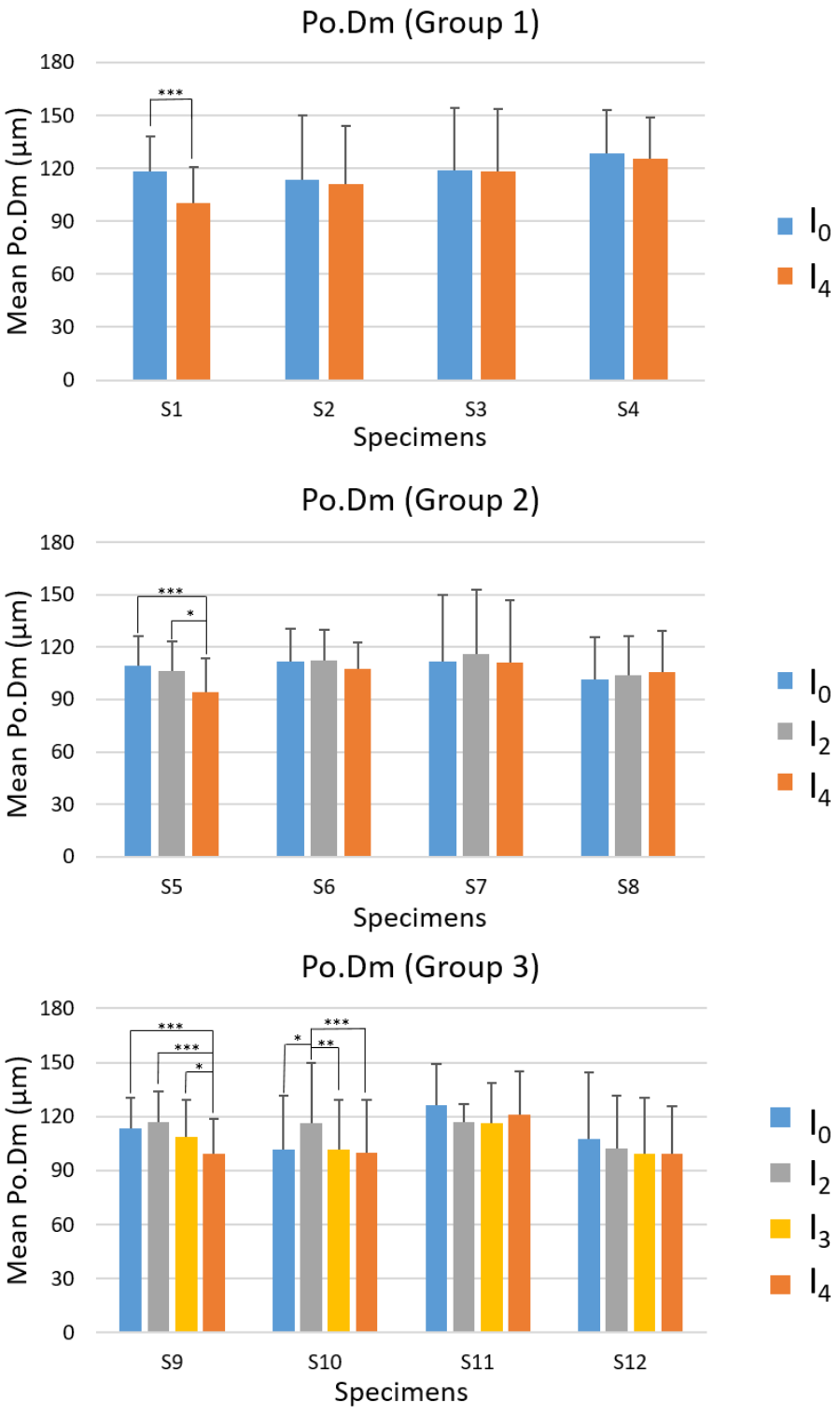

Figure A13: Graphical analysis of the mean pore network diameter (Po.Dm) of all the specimens in the different groups. Blue bar: mean Po.Dm at I_0 prior to defect; grey bar: mean Po.Dm at I_2 after 0.2 mm tip displacement; yellow bar: mean Po.Dm at I_3 after 0.3 mm tip displacement; orange bar: mean Po.Dm at I_4 after 0.4 mm tip displacement. The significant difference between the indentation stages was estimated with a Kruskal-Wallis test.

1st principal strain

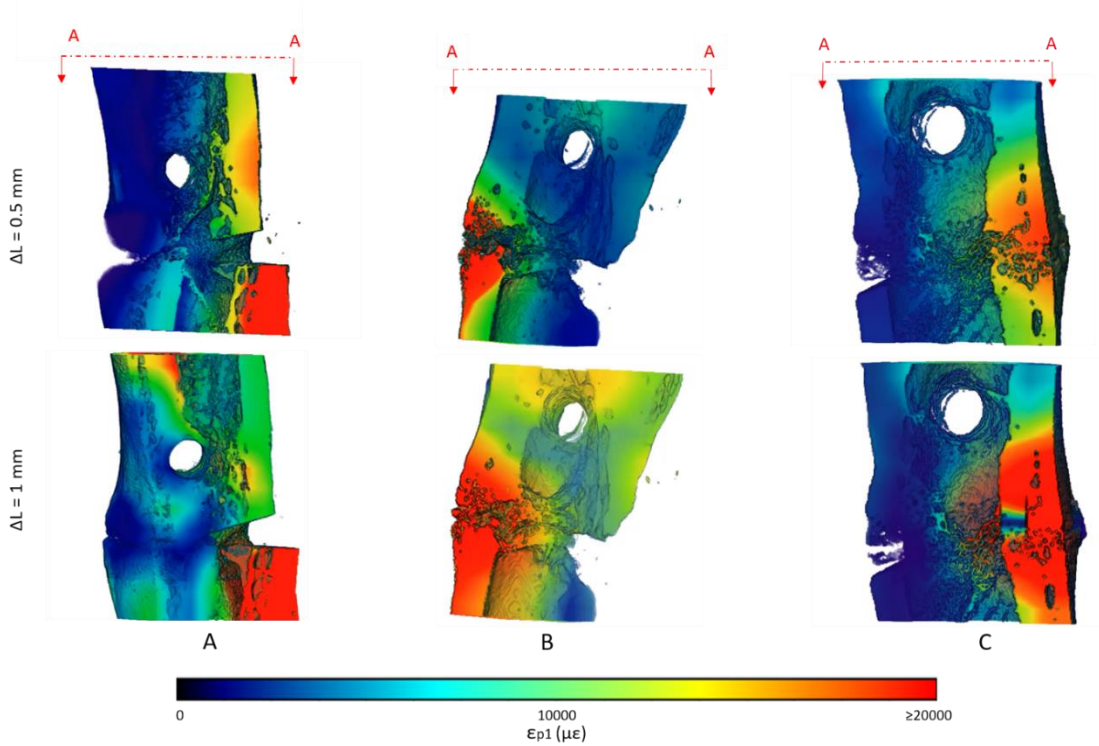

Figure 13: DVC analysis of 1 mm osteotomy gap, showing ε_{p1} of cross sections (A-A) in the ROIs of S2 (A), S3 (B) and S4 (C) in the first and second compression steps (top and bottom row, respectively)

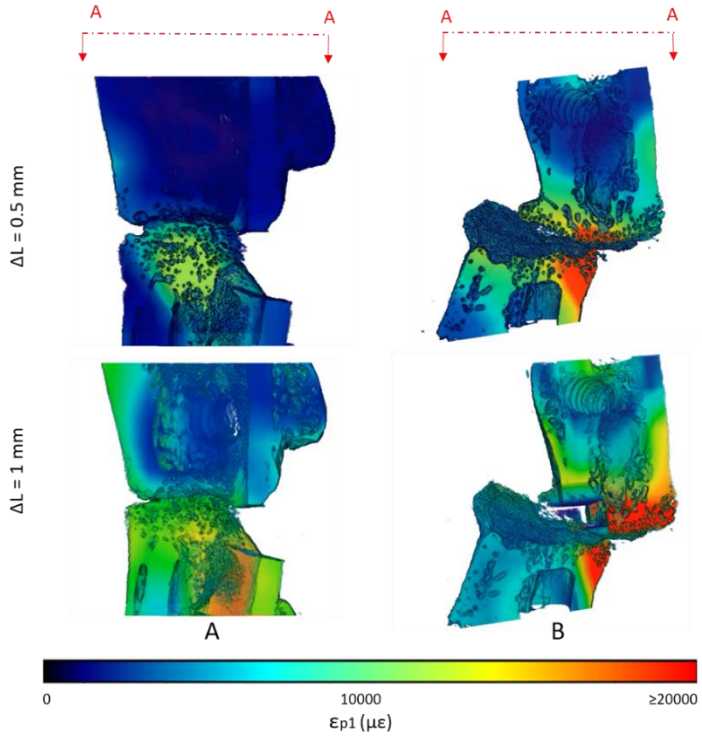

Figure A14: DVC analysis of 2 mm osteotomy gap, showing ε_{p1} of cross sections (A-A) in the ROIs of S6 (A) and S7 (B) in the first and second compression step (top and bottom row respectively)

Curriculum Vitae

Aikaterina Karali

Education

2016-2019	**PhD Student in Biomechanics (School of Mechanical and Design Engineering, University of Portsmouth)**
2011-2016	**MEng Mechanical Engineering University of Portsmouth**

Journal papers (published)

Peña Fernández, M., Kao, A., Karali, K., Bodey, A., Dall'Ara, E., Blunn, G., Barber, A., Tozzi, G., (2018). Preservation of bone tissue mechanics with temperature control for *in situ* SR-microCT experiments. Materials, 11(11), 2155, doi: 10.3390/ma11112155.

Journal papers (in preparation)

Aikaterina Karali, Enrico Dall'Ara, Jurgita Zekonyte, Alexander P. Kao, Gordon Blunn, Gianluca Tozzi, (2019). Effect of Radiation-Induced Damage of Trabecular Bone Tissue Evaluated Using Microindentation. To be submitted to J Biomech.

Aikaterina Karali, Alexander P. Kao, Jurgita Zekonyte, Gordon Blunn, Gianluca Tozzi, (2019). Mechanical and morphometric evaluation of cortical bone through in situ XCT indentation. To be submitted to JBBM.

Aikaterina Karali, Alicia Nadal, Alexander P. Kao, Richard Meeson, Marta Roldo, Gordon Blunn, Gianluca Tozzi, (2019). Micromechanical Evaluation of Regenerated Bone in rat Femurs Using Digital Volume Correlation. Submitted to J Mic.

Conference Attendance

A. Karali, A. Nadal, R. Meeson, A. P. Kao, G. Blunn, G. Tozzi, 2019. "Micomechanical evaluation of regeneratred regenerated bone in rat femurs using digital volume correlation", oral presentation, 25th Congress of the European Society of Biomechanics, Vienna, Austria.

A. Karali, A.P. Kao, J. Zekonyte, G. Blunn, G. Tozzi, 2019. "Mechanical and morphometric evaluation of cortical bone through in situ XCT indentation", poster presentation, Research and Innovation Conference, Portsmouth, UK

A. Karali, A. Nadal, R. Meeson, A. P. Kao, G. Blunn, G. Tozzi, 2019. "Micomechanical evaluation of regeneratred regenerated bone in rat femurs using digital volume correlation", oral presentation, ToScA, Southampton, UK.

A. Karali, E. Dall'Ara, J. Zekonyte, A. P. Kao, G. Tozzi, 2018. "Effect of Radiation-Induced Damage of Trabecular Bone Tissue Evaluated Using Microindentation", oral presentation, 8th World Congress of Biomechanics, Dublin, Ireland.

A. Karali, E. Dall'Ara, J. Zekonyte, A. P. Kao, G. Tozzi, 2018. "Mechanical Property Radiation-Induced-Damage Examination of Trabecular Bone Tissue Through Nano-Indentation and Digital Volume Correlation", oral presentation, Annual Research and Innovation Conference University of Portsmouth.

A. Karali, E. Dall'Ara, J. Zekonyte, A. Barber, G. Tozzi, 2017. "Nanoindentation and Digital Volume Correlation of trabecular bone tissue", oral presentation, PGEM BSSM, Imperial College London.

A. Karali, E. Dall'Ara, J. Zekonyte, A. Barber, G. Tozzi, 2017. "Nanoindentation and Digital Volume Correlation of trabecular bone tissue", poster presentation, ToScA2017, University of Portsmouth.

Awards

Travel Award, European Society of Biomechanics (ESB) 2019.

Ethics form

FORM UPR16

Research Ethics Review Checklist

UNIVERSITY OF PORTSMOUTH

Please include this completed form as an appendix to your thesis (see the Research Degrees Operational Handbook for more information

Postgraduate Research Student (PGRS) Information			**Student ID:**	638296	
PGRS Name:	Aikaterina Karali				
Department:	SMDE	**First Supervisor:**	Dr Gianluca Tozzi		
Start Date: (or progression date for Prof Doc students)	03/10/2016				
Study Mode and Route:	Part-time ☐	MPhil ☐	MD ☐		
	Full-time ☒	PhD ☒	Professional Doctorate ☐		

Title of Thesis:	Multi-scale evaluation of bone combining indentation, in situ XCT mechanics and digital volume correlation
Thesis Word Count: (excluding ancillary data)	~45000

If you are unsure about any of the following, please contact the local representative on your Faculty Ethics Committee for advice. Please note that it is your responsibility to follow the University's Ethics Policy and any relevant University, academic or professional guidelines in the conduct of your study

Although the Ethics Committee may have given your study a favourable opinion, the final responsibility for the ethical conduct of this work lies with the researcher(s).

UKRIO Finished Research Checklist:
(If you would like to know more about the checklist, please see your Faculty or Departmental Ethics Committee rep or see the online version of the full checklist at: http://www.ukrio.org/what-we-do/code-of-practice-for-research/)

a) Have all of your research and findings been reported accurately, honestly and within a reasonable time frame?	YES NO	☒ ☐
b) Have all contributions to knowledge been acknowledged?	YES NO	☒ ☐
c) Have you complied with all agreements relating to intellectual property, publication and authorship?	YES NO	☒ ☐
d) Has your research data been retained in a secure and accessible form and will it remain so for the required duration?	YES NO	☒ ☐
e) Does your research comply with all legal, ethical, and contractual requirements?	YES NO	☒ ☐

Candidate Statement:		
I have considered the ethical dimensions of the above named research project, and have successfully obtained the necessary ethical approval(s)		
Ethical review number(s) from Faculty Ethics Committee (or from NRES/SCREC):		1018E
If you have *not* submitted your work for ethical review, and/or you have answered 'No' to one or more of questions a) to e), please explain below why this is so:		
Signed *(PGRS)*:	Aikaterina Karali	**Date: 14/10/2019**

UPR16 – April 2018